Study of the stress state and failure in adhesive joints with composite materials

With the increasing demand for composite materials by the industry, the adhesive joints emerge as an attractive alternative to traditional mechanical joints. The latter require as a preliminary step, the drilling of the laminates with consequent damage to the fibres, increasing the weight of the structure and facilitating the development of galvanic corrosion, among other problems. Currently, there are adhesives with excellent mechanical properties and wide temperature ranges, designed for such applications.

This PhD Thesis focused, essentially, on the study of the local stress state of a bimaterial corner which typically appears in double lap joints with two plates made of a carbon fibre laminate and one plate of aluminium. To narrow the scope of the methodology to be applied, initially several important aspects of the problem were analyzed. In particular, the three-dimensional elastic study of such joint, followed by a two-dimensional elastoplastic analysis, the inclusion of the influence of curing temperature and comparative analysis of two manufacturing processes were carried out.

This work culminated with the proposition of a failure criterion based on critical values of generalized fracture toughness for multimaterial corners, with the development and accomplishment of a test method for determination of these values. Such testing methodology was inspired by the well-known Brazilian Test. Finally, the analyses of these new specimens under fatigue loading allowed the reduction of the load levels, the possible local effects of yielding and permitted the development of the knowledge of the stress state as well as the failure of the corner under study.

The proposed failure criterion has been experimentally evaluated with specimens of real adhesive joints, giving an excellent agreement.

Ph.D. Thesis by Daniane Vicentini, University of Seville 2012

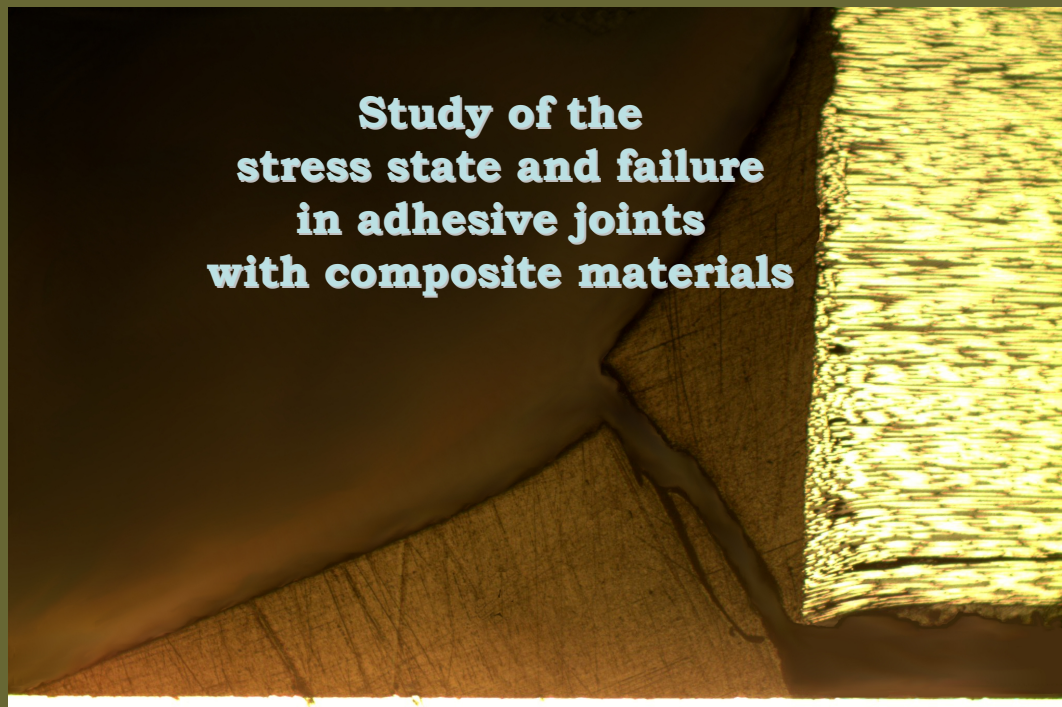

Ph.D. Thesis by
Daniane Franciesca Vicentini

February 2012

UNIVERSITY OF SEVILLE

School of Engineering

STUDY OF THE STRESS STATE AND FAILURE IN ADHESIVE JOINTS WITH COMPOSITE MATERIALS

Thesis presented in the University of Seville as a part of the requirements to obtain the PhD academic degree in Advanced Design in Mechanical Engineering, in fulfilment of the requirements for the European Doctorate Mention.

Author: DANIANE FRANCIESCA VICENTINI

Advisors: ALBERTO BARROSO CARO,

VLADISLAV MANTIČ LEŠČIŠIN,

FEDERICO PARÍS CARBALLO

Keywords: adhesives, composites, composite materials, adhesively bonded joints, double lap joint, aeronautic industry, stress state, plasticity, 3D edge effect, temperature, cure, curing stress, stress relaxation, Brazilian Test, generalized stress intensity factors, fatigue, multimaterial corners, manufacturing processes.

Revised version, June 2014.

First version printed on Seville in February 2012.

ISBN-13: 978-84-697-0738-8

ISBN-10: 84-697-0738-8

Acknowledgements

In these pages, I would like to express my feelings and personal thanks over these years, during the execution of this work and even prior to this stage.

Firstly, I would like to register my deep gratitude for the Supreme Being who leads my existence and give me health, strength, hope and perseverance to keep my mind focused on the objectives of this work.

I would like to express my deepest gratitude to my advisors, the Contracted Doctorate Professor Alberto Barroso Caro, for his patience and dedication; to Professor Vladislav Mantič and Professor Federico París for their support throughout these years, for their patience and confidence in me. I appreciate this opportunity afforded by them to me.

I am very grateful to CAPES (Coordenação de Aperfeiçoamento de Pessoal de Nível Superior), from the Brazilian Ministry of Education for the financial support through the process BEX 3933/06-7, without which, this work would not have been possible.

My thanks to the other colleagues and professors in the group who collaborated directly or indirectly with this work. In

particular, thanks to the Professor Rafael Picón for the valuable discussions on the subject of Plasticity and Alejandro for the help with my "first steps" with ANSYS. I am also grateful to the laboratory staff, without whom the extensive testing program of this Thesis would not have been fulfilled on time, especially to Jesus, Diego Canales, Antonio Cañas, Isabel, José Ramón, Professor Pepe Cañas and Justo. I would also like to thank Rocío and Ana Galindo for their kindness and patience spent in administration throughout these years.

I would like to acknowledge the Professors Manuel Doblaré, Andrew Crocombe, Marino Quaresimin, Dominique Leguillon and Henrique Graciani who composed the examining committee for judgment of this work and valuable discussions around the subject.

After so many months sharing the Ph.D. Students' Office, I could not forget to express my gratitude to the guys there; especially to the newest Assistant Professor Luis, Israel, Tom and Afonso for pleasant discussions and diverse help.

With regards to my stay in England, I am grateful to Professor Andy Crocombe for the confidence and attention devoted to my work. Special thanks must be made to Sugiman, Rahmah and Hilton, for their diverse help and friendship. Also I express my gratitude to Peter Haynes for the help in setting up the testing machine in the laboratory, and to Sandy and Tracy for the help

with paperwork and kindness. Finally, I would like to thank to Lynn Lawton for companionship during my stay in England.

I must to acknowledge EADS Chair in Seville for the financial support during the stay, without which it would not have been possible.

I am also very grateful to AICIA for the financial support during the extra period when I was finishing writing the Thesis.

Last of all, I would like to take this opportunity to give a special thanks to my family. To my parents, for celebrating with me the success, for sharing with me the difficulties and mainly for supporting me in the separation which has been necessary in order to fulfil this dream. Thanks for your love and understanding. Also, I would sincerely like to express my gratitude to Jean Carlo, my partner, for understanding and for supporting me. Thank you for the sacrifices you have made to stay with me, thank you for your love.

I would like to register my gratitude (in memoriam) to Professor Venturini for his dedication, many reports and infinite patience, which has led me to this Doctorate.

Thanks to ANSYS and CYTEC staff technical support for the attention received.

I would like to express my gratitude to the Spanish people for their hospitality and receptivity. Also, my thanks to the Brazilian

people, for contributing indirectly with the financial support of this work.

Dedico este trabalho

a Jean Carlo e aos meus pais.

“In those days, in Brazil,
to talk of inventing a flying-machine,
or dirigible balloon,
would have been to stamp one's self
as unbalanced and visionary.”

Alberto Santos Dumont

Index

d) Conference papers

List of symbols and abbreviations

AC	Autoclave
BEM	Boundary Element Method
BT	Brazilian Test
CFRP	Carbon Fibre Reinforced Polymer
CFRP-Al	CFRP and Aluminium
DLJ	Double Lap Joint(s)
DOF	Degree(s) of freedom
EPFM	Elastic Plastic Fracture Mechanic
FEM	Finite Element Method
GERM	Group of Elasticity and Strength of Materials (in Spanish)
GSIF	Generalized Stress Intensity Factor(s)
HPP	Hot Plate Press

LEFM	Linear Elastic Fracture Mechanics
LERM	Laboratory of Elasticity and Strength of Materials (in Spanish)
SG	Strain gauge(s)
A	Constant obtained by the least squares method
A_{lap}	Total area of the overlap (mm^2)
a_i^S	Vector component in Stroh formalism
B	Constant obtained by the least squares method
b	Power parameter for introduction of plasticity in ANSYS
b_i^S	Vector component in Stroh Formalism
C	Constant obtained by the least squares method
C_{ijkl}	Components of the stiffness tensor
D	Constant obtained by the least squares method
Dz	Damage zone (or crack) length

E	Young modulus
F	Constant obtained by the least squares method
f	Generic yield function in plasticity
f_{VM}	Von Mises yield function
f_{DP}	Drucker-Prager yield function
f_S	Arbitrary function in Stroh formalism
f_1, f_2, f_3	Approximated functions
f_{ij}^k	Angular shape function for stresses
$f_{BC}^{1\ up\ to\ 3}$	Functions in the Bigwood-Crocombe model
f_{GR}^1, f_{GR}^2	Functions in the Goland-Reissner model
f_{HS}^1, f_{HS}^2	Functions in the Hart-Smith model
f_V^1, f_V^2	Functions in the Volkersen model
f_W	Functions in the Williams model

$F_{\max}$	Failure load
F_{press}	Force to be applied on the overlap by the HPP
G	Shear modulus
G_1, G_2	Shear modulus (the index indicates the material 1 or 2, in Dundurs' parameters)
g_i^k	Angular shape functions for displacements
i, j, k	Index
I, II, III	Index
I_I	First stress invariant
I_{II}	Second stress invariant
J_{II}	Second deviatoric stress invariant
$K_{tg}, K_{tg}^C, K_{tg}^T$	Tangent modulus (from the bilinear uniaxial stress-strain curve), super index referring to tensile or compression
K_k	k-th GSIF (referred to the mode k)

K_k^{num}	k-th GSIF obtained from numerical analyses
K_k^{spec}	k-th GSIF computed from the experiment for the tested specimen
K_{kC}	Critical value of GSIF or generalized fracture toughness
K_*	GSIF associated with rigid body rotation
k_S	Yield strength in pure shear
L_a	Free-adherend length
L_o	Overlap length
M	Modulus (or absolute value) of measurement at point (see Fig. 6.27)
N	Number of cycles in fatigue
n	Number of terms
N_0	Number of cycles in which the first change is observed in the corner

N_{1mm}	Number of cycles necessary to the failure reaching at least 1 mm long
N_{3mm}	Number of cycles necessary to the failure reaching at least 3 mm long
P	Applied load per unit length
p	Pressure to be applied on the overlap (MPa)
$P_{\max}$	Maximum applied load in fatigue
$P_{\min}$	Minimum applied load in fatigue
P^{num}	Load used in the numerical analysis
p_S	Parameter in Stroh formalism
P^{spec}	Ultimate (compressive) load given from the BT
P_u	Ultimate static load
Pos_{final}	Final position of the cross head
Pos_{middle}	Middle position of the cross head
q	Von Mises equivalent stress

Q	Matrix containing components of the elastic tensor in Stroh formalism
R	Radius, or in Chapter 2, matrix containing components of the elastic tensor in Stroh formalism
r	Radius, in polar coordinate system (r,θ), where the parameter (stress or displacement component) is measured
R^{num}	Radius of the amplified corner in numerical analysis
R_S	Matrix containing components of the elastic tensor (in Stroh formalism)
R^{spec}	Radius of the BT specimen
R_L	Load ratio ($R_L = P_{\min}/P_{\max}$) in fatigue
S	Ultimate (tensile or compressive, according to the upper index) strength for composites
w	Width
t	Thickness
t_{a1}	CFRP laminate thickness

t_{a2}	Aluminium half-thickness
t_{a3}	Adhesive thickness
t^{num}	Thickness of the amplified corner in numerical analysis
t^{spec}	Thickness of the BT specimen
T	Final temperature or, in Chapter 2, matrix containing components of the elastic tensor in Stroh formalism
T_0	Initial temperature
u_i	Displacement component
z	Arbitrary equation in Stroh formalism.
α	Angle for load application
α_D	Dundurs' parameter
α^t	Thermal expansion coefficient of the material
β	Material constant (for plasticity)

β_D	Dundurs' parameter
Γ	Ratio of shear modulus of two materials (Dundurs' parameters)
$\gamma, \gamma_{DP}, \gamma_{RCY}$	Pressure sensitive parameter (for plasticity) which index is according to the Drucker-Prager or Raghava-Caddell-Yeh models
Δ	Ratio between the differences of measurements at the final and middle positions, and middle positions of the cross head in the considered range of data
Δ_0	Ratio (Δ) measured when the crack started
Δ_{1mm}	Ratio (Δ) measured when the crack reached 1 mm long
Δ_{3mm}	Ratio (Δ) measured when the crack reached 3 mm long
ΔT	Difference of thermal loading or temperature increment

θ	Angle measured according to a polar coordinate system (r,θ) of reference from the corner (where x would coincide with r axis)
κ, κ_1, κ_2	Elastic constant (s), the index referring to the material in Dundurs' work
λ	Ratio between the yield stress in compression and in tension test
λ_{DS}	Characteristic exponents used in Dempsey & Sinclair's study
λ_k	Characteristic exponent
λ_V	Characteristic exponent used in Vasilopoulos' study
λ_W	Characteristic exponent used in William's study
ν	Poisson's ratio
σ	Applied pressure
σ_{adm}	Admissible stress
σ_{ij}	Stress component

$\sigma_I, \sigma_{II}, \sigma_{III}$	Principal stresses
σ_m	Hydrostatic (or mean) stress
σ_r	Radial stress component
σ_θ	Circumferential stress component
$\sigma_{r\theta}$	Tangential stress component
σ_u	Ultimate strength of the material
σ_{eq}^{DP}	Drucker-Prager equivalent stress
σ_{eq}^{VM}	Von Mises equivalent stress
$\sigma_y, \sigma_y^T, \sigma_y^C$	Yield stress of the material (upper index for compression or tensile, when neglected the property is supposed the same in compression and tensile)
$\sigma_\perp$	Strength (for tensile stress) in the direction perpendicular to the load application in the BT
$\sigma_{x'y'}$	Shear stress in the overlap

$\sigma_{x'}$	Tensile stress in the overlap
$\sigma_{y'}$	Peel stress in the overlap
$\tau_{\max}$	Apparent shear strength
ϕ	Airy function
φ	Internal friction angle (material property for plasticity)
φ_i	Stress function component in Stroh formalism
ω	Angle of measurement at point

The upper index T or C is referred to tension or compression test. When it is not indicated, the same property is assumed.

Abstract

With the increasing demand for composite materials by the industry, the adhesive joints emerge as an attractive alternative to traditional mechanical joints. The latter require as a preliminary step, the drilling of the laminates with consequent damage to the fibres, increasing the weight of the structure and facilitating the development of galvanic corrosion, among other problems. Currently, there are adhesives with excellent mechanical properties and wide temperature ranges, designed for such applications.

This PhD Thesis focused, essentially, on the study of the local stress state of a bimaterial corner which typically appears in double lap joints with two plates made of a carbon fibre laminate and one plate of aluminium. To narrow the scope of the methodology to be applied, initially several important aspects of the problem were analyzed. In particular, the three-dimensional elastic study of such joint, followed by a two-dimensional elastoplastic analysis, the inclusion of the influence of curing temperature and comparative analysis of two manufacturing processes were carried out.

This work culminated with the proposition of a failure criterion based on critical values of generalized fracture toughness for multimaterial corners, with the development and accomplishment of a test method for determination of these values. Such testing methodology was inspired by the well-known Brazilian Test. Finally, the analyses of these new specimens under fatigue loading allowed the reduction of the load levels, the possible local effects of yielding and permitted the development of the knowledge of the stress state as well as the failure of the corner under study.

The proposed failure criterion has been experimentally evaluated with specimens of real adhesive joints, giving an excellent agreement.

Resumen

Con la creciente demanda de los materiales compuestos por parte de la industria, las uniones adhesivas se destacan como una atractiva alternativa frente a las tradicionales uniones mecánicas, que exigen como paso previo, el taladro de los laminados con el consiguiente daño a las fibras, incrementan el peso de la estructura, facilitan la aparición de la corrosión por par galvánico, entre otros inconvenientes. Actualmente existen en el mercado adhesivos con excelentes propiedades mecánicas y en rangos de temperatura amplios, pensados para este tipo de aplicaciones.

La presente Tesis Doctoral se centró, básicamente, en el estudio del estado tensional local de una esquina bimaterial que típicamente aparece en las uniones adhesivas de doble solape con placas hechas de un laminado de fibra de carbono y una placa de aluminio. Para acotar el alcance de la metodología a aplicar, inicialmente se analizaron varios aspectos importantes del problema. En particular, se llevó a cabo un estudio elástico tridimensional de dicha unión, seguido de un análisis elastoplástico bidimensional, inclusión de la influencia de la temperatura de curado y del análisis comparativo de dos procesos de fabricación.

Este trabajo culminó con la proposición de un criterio de fallo basado en valores críticos de tenacidad a fractura generalizada para esquinas multimateriales, junto con el desarrollo y realización de un método de ensayo para la determinación de estos valores. Dicha metodología de ensayo fue inspirada en el bien conocido Ensayo Brasileño. Finalmente, los análisis de estos nuevos especimenes con cargas a fatiga permitieron disminuir los niveles de carga, los posibles efectos locales de la plastificación y permitieron ampliar el conocimiento del estado tensional así como del fallo de la esquina bajo estudio.

El criterio de fallo propuesto se ha evaluado experimentalmente con especimenes de uniones adhesivas reales, dando un acuerdo excelente.

Resumo

Com o aumento da demanda dos materiais compósitos por parte da indústria, as juntas adesivas despontam como uma atraente alternativa em comparação com as tradicionais juntas mecânicas, que exigem perfuração prévia dos laminados com o consequente dano de fibras, incrementando o peso da estrutura e facilitando o aparecimento da corrosão galvânica, entre outros inconvenientes. Atualmente existem no mercado adesivos com excelentes propriedades mecânicas, capazes de suportar grandes diferenças de temperatura, pensados para este tipo de prestação.

Este trabalho centrou-se, basicamente, no estudo do estado tensional local de uma quina bimaterial que usualmente aparece nas juntas duplas coladas com duas placas de laminado de fibra de carbono e uma placa de aluminio. Para delimitar o alcance da metodologia aplicada, inicialmente analisaram-se vários aspectos importantes do problema. Mais especificamente, realizou-se um estudo elástico tridimensional da junta, seguido de uma análise elastoplástica bidimensional, a inclusão da influência da temperatura durante o processo de cura e da análise comparativa entre dois processos de fabricação.

Este trabalho culminou com a proposta de um critério de falha, baseado em valores críticos de tenacidade à fratura generalizada para quinas (ou cantos) multimateriais, juntamente com o desenvolvimento e realização de uma metodologia de ensaio para determinação destes valores. Tal metodologia foi inspirada no bem conhecido ensaio de compressão diametral (*Brazilian Test*). Finalmente, a análise destes novos exemplares submetidos à fadiga permitiram diminuir os níveis de carga, os possíveis efeitos locais de plastificação e permitiram ampliar o conhecimento do estado tensional, bem como do processo de falha na quina em estudo.

O critério de falha proposto foi aplicado experimentalmente em amostras de juntas adesivas reais, apresentando excelente concordância.

Chapter

1 Introduction

In recent decades, the applications of composite materials in industry have increased significantly due to their better specific (per unit weight) characteristics in strength, fatigue and impact. Their versatility, associated with the progressive comprehension of their behaviour under some particular situations, now enables composites to be used in electronic, transportation, aerospace, civil engineering (Mays & Hutchinson, 1992) and the sport industry. These materials have gained particular attention in the aeronautic industry where weight plays an important role. An example of this is the Airbus A350 and Boeing 787 in which approximately 50% of the weight of the materials employed in their manufacture are composites. Thus, from a mechanical point of view, there is a great interest in studying these materials and the methods by which they may be joined with non-composite materials such as the traditional metals employed in aircraft structures until now.

As an alternative choice to joining methods such as welding, bolting and riveting for aircrafts, adhesive joints present some advantages as to offer fewer points of stress concentrations, lighter structures, better fatigue and corrosion properties, and they also avoid problems arising in mechanization such as

cutting of the fibres. Thus, due to the increased use of composite materials by industry and the need for joining dissimilar materials, the dissemination of the utilization of adhesives is expected to continue in the future.

This work focuses on the mechanical performance and failure behaviour of adhesive joints between Carbon Fibre Reinforced Polymer (CFRP) and Aluminium using a structural adhesive that is common in the aeronautic industry. Citing Cognard (2006): "*If adhesives can work for aircraft parts, then they may be used for all other high performance applications*."

This explains why the Group of Elasticity and Strength of Materials (GERM, in Spanish) became interested in the comprehension of the stress state of adhesive joints in recent years, which gave rise to a previous Ph.D Thesis (Barroso, 2007). Barroso suggested some aspects for future development in order to complete this study. The current Thesis was proposed with this idea in mind, aiming to give continuity to the research line of the GERM.

1.1 Description of the problem

In this work a Double Lap Joint (DLJ) subjected to shear in tension is studied in detail. CFRP and Aluminium, the dissimilar adherends, were bonded by means of a structural adhesive. A

scheme of the geometry is presented in Fig. 1.1 (following the ASTM D3528, in the absence of a more specific standard to composite-metal adhesive joints) and will be referenced frequently in order to avoid repetition:

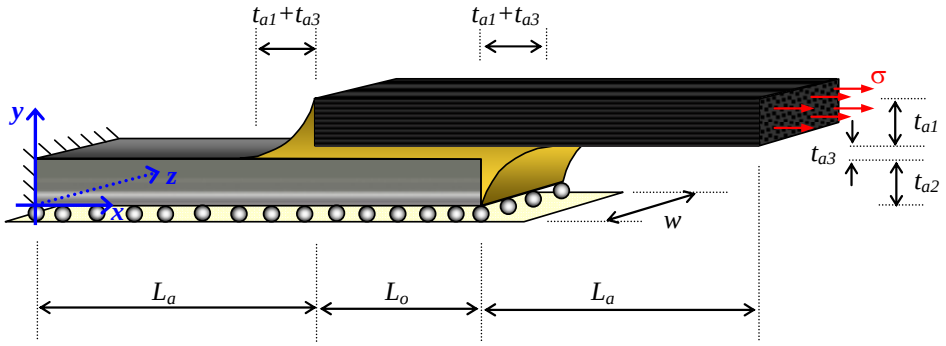

Fig. 1.1 – Geometry of the DLJ.

The dimensions, L_a, L_o are the free-adherend and overlap lengths respectively; t_{a1} and t_{a3} are the CFRP and Adhesive thicknesses respectively and w is the width of the specimen. t_{a2} is the half-thickness of the Aluminium plate, due to the symmetry in plane *xz*. σ is the applied tensile stress and the axes are considered according the representation in this figure (in a right-handed coordinate system). The fibres of the CFRP unidirectional laminate adherend are oriented along the *x* axis, and the symmetry in plane *xz* appears as indicated in Fig. 1.1.

According to previous evidence (Barroso, 2007), the failure starts at the critical corner which is located between the adhesive

and CFRP, more specifically in the (L_a, $t_{a2}+t_{a3}$, z) coordinates according the axes in Fig. 1.1. Thus, all the analyses in this work focus particularly on the stress state in this particular corner.

1.2 General review of the literature

In recent years, some proposals to determine the stress state and the assessment for failure prediction in adhesive joints have been presented. In the literature, several analytical works developed for adhesive lap joints can be found. Volkersen (1938) and de Bruyne (1944) are classic studies using shear-lag models. Goland & Reissner (1944) carried out what is generally recognised as the initial work in this field using beam models. In 1973, Wah introduced composites in the analysis of lap joints and Hart-Smith (1973[A, B, C], 1974), included other improvements for designing adhesive joints, such as the study of thermal stresses, joint efficiency, the effect of the stacking sequence, and unbalanced joints. More recently, the work of Tsai et al. (1996, 1998) in which the shear stresses are assumed to vary linearly through the thickness direction can be highlighted. Bigwood & Crocombe (1989, 1990) proposed a generic analysis from plate bending theory for different types of configurations under complex loading. A good review of the literature concerning the stress analysis of adhesive joints can be found in da Silva et al.

(2009[A]). Another interesting work by da Silva et al. (2009[B]) compares some of the analytical models against experiments, finding that models were overly conservative. All these works, however, aimed in part to predict the joint strength based on nominal stresses.

Other proposals using a fracture mechanics approach and motivated by the existence of stress singularities at the corners in the joints, have been presented by Gradin (1982) and Groth (1985, 1988), with significant contributions to the strength prediction of adhesive joints using local stress states. Their studies have a similar focus to that considered in this work. Based on the singular stress representation at the neighbourhood of the multimaterial corner, they defined a failure criterion based on critical values of Generalized Stress Intensity Factors (GSIF) which was verified experimentally. More recently, Hattori (1991) studied the strength[1] of single lap joints in terms of critical values of the stress intensity factors, having good agreement with experimental results.

[1] Although there is a clear difference between criteria based on toughness (associated with GSIF values) and strength (associated with nominal stress states), the word "strength" was kept in order to preserve the nomenclature adopted by Hattori.

Banks-Sills & Ashkenazi (2000) also evaluated the failure predictions of epoxy/glass specimens in terms of critical values of the stress intensity factors (and actually using Brazilian disk specimens), but considering a pre-crack introduced inside the multimaterial corner. In 2001, Dunn et al. presented an interesting study which compared the stress intensity factors from fracture mechanics in an open corner with different geometries at the corner tip.

For this work, "corner" is defined as a particular geometrical shape that can be either a wedge shape or sharp notch (in this case it is called open corner); or the point at which different perfectly bonded materials converge (closed corner).

In the vertex of the corner, the stresses predicted by the Linear Elasticity theory are unbounded. For example, Williams (1952) is taken as a classical work in the literature for plates with isotropic materials in state of plane stress. Changing the angles of the wedge, Williams obtained the stress state considering several boundary conditions. In 1988, Vasilopoulos obtained the solutions for the positive (real and imaginary) part of the singularities.

Later, Dempsey & Sinclair (1979, 1981) obtained the plane (plane strain and generalized plane stress) solution for bi and multimaterial isotropic corner. They presented analytic equations (as eigenvalue type) for the analysis of the singularities.

Mantič et al. (1997), using the Anisotropic Elasticity theory, presented a study of the singularities for orthotropic corners. This work represented an important contribution for composite material applications which later became a useful basis for Barroso's developments (2003, 2008), which extended the study for corners in presence of every type of material (including the degenerated materials in the Stroh formalism framework).

From a Linear Elastic Fracture Mechanics (LEFM) point of view, the corner is a prone point for failure initiation due to the unbounded character of local stresses involved. The asymptotic stress and displacement fields are given by a sum of n terms as:

$$\sigma_{ij}\left(r,\theta\right)=\sum_{k=1}^{n}\frac{K_k}{r^{1-\lambda_k}}f_{ij}^{k}\left(\theta\right) \tag{1.1}$$

$$u_i\left(r,\theta\right)=\sum_{k=1}^{n}K_k r^{\lambda_k}g_i^{k}\left(\theta\right) \tag{1.2}$$

where σ_{ij} and u_i are the component of stress and displacement respectively; which are dependent on the polar coordinates located at the corner tip. K_k are the GSIF, λ_k are the characteristic exponents and f_{ij}^{k}, g_i^{k} are the angular shape functions for stresses and displacements respectively. The value $\left(1-\lambda_k\right)$ is called order of singularity when $0<\lambda_k<1$.

Under certain conditions and geometry, if $\lambda_k = 0.5$, the expressions (1.1) and (1.2) could fall into the definition of a crack problem. For example, let us consider an infinite plate with isotropic material, subjected to different loading in its own plane. Considering only the first two terms of the expansions (1.1) and (1.2), and the crack tip located as indicated and according to the coordinate system in Fig. 1.2, this well known problem in mixed mode can be separated in a sum of terms (ignoring the superior order terms), being the components of the expressions (1.1) and (1.2) shown in Fig. 1.2 (in Broek, 1984 the expressions for stresses and displacements are presented in polar coordinate system). In this figure, G is the bulk modulus and $\kappa = 3 - 4\nu$ for plane strain and $\kappa = (3-\nu)/(1+\nu)$ for plane stress.

Despite the expressions in stresses and displacements, the analogy, in principle, can not be suitable for all concepts within the LEFM. For example the three deformation modes (opening, in-plane shear and out-of-plane shear) do not always correspond, in a generic multimaterial corner in pure mode I or II, to the symmetry or antisymmetry along the plane of the crack. This means that, for corners such as those considered here, the pure modes lack of physical sense and the concept of energy release rate loses the sense given by the LEFM (see Dunn et al., 2001 and Barroso, 2007 for further information).

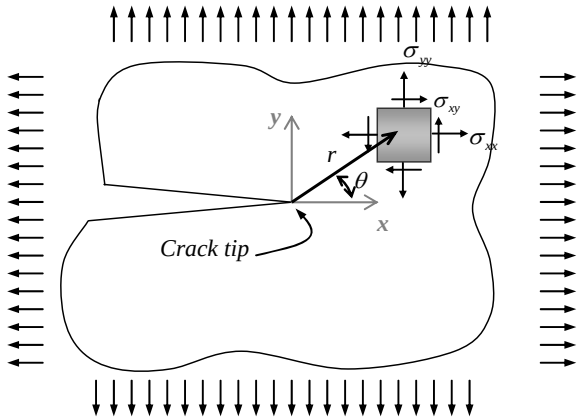

$$\sigma_{xx} = K_I\, r^{-0.5} \frac{1}{\sqrt{2\pi}} \cos\left(\frac{\theta}{2}\right)\left[1-\sin\left(\frac{\theta}{2}\right)\sin\left(\frac{3\theta}{2}\right)\right] + K_{II}\, r^{-0.5} \frac{1}{\sqrt{2\pi}} \sin\left(\frac{\theta}{2}\right)\left[-2-\cos\left(\frac{\theta}{2}\right)\cos\left(\frac{3\theta}{2}\right)\right]$$

$$\sigma_{xy} = K_I\, r^{-0.5} \frac{1}{\sqrt{2\pi}} \cos\left(\frac{\theta}{2}\right)\sin\left(\frac{\theta}{2}\right)\cos\left(\frac{3\theta}{2}\right) + K_{II}\, r^{-0.5} \frac{1}{\sqrt{2\pi}} \cos\left(\frac{\theta}{2}\right)\left[1-\sin\left(\frac{\theta}{2}\right)\sin\left(\frac{3\theta}{2}\right)\right]$$

$$\sigma_{yy} = K_I\, r^{-0.5} \frac{1}{\sqrt{2\pi}} \cos\left(\frac{\theta}{2}\right)\left[1+\sin\left(\frac{\theta}{2}\right)\sin\left(\frac{3\theta}{2}\right)\right] + K_{II}\, r^{-0.5} \frac{1}{\sqrt{2\pi}} \left[\sin\left(\frac{\theta}{2}\right)\cos\left(\frac{\theta}{2}\right)\cos\left(\frac{3\theta}{2}\right)\right]$$

$$u_x = K_I\, r^{0.5} \frac{1}{2G\sqrt{2\pi}} \cos\left(\frac{\theta}{2}\right)\left[\kappa-1+2\sin^2\left(\frac{\theta}{2}\right)\right] + K_{II}\, r^{0.5} \frac{1}{2G\sqrt{2\pi}} \sin\left(\frac{\theta}{2}\right)\left[\kappa+1+2\cos^2\left(\frac{\theta}{2}\right)\right]$$

$$u_y = K_I\, r^{0.5} \frac{1}{2G\sqrt{2\pi}} \sin\left(\frac{\theta}{2}\right)\left[\kappa+1-2\cos^2\left(\frac{\theta}{2}\right)\right] + K_{II}\, r^{0.5} \frac{1}{2G\sqrt{2\pi}} \cos\left(\frac{\theta}{2}\right)\left[1-\kappa+2\sin^2\left(\frac{\theta}{2}\right)\right]$$

Fig. 1.2 – Stress state ahead of the crack tip (Anderson, 1995).

Thus, following the analogy with the LEFM, the expressions (1.1) and (1.2) would indicate that the failure could be assessed from a local point of view (and previous of failure initiation, i.e., the crack onset). However, this approach is limited in the case of significant plasticity around the corner. This aspect will be analysed in Chapter 3 of this Thesis.

The Elastic Plastic Fracture Mechanic (EPFM) approach makes it possible to predict the plastic zone in the crack tip

(Gdoutos, 2005) by substituting the stress state equations in a specific plasticity criterion, as von Mises for metallic materials (Chen & Han, 1988) for example. Following the analogy to the EPFM, the evaluation of local plasticity can drive the stress state as presented in Eq. (1.1) and (1.2) is or is not representative for a failure prediction based on stress intensities.

For polymeric materials, Bowden & Jukes (1972) found experimentally that plasticity is strongly influenced by the hydrostatic component of the stress tensor. Considering plasticity in polymers, Broughton et al. (2001) used von Mises and Drucker-Prager criteria, Chiang & Chai (1994) and Chowdhury & Narasimhan (2000) used Drucker-Prager criterion, Crocombe et al. (1995) and Aydn (2008) between others, applied the proposed criterion by Raghava et al. (1973).

The cohesive model, initially established to quasi-brittle materials (Barenblatt, 1962; Hillerborg et al., 1976; Lopes & Venturini, 1997; Vicentini, 2006), is used to simulate the failure process in polymers (Chowdhury & Narasimhan, 2000; Liljedahl et al., 2006) and damage (Crocombe et al., 1995). These are other possibilities in simulating the failure process in polymers, although not considered in this Thesis.

Among several possibilities for modelling adhesive joints, this work focuses on the singular stress field of a particular bimaterial closed corner (between the composite laminate and the

adhesive fillet), where the failure is expected to initiate in real specimens, as observed experimentally by Adams et al. (1978), and Barroso et al. (2009[B]).

Further more specific bibliography is given along the text in each chapter, classified according to the corresponding subject.

1.3 Scope of the Thesis

This section presents the topics studied in this work.

In Chapter 2, a brief introduction to the subjects covered by this Thesis is presented. Then a summary of Barroso's work is introduced, due to its importance as a precursor of the present work. Properties of the common materials used in this Thesis are also presented.

It is necessary to keep in mind that the central objective of this work is the suitability of the stress state in the critical corner, mainly for the DLJ under study (Fig. 1.1), culminating with the proposal of a new testing procedure for failure prediction and characterization of joints in terms of critical values of the GSIF. In this sense, every chapter contributed to corroborate or discard some assumptions.

The Chapter 3 for example, presents some considerations about the validity of the use of 3D numerical models in the

assessment of the stress state in the corner. Before assuming the simplest 2D behaviour, it should be verified that the stress field at the free edges is less severe than the one obtained inside the joint, allowing looking for a failure criterion and allowable values of the stresses and/or GSIF by using 2D numerical models. In the third chapter, three plasticity models are also considered for the plane numerical problem in order to check if/how the existence of yielding could affects the stress state and the onset of failure at the critical corner. For this purpose, three yielding criteria have been considered: von Mises, Drucker-Prager and Raghava-Caddell-Yeh. There is a reasonable agreement that yielding criteria which do not depend on the hydrostatic pressure are less suitable for representing the yielding behaviour in polymeric adhesives. This chapter presents qualitative and quantitative analyses between these three criteria, comparing themselves in order to evaluate the influence of plasticity in the critical corner.

In Chapter 4, the effect of the temperature during the curing process was considered for the numerical DLJ model and, in particular, the thermal stresses arising in the cooling stage from the curing temperature to the room temperature. Several numerical simulations and experimental tests were carried out in order to understand the influence of temperature on the asymptotic stress field in the corner.

Chapter 5 shows a comparative study between two different manufacturing techniques for the joint under study: hot plate press and autoclave. Static and fatigue tests were carried out and both processes compared, using the same geometry and materials. The study of this chapter allowed knowing the performance of the joint in terms of mechanical characteristics strength, as well in fatigue life, according to these curing techniques.

In Chapter 6, a criterion for failure prediction with a procedure for testing in multimaterial closed corners is proposed. This criterion is based on critical values of GSIF and its application was verified for the particular bimaterial joint under study, although the method could be extended for other type of configurations. The proposed methodology allows obtaining a failure envelope based on critical GSIF values. Moreover, an experimental procedure for the evaluation of these values is presented, based on the original Brazilian Test. The procedure chosen allows covering the entire range of mode mixities at the corner.

Chapter 7 refers to the work carried out mainly during the stay undertaken in the University of Surrey, UK, under the advisory of the Professor Andrew Crocombe as a collaboration project. An extensive experimental programme was carried out in fatigue loading in order to characterize the failure onset, and

more specifically the initiation and progression, for the specimens proposed in previous chapter. These tests allowed reducing the load level, the possible effects of local plasticity and amplifying the knowledge of the stress state and failure of the corner under study.

Finally a summary of the main conclusions and contributions of this work is presented in Chapter 8. This Thesis finishes leaving some suggestions for future developments.

1.4 Hypotheses and limitations

The following hypotheses and/or limitations (not necessarily chronologically ordered, or according to the importance) assumed in this work are:

- Plane strain or generalized plane strain assumptions. In generalized plane strain, the three-dimensional displacement field depends only on the coordinates of one plane, i.e. $u_x = u_x(x,y)$ and $u_y = u_y(x,y)$, being the third component u_z defined by a function. In this sense plane strain would be a particular case of the generalized plane strain, in which the third component is assumed to be constant and null ($u_z = 0$). The generalized plane strain assumes that neither geometry, material properties nor

external actions change along the z direction. Assuming plane strain for the joint under study, in the region of interest, the strains are quite constant and equal to zero, along the width direction. This hypothesis is based on studies carried out in Chapter 3, which will clarify this question in detail. However when the computation of the GSIF were involved (i.e. Chapter 5 and 6), a generalized state of plane strain was considered (through the algorithm of V10_2008.MA, by Barroso in 2007).

- The failure starts at the corner and can be controlled by GSIF values. This hypothesis is based on studies carried out in Chapter 7, which will clarify this question in detail.
- Composites are considered as equivalent homogeneous orthotropic materials in numerical and analytical analyses, while adhesive and aluminium are considered as isotropic materials.
- Material properties do not change with temperature. This hypothesis was assumed in all chapters, with the exception of the studies presented in Chapter 4, dedicated exclusively to the study of temperature effects.
- Assumption of linear elasticity (for all materials) and brittle behaviour for CFRP and adhesive (although in Chapter 3 the plasticity is exceptionally assumed for the adhesive, in the numerical 2D study).

- The study presented in Chapter 6, with a proposal for failure prediction is restricted to the instant previous to crack initiation (crack onset), i.e., no pre-crack exists in the corner.
- Neither non-logarithmic nor trigonometric terms of the series expansion, Eq. (1.1), when $r \to 0^+$ are considered in this work. Also the order of singularity $(1-\lambda_k)$ is defined as positive and although the program *V10_2008.MA* has the capability of including real and complex singularities, the particular geometry under analysis (inside the range of interest) only has real values of stress singularities.

Numerical simulations carried out with Finite Element Method (FEM) used ANSYS commercial code and the simulations with the Boundary Element Method (BEM) used a code implemented by the GERM (Graciani, 2006). All the numerical and analytical analyses considered the presence of the adhesive spew fillet.

The entire tests were carried out in a displacement controlled machine at room temperature (unless in Chapter 7, in which load control was used instead).

Chapter

2 Fundamentals and generalities

This chapter presents a summary of the main concepts of basic theory required for an understanding of this work. Further information is provided in the references. As mentioned in Chapter 1, this work gives continuity to the previous research activities of GERM (Barroso, 2007) in the field of adhesives, thus a brief summary of the contributions of Barroso's work is also presented. This chapter ends with a description of the materials used in the analyses, their mechanical properties being presented in the last section.

2.1 Composites and adhesive joints design

The concept of using a fibrous material in a preferential direction in order to improve mechanical qualities is not new. Historically, mankind has intuitively used this concept in ropes (made of jute or cotton) or seats made from woven straw for example, contributing to improvement in lifestyle. Composite structures, i.e., two or more materials working together in order to optimize their mechanical properties in one or more directions

may be seen in nature, for example in trees, the human body and nests built by birds, as shown in Fig. 2.1 a.

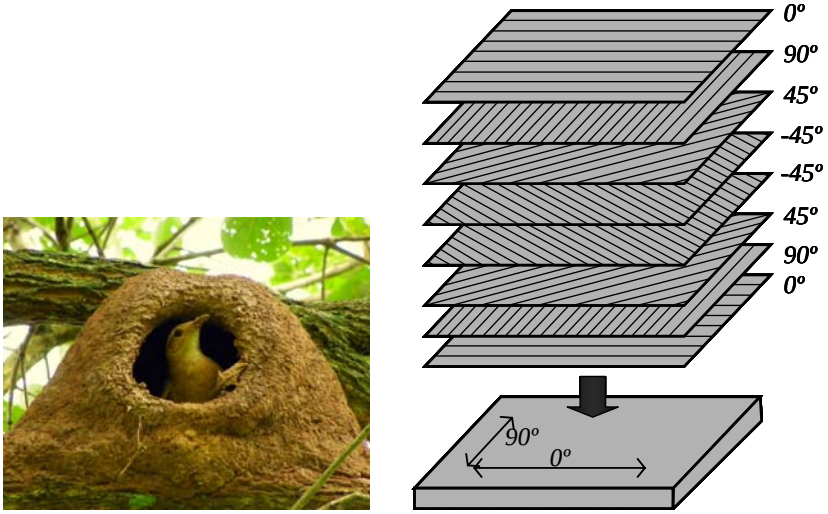

a) Bird making the nest of clay and natural fibres

b) Symmetrical laminate $[0/90/45/-45]_S$

Fig. 2.1 – Association between materials a) in nature, and b) an example of laminate.

Today the scientific community has consensus in defining composite materials. The fibres are often made from carbon or glass and manufactured in conditions of high technology and control, and are embedded in an epoxy matrix. They present superior mechanical properties per unit weight than most metals used in industry; for example, aluminium when compared with unidirectional laminated carbon fibre. Composites are particularly advantageous when subjected to tensile loading, as

the fibres are mainly positioned accordingly to give more strength in the direction in which the structure is going to be subjected to direct or indirect tensile loading.

At the macro scale, i.e. much larger than $7\ \mu m$, the characteristic length of the approximate diameter of a carbon fibre, the composites are essentially homogeneous elastic materials, with anisotropic behaviour, in which the normal and tangential effects can be coupled. For example, this could be, depending on the number of the elastic symmetries: orthotropic, in which there are three orthogonal planes of elastic symmetry, being defined by 9 constants, with the normal and tangential effects uncoupled for the axes of orthotropy; transversally isotropic, where in addition there is a plane in which all directions have similar behaviour, being defined by 5 elastic constants with the normal and tangential effects uncoupled for the axes of orthotropy or principal axes; or quasi-isotropic, in the case of short fibres randomly distributed in a matrix, where isotropy is defined by only two material constants and the normal and tangential effects uncoupled.

For the laminates, usually the first direction is conveniently chosen aligned to the position of some fibres as reference for laminating, being the stacking sequence of the plies in the final laminate indicated between brackets. For example, $[0_2/90_2]_S$ is a cross-ply laminate with 8 plies in total, considering the

symmetry, indicated by the lower index. The laminate $[0_2/90_2]_S$ may be considered to exhibit orthotropic behaviour while a $[0/90/45/-45]_S$ laminate, for example, may be considered as quasi-isotropic (see Fig. 2.1 b). The fibres can be supplied by the manufacturer, as for example, pre-impregnated (known as pre-preg) woven fabric or tape (unidirectional). Further information about composites may be seen in París et al. (2006), Jones (1999), Campbell (2006).

Composites are frequently used in structures with other materials, so from a structural point of view, it is very important to understand the interaction among them. Traditionally, mechanical fastening joints are used, although it is well known that adhesive joints are superior in some aspects as fatigue, corrosion, lightness of weight and impact. The wide use of adhesive joints in industry becomes difficult due to the absence of a general design criterion (Bigwood & Crocombe, 1989).

Adhesive joints are especially advantageous in joining thin plates systems where the adhesive is mainly subjected to shear stresses (Campbell, 2006). Typical joints, either mechanical or using adhesives, are mentioned in Campbell (2006) and Matthews (1994) as the following: single lap joint, DLJ, double strap joint, tapered (double) strap joint, stepped lap joint and scarf joint. These are presented in increasing order of joint

efficiency (see Fig. 2.2, which is not to scale for the sake of clarity).

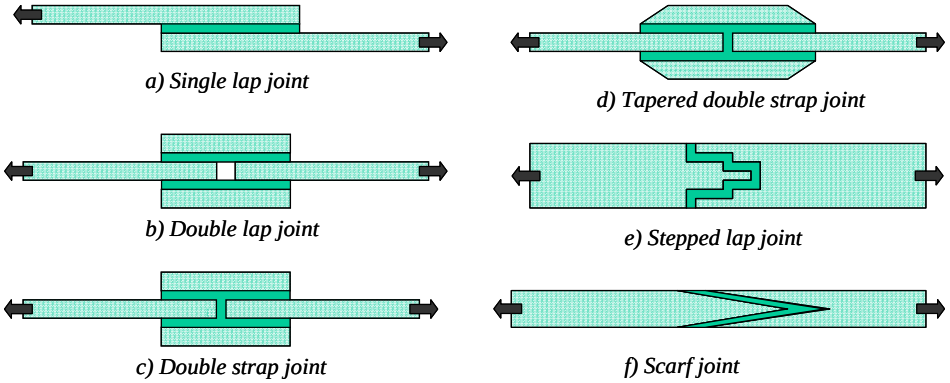

Fig. 2.2 – Some typical adhesive joint configurations (Campbell, 2006), from a) to f) in increasing order of efficiency.

Strap and scarf joints are the most difficult to manufacture in practice whereas stepped ones are particularly simple when manufacturing using composites as adherend.

Concerning some adhesively bonded joint generalities, Baldan (2004) cites several authors (Davis & Bond, 1999; Ansarifar et al., 2001; Balkova et al., 2002; Landrock, 1985) who adopt the following classification according the character of failure for adhesive joints:

- Adhesive failure (or quasiinterfacial) failure. This consists of the rupture of the adhesive bond, such that the separation appears to occur along one of the two adhesive-adherend interfaces.

- Cohesive failure mode, where the rupture of the adhesive bond occurs, such that the separation appears to be within the thickness of the adhesive layer.

- Mixed failure mode, where the crack goes partly between adhesive and adherend and partly through adhesive and/or adherend.

The cohesive is the most desirable mode of failure, because it means that the process of bonding was properly carried out. On the other hand, processing deficiencies, i.e. defects appearing in the manufacturing process, as voids, other bond line defects, contamination or inadequacy of the surface preparation, are usually characterized by interfacial, the adhesive mode, of failure.

Regarding the role of the spew fillet, Crocombe & Adams (1981), studying a single lap joint using aluminium as adherend, showed that the peak of peel and shear stresses can be reduced by approximately 40% and 60% respectively, in average values at the overlap end, depending on the type of materials used. Also Tsai & Morton (1995) presented a numerical non-linear study for single lap joints in composite laminates which results were compared with experiments using Moiré interferometry, corroborating the fact that the shear and peel stress concentrations can be reduced significantly by the presence of the fillet.

Belingardi et al. (2002) and Baldan (2004) proposed a type of classification for adhesive joints considering the geometry of the fillet which appears during the cure cycling, when the adhesive is in a viscous phase. Bodganovich et al. (1999) demonstrated the importance of considering the presence of the spew fillet when the (local) stress distribution at the edges of the overlap changes significantly (up to 40% less in some cases). They also suggested that the spew fillet could be indicative of how the failure in the overlap will occur: whether the failure is of the cohesive or adhesive mode.

Generally shear and peel stresses need the most consideration in design of adhesive joints (the peel stress is normal to the adhesive thickness direction). Fig. 2.3 presents the stress state along the overlap region (L_0) for a generic DLJ. In fact this is the particular symmetrical joint configuration studied throughout this work (Fig. 1.1), but it is not defined in detail here. This is because the present aim is to give a generic representation of the stress state along the overlap. All simplified analytical and numerical models predict the shear ($\sigma_{x'y'}$) and peel ($\sigma_{y'}$) stresses reaching their maximum values very close to the ends of the overlap zone, having lower values in the intermediate overlap region. The trend of peel ($\sigma_{y'}$) stress is changed approximately at the middle overlap region, with the presence of compression states. If the adherends were identical, the shear stresses would

be symmetrical, presenting maximum values at both extremes of the overlap. Peel and tensile stresses would present the maximum values at both edges but with the opposite sign (in an antisymmetric shape, with one edge in compression and other in tension), being the plot inverted from the middle up to the end of the overlap length (L_0).

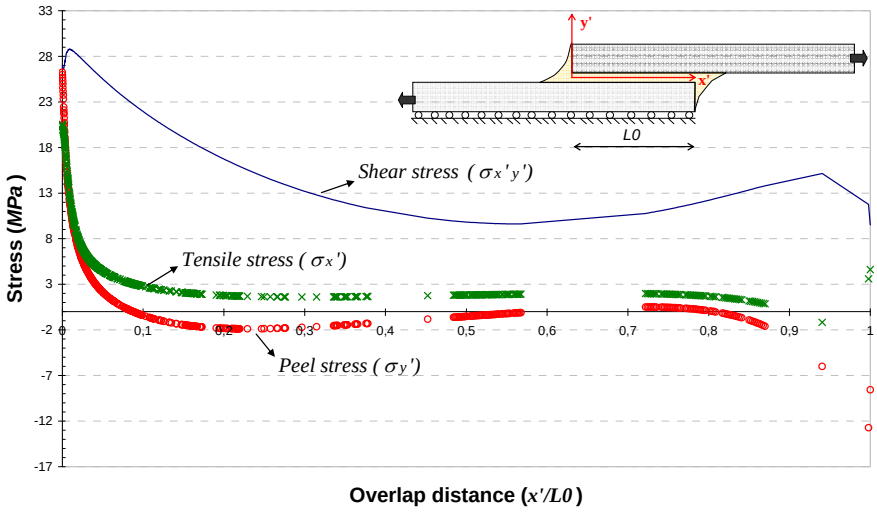

Fig. 2.3 – Bond line stresses distribution for a generic DLJ (with different adherends).

Some proposals for failure prediction of adhesive joints are based on the nominal stress state, as that obtained in Fig. 2.3. Some of these (analytical or numerical) are briefly discussed in the following sections, from 2.1.1 to 2.1.5. A very clear and summarized discussion regarding theories for failure prediction

in adhesive joints can be found in da Silva et al. (2009[A,B]), besides the specific references which will be addressed in the referred sections. In order to generate strength criteria, shear or peel stresses are computed and compared with the shear or peel strength of the joint, respectively, in experimental tests.

Although widely used, the models based on nominal states of stresses are limited when the problem involves stress singularities. Since the existence of the peak of stresses in the extremity at the ends of the overlap is known, for an adhesively bonded joint such as the one represented in Fig. 1.1 for example, the failure is prone to start firstly at that location. Studying that location in detail, a singularity is detected, due to the presence of a multimaterial corner. When the linear elasticity predicts infinite values, the problem should be studied using a different approach, as nominal stress values are meaningless. This was the approach adopted in the present Thesis, in order to establish a new proposal for failure prediction in adhesive joints and multimaterial closed corners in general.

In section 2.2 a summary of fracture mechanics focusing the multimaterial corner problem is presented.

2.1.1 Strength prediction based on nominal stress values

Considering sufficiently rigid and similar (i.e. only one type of) adherends, isotropic materials in a linear elastic regime, the simplest way to analyse the stress state of the joint is based on the assumption that the adhesive deforms under constant shear stress. Admissible shear stress is then obtained by:

$$\sigma_{x'y'} = \frac{P}{A_{lap}} \tag{2.1}$$

where P is the applied load and A_{lap} is the overlap area. This option is too simple for representing the maximum values that appear in the edges of the overlap.

2.1.2 Volkersen model

Volkersen (1938) also considered isotropic materials in a linear elastic regime, and similar flexible adherends. He assumed that the adhesive deforms only in shear whereas adherends only in tension. The tensile stress in the adherends along the overlap region is reduced, causing non-uniform shear stress distribution in the adhesive layer, which may be represented by an expression in the form:

$$\sigma_{x'y'} = \frac{P}{A_{lap}} f_v^1 + f_v^2 \tag{2.2}$$

where f_V^1 and f_V^2 are hyperbolic sine and cosine functions of the mechanical and geometrical parameters of the joint (see Appendix A for more details). Although this model takes into account the thickness of the adhesive and adherends, this approximation is more suitable for double overlap joints than single ones, since it does not consider the bending effect that appears in this type of joint, due to the load path eccentricity.

2.1.3 Goland-Reissner model

The study of a single lap joint is more complex than that of a DLJ, because in the former an eccentricity due to the load path appears. Goland & Reissner (1944) took this effect into account, making the equilibrium between the applied load and the generated bending moment and transverse force. Still considering linear elastic, isotropic materials and similar adherends, the prediction of failure according to their model in terms of shear stress is given by:

$$\sigma_{x'y'} = \frac{P}{4L_0} f_{GR}^1 \tag{2.3}$$

where L_0 is the overlap length and f_{GR}^1 is function of the parameters of the joint with hyperbolic sine and cosine terms. Additionally, in this proposal, the prediction of failure according to their model in terms of peel stress is given by:

$$\sigma_{y'} = \frac{4Pt}{L_0^2} f_{GR}^2 \tag{2.4}$$

where t is the thickness of the adherends (must be similar for this model) and f_{GR}^2 is a function of the parameters of the joint and applied load P, with hyperbolic sine and cosine terms. For more details for Eq. (2.4) and (2.3), see Appendix A. This model also considered the effect of large deflections of the adherends, assuming the adhesive as an infinite thin layer.

2.1.4 Hart-Smith model

Assuming dissimilar adherends (composites inclusive) and from the previous work of Volkersen and de Bruyne (1944), the proposal of Hart-Smith (1973[A,B]) considered the individual deformation of the upper and lower adherends and not assuming the adhesive as an infinite thin layer. This fulfils the boundary condition at the extremities of the overlap zone, in which the tangential stress is null. For materials in a linear elastic regime, shear stress for DLJ is given by the equation:

$$\sigma_{x'y'} = f_{HS}^{1} + f_{HS}^{2} \tag{2.5}$$

where f_{HS}^{1} and f_{HS}^{2} are functions of the parameters of the joint, with hyperbolic sine and cosine terms (see Appendix A for more details).

Hart-Smith also considered nonlinearity effects in his analyses for shear stress in the adhesive. The adhesive was assumed to have bilinear elastic perfectly plastic behaviour, given a modification for the Eq. (2.5) in the elastic region and the shear strain in the plastic region, where the terms of each expression must be iterated until convergence is reached.

In addition, Hart-Smith (1973[A,B,C], 1974) included other significant improvements for designing adhesive joints, such as the study of thermal stresses, joint efficiency, the effect of the stacking sequence and unbalanced joints.

2.1.5 Bigwood-Crocombe model

In this model, Bigwood & Crocombe (1989) also considered dissimilar adherends, isotropic materials in linear elastic regime. They proposed a more general model, designed to cover the lack of a general criterion applicable for all configurations of joints, as those represented in Fig. 2.2 for example, under complex loading, including tensile, shear and moment loading at the extremities of

the adherends. The overlap region is modelled as a sandwich type, thus the adhesive is no longer considered an infinitely thin layer. Their analysis is presented in both full and simplified versions. The problem was studied with plate bending theory and the expressions were compared with the numerical response (using FEM), being the shear stress (in the simplified analysis) given by the equation:

$$\sigma_{x'y'} = f_{BC}^{1} + f_{BC}^{2} + f_{BC}^{3} \tag{2.6}$$

where f_{BC}^{1} and f_{BC}^{2} are functions of the loading and parameters of the joint, with hyperbolic cosine and sine terms, while f_{BC}^{3} is function of only the elastic parameters and loading (see Appendix A for further information).

Bigwood and Crocombe also extended their analysis to a nonlinear model, modelling the adhesive plasticity with von Mises and Raghava et al. (1973) criteria (Bigwood & Crocombe, 1990).

2.2 Fracture mechanics in multimaterial corners

The work of Williams (1952) is always reminded as a classical work on the subject of fracture mechanics. He studied the stress singularities in a problem of a sharp and infinite wedge for an

isotropic thin plate, varying the wedge angles from 0º up to 360º considering different boundary conditions on the faces of the wedge (Fig. 2.4). Williams obtained the stress and displacement field at the neighbourhood of the vertex of the wedge using Airy function. He assumed $\phi = \mathrm{r}^{\lambda_W+1} f_W(\theta, \lambda_W)$ as the biharmonic function which admits separation of variables, where f_W is a sum of sin and cosine terms. After solving the system, the solution obtained by Williams was $\sigma_{ij} = r^{\lambda_W - 1} f_{ij}(\lambda_W, \theta)$ and $u_i = r^{\lambda_W} g_i(\lambda_W, \theta)$ for stresses and displacements, respectively. See Williams (1952) for more details.

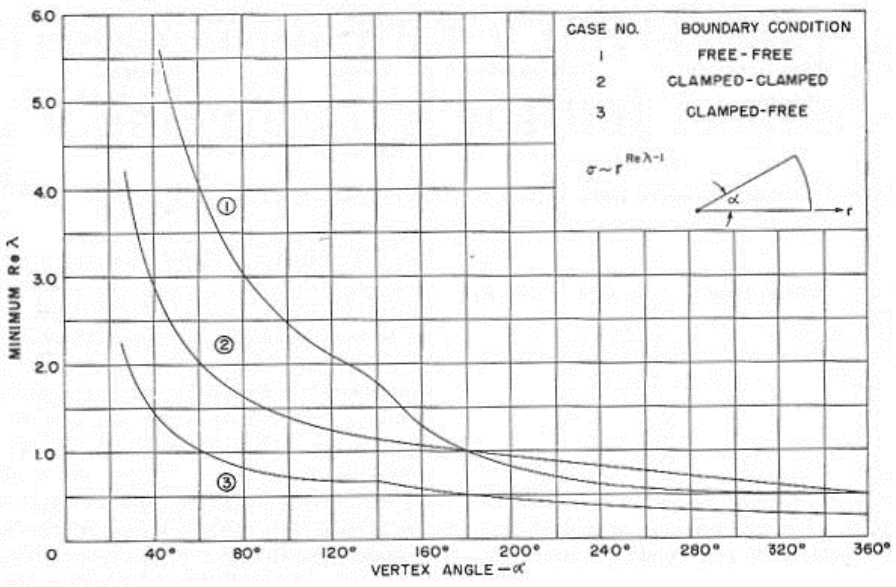

Fig. 2.4 – The wedge problem studied by Williams (1952).

As can be appreciated in Fig. 2.4, Williams found that unbounded stresses, i.e., stress singularity (for $0<\lambda_W<1$) may appear for wedge angles from 180º up to 360º (i.e., re-entrant corner) for the boundary conditions considered. He also observed that the stress singularity may appear for wedge angles less than 180º inclusive, when the boundary condition is free-clamped. Later, in 1957, Williams applied this study to the particular case of the wedge angle of 360º, which corresponds to a crack problem.

Beyond the subject of singularities, Dundurs (1969), who studied the interaction between two isotropic elastic materials, introduced the parameters which allowed the posterior studies in bimaterial problems. This is because his work is briefly introduced here. For a plate in plane stress or plane strain state, the following constants can be defined:

$$\alpha_D=\frac{\Gamma\left(\kappa_1+1\right)-\left(\kappa_2+1\right)}{\Gamma\left(\kappa_1+1\right)+\left(\kappa_2+1\right)},\qquad \beta_D=\frac{\Gamma\left(\kappa_1-1\right)-\left(\kappa_2-1\right)}{\Gamma\left(\kappa_1+1\right)+\left(\kappa_2+1\right)} \tag{2.7}$$

where $\Gamma=G_2/G_1$ (the ratio of shear moduli of both materials) with α_D and β_D known as Dundurs' parameters. The constants κ_1 or κ_2, for material 1 and 2 respectively, are equal to $\kappa=3-4\nu$ for plane strain or equal to $\kappa=\left(3-\nu\right)/\left(1+\nu\right)$ for plane stress, using the lower index for material 1 or 2 as appropriate.

Following the line of Williams' research, the work of Dempsey & Sinclair (1979) was dedicated to the singularities in an infinite wedge composed of two or more materials. From the Airy stress function and using the Dundurs' parameters, they generalized the solution given by Williams for N-material wedges, allowing real and complex characteristic exponents λ_{DS}. Later, Dempsey & Sinclair (1981) additionally particularized the previous study, applying their development to a bimaterial wedge problem.

Another significant contribution was provided by Vasilopoulos (1988), who latter developed the connection between the LEFM as presented by Irwin (1957) and with the wedge problem studied by Williams, relating the stress intensity factors for mode I and II with the corresponding eigenvalue (singularity exponents) λ_V, introducing the concept of Generalized Stress Intensity Factors (GSIF) or so called "higher order stress intensity factor" (K_k in this work).

These were very important contributions to the study of singularities in the subject of isotropic multimaterial corners. However, the consideration of anisotropy in one or more materials makes the corner singularity analysis much more complicated. Further details may be found in Leguillon & Sanchez-Palencia (1987).

In 1997, Mantič et al. presented a novel general proposal based on Stroh (1962) and Lekhnitskii (1981) Formalism for singularity analysis of orthotropic corners in generalized plane strain state. They applied the procedure to the CFRP for different angles and boundary conditions. Barroso (in Barroso et al., 2003 and Barroso, 2007) then applied the technique to multimaterial anisotropic corners, producing significant contributions to this subject, especially to adhesive joints with composite materials, where multimaterial corners formed by an orthotropic laminate are frequently found and some of them may be related to the failure initiation. The procedure implemented by Barroso (in the *V10_2008.MA* code) is able to calculate the case of anisotropic and especially transversally isotropic materials for all mathematical degeneracies in the framework of Stroh Formalism. To close this topic, Fig. 2.5 shows the variation of the stress singularity order $(1-\lambda_k)$ in a closed bimaterial corner including an adhesive and CFRP, for different angles of the CFRP laminate. This is the critical corner in the DLJ in Fig. 1.1, where the angle would be 0º.

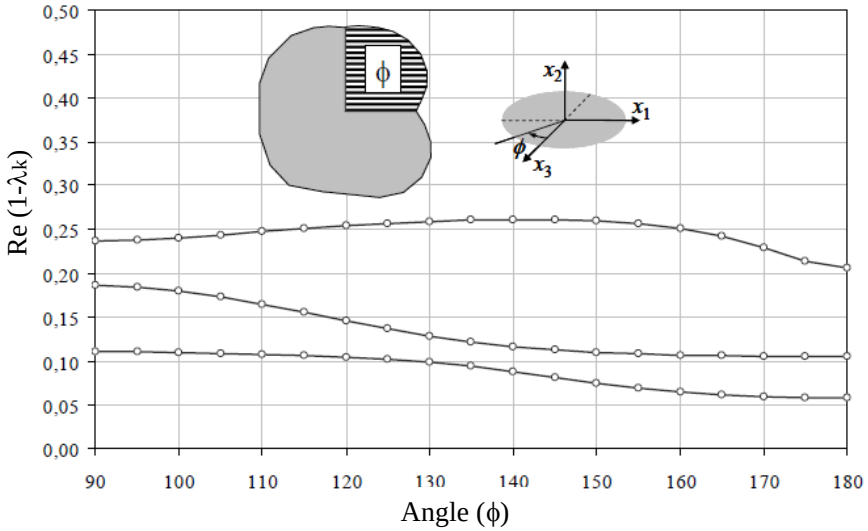

Fig. 2.5 – Stress singularity order in a closed bimaterial corner (see Fig. 1.1), considering the fibres directions in the x_1x_3 plane. Angles vary from 90º up to 180º (from Barroso, 2007).

The following section is a brief introduction to the Stroh Formalism, as it formed the basis for the pioneering works of Mantič et al., 1997 and Barroso, 2007.

2.2.1 Stroh formalism

Significant advances were introduced in the anisotropic elasticity since Lekhnitskii, in 1930s proposed a general expression for the solution in an anisotropic elastic material by using the strain compatibility equation and a generalization of

the Airy function. In 1981, Lekhnitskii work was republished in a comprehensive book.

In 1962, Stroh assumed generalized plane strain for elastic anisotropic material and introduced the constitutive law (generalized Hooke's law) in the internal equilibrium equation (neglecting body forces). He investigated the conditions under which the following displacement form solves the equilibrium equation:

$$u_i = \mathrm{Re}\ \ a_i^S f_S\left(z_S\right) \text{ for } \ \ z_S = x_1 + p_S x_2 \tag{2.8}$$

where p_S is a complex scalar, a_i^S is the vector component, f_S is an arbitrary function of z_S and $u_i\left(x_1, x_2\right)$ is the displacement component in generalized plane strain, in Cartesian coordinate system x_i $(i = 1,2,3)$ in which the displacement field is independent of the x_3 coordinate.

Substituting Eq. (2.8) in the combined expression (equilibrium with constitutive law), a matrix system is achieved:

$$\left| Q + p_S\left(R + R^T\right) + p_S^2 T \right| a = 0 \tag{2.9}$$

in which the non-trivial solution is given by solving the vanishing determinant condition:

$$\left| Q + p_S\left(R + R^T\right) + p_S^2 T \right| = 0 \tag{2.10}$$

where $Q_{ik} = C_{i1k1}$, $R_{ik} = C_{i1k2}$ and $T_{ik} = C_{i2k2}$ are 3x3 matrixes whose coefficients are components of the tensor of elastic stiffnesses. Eq. (2.10) is called the characteristic equation of the material and any anisotropic elastic generalized plane strain problem reduces to the solution of an eigenproblem, where p_S is the eigenvalue and a_i^S are the components of the eigenvector, in terms of elastic stiffness constants only. When the roots p_S are equal, as for example in the case of isotropic materials, the system is a mathematically degenerated. For stresses there is an analogous representation to Eq. (2.8):

$$\varphi_i = b_i^S f_S(z_S) \tag{2.11}$$

where φ_i is the stress function component and b_i^S is (by definition) the vector component. Then, a general representation of displacements and stress function vector is given by:

$$\begin{bmatrix} u_i \\ \varphi_i \end{bmatrix} = \begin{bmatrix} a_i^S \\ b_i^S \end{bmatrix} \left[f_S(z_S) \right] \tag{2.12}$$

Finally the following stress components are obtained: $\sigma_{i1} = (Q_{Sik} + p_S R_{Sik}) a_k^S f_S'(z_S)$ and $\sigma_{i2} = (R_{Ski} + p_S T_{Sik}) a_k^S f_S'(z_S)$ where $\sigma_{i1} = -\varphi_{i,2}$ and $\sigma_{i2} = \varphi_{i,1}$.

In 1996, Ting published a complete and relevant work on anisotropic elasticity, based on the Stroh Formalism and

including many examples. Ting also presents (Ting, 1997) the characteristic equations for multimaterial anisotropic corners, considering a few boundary conditions. Independently of the number of materials, the characteristic equation is computed by solving a 3x3 determinant for open corners and 6x6 in the case of closed corners.

In the next section a brief explanation of the differences between the two numerical methods used in this work, the Finite Element Method (FEM) and Boundary Element Method (BEM), is presented.

2.3 FEM and BEM

The use of numerical models was essential to complete the analyses of this work. The Finite Element Method (FEM, as previously defined) and the Boundary Element Method (BEM) are the most disseminated methods. FEM was used in Chapter 3 in order to study plasticity and 3D effects, and also in Chapters 6 and 7, for the obtainment of the GSIF and also for several verifications in the stress state of the Brazilian Test (BT) specimens, although not all of these are presented here. FEM and BEM were used in the simulations of thermal stresses in curing, in Chapter 4, although only the results obtained by using the BEM are presented in this Thesis.

The BEM consists of a numerical tool for solving integral equations which govern the elastic problem. By this method, the geometry of the problem is approximated through the boundary of the geometry, differently of FEM, in which the entire domain must be discretized. A generic problem is represented in Fig. 2.6, which shows a simple meshing scheme and compares both methods.

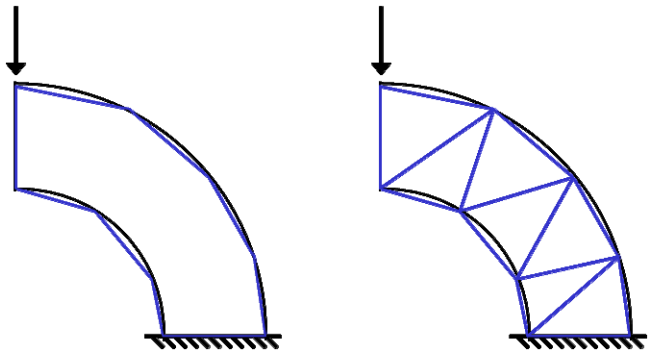

Fig. 2.6 – BEM vs FEM mesh.

According to the schematic Fig. 2.6 a), in BEM only the boundary of the problem needs to be discretized, which implies smaller matrices and less input data. The matrices of the system in BEM are dense, whereas in FEM the matrices are sparse, which enables easier programming and verification during the implementation process.

BEM is especially advantageous in problems with infinite regions or high stresses concentration (singularities). Modelling

initiation and progression of crack is frequently simpler using BEM and the solution is usually more precise as the system is solved for stresses and displacements directly. In FEM, however, the acquisition of the stresses must be derived from the solution given after solving the system for displacement unknowns. For further information regarding BEM, see Brebbia & Dominguez (1992), París & Cañas (1997); and for FEM see Oñate (1992), Crisfield (1997), Fish & Belytschko (2007).

In Chapter 4, the BEM program implemented by Graciani (2006) enables simulation of several solids (isotropic, orthotropic and transversally isotropic ones) and contact conditions. The module for temperature analysis was not implemented until Barroso (2007), so in this work the program was utilized on a user level only.

Due to its importance, the following section summarizes the main contributions of Barroso's work, presented in 2007.

2.4 Summary of Barroso's work

Barroso's work focused on the local stress state for a CFRP-Aluminium double lap joint and it can be divided into three main blocks, summarized as followed:

Analytic work: The *V10_2008.MA* code (written in *Mathematica*) was implemented by the semi-analytical computation of the characteristic exponents (λ_k) and numerical computation of the characteristic functions (Eq. (2.10) type) based on Stroh Formalism from anisotropic elasticity. This code includes degenerated and extraordinary degenerated materials and gave special attention to transversely isotropic materials. The code is summarized bellow:

In the first block of the program, the eigenvalues (p_S, in Eq. (2.10)) and eigenvectors, in which a_i^S and b_i^S are the components, Eq. (2.12), are computed, based on the input data from elastic constants and orientation of the materials. The eigenvalues are evaluated numerically for orthotropic materials, based on Lekhnitskii procedure, and analytically for degenerate materials.

After considering the boundary conditions of the corner, the characteristic exponents (λ_k) are evaluated (numerically), stored and presented as a graphical output for verification in the second block of the program.

In the third block, the stresses and displacements are computed after solving the system (2.12).

Numerical work: The fourth block of *V10_2008.MA* code was implemented after the publication of his Thesis (Barroso, 2007). It takes as input data the values of a numerical analysis (in both

BEM or FEM) in stresses and displacements, which were previously evaluated. This response is then compared with the one calculated in the third block. Then by using an adjustment in least square method, the GSIF (K_k) are achieved.

Experimental work: A test program including so many different geometries of Double Lap Joints (DLJ) was carried out. This included manufacture of lap joints, static tests which considered total and partial failure load and optical microscope observation. The failure load for each specimen was obtained in order to correlate with future developments using the same stress field and GSIF obtained from the analytical and numerical work. The manufactured specimens had the same local configuration in order to compare the results between different geometric parameters and overlap lengths.

The main conclusions and contributions of Barroso's research may be summarised as:

- The code implemented enabled analysis of different materials, including degenerated ones, close and open corners (Barroso et al., 2003 and Barroso et al., 2009[A]);

- The analytical and numerical analyses made it possible to estimate the range where the singular stress field for general corners is valid (Barroso et al., 2012[A]);

- Additionally, the analyses were able to characterise each type of corner according to the GSIF, being the stress and displacement field represented by an expression as a sum of (singular and not singular) terms (Barroso et al., 2009[B]);

- The failure in experiments suggested that failure is governed by the maximum circumferential stress component, and a good agreement was found with the failure angle predicted by numerical analysis (Barroso et al., 2009[B]);

- The work strongly suggests that the singular stress state at the corner controls the failure in the joint.

Finally, in his suggestions for future developments, Barroso indicated some topics that could complete his work, for example to extend the studies for 3D situations, to consider other constitutive laws (as bilinear or cohesive model) and fatigue tests.

2.5 Knowing the materials

The double lap joint studied in this work is usual in the aeronautic industry; it is manufactured in Aluminium and unidirectional CFRP as adherends joined by a structural adhesive. Fig. 2.7 gives a comparison of the strength and stiffness of the three (separated) materials involved in these analyses.

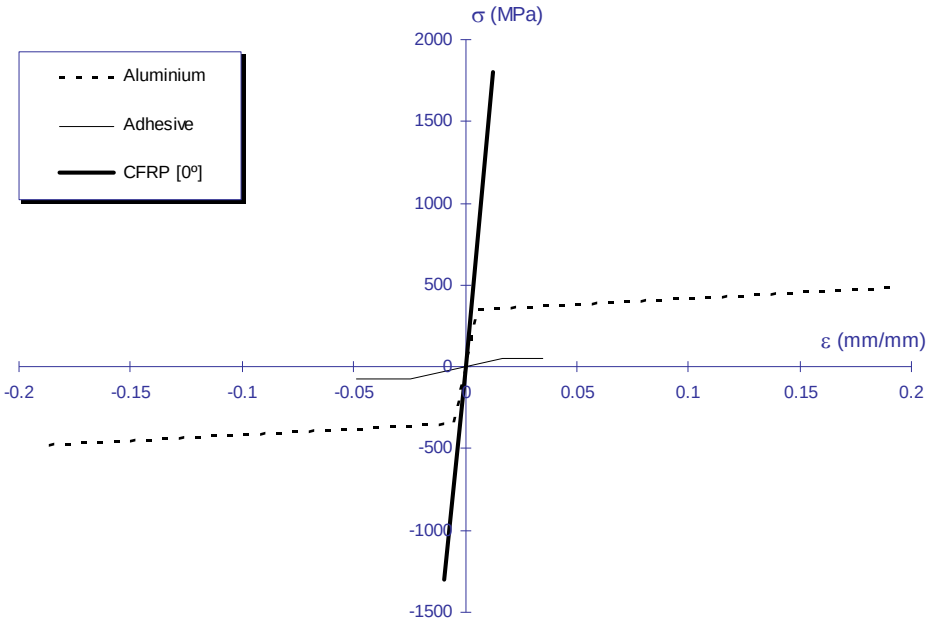

Fig. 2.7 – Mechanical behaviour of the materials.

The adopted constitutive law and available literature for these materials was given by the manufacturers. It may be appreciated that CFRP, considering its property in 0º load direction, has the highest strength and stiffness, while the adhesive has the lowest characteristics. When compared to Aluminium, the adhesive has the shortest yielding range; the yielding stress (in compression as much in tensile) is also smaller for the adhesive compared to Aluminium. These characteristics are convenient for the purposes of use of the adhesive. It plays an important role between the two stiffer materials, i.e. to joint these structures, and in order to allow a smooth transmission of the stresses along

the joint, the adhesive must have lower strength and be more flexible than the adherends.

In the next subsections, each material used in this work is separately introduced, and characteristics, properties and applications of each are also discussed.

2.5.1 Adhesive (Cytec FM73)

Cytec FM73 is a typical film adhesive, generally used for metal-metal joints but also suitable for bonding many structural composite systems. It is a thermosetting epoxy film with excellent mechanical properties at room and service temperatures. Its application on Aluminium requires surface preparation with Cytec BR127 chromated epoxy phenolic primer, in order to avoid corrosion. Bonding is usually carried out at 117ºC ~ 123ºC with a bond line pressure maintained at 0.25 MPa ~ 0.31 MPa and held for 60 minutes in a cure cycle (heated for 30 minutes to 120º).

It is known that this adhesive was employed, for example, in some aircraft structures as SAAB 340, Airbus A300 and Airbus A310 (from Higgins, 2000).

For this work, the material properties given on Table 2.1 were considered for the adhesive. These were obtained by the

manufacturer Cytec data sheet, and the literature (Aydn, 2008) for K_{tg} .

Properties		
$\sigma_y^T = 50\ MPa$	$\sigma_y^C = \lambda\,\sigma_y^T = 73\ MPa$	$\lambda = 1.46$
$\sigma_u^T = 55\ MPa$	$\sigma_u^C = \lambda\,\sigma_u^T = 80.3\ MPa$	$\nu^T = \nu^C = 0.35$
$E^T = E^C = 3000\ MPa$		$\alpha^t = 45\times10^{-6}\ ^oC^{-1}$
$K_{tg}^T = K_{tg}^C = 12\ MPa$		

Table 2.1 – Material properties for adhesive.

Where σ_y is the yield stress, σ_u is the ultimate strength, E is the Young modulus, K_{tg} is the tangent modulus (from the bilinear uniaxial stress-strain curve), λ is the ratio between the yield stress in compression and tension test, ν is the Poisson's ratio and α^t is the thermal expansion coefficient. The upper index T or C is referred to as the tension or compression property, respectively.

The curing cycles used for the analyses in this work, were:

a) 115ºC with a 0.28 MPa pressure hold for 60 minutes, heated for in 30 minutes to 115ºC, for residual thermal stresses analysis

(Chapter 4) and also for the specimens manufactured in autoclave (in Chapter 5);

b) 120ºC with a 0.28 MPa pressure hold for 60 minutes, heated for 30 minutes to 120ºC for the remainder of experimental analyses (in Chapter 6 and 7).

2.5.2 Aluminium (AA 2024)

The Aluminium 2024-T3 (according the Aluminium Association US) or L-3140 (according U.N.E. specification) is a high strength alloy obtained under solution, temper and maturation treatments. Its main applications are in aircraft fittings, gears and shafts, bolts, clock and computer parts, couplings, fuse parts, hydraulic valve bodies, missile parts, munitions, nuts, pistons, rectifier parts, worm gears, fastening devices, veterinary and orthopaedic equipment, structures, welding. Although this is an extensive list, probably the main application is in the aeronautic and military industries: fuselage structures, wing tension members, shear webs, ribs or structural areas where stiffness, fatigue performance and good strength are required. Sheet products are used extensively in commercial and military aircraft for fuselage and wing skins or engine areas where elevated temperatures of up to 121°C are often encountered.

For a better corrosion-resistance performance, this aluminium is typically anodized or etched.

The properties given on Table 2.2 were considered for the aluminium in this work.

Properties		
$\sigma_y = 350\ MPa$	$\sigma_u = 480\ MPa$	$\nu = 0.33$
$E = 68670\ MPa$	$K = 700\ MPa$	$\alpha^t = 24.5\times10^{-6}\ ^oC^{-1}$

Table 2.2 – Material properties for aluminium.

The same values for tensile and compressive test were assumed, so the upper index is neglected when this property applies.

2.5.3 CFRP (AS4/8552)

The laminates used in this work were made with AS4 Magnamite® unidirectional carbon fibres and 8552 Epoxy Matrix by HEXCEL. The use of this type of continuous carbon fibres was led by the military industry, for example in the V22, F22, F35, Eurofighter Typhoon, F18 aircrafts, among others. These fibres combined with the resin give a product with excellent corrosion, creep and fatigue resistance, and is light-weight with high specific strength and stiffness characteristics. The curing cycle is

carried out at 177ºC (held for 110 ~ 130 minutes) heated to 107ºC (held for 30 ~ 60 minutes). A pressure of 0.6 ~ 0.7 MPa previously heated to 107ºC is maintained during the cycle. At the end of the process the material is ready to operate in environments of up to 121°C.

The company SACESA supplied cured panels for this Thesis. The properties considered for the CFRP (being x the axis along the fibres direction) are given in Table 2.3.

Properties		
$S_{xx}^{T} = 1800\ MPa$	$G_{yz} = 3500\ MPa$	$\nu_{yz} = 0.32$
$S_{xx}^{C} = 1300\ MPa$	$G_{xy} = G_{xz} = 5000\ MPa$	$\nu_{xy} = \nu_{xz} = 0.3$
$E_{xx} = 141300\ MPa$		$\alpha_{xx}^{t} = -1\times10^{-6}\ ^{o}C^{-1}$
$E_{yy} = E_{zz} = 9580\ MPa$		$\alpha_{yy}^{t} = \alpha_{zz}^{t} = 26\times10^{-6}\ ^{o}C^{-1}$

Table 2.3 – Material properties for CFRP.

When not explicit, the same value was assumed for tension and compression, S is the yield stress and ultimate strength (as for brittle material it practically coincides) and G is the shear modulus.

Chapter

3 Stress state assessment with numerical models

Detailed numerical analyses of complex problems involving orthotropic materials are usually carried out by means of the FEM and BEM. Most commercial software uses specific modules to take into account laminates and failure criteria, for example. The literature for these methods is quite broad and includes Brebbia & Domínguez (1992), París & Cañas (1997) in BEM, Fish & Belytschko (2007), Oñate (1992) and Crisfield (1997) in FEM. These methods are powerful tools for engineering analyses, in stress state assessment as well as in singularities detection. This is because of their ease of use and the many possibilities they permit for the simulation of many types of problems.

In this chapter the joint presented in Fig. 1.1 was studied in two main aspects: 3D elastic analysis and elastic-plastic models in 2D. The objective was to check the suitability of the 2D stress representation carried out in Barroso et al. (2007), considering 3D effects and plasticity, particularly focusing the stress state around the critical corner, where the failure is expected to initiate in real specimens (Barroso et al., 2009[B]). For this purpose, a more refined mesh was used and the closest area containing the corner was defined as the "control circle" (or cylinder in case of 3D analysis). The geometry includes the adhesive spew-fillet.

For the analyses the commercial program ANSYS (release 11.0) was used. Material properties and parameters were adopted according to those specified in Tables 2.1, 2.2 and 2.3. In the simulations including plasticity only the adhesive layer was considered to behave according to an elastic-plastic law, while the CFRP and Aluminium were modelled as linear-elastic materials (as the yield stress for adhesive is previous and too far from the aluminium yielding, as shown in Fig. 2.7).

3.1 Three-dimensional elastic analysis of the joint

In the numerical and analytical models by Barroso (2007, 2009[B]), plane strain and generalized plane strain states were considered for the joint under study. However, it was not verified whether the 2D model for the DLJ was really representative of the real 3D state or not. The aim of this topic is to check the validity of 2D models for the particular configuration indicated in Fig. 1.1, once the 3D model would be more realistic. Another important point to consider is that experimental tests can measure the stress state on the free lateral surfaces of the specimen, using strain gauges, for example, while these surfaces do not exist in the mathematical problem formulation for plane strain.

In the literature, there are several numerical works which use 3D multimaterial corners with adhesive wedges. Richardson et al. (1993) carried out 3D numerical analysis aiming to validate bidimensional models in plane strain state. He found that the bidimensional solution was valid over than 80% of the joint. In 1997, Yosibash implemented a numerical procedure for the eigenpairs computation of singularities in 3D multimaterial corners, achieving good convergence with numerical analyses. Regarding the more specific subject of modelling and application in adhesive joints, the work of Bogdanovich & Kizhakkethara (1999), who used submodeling in FEM analysis and composites as adherends, can be highlighted. Later Andruet et al. (2001) and Gonçalves et al. (2002) used special finite elements, considering geometric nonlinearities. Their results however are limited to single lap joints only, and do not consider any spew or fillet. Ichikawa et al. (2008) evaluated the strength of the stepped-lap joints in 3D FEM and obtained good agreement with experimental analysis. Using steel as adherend and an epoxy adhesive, their simulations considered the load being applied in the overlap and interface direction. This particular geometry enabled assessment of the complex stress state of the adhesive. An effect of the minimum mesh size is reported, with the time for computations. Aydn (2008) also presents a 3D FEM analysis but his study is limited to only a single lap joint without fillet.

3.1.1 Three-dimensional effects

Typically, adhesively bonded joints between thin layers of metallic or composite materials have much smaller dimensions in the thickness direction than the other two directions. This fact, together with the evidence that in most cases, geometry and loading do not change significantly along the bond line, enables analysis in many cases of the real three-dimensional configuration as a bi-dimensional case (state of generalized plane strain) which is uncoupled from the antiplane problem.

There are some 3D effects such as the anticlastic bending of the adherends (Silva et al., 2009[A]) which produces a concave-convex deformation in the joint, due the Poisson's ratio effect in the adherends and the expected bending produced by the load eccentricity, mainly in single lap joints. In DLJ the bending effect is not significant.

Some 3D free edge effects in adhesively bonded joints have also been analyzed by Tsai & Morton (1994) and Aydn (2008) as well the bending-twisting coupling effect, analyzed by Bogdanovich & Kizhakkethara (1999) and Aydn (2008).

Independently of the above introduced 3D effects, finite-width adhesive joints present, near the free edges, a pure three dimensional behaviour, with different stress fields than those obtained far from these lateral free edges. The characteristic

exponents (stress singularities) arising at these edges differ from those corresponding to 2D cases (Ortiz et al., 2005), depending on particular material and geometrical combinations. It should be verified, before assuming the 2D behaviour, that the stress field at the free edges (by means of a 3D numerical analysis) is less severe than the one obtained inside the joint, to be able to look for failure criteria and allowable values of the stresses and/or GSIF using 2D numerical models.

3.1.2 Numerical model and results

The geometry in this study is represented in Fig. 1.1, in which $L_a = 50\ mm$, $L_o = 12.5\ mm$, $w = 25\ mm$, $t_{a1} = t_{a2} = 1.6\ mm$ and $t_{a3} = 0.1\ mm$ are the dimensions. The adhesive spew-fillet and the thickness t_{a3} were obtained by micrography and, in the absence of a specific standard that covers adhesively bonded DLJ between metallic and composite materials, the standard ASTM D3528 (2002) was taken as a reference guide. In the numerical model, however, two symmetries were considered in order to simplify the problem: one in the mid-half *xy* plane, where $z = w/2 = 12.5\ mm$ and the other one is already indicated in the Fig. 1.1, where $y = 0\ mm$ it lies in the *xz* plane.

Two cylindrical control volumes were used in order to properly refine the mesh at the neighbourhood of the critical corner. This is a closed corner, and all material wedges are assumed to be perfectly bonded. This critical corner is located between the end of the 0º laminate in contact with the adhesive layer and adhesive spew-fillet, where a singularity is known to occur, in terms of the Linear Elastic solution at this point. In this control cylinder (where $r \cong t_{a3}/3 = 0.033\ mm = 33\ \mu m$ is the radius, equal to a third part of the adhesive thickness approximately) the mesh has been progressively refined towards the bimaterial corner tip (the edge of the smaller element being $\cong 0.00074\ mm = 0.74\ \mu m$). This is done in order to accurately reproduce the high stress gradients near the corner. Each finite element around the exterior circumference of the cylinder has around 10.4 μm width, thus giving rise to 1200 uniform elements across the *z* axis. Fig. 3.1 shows part of the geometry (volumes) and the mesh used in the analysis. This size is required in order to achieve satisfactory results in presence of the singular stress field and avoid the typical numerical errors associated with the discretization appearing at the characteristic distance of interest.

The CFRP laminate has been modelled as an equivalent linear elastic homogeneous orthotropic material, whereas the adhesive and the aluminium have been modelled as linear elastic isotropic materials, all in linear elastic regime. The properties of the

materials are indicated in Tables 2.1, 2.2 and 2.3; and in the case of the CFRP laminate, *x* corresponds to the fibre direction.

ANSYS software was used for the analysis. The element SOLID45 with 8 nodes and 3 Degrees of Freedom (DOF) per node was used for both aluminium and adhesive. For the composite, SOLID64 with 8 nodes, 3 DOF per node for orthotropic material was used. The model, illustrated in Fig.3.1, has 1010060 nodes and 2131998 elements. Due to the very refined mesh in the control cylinder, and the particular geometry of the adhesive layer (12.5 *mm* width x 12.5 *mm* lap-length and only 0.1 *mm* thickness) a refinement was also necessary for practically the entire domain in almost all volumes close to the overlap area, in order to allow a smooth transition between all the elements and to ensure reasonable aspect ratios for the elements.

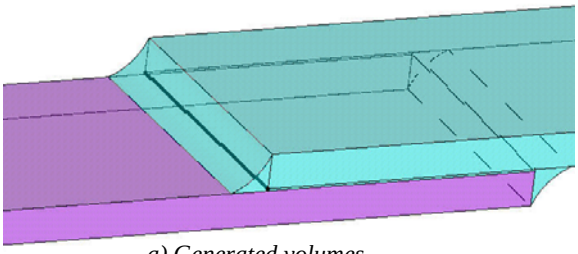

a) Generated volumes

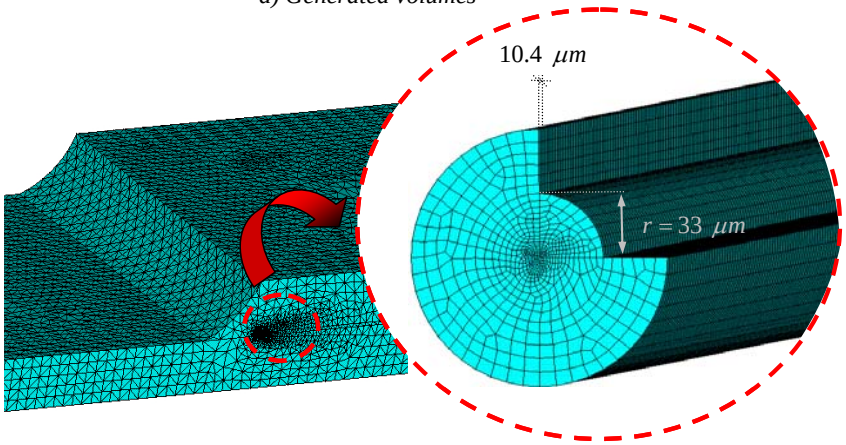

b) Mesh and detail of control cylinder

Fig. 3.1 – Volumes and mesh for the 3D model.

The external stress $\sigma = 100\ MPa$ is applied according to Fig. 1.1. Figures 3.2 and 3.3 show the stress distribution on the cylinder surface ($r = 33\ \mu m$) along the z axis for some arbitrary constant angles θ, here chosen equal to 270° and 220° respectively. The 3D FEM solution is divided by the plane strain BEM (2D) solution, where σ_r indicates the radial stress, σ_θ the circumferential stress and $\sigma_{r\theta}$ the tangential stress. $\theta = 220°$ was

chosen because the radial and circumferential stresses are maximum and minimum respectively at this angle.

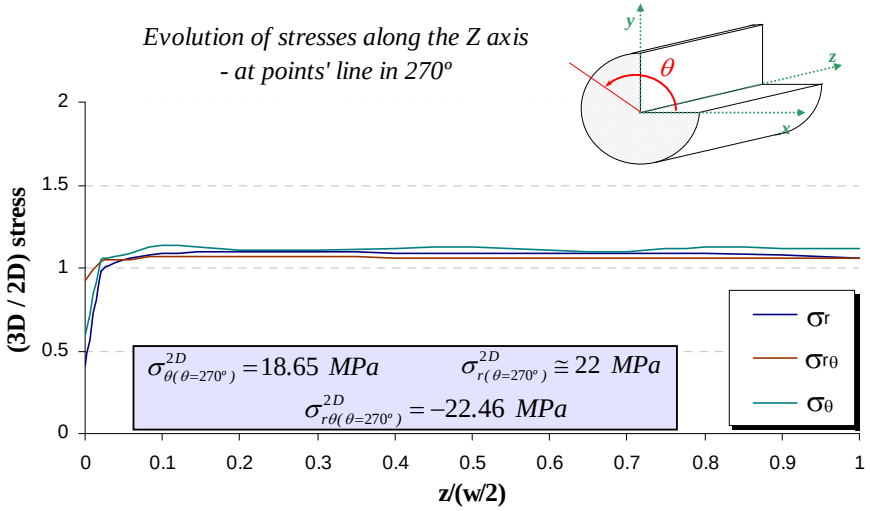

Fig. 3.2 – Stresses at point's line in 270º.

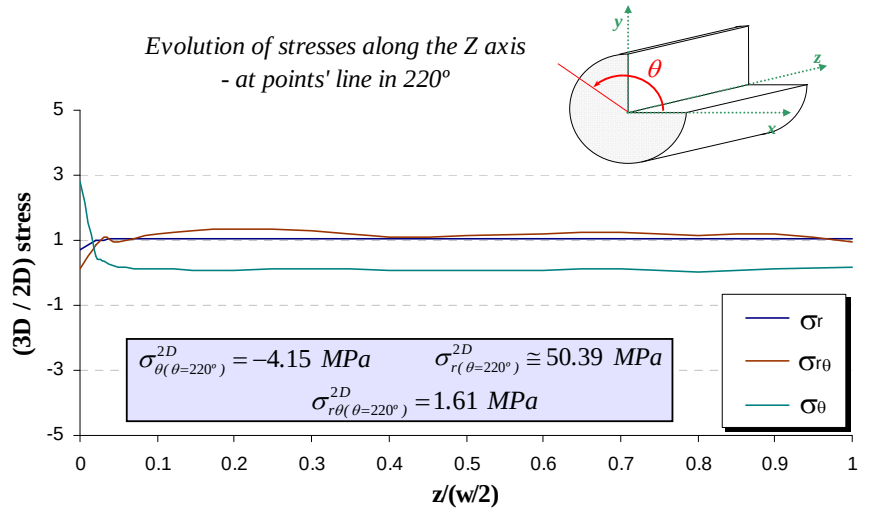

Fig. 3.3 – Stresses at points' line in 220º.

The edge effects can be observed in both figures (when the dimensionless $z/(w/2)$ trends to zero, which corresponds to the free lateral edge) and all the stresses are quite constant along the z axis, showing low dispersion with respect to the 2D BEM solution.

Another, possibly clearer, representation of the edge effect can be observed by means of the angular evolution of σ_θ, σ_r and $\sigma_{r\theta}$ at different positions along the z axis, which are depicted in Fig. 3.4, 3.5 and 3.6.

In Fig. 3.4 and 3.5 the edge effects can be clearly observed, where $z=0$ (which represents the free edge) and $z=12.5\ mm$ is the symmetry plane. The edge effect does not appear so clearly in the tangential stresses component, Fig. 3.6 and agrees with the results by Tsai and Morton in 1994, which used aluminium as adherend in a single lap joint. The stresses at the free edge were reduced by $\cong 11\ MPa$ in the worst case.

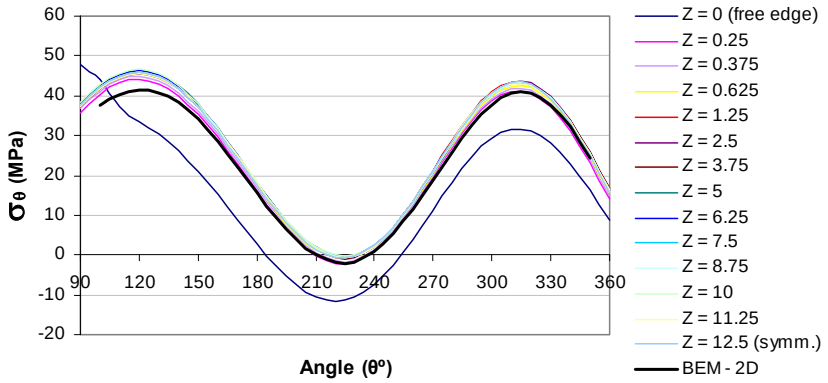

Fig. 3.4 – Angular evolution of σ_θ stresses.

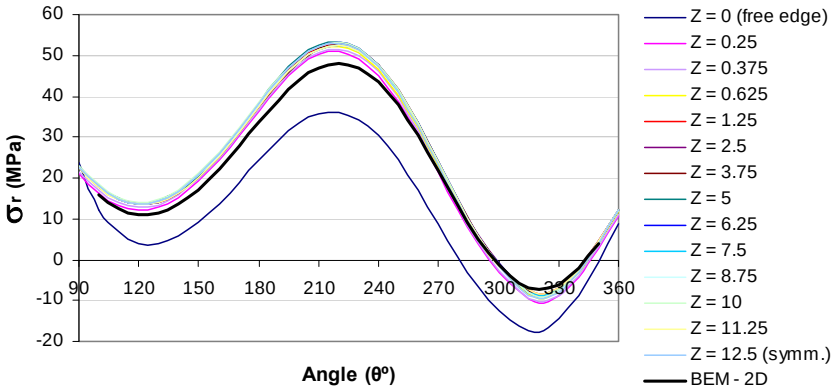

Fig. 3.5 – Angular evolution of σ_r stresses.

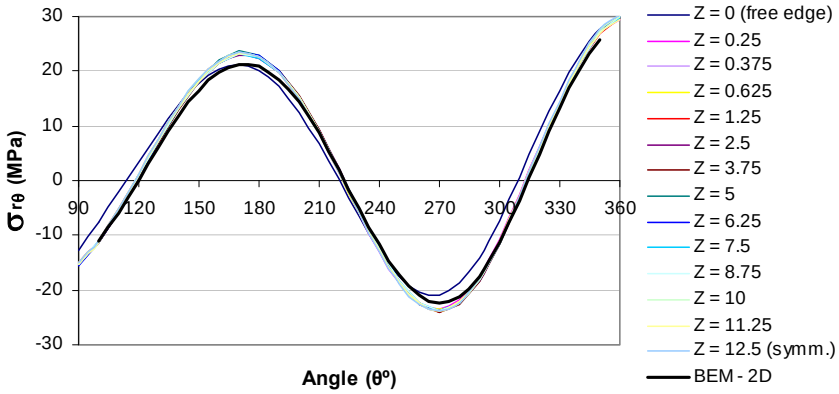

Fig. 3.6 – Angular evolution of $\sigma_{r\theta}$ stresses.

In addition, a general view of the stresses along the surface of the control cylinder was taken for evaluation. Fig. 3.7 shows the 3D FEM solution in terms of the circumferential stresses distribution, as a representative surface distribution that gives a qualitative idea of the edge effect.

Another important observation from Fig. 3.7 and 3.4 is that the maximum circumferential stress (probably the most directly related to the failure initiation process) occurs at 120º, coinciding with the experimental evidence for failure, in Barroso (2007).

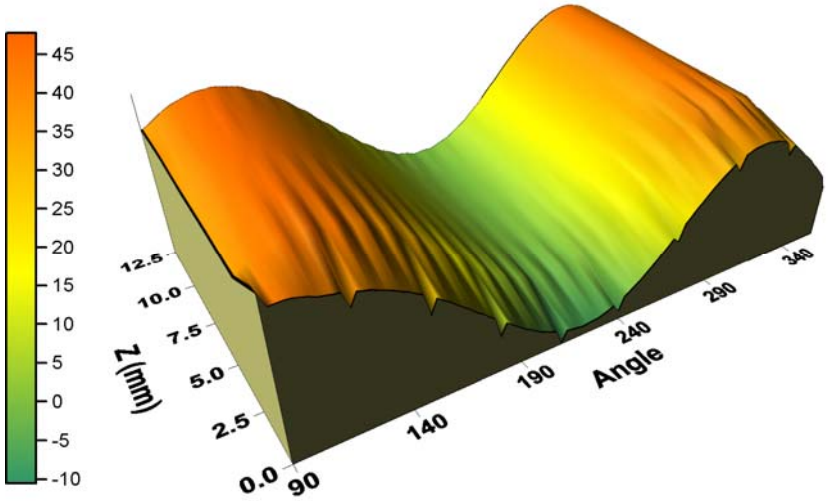

Fig. 3.7 – Distribution of circumferential stresses.

3.2 Bidimensional elastic-plastic analysis of the joint

Once verified (according to the first section of this chapter) that: a) 3D effects only affect a small length close to the free edge and b) the stress state at the free edge is less severe (≈ 97%) than in the central part of the joint, a simplified 2D model could be used for studying the stress state of the corner, which involves less computational costs. In this section, a 2D elastic-plastic numerical simulation (using finite elements in plane strain) was carried out in order to check the extent of the yielded zone at the neighbourhood of the bimaterial corner appearing at the end of

the overlap, which could be compared with the purely elastic solution. Secondly, a LEFM approach could be inadequate in the case of relevant plasticity in the corner, more specifically in the adhesive. For this purpose, in this section three yielding criteria were analyzed for the adhesive, taking or not into account, the influence of the mean stress (Raghava-Caddell-Yeh, Drucker-Prager and von Mises). In the literature (Caddell et al., 1973; Crocombe et al., 1995; Chowdhury & Narasimhan, 2000; Wang & Chalkley, 2000; Broughton et al., 2001; Dean & Crocker, 2001, Aydn, 2008; among others), there is a reasonable agreement that criteria which do not depend on the hydrostatic pressure are less suitable for represent the yielding behaviour in polymeric adhesives. Thus, a yielding criterion as the one by von Mises for example, would not be suitable, because assumes that the plastic strain appears independently of volume changes. In Fig. 3.8 a scheme of these criteria is presented for the sake of clarity. In what follows, each criterion will be explained in more detail.

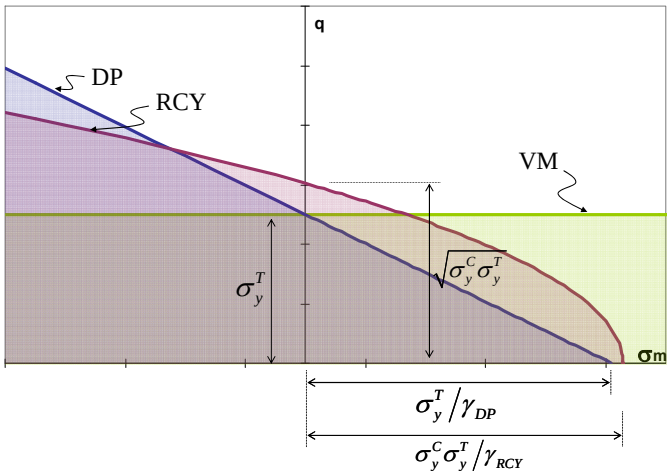

Fig. 3.8 – Scheme of the three criteria considered.

3.2.1 Von Mises criterion

The von Mises criterion for metallic materials proposes a cylindrical surface (see Chen and Han, 1988; Wilson, 2002 for more details) in the principal stress space (which rotates around the hydrostatic $\sigma_I = \sigma_{II} = \sigma_{III}$ axis). This criterion can be expressed by the following function:

$$f_{VM} = \sqrt{J_{II}} - k_S \tag{3.1}$$

where

$J_{II} = (1/6)\left[(\sigma_I - \sigma_{II})^2 + (\sigma_{II} - \sigma_{III})^2 + (\sigma_{III} - \sigma_I)^2\right] = (1/3)\left(I_I^2 - 3I_{II}\right)$ is the second deviatoric stress invariant, $I_I = \sigma_I + \sigma_{II} + \sigma_{III}$ and

$I_{II} = \sigma_I \sigma_{II} + \sigma_{II} \sigma_{III} + \sigma_{III} \sigma_I$ are the first and second invariants of the stress tensor, in terms of principal stresses. k_S is the yield strength in pure shear that can be written as $k_S = \sigma_y^T / \sqrt{3}$ (where σ_y^T is the yield stress of the material in pure tension).

Equation (3.1) can be rewritten as:

$$f_{VM} = q - \sigma_y^T \tag{3.2}$$

where $q = \sqrt{3 J_{II}}$ is the von Mises equivalent stress. According to Eq. (3.2), plasticity occurs when $f = 0$, thus:

$$\sigma_{eq}^{VM} = q = \sigma_y^T \tag{3.3}$$

In Fig. 3.8 the von Mises criterion is represented as a straight line in the plane of σ_m versus q, where $\sigma_m = I_1 / 3$ is the hydrostatic (or mean) stress.

3.2.2 Drucker-Prager criterion

Originally proposed for soils (Drucker & Prager, 1952), this criterion is a conic surface in the principal stress space. It can be considered as a von Mises modified criterion including the dependence on the hydrostatic stress component. Drucker-Prager yield function can be expressed as:

$$f_{DP} = \sqrt{J_{II}} + \beta I_I - k_S \tag{3.4}$$

where β depends on material constants and k_S was defined previously. Writing Eq. (3.4) in terms of the yield stress in tension ($k_S = \sigma_y^T / \sqrt{3}$), we obtain:

$$f_{DP} = \sqrt{3J_{II}} + \sqrt{3}\beta I_I - \sigma_y^T \tag{3.5}$$

Equation (3.5) can be rewritten in a more compact form as:

$$f_{DP} = q + \gamma_{DP}\sigma_m - \sigma_y^T \tag{3.6}$$

where $\gamma_{DP} = 3\sqrt{3}\beta = (6\sin\varphi)/(3-\sin\varphi)$ is the pressure sensitive parameter which is obtained doing the conic surface to contact the Mohr-Coulomb hexagonal pyramid in its vertices, φ is the internal friction angle.

According to this model, plasticity occurs when $f_{DP} = 0$, thus:

$$\sigma_{eq}^{DP} = q + \gamma_{DP}\sigma_m = \sigma_y^T \tag{3.7}$$

See Fig. 3.8 for the σ_m versus q representation according to this criterion.

3.2.3 Raghava-Caddell-Yeh criterion

According to the criterion proposed by Raghava el al. in 1973 for polymers, macroscopic yielding occurs when:

$$\left(\sigma_I - \sigma_{II}\right)^2 + \left(\sigma_{II} - \sigma_{III}\right)^2 + \left(\sigma_{III} - \sigma_I\right)^2 + \\ +2\left(\sigma_y^C - \sigma_y^T\right)\left(\sigma_I + \sigma_{II} + \sigma_{III}\right) = 2\sigma_y^C\sigma_y^T \tag{3.8}$$

where σ_y^C is the material yield stress in compression. Note that if $\sigma_y^C = \sigma_y^T$ the hydrostatic component vanishes and this criterion leads to the von Mises criterion.

Eq. (3.8) may be used to obtain the Drucker-Prager structure as in Eq. (3.6) or (3.7). This is necessary to properly introduce the parameters in the FEM commercial software, as in ANSYS as well in ABAQUS. This alternative is usually known as Extended Drucker-Prager (EDP) in the literature (Aydn, 2008; Chiang and Chai, 1994; Dean and Crocker, 2000). Thus Eq. (3.8) can be divided by two and rewritten as:

$$q^2 + \left(\sigma_y^C - \sigma_y^T\right) I_I = \sigma_y^C\sigma_y^T \tag{3.9}$$

Representing the right side term of this equation as a geometric average between the yield stress in tension and compression, it can be written as:

$$q^2 + \left(\sigma_y^C - \sigma_y^T\right)3\sigma_m = \sigma_{adm}^2 \tag{3.10}$$

where $\sigma_{adm} = \sqrt{\sigma_y^C \sigma_y^T}$ is an admissible stress. Another parameter which relates the yield stress in tensile and compression can be defined, i.e. $\lambda = \sigma_y^C / \sigma_y^T$ to obtain:

$$q^2 + \gamma_{RCY}\sigma_m = \sigma_{adm}^2 \tag{3.11}$$

where $\gamma_{RCY} = 3\sigma_y^T\left(\lambda - 1\right)$ and $\sigma_{adm} = \sigma_y^T\sqrt{\lambda}$, with stress units.

This criterion is a conic surface in the principal stress space but with its vertex rounded, which is much more efficient and stable from a numerical point of view when compared to the sharp cone vertex of the Drucker-Prager model.

In Fig. 3.8 the Raghava-Caddell-Yeh criterion is represented in the plane of σ_m versus q.

3.2.4 Numerical model and results

The geometry of the problem under study is depicted in Fig. 1.1, being $L_a = 50\ mm$, $L_o = 12.5\ mm$, $t_{a1} = t_{a2} = 1.6\ mm$ and $t_{a3} = 0.1\ mm$ the dimensions. The mesh used for the plane strain model is presented in Fig. 3.9:

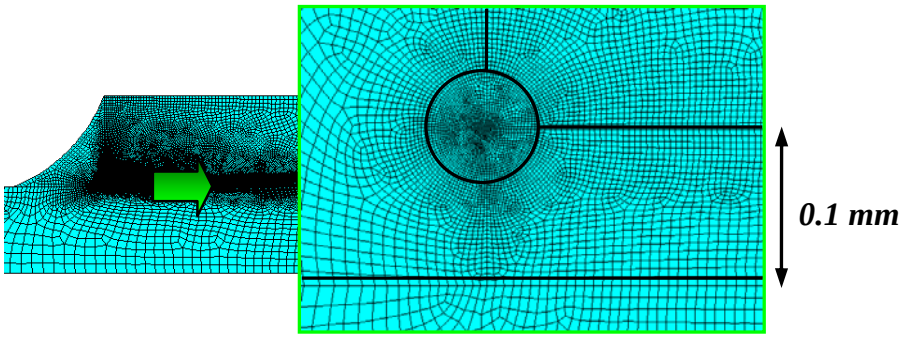

Fig. 3.9 – Mesh detail showing the control circle.

The value of the tensile stress applied in the left edge of the aluminium, Fig. 1.1 is of the order of that obtained experimentally at the instant of failure of the component, i.e. $\sigma = 172\ MPa$.

The mesh was sufficiently refined near the corner (inside a control circle of radius $r = 33\ \mu m$) in order to catch the high stress gradients near the bimaterial corner tip. Three plasticity models have been considered for the adhesive layer: von Mises, Drucker-Prager and Raghava-Caddell-Yeh model, all assuming bilinear isotropic hardening. Aluminium and CFRP were modelled as simple linear elastic materials, isotropic and orthotropic respectively. The smallest finite element used in the mesh is around $0.9\ \mu m$ at the corner. The FEM simulation was performed with ANSYS commercial software.

In von Mises model the quadrilateral PLANE42 element option was used, with four nodes and two DOF, 37733 nodes and 37306 elements in total. Hardening was activated with the "TB,BISO" command, considering the tangent modulus as $K_{tg}^{T} = 12\ MPa$ and $\sigma_{y}^{T} = 50\ MPa$ as the yield stress in tensile for the adhesive (Aydin, 2008).

Commercial FEM software (ANSYS or ABAQUS) is usually supplied with an extended form, designed to cover some inadequacies in the basic Drucker-Prager model, such as to allow the hardening of the material and smoothing of the sharp extremity of the conic surface. The Extended Drucker-Prager model (EDP in what follows) is introduced by means of a polynomial generic form:

$$f = q^{b} + \gamma\sigma_{m} - \sigma_{y}^{b} = 0 \tag{3.12}$$

where b is the exponent of the power law.

The Drucker-Prager and Raghava-Caddell-Yeh models were simulated using the EDP option (activated via "TB,EDP" command), with Linear ($b = 1$) and Power law ($b = 2$) yield functions respectively. The PLANE182, four nodes with two DOF element option was used, with 115343 nodes and 114507 elements in total. Associated flow rule was considered in both cases. Hardening was activated with the "TB,MISO" command for

these EDP models. The Linear EDP ($b=1$) was activated by using $\gamma=\gamma_{DP}=0.98$ (dimensionless), σ_y^b from Eq. (3.12) is equal to $\sigma_y^T=50\ MPa$ (parameters defined in (3.6)), where $\varphi=25^o$; and the Power EDP ($b=2$) by using $\gamma=\gamma_{RCY}=69\ MPa$, $\sigma_{adm}=\sigma_y^T\sqrt{\lambda}=60.4\ MPa$ (being this value introduced as the required σ_y in Eq. (3.12)) where $\lambda=1.46$, parameters which were defined in Eq. (3.11). Other general material properties are presented in Tables 2.1, 2.2 and 2.3 (given by the manufacturer and experimental tests), used for these analyses. Dean & Crocker (2001) state that the EDP in ABAQUS has the limitation of only modelling non-associated flow. This may impose some restrictions for modelling the Raghava-Caddell-Yeh criterion, for example (or known as "exponent Drucker-Prager" by Dean & Crocker). It is important to notice however; that the pressure sensitive parameter γ in Eq. (3.12) for modelling adhesives has different units when considering the Drucker-Prager (γ_{DP} dimensionless) and Raghava-Caddell-Yeh (γ_{RCY} has units of stresses) models. In ANSYS tutorials there is no advice about this caution for inexperienced users.

The results were obtained for a control circle around the corner, as indicated in Fig. 3.9. Figure 3.10 shows a

representation of the yielded zone according the three yielding criteria considered.

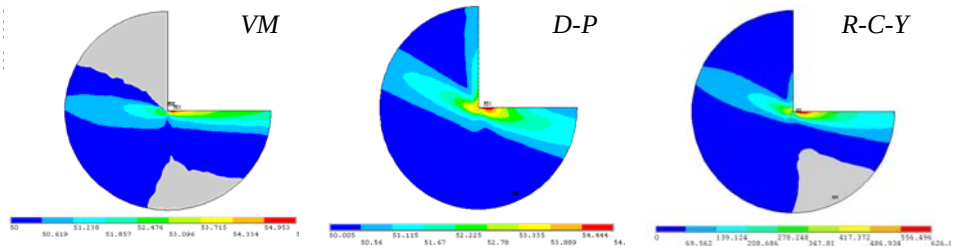

Fig. 3.10 – Yielded zone for the three criteria considered.

The coloured area inside the control circle (in which $r = 33\ \mu m$) represents plasticity and the grey colour represents no yielded zone. Plasticity occurs in the entire region only for the Linear EDP (or Drucker-Prager) criterion. In all models, a peak of stresses in the horizontal edge of the corner can be observed. This suggests that failure probably starts in this edge of the corner. Another important characteristic can be observed in both EDP models – the ones that include the hydrostatic stress influence – where the yielded area is oriented (considering it as the initiation of the failure path) to a certain angle above the horizontal line (about 30º clockwise from the horizontal axis), i.e. the hydrostatic stress increases the level of the stresses around the corner in this direction. An experimental validation of the yielded zone is not easy to obtain because the characteristic length at which yielding occurs is very small ($r = 33\ \mu m$).

Figures 3.11, 3.12 and 3.13 present the $\sigma_{r\theta}$, σ_r and σ_θ stresses distribution at points located at a $r = 33\ \mu m$ radius, at the boundary of the control circle (Fig. 3.9) in the bimaterial corner by the adhesive side (3/4 of the circumference, from 90º up to 360º according to a polar coordinate system in the corner tip), according to the different models.

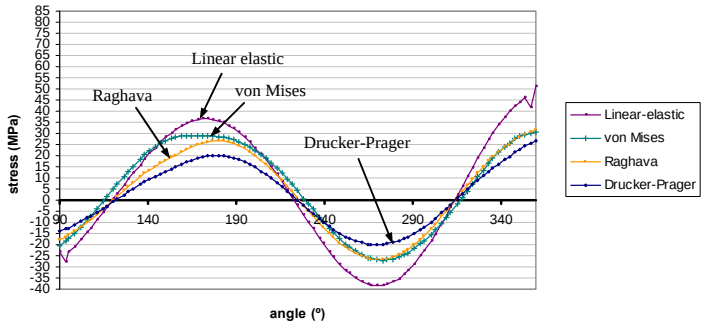

Fig. 3.11 – Tangential stresses ($\sigma_{r\theta}$) distribution.

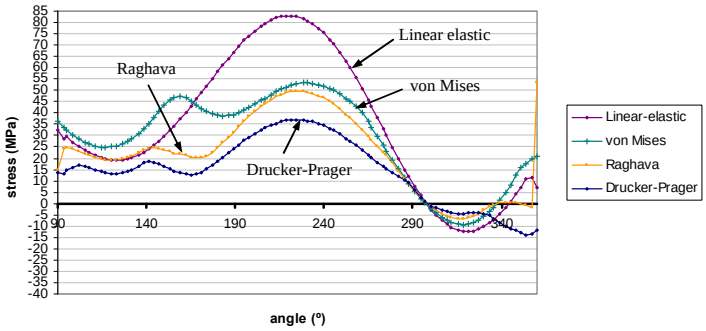

Fig. 3.12 – Radial stresses (σ_r) distribution.

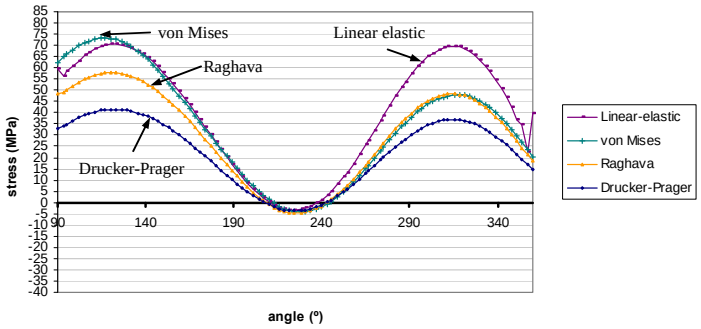

Fig. 3.13 – Circumferential stresses (σ_θ) distribution.

Tangential stress distribution is qualitatively similar between the different criteria and with respect to the linear-elastic solution, following similar paths. The Drucker-Prager model presents the greatest yielding at circumferential points, for all components of stress. Raghava criterion coincides mainly with von Mises response for the circumferential stresses, except for the interval between 90º and 190º, where the stress level drops by the order of 18% respect to the linear-elastic response. The Drucker-Prager is the model which presents the biggest yielding extent.

Figure 3.14 presents the hydrostatic stress for the adhesive inside the control circle radius $r = 33\mu m$ obtained by the three yielding criteria considered and also for the simple linear elastic case. For Drucker-Prager and Raghava criteria (both include the pressure effect) the strong tendency to lead the stress state at a certain angle is observed. This suggests that a yielding criterion

that includes the hydrostatic pressure leads to a hypothetical failure path, controlled by plasticity mechanisms, in that direction (around 30º from the CFRP-adhesive vertical interface in the corner). This angle was experimentally observed in the failure path by Barroso et al. (2009[B]).

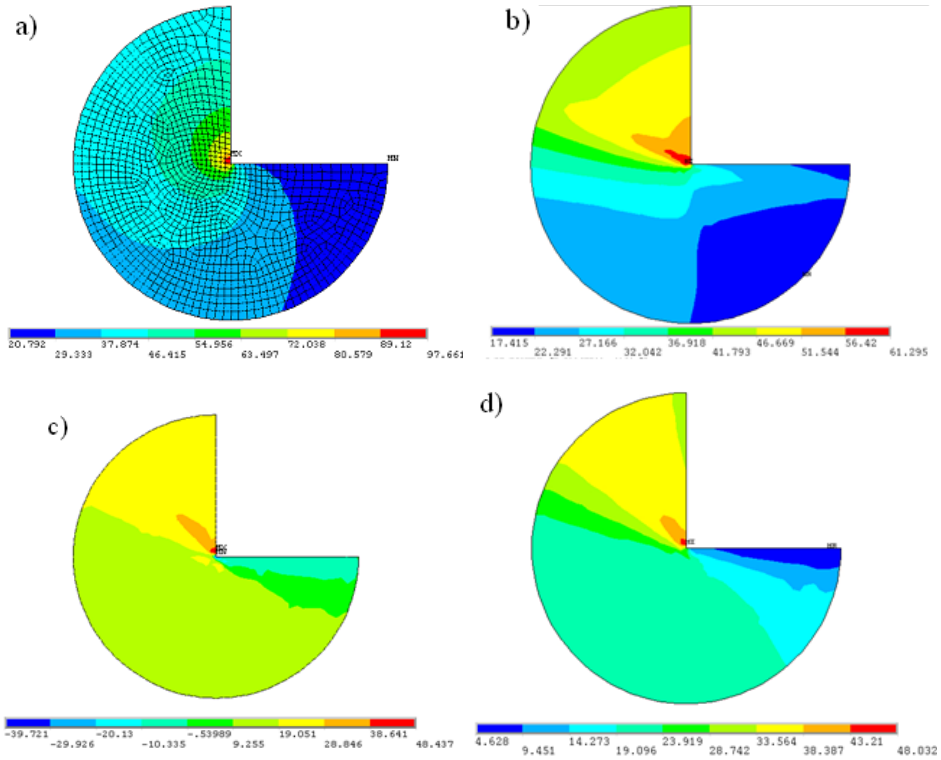

Fig. 3.14 – Hydrostatic stress in the cases: a) Linear elastic with the mesh used; b) von Mises; c) Drucker-Prager and d) Raghava-Caddell-Yeh.

The linear-elastic response presented was successfully verified with analytical and BEM numerical models carried out by Barroso (2007) although it is not presented here.

3.3 Bidimensional elastic analysis of the joint

This section presents some photographs of the linear elastic stress state of the joint, and more specifically of the corner under study, for comparison with other topics of this Thesis. The mesh is the same as used in the previous section, being the model (type of finite element, mesh, etc.) detailed previously. In this analysis, the applied stress was $\sigma = 100\ MPa$.

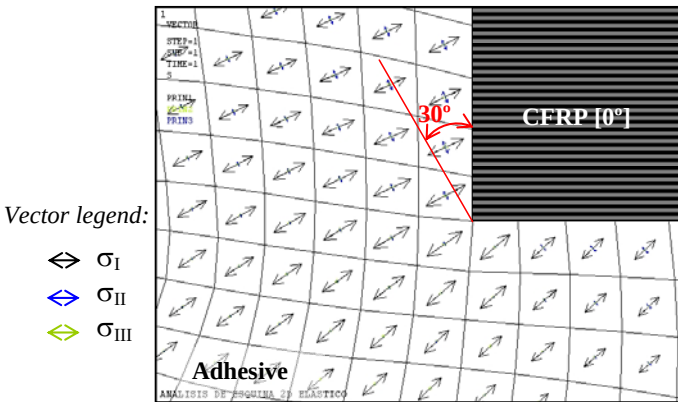

Fig. 3.15 – Detail of the principal stresses in the adhesive at the corner tip (vectorial representation).

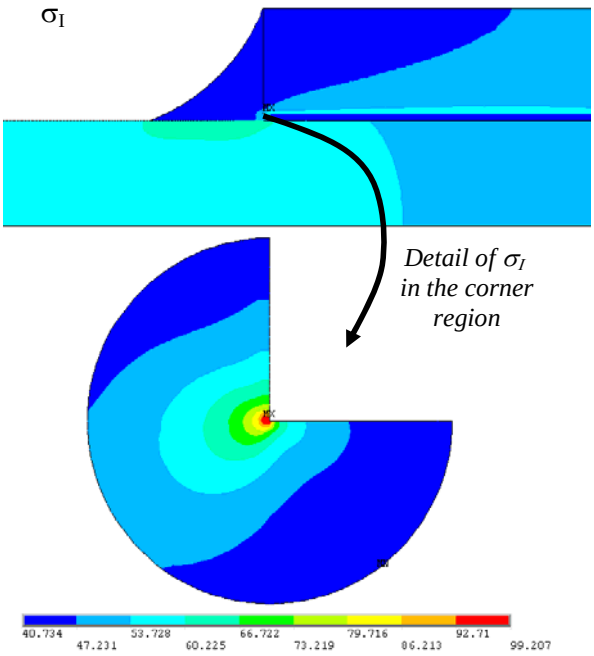

Fig. 3.16 – Principal stress σ_I of the joint and detail of the corner of interest.

From these figures, some information of the stress state can be obtained. For example, a three-axial stress state is present, closed to the corner at the vertical CFRP-Adhesive interface. It is well known that this type of stress state is prone to initiate failure in metals. In addition, the angle of 30º from the vertical CFRP-Adhesive interface is indicated in Fig.3.15. This angle was approximately the same angle for failure in the joint, based on Barroso's observation. From Fig. 3.15 and by comparison, it can

be inferred that the 30º angle is practically perpendicular to the direction of σ_1 (principal direction).

3.4 Discussion

In the 3D numerical analysis, the local stress state at the bimaterial corner appearing in the studied Al-CFRP adhesively bonded DLJ have been analyzed in detail. The singular stress state at this corner changes at the free lateral edge where 3D geometry affects the 2D solution.

The edge effect was observed in the particular joint under analysis. The 2D plane strain model successfully caught the stress state in the corner of interest, which is the focus of this work. The circumferential and radial stresses became lower at the edge, the 2D solution (plane strain) being valid in about 97% of the width of the specimen (Fig. 3.4 and 3.5). Thus the commonly used 2D plane strain analysis has been shown to be sufficiently accurate for predicting the stress state in the region away (equal to the adhesive thickness, in distance) from free edge, for the configuration analyzed. Thus it can be inferred that 2D analyses control the failure initiation in the central region of the joint close to the corner edge, being plane strain the state which yields to the failure.

The size of the adhesive thickness ($0.1\ mm$) made the 3D model computationally expensive as it is a large area with a very low thickness and stresses varying in the thickness direction need a very fine mesh. 2D solutions are therefore easier to handle. However, not all material combinations lead to the same result because stresses are less severe at the free edge. Thus for every case this fact should be verified before using representative 2D models. The use of submodeling (Bogdanovich et al. 1999) could be a known alternative to the present expensive 3D numerical simulations.

Next, the plasticity influence was analyzed in the vicinity of a bimaterial corner, by means of a FEM commercial code. The presence of yielding in the corner can significantly change the local stress state. In this work the von Mises, Drucker-Prager and Raghava criteria have been considered by introducing plasticity in the adhesive layer, the last two models being dependent of the hydrostatic pressure. The hydrostatic stress affected the stress state and yield path. In this study a trend to orient the yielded zone and hydrostatic stress to a certain angle (about 60º and 30º counter clockwise, respectively, from the vertical CFRP-Adhesive interface) was observed. Among the three criteria, the Raghava-Caddell-Yeh model can be considered as the most suitable for this type of adhesive, which exhibits strong dependency of the

hydrostatic pressure in yielding, as confirmed by preliminary experimental results.

The most important conclusion of this chapter is the verification of the validity of the plane strain elastic solution instead of a 3D model. The plasticity is significantly small because it slightly decreases the level of stresses, as may be seen in Figs. 3.11 to 3.13. Thus the bidimensional linear elastic model can be considered to be, in a first approximation to the problem, sufficiently accurate for further studies (Chapter 6 and 7), where the evaluation of the critical values of GSIF is required and the plasticity influence needs to be discarded.

Chapter

4 Thermal stresses in curing

The use of adhesives curing at temperature in bonded joints between dissimilar materials (composites and metals) gives rise to residual stresses due to the difference in the value of the thermal expansion coefficients of the adherends. This chapter presents numerical results of the double-lap joint under study, including the thermal stresses which arise during the cure process. The uniform temperature variation from curing to room temperature has been shown, numerically, to have a significant influence on the local stress field in the neighbourhood of the critical corner. Due to the fact that high stress gradients are developed at the corners in the curing process and stress relaxation effects may occur due to the viscoelastic behaviour of the polymeric adhesive at room temperature (Dean & Crocker, 2001), experimental tests have also been carried out to study the influence of uniform temperature fields on the strength of the joints based on parameters which define the singular stress state at these multimaterial corners.

Residual thermal stresses are generally associated with the geometry of the joint and the high difference in the values of thermal expansion coefficients of these materials, in conjunction with their lack of thermoelastic isotropy. The importance of these

thermal residual stresses in adhesively bonded joints has been widely reported in the literature (Weitsman, 1980; Jumbo et al., 2007). Furthermore, a comprehensive analysis of the influence of these thermal effects on the efficiency of adhesively bonded lap joints was presented by Hart-Smith (Hart-Smith, 1973[A]). Thermal residual stresses increase with the curing temperature of the adhesive and also with the difference in the thermal expansion coefficient of the materials. If these values (adhesive curing temperature and the difference in the thermal expansion coefficients) are high enough, the joint may fail even before reaching room temperature (Hart-Smith, 1973[A]).

In previous works (Gradin & Groth, 1984; Hattori, 1991; Barroso, 2007) the effect of residual stresses arising from the curing process was not included. However, it is well known that the thermal stresses in multimaterial corners with singularities play an important role in the asymptotic stress state (see Yang & Munz, 1995; Lee, 1998 and Qian et al., 2000 among others).

Nevertheless, the presence of high stress gradients, in combination with the known viscoelastic behaviour of polymeric adhesives, may lead even at room temperature (Hojjati et al., 2004), at least in the neighbourhood of these highly stressed corners, to an important stress relaxation, as pointed out by Yadagiri et al. (1987), Atkinson & Bourne (1990), Lee (1998), Qian et al. (2000) or Feldstein (2009). In particular, Yadagiri et al.

(1987) predict, numerically, a relaxation of 40% of the peak stress values developed at the ends of the overlap in the first few hours after the curing process. Feldstein (2009) reports stress relaxations for polymeric adhesives within a time range of 800 s less than 15 minutes in a wide range of polymeric materials. Lee (1998) obtained a relaxation effect of the edge stress intensity factor values and an increment of the order of stress singularities. Qian et al. (2000) also calculated a relaxation effect in the σ_θ stress component in an elastic/viscoelastic adhesive joint if the load is applied in the elastic material (the outer adherend), and not in the viscoelastic material (the inner adhesive). Atkinson & Bourne (1990) computed numerically, from analytical expressions, the short and long term variation of singularity stresses in angular sectors of viscoelastic media. Kay et al. (2002) found significant relaxation effects in bimaterial joints considering the viscoelastic behaviour of the materials.

The above considerations on whether or not the thermal stresses play a role in the asymptotic stress field, at the multimaterial corners, which have been shown to control the initiation of failure of these adhesively bonded joints, are the reason for the present study.

Among the various complex processes affecting the generation of thermally induced residual stresses in polymer composites (Liu, 1999; Gopal el al., 2000; Zhang et al., 2004; Parlevliet et al.,

2006; Zhao et al., 2006; MIL-HDBK-17), different thermal contraction values of the materials and the temperature dependent mechanical properties have been included in the numerical analyses of this work. Thus, viscoelastic behaviour and volume shrinkage of the adhesive layer during isothermal curing have not been considered in the numerical evaluation but experiments have been conducted to see their effect.

The presence of singular stress states at multimaterial corners makes the Boundary Element Method (París & Cañas, 1997) an efficient tool for a detailed analysis of problems of this kind (Barroso, 2007; Lee, 1998). In the present chapter, a BEM code by Graciani (2006) has been used to study the influence of the residual thermal stresses in the asymptotic stress state at corners in an Aluminium-CFRP double lap joint loaded in shear by tension (Fig. 1.1).

The next section presents details of the numerical model and analysis carried out. Numerical results with and without thermal effects are compared (in this work only this configuration is presented, but the same effect for another configuration can be seen in Barroso et al., 2011). The following section describes the experimental tests carried out, including the analysis of the influence of uniform temperature fields on the strength of adhesive joints containing thermal residual stresses, and

covering the study of the role of possible residual stress relaxation over the time on the strength of the joints.

The aim of the present chapter is to analyse only the role of the thermal effects on the asymptotic stress and displacement fields at the neighbourhood of the corner tip.

4.1 Numerical analysis

The problem under analysis is represented in Fig. 1.1, where $t_{a1} = t_{a2} = 1.6\ mm$, $t_{a3} = 0.1\ mm$, $L_0 = 12.5\ mm$ and $L_a = 50\ mm$. The composite adherend is formed by 8 plies of unidirectional CFRP 8 plies laminate.

A tensile stress of $\sigma = 125\ MPa$ is applied at the left-hand side of the aluminium plates for both configurations in order to compare these analyses with previous studies (Barroso, 2007).

A linear elastic analysis, assuming plane strain state, was carried out using a BEM (París & Cañas, 1997) software (by Graciani, 2006), which includes the capability to consider uniform temperature effects in orthotropic materials. Once the 3D analysis presented in Chapter 3 confirmed the validity of generalized plane strain assumption, a simple linear elastic analysis, assuming plane strain state, was performed.

The thermo-elastic properties for the CFRP, modelled as for an orthotropic material, are given in Table 2.3, whereas the isotropic elastic properties of the epoxy adhesive and aluminium are given respectively in Tables 2.1 and 2.2.

During the cooling process the mechanical properties, mainly those associated with the adhesive and composite resin, are temperature-dependent. However, under the present assumptions the final stress and displacement states at room temperature depend only on the final stiffnesses at room temperature and the mean value of the variation of the thermal expansion coefficient from the curing to room temperature (Noda, 1986; Matsumoto et al., 2005; Argeso & Eraslan, 2008). In the case of the particular adhesive used in this work, the difference of the thermal expansion coefficient at room temperature and its mean value (over the range of temperatures from 115ºC to 25ºC) is less than a 10%. Results including the temperature dependent properties of the adhesive layer were also computed, and the relevant results were also below a 10% difference with the results computed using constant values at room temperature. Thus, the latter results (considering all the mechanical properties at room temperature) were used in what follows.

The stress and displacement fields were evaluated, including the thermal effects in the curing process. The corner under analysis is the critical corner between the 0º laminate and the

adhesive layer and fillet, at the left-hand side of the overlap (Fig. 1.1).

Both the mechanical loading ($\sigma = 125\ MPa$) and the thermal loading ($\Delta T = -90^{o}C$, from the curing temperature 115ºC to the room temperature 25ºC) were considered, as well as other intermediate values of the temperature decrement ($\Delta T = -60^{o}C$, $\Delta T = -45^{o}C$, $\Delta T = 0^{o}C$). Although it is well known that there is a radial dependency of the stresses and displacements, in Barroso (2007) and Barroso et al. (2009[B]) it was shown that in the range $10\mu m < r < 33\mu m$ no significant changes appear in the qualitative stress and displacement distributions along the circumferential coordinate and the failure path was in good agreement with the experimental evidences.

The BEM model includes aluminium, adhesive and the CFRP laminate. Perfect adhesion is considered along the common boundaries. Symmetry conditions are applied at the bottom side of the aluminium plate, while clamped conditions ($u_x = u_y = 0$) and uniform tensile stress of $\sigma = 125\ MPa$ are respectively applied at the extremity, as indicated in Fig. 1.1. The model has 1364 linear elements and for an accurate evaluation of the stress field at the neighbourhood of the CFRP-Adhesive corner, a progressive refinement towards the corner was performed with a final element length of $10^{-6}\,mm$ at the corner tip. This size, without

physical meaning, is required to achieve satisfactory results in presence of a singular stress field and avoid the typical numerical errors associated with the discretization appearing at the characteristic distance of interest ($r \approx 0.02\ mm$). No result is obtained at such small distance ($10^{-6} mm$). A detail of the BEM model and the overlap zone is shown in Fig. 4.1.

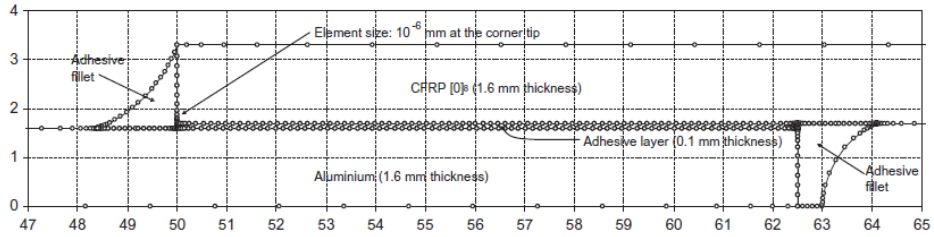

Fig. 4.1 – BEM model, detail of the overlap zone.

Taking into account both the mechanical ($\sigma = 125\ MPa$) and thermal loading, displacements (u_r, u_θ) and stresses (σ_r, σ_θ, $\sigma_{r\theta}$) were evaluated around the corner notch at a distance of $r = 0.0194\ mm$ from the corner tip. The displacements are shown in Fig. 4.2 considering four cases of decreasing temperatures, where $\Delta T = 0^o C$ denotes the application of the mechanical load and $\Delta T = -90^o C$ the inclusion of the curing effect (from 115°C up to 25°C) besides the mechanical load. Almost the completely opposite behaviour can be observed in Fig. 4.2, in the cases with only mechanical loading and the actual case with $\Delta T = -90^o C$

plus mechanical loading. The cases with mechanical and intermediate temperature decrements $\Delta T = -60^{o}C$ and $\Delta T = -45^{o}C$ give rise to intermediate results.

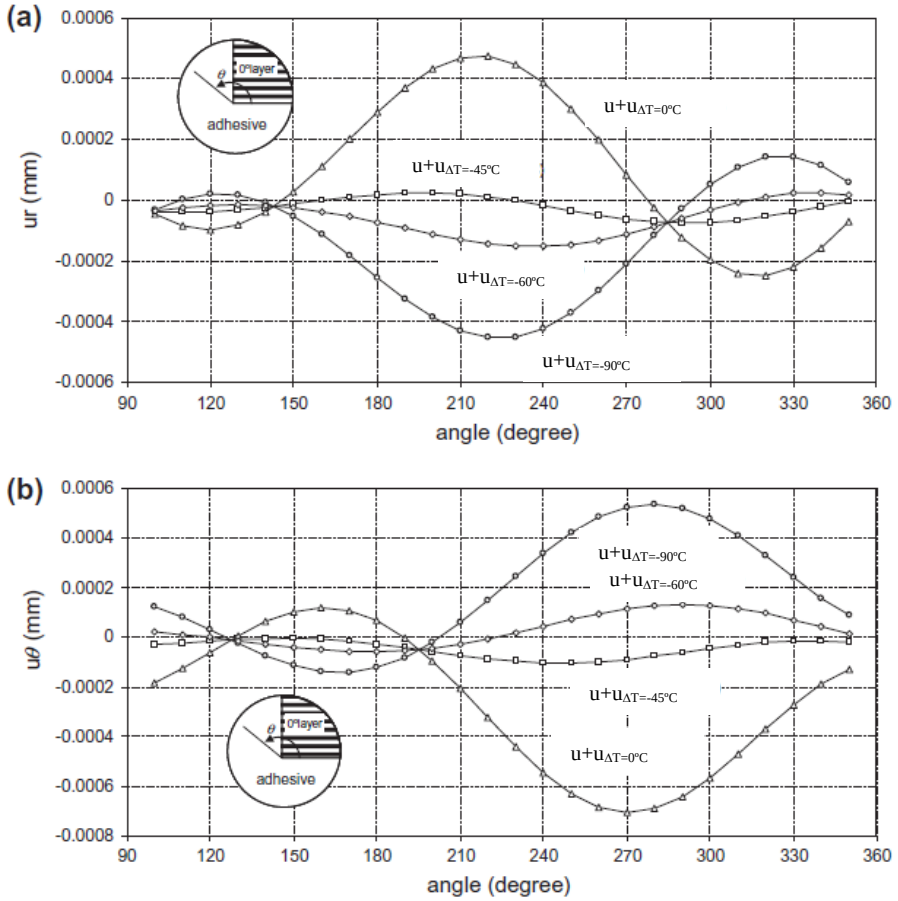

Fig. 4.2 – Displacements inside the adhesive u_r (a) and u_θ (b), at $r = 0.0194\ mm$ under mechanical and different thermal loadings.

The three components of the stresses (σ_θ, σ_r, $\sigma_{r\theta}$) around the corner at $r = 0.0194\ mm$ are shown, for the same four cases considered above, in Fig. 4.3.

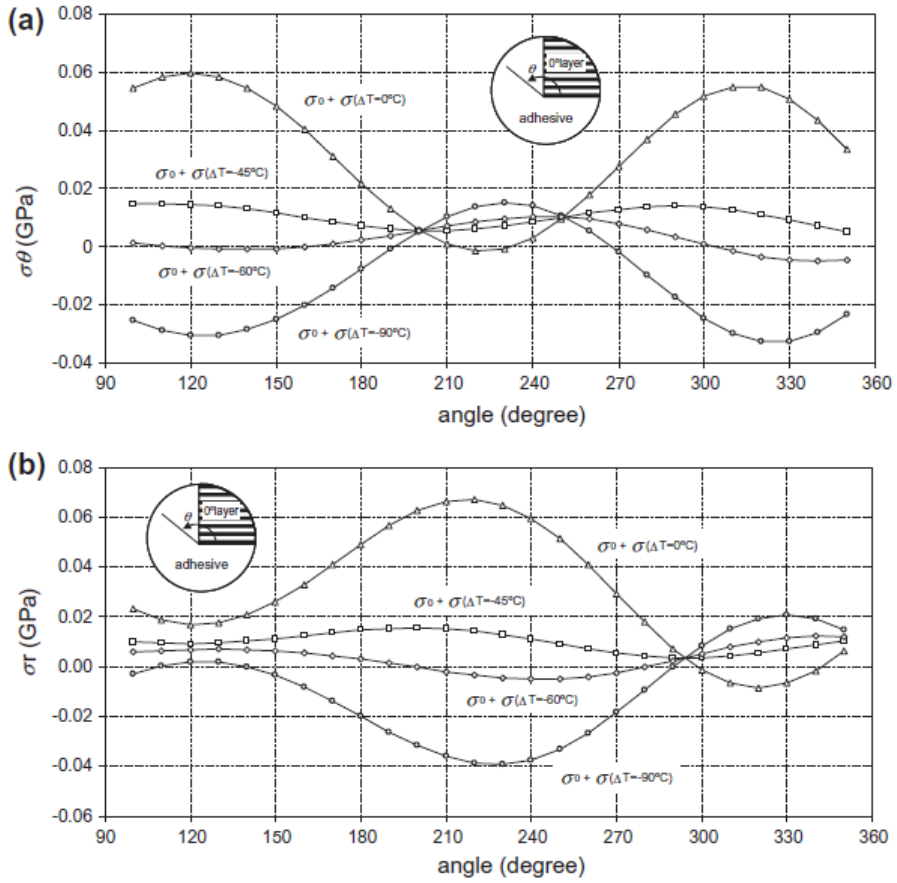

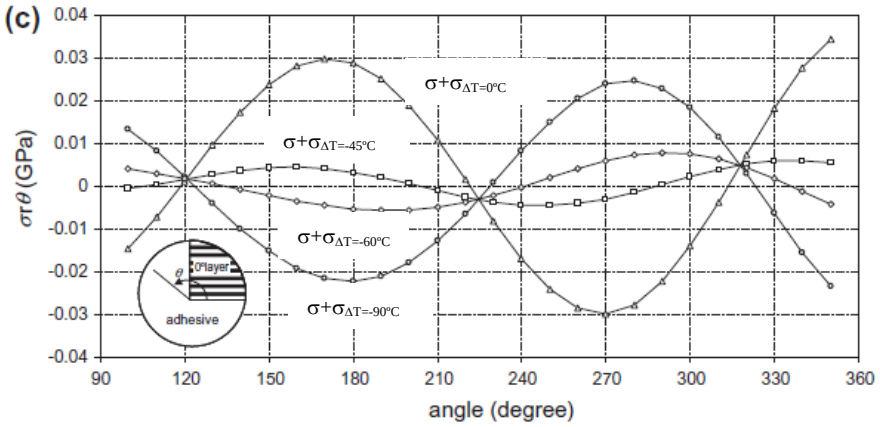

Fig. 4.3 – Stresses inside the adhesive, (a) σ_θ, (b) σ_r and (c) $\sigma_{r\theta}$ at $r = 0.0194\ mm$ under mechanical and different thermal loading.

The angular behaviour of the stresses is, as in the case of the displacements, roughly opposite depending on whether or not the thermal effect of $\Delta T = -90^{o} C$ is included. For the intermediate cases $\Delta T = -60^{o} C$ and $\Delta T = -45^{o} C$ it is important to observe that the computed stresses around the corner are very low (in absolute values) if compared with the cases with $\Delta T = 0^{o} C$, which would correspond to an adhesive curing at room temperature, and $\Delta T = -90^{o} C$ which corresponds to the real case. This fact opens up a future line of work in which the effects of the thermal stresses during curing may be used to compensate mechanical stresses caused by nominal loads. Thus, in the clearly identified context given in the introduction to this chapter,

thermal stress is the unique source of residual stresses considered in this work.

If the stress field in the neighbourhood of the corner is controlling the initiation of failure, as suggested by (Hattori, 1991; Reedy, 2000; Leguillon, 2001; Leguillon, 2002; Quaresimin & Ricotta, 2006[B]; Barroso, 2009), the results shown in Fig. 4.3 would imply, for instance, a higher static strength, or fatigue life, in adhesively bonded double-lap joints under the configuration analyzed with adhesives curing at temperatures between 70ºC and 85ºC (which correspond to cooling stages of $\Delta T = -45^{o} C$ and $\Delta T = -60^{o} C$ respectively). This assumes that the initiation of failure is controlled by the asymptotic linear elastic solution.

4.2 Experimental analyses

The numerical results obtained here have shown the significant influence of the thermal stresses in joints of this kind, changing completely the predicted local stress (and displacement) distribution depending on whether or not the thermal effects during the cooling stage of the curing cycle are taken into account.

As mentioned in the introduction of this chapter, previous experimental results (Barroso et al., 2009[B]) show that failure

paths in the configuration analyzed in last section are properly predicted considering only the mechanical loading and the maximum circumferential stress criterion, without taking into account the thermal loading. The satisfactory agreement between experimental and numerical results in (Barroso et al., 2009[B]) prompts the question of whether the local residual stresses due to temperature (obtained numerically) were actually present in the joint at the time the tests were carried out or, on the contrary, they progressively relax and disappear with time, as pointed out by Yadagiri et al. (1987), Atkinson & Bourne (1990), Lee (1998), Qian et al. (2000) and Feldstein (2009). For this reason, and in order to further investigate the presence or not of these local residual stress fields, two different experiments were proposed. The first consisted of the DLJ (represented in Fig. 1.1) subjected to shear by tension at different temperatures, and the second had the same configuration but tested at different times from the end of the curing cycle. Both experiments are detailed in the following sections.

For both tests, all the specimens were manufactured by bonding the composite laminate with the aluminium plate in a hot plate press; the curing cycle recommended by the manufacturer of the adhesive was specified in Chapter 2 (the same adopted by Barroso in 2007). For each type of test, all the specimens were obtained from a single batch of samples to reduce uncertainty associated with the curing process.

4.2.1 Testing DLJ at different temperatures

The results in Fig. 4.3, show completely different stress distributions for all stress components depending on whether or not the $\Delta T = -90^{o}C$ is considered. This suggests that, if failure is controlled by the stress state at the neighbourhood of the corner, failure initiation in these joints, using adhesives curing at lower temperatures, would occur at higher mechanical load values. In Fig. 4.3, the mechanical load is the same for all values of ΔT. Thus, failure should occur at a higher value of the applied mechanical loading for adhesives curing at $\Delta T = -60^{o}C$ or $\Delta T = -45^{o}C$ than that observed for the configuration with $\Delta T = -90^{o}C$, if the same value of any of the stress components is obtained at failure. In any case, the failure mechanism, including the thermal loading, may vary from that obtained without thermal loading due to the fact that the stress state is different.

Curing the joints at a different temperature than that recommended by the manufacturer can greatly affect the mechanical properties of the adhesive. For this reason a different strategy has been used, as the simplest approach to try to observe the influence of different curing temperatures on the residual stress field developed at the joint, which may be considered as an alternative to analyzing this effect. The samples bonded with the adhesive curing at $T = 115^{o}C$ tested at a

temperature T_0, higher than room temperature, may be considered to have a similar stress state to that developed with an adhesive curing with $\Delta T = -\left(115 - T_0\right)\ ^{o}C$. In particular, testing at $T_0 = 65^{o}C$, which is 40ºC over the room temperature, would be similar to having an adhesive curing with a cooling jump of $\Delta T = -50^{o}C$, 40ºC lower than the reference value of $\Delta T = -90^{o}C$. The previous arguments are only a rough approximation of both situations, as the mechanical properties of the adhesive change at $T = 65^{o}C$, although this is only 40ºC above room temperature; however, they can help in a preliminary attempt to analyze the influence of the temperature on the residual stress field.

The suggested tests were carried out from room temperature, 25ºC, to 65ºC, at intervals of 10ºC, using two samples at each temperature level. The tests were done after letting the samples stabilize at the test temperature (≈ 25 min). The temperature was monitored by means of a thermocouple located closed to the centre of the specimen. For each pair of samples to be tested at the same temperature, the procedure was the same: while the first specimen was being tested, the second was inside the oven at the prescribed temperature to avoid a temperature change. The time between the first and second test at each temperature level was only one or two minutes. The results for all the tests are

shown in Fig. 4.4, where the apparent shear strength (the failure load divided by the bonding area $\tau_{\max} = F_{\max}/2A_{lap}$ where $F_{\max}$ is the failure load and A_{lap} is the overlap area) is plotted versus the temperature in the test chamber.

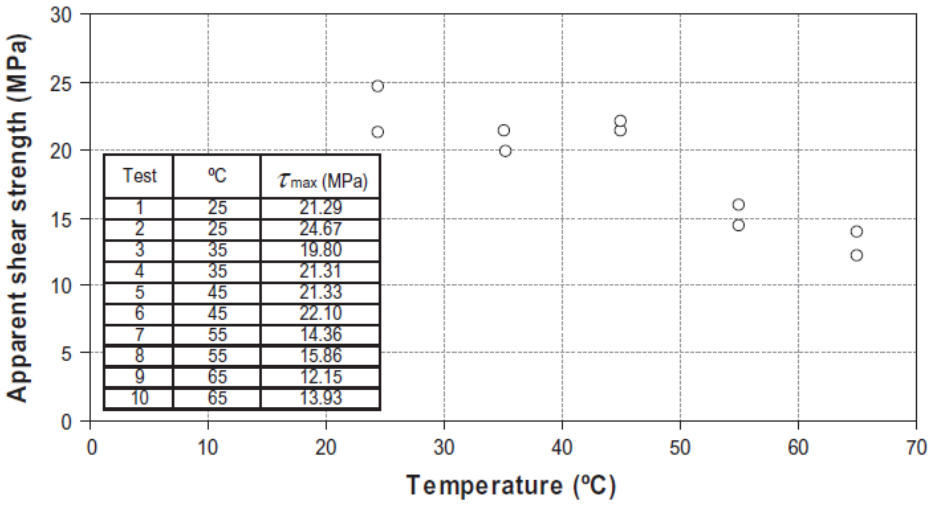

Test	ºC	$\tau_{\max}$ (MPa)
1	25	21.29
2	25	24.67
3	35	19.80
4	35	21.31
5	45	21.33
6	45	22.10
7	55	14.36
8	55	15.86
9	65	12.15
10	65	13.93

Fig. 4.4 – Apparent shear strength at different temperatures.

Results in Fig. 4.4 show a decrement of the apparent shear strength with temperature. In the range $25^{o}C < T < 45^{o}C$ the shear strength obtained in the tensile tests is quite constant and then decreases for $T \geq 55^{o}C$. No increment of the failure load is observed even for moderate temperatures, where adhesive mechanical properties are expected not to change significantly. In fact, it seems that due to the drop in the adhesive mechanical properties with temperature (although ΔT is moderate with

respect to room temperature), the apparent shear strength also decreases.

Photographs of the failure path were taken after failure. Figure 4.5 shows the failure details of the adhesive fillet at the end of the overlap (50 times magnification) for tests carried out at $T = 25^{o}C$, $55^{o}C$ and $65^{o}C$ respectively.

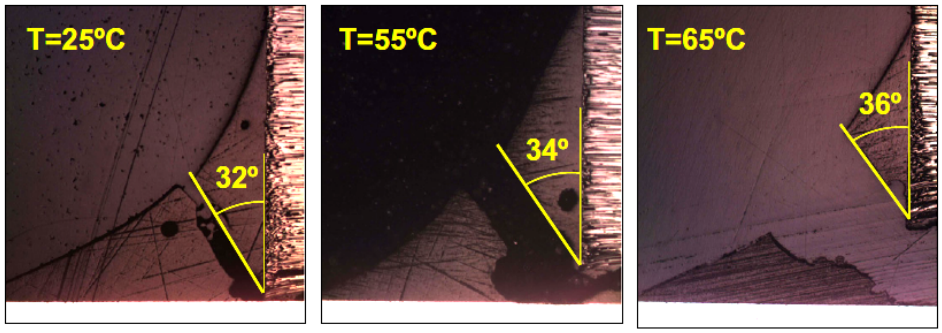

Fig. 4.5 – Failure path orientations for specimens tested at 25ºC, 55ºC and 65ºC.

Failure path orientation was observed to be quite similar in the three samples, showing failure angles in the range 32º up to 36º, measured from the vertical CFRP-adhesive interface. Results in Fig. 4.5 show a significant independency of the failure path orientation with respect to the test temperature, in contrast with the numerical results obtained in Fig. 4.3.

4.2.2 Testing DLJ at different times (stress relaxation)

The residual stresses developed in the adhesive layer during the cooling stage of the curing cycle could decrease over time due to stress relaxation effects, as pointed out in the introduction (Yadagiri et al., 1987; Atkinson & Bourne, 1990; Lee, 1998; Qian et al., 2000; Hojjati et al., 2004; Feldstein, 2009). This relaxation effect is more intensive at highly stressed areas such as those considered in this work with singularity stress fields. In such cases, the discrepancies observed between the experimental (Barroso, 2007 and Barroso et al., 2009[B]) and numerical predictions obtained in this work would be justified, as the tests carried out in Barroso (2007) and Barroso et al. (2009[B]) were done several weeks after curing the samples, and the residual stresses due to the bonding process may therefore be less significant.

For this reason a new experiment was also conducted curing 24 identical samples of the double-lap joint under study (shown in Fig. 1.1). The samples were tested at different times from the end of the bonding process. The first test was performed only 15 minutes after the bonding was done, the minimum time required to prepare the sample, which is above the relaxation time reported by Feldstein (2009) for stress relaxation. The second

pair of tests were done one hour after the first, and then each pair of tests were separated from the previous ones by a factor of $2.2^{(j)}$ (for $j = 1, 2, 3, ...$) with a final time schedule (in hours) of: (1, $3.2 = 1 + 2.2$, $8 = 3.2 + 2.22$, $18.7 = 8 + 2.23$, ...). This allowed tests to be carried out from 15 minutes to 203 days (approximately 7 months), equally spaced in time, in a logarithmic scale in the time axis (see Fig. 4.6). The samples were stored at $23 \pm 3^{o} C$ and $50 \pm 10\%$ *RH*. Each test was done using two samples, thus producing 12 pairs of results. Each pair of samples was tested with a delay of just 1 or 2 *min* between every specimen, the typical testing time to failure. A photograph of some of the tested specimens, and the complete data for the 24 samples, is shown in Fig.4.6, including the apparent shear strength obtained from the tests.

The results shown in Fig. 4.6 do not show a clear variation, or trend, in the apparent shear strength over time. In fact the average value for the 24 tests is 19.3 *MPa*, with a standard deviation of 2.6 *MPa* (a variation coefficient of 13.3 %) which is a usual deviation value reported for this type of test (see for example ASTM D3528.

The fact that the geometry of the samples has a relatively short overlap length (12.5 *mm*) makes the whole overlap area highly stressed, and the relaxation effects may possibly affect not

only the edge zones of the overlap but also the central part. DLJ with a higher "overlap length to thickness" ratio would have loaded the central part of the overlap much less than that which was analyzed and tested in the present work.

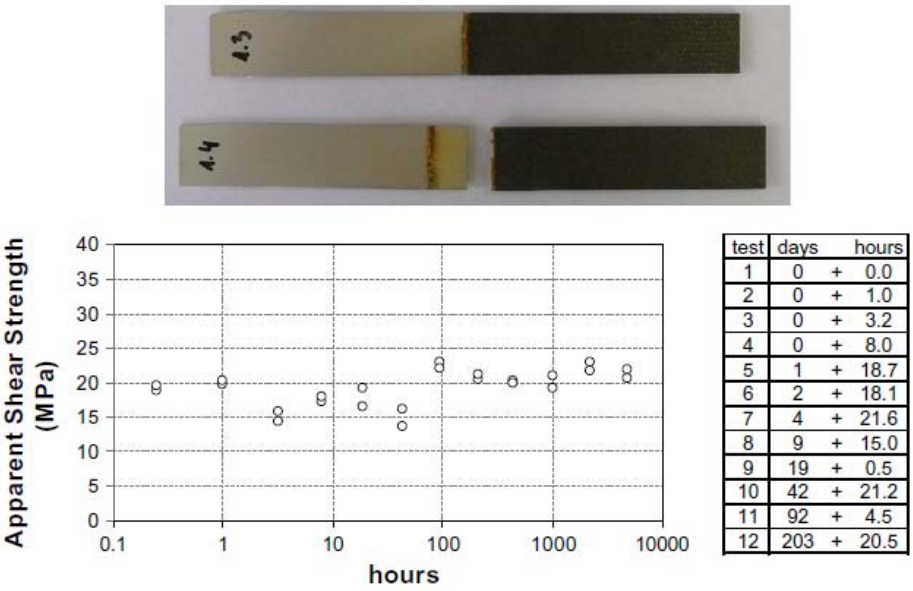

test	days		hours
1	0	+	0.0
2	0	+	1.0
3	0	+	3.2
4	0	+	8.0
5	1	+	18.7
6	2	+	18.1
7	4	+	21.6
8	9	+	15.0
9	19	+	0.5
10	42	+	21.2
11	92	+	4.5
12	203	+	20.5

Fig. 4.6 – Tested specimens and apparent shear strength at different times.

4.3 Discussion

The experiments showed that the thermal stresses during curing did not significantly alter the behaviour, type and load failures of the joint.

Previous experimental results on composite-to-metal adhesively bonded double-lap joints had shown that the local stress field at the multimaterial corners at the ends of the overlap may play an important role in the prediction of failure initiation (Barroso, 2007). These previous studies did not include the residual stress field which appears in the curing cycle due to the difference in the thermal expansion coefficients of the materials. The importance, for design, of this residual stress field is widely reported in the literature.

To analyze the influence of the thermal stresses between dissimilar materials on the asymptotic stress state in the neighbourhood of the corner under study, detailed numerical analyses has been performed. The attention has been focused on the residual stress field in the neighbourhood of the bimaterial corner, which is the potential point for failure initiation. Assuming the presence of significant thermal stresses during curing, it has been proved in this chapter that they might have a great influence on the nominal local stress state at these corners, changing the stress distribution completely (qualitatively), and in fact reaching approximately the opposite distribution of the stresses around the corner. For the analyzed configuration, it has been observed, numerically, that locally, i.e. close to the corner, the temperature effect generates a stress field which tended to compensate (almost the same shape, with opposite sign) the stresses generated by the mechanical loading. This fact might

imply the re-evaluation of the numerical and experimental agreement observed in the previous works mentioned.

However, many researchers have reported relaxation effects on the stress state of polymeric materials due to their viscoelastic behaviour, even at room temperature, mainly at highly stressed areas. Thus, the satisfactory agreement observed in Barroso (2007) between numerical and experimental results without incorporating the thermal stresses, raises the question of whether these thermal stresses really affect the local stress field at the multimaterial corner or, on the contrary, they do not play any significant role due to relaxation effects.

For this reason two preliminary experimental tests were carried out, the first one testing the adhesive joint at different temperatures (moderate temperatures over room temperature), which could be assumed to simulate adhesives curing at temperatures lower than the real curing temperature. Adhesives curing at lower temperatures were shown (in the numerical analyses) to develop lower residual stresses, which could influence initiation of failure. The second tested the adhesive joint at room temperature but at different times from the end of the bonding process, in an attempt to discover if there was any stress relaxation effect over time, especially at highly stressed areas.

Assuming that the local singularity stress field is controlling failure initiation in joints of this type, no test showed a significant influence of the thermal stresses during curing on the failure load. Thus, the numerical results together with the experimental evidence seems to indicate that for prediction of failure initiation, based on the singularity stress field at the bimaterial corner, the evaluation of the parameters which define the asymptotic singularity stress field can be computed without including the thermal stresses during curing.

Chapter

5 Effect of manufacturing processes

The use of adhesive joints gives rise to better mechanical behaviour in fatigue than that of riveted joints. This is because there is smoother load transmission, plus the incomparable advantage of their use in light-weight structures. However, their behaviour in failure is not yet completely understood, bearing in mind that the failure mechanism includes crack initiation, progression and finalizes with the rupture of the component. As a proof of this, current design procedures are often based, even now, on the well-established static approaches for almost all structures (Schön & Starikov, 2003). Despite this, studies investigating fatigue failure predictions in adhesive joints have been carried out, as can be appreciated in recent works such as Kinloch & Osiyemi (1993), Erpolat et al. (2004), Quaresimin & Ricotta (2006[A]) and Pirondi & Moroni (2009). More complete information about fatigue in polymers is available in Sauer & Richardson (1980) or in Ashcroft & Crocombe (2008) for adhesive joints. Fatigue threshold characterization in DLJ, can be found in Ashcroft & Shaw (2002) and Erpolat et al. (2004).

Further studies regarding adhesive joints under fatigue, although not directly related to this work, include some interesting studies of the environmental influence under different

conditions (Ashcroft et al., 2001), (Hadavinia et al., 2003), (Ashcroft & Shaw, 2002) or configurations of joints as in Potter et al. (2001), Erpolat et al. (2004), Deng & Lee (2007), Zhang et al. (2008). In Markolefas & Papathanassiou (2009) a particular elastic-plastic shear-lag analysis proposed to cover the stress redistributions (including thermal stresses) revealed sign changes on shear stresses in the adhesive layer under cyclic load.

Nevertheless, all previously mentioned results could change whether the optimal procedure in manufacturing of real joints is carried out or not. In this specific subject, one of the few works that can be found in the literature (according to the author's knowledge) is the study of Bascom & Cottington in 1972, who studied the complete stage of void formation during the cure process in a vacuum chamber under atmosphere pressure. Using aluminium as adherend, they found that the strength of joints for peel stress improves from 20% up to 30% when the voids are completely removed (using vacuum release technique) and suggested that the void formation is caused by the air entrapment between the adhesive and adherend. In 2004, da Silva et al. basically compared two different manufacturing procedures, vacuum release technique and autoclave, for a particular Redux 326 adhesive system. They analysed the adhesive under temperature exhaustively, during and after the manufacturing process, quantifying the amount of voids in each case. However, with respect to mechanical tests, they carried out

shear lap test by static tensile loading only (among other aspects which were further studied) in single lap joint with steel as adherend.

Among the manufacturing processes for adhesive joints made with structural epoxy thermosetting film, the Autoclave (AC) and Hot Plate Press (HPP) were compared in this chapter, in terms of mechanical characteristics such as in performance of the joint. Static (ASTM D3528) and fatigue (ASTM D3166) experimental tests in adhesive DLJ between CFRP and aluminium plates were carried out. Eleven specimens had previously been manufactured (Barroso, 2007) in HPP, and five of these had already been tested under static load. For comparison purposes, eleven additional specimens were manufactured in AC, seven of which were tested under fatigue and four under static load.

This chapter presents the comparison between HPP and AC technique in terms of mechanical characteristics as well as in mechanical performance of the joint. It may be noted that this type of study is also useful when only one of these techniques is available, either for cost or operational restrictions.

5.1 Manufacturing of the joint

The geometry of the final sample is depicted in Fig. 1.1. The specimen has $w = 25\ mm$ along the width, $L_a = 50\ mm$ and $L_0 = 12.5\ mm$ as the free and overlap lengths, respectively. The aluminium has $2t_{a2} = 3.2\ mm$ as total thickness and the CFRP (with 12 unidirectional plies) has $t_{a1} = 2.2\ mm$; both were joined by the adhesive, which is $t_{a3} = 0.1\ mm$ thick. Material properties are given on Tables 2.1 to 2.3.

With respect to the surface preparation, the aluminium was anodized or etched. On the CFRP surface a peel ply was used in order to protect the surface and improve the surface roughness for adhesion.

In both processes (HPP and AC) the adhesive was cured using a bonding pressure of 0.28 MPa (2.8 bar) at 115°C for 90 min in total, with an intermediate piece of plate between the panels. In this stage, the only difference between the AC and HPP manufacturing processes is that in the former, the hydrostatic pressure of 0.28 MPa is applied uniformly in all directions of the specimen; whereas in the latter, force is applied instead. In this case, attention must be paid when converting the necessary pressure to the real force that would be applied in the overlap by the press. This force (in kN) is given by:

$$F_{press} = \frac{p\ (MPa) A_{lap} (mm^2)}{1000} \tag{5.1}$$

where $p = 0.28\ MPa$ is the pressure recommended by the manufacturer and A_{lap} (in mm2) is the total area of the overlap (taking as example one DLJ specimen, the area would be $A_{lap} = 2 \times 12.5 \times 25 = 625\ mm^2$). Fig. 5.1 presents the application of pressure in each case.

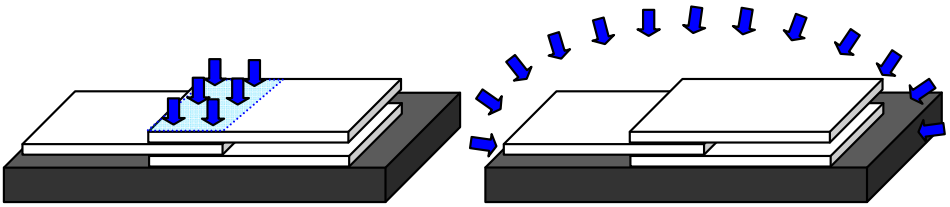

a) Hot Plate Press *b) Autoclave*

Fig. 5.1 – Applied pressure during manufacturing.

Figure 5.2 a) to e) shows some stages of the manufacturing process for AC specimens. The adhesive was supplied as a tacky film which should defrosted some hours before use. The procedure was carried out inside a clean room. Once the adherends had been cleaned (in the case of CFRP the peel ply needs only to be pulled out) the adhesive lamina was cut and fixed in the position in which the overlap would take place for both sides of the middle adherend surfaces in DLJ (see Fig. 5.2

a). For more details regarding the manufacturing process of adhesive joints, see Pate (2002).

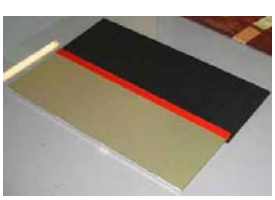

a) Adhesive on the overlap position

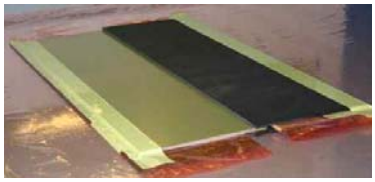

b) The entire set fixed and supported

c) Vacuum bag and thermocoupling

d) Autoclave curing

e) DLJ after machining

Fig. 5.2 – Manufacturing of the DLJ and curing in autoclave.

Two plates of CFRP, which had been previously cured, were covered with Teflon and used to sustain the adherends in the correct position (see Fig. 5.2 b). The entire set was additionally fixed with high temperature tape (Fig. 5.2 b) and covered with Teflon and then by airwave fabric. Next, a vacuum bag was prepared; leaving a thermocouple in the CFRP for a better temperature monitoring (Fig. 5.2 c and d); the lay-up and compaction process took place before the final autoclave curing as shown in Fig. 5.2 e. Since the cure cycle was ended, the

composite plate was carefully cut by a water-cooled diamond circular disk from one side, and from the other, aluminium, side by a vertical saw for metallic materials. Finally the specimens were abraded for removing some irregularities on lateral surfaces.

5.2 Experimental tests

For static tests, ASTM D3528 was taken as reference and four AC specimens (named AC 1, AC 2, AC 3 and AC 4) were manufactured and tested, giving the average apparent shear strength of 30.1 MPa. The data for the five HPP specimens tested by Barroso in 2007 were taken for comparison with this work, in which the average strength was 22.6 MPa.

In the absence of another more specific standard, the fatigue test procedure was carried out following the ASTM D3166. Table 5.1 summarizes fatigue data for each specimen tested. Six HPP specimens were tested and seven AC specimens were manufactured and tested in fatigue under load control. Humidity and temperature were kept constant during the experiments, being 35% and 20±1°C respectively. A positive asymmetric cyclic load was applied considering $R_L = 0.1$ ($R_L = P_{\min}/P_{\max}$ in terms of load but generally written in function of stresses) as load ratio. Table 5.1 also summarizes the extreme maximum and minimum

applied load ($P_{\max}$, $P_{\min}$, both in kN) and the percentage of $P_{\max}$ with respect to the ultimate static load (P_u, in average) in shear test by tensile static load.

Specimen	P_{max}, P_{min}	% P_u	Specimen	P_{max}, P_{min}	% P_u
HPP 1	6.9 , 0.69	≈ 50%	AC 5	9.21 , 0.92	≈ 50%
HPP 2	9.7 , 0.97	≈ 70%	AC 6	12.9 , 1.29	≈ 70%
HPP 3	8.3 , 0.83	≈ 60%	AC 7	11.05 , 1.105	≈ 60%
HPP 4	8.3 , 0.83	≈ 60%	AC 8	11.05 , 1.105	≈ 60%
HPP 5	6.9 , 0.69	≈ 50%	AC 9	9.21 , 0.92	≈ 50%
HPP 6	6.9 , 0.69	≈ 50%	AC 10	9.21 , 0.92	≈ 50%
			AC 11	12.9 , 1.29	≈ 70%

Table 5.1 – Summary of the data in experimental tests.

A frequency of 1200 cycles/min (or 20 Hz) was used for all specimens. For the correct position of the specimen in the machine, one auxiliary aluminium plate with the same thickness of the metallic adherend ($2t_{a2} = 3.2\ mm$) was used as a tab to avoid the slippage of the composite adherend. It was positioned between both CFRP plates.

5.3 Results

Ashcroft and Shaw in 2002 claimed that for bonded joints a more complex analysis, such as Finite Elements, is necessary for a correct representation of stresses in an averaged value of the S-N (stress-life) approach that is usual for homogeneous materials.

In page 152, they point out that in a bonded lap joint "*the shear stress is not uniform, there is no direct relationship between the average and maximum shear stresses and it is widely accepted that initial failure is attributable to the peel stresses rather than the shear stress*". In addition, they pointed out that the maximum peel stress could be used instead; however, this should be calculated by means of a numerical procedure with a careful treatment of the mesh "*to avoid a mesh-dependent maximum stress*". For this work the load-life representation was chosen instead of stress-life (as much for peel as for shear stress), following their suggestion. Figure 5.3 shows the experimental data obtained for maximum applied load ($P_{\max}$) against number of cycles (N) for maximum tensile loading values.

These graphs consider the static case as an averaged point corresponding to one cycle of load. The first HPP specimen (HPP 1) was not tested until the failure in order to verify any damage or crack initiation in the overlap.

In the graphs in Fig. 5.3, the arrows represent the specimens in which no failure occurred, i.e. infinite life. In this chapter, the fatigue threshold was considered as the maximum load under which the final, detectable, failure was not produced for at least 10^6 cycles. Approximately 6 kN and 10 kN for HPP and AC specimens was found for fatigue threshold respectively. This

corresponds to 43% and 53% of the ultimate static load for HPP and AC specimens, respectively.

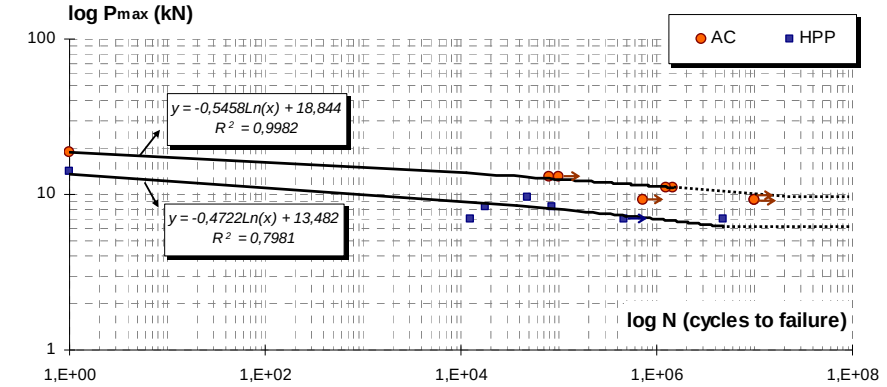

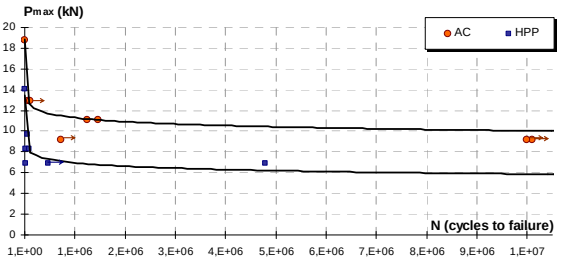

Specimen	Number of cycles tested
HPP 1	468916
HPP 2	47248
HPP 3	17502
HPP 4	84752
HPP 5	12525
HPP 6	4793395
AC 5	714786
AC 6	80923
AC 7	1467918
AC 8	1243767
AC 9	10000000
AC 10	10100000
AC 11	100000

Fig. 5.3 – Load-life curve obtained for the tested specimens.

Despite little available data, it can be observed from these figures that experimental tests show a clear trend (depicted in a black continuous and dashed line) presented in logarithmic scale. However, the ASTM D3166 recommends 25 specimens as the minimum number for a better statistical correlation of the load-life curve in adhesive joint characterization. Nevertheless, as mentioned above, the number of samples was limited to a single

batch, and in order to avoid uncertainties associated with different batches, no further specimens were manufactured with newer materials, even when they had similar properties.

The closed critical corner (from Fig. 1.1) was chosen for checking failure by microscope, due to the fact that this is a singular point where the failure is expected to initiate. From two specimens, one from HPP and the other from AC procedure, which were tested until infinite life (HPP 1 and AC 11), the four corners are presented for each specimen, using 50× magnification (Figures 5.4) for HPP, and 35x (Figures 5.5) for AC. For HPP corners (Fig. 5.4) no failure was observed, but the presence of pores or bubbles was identified. In the specimen AC 11 (infinite life) no failure was observed (Fig. 5.5); neither bubbles nor voids were found in the adhesive for any AC specimens. In Figure 5.5, the spew fillet does not exist, and even the presence of a little entering void was observed. This gap is the result of the applied pressure during the manufacturing in conjunction with a quantity of remaining adhesive, which did not allow the complete spew fillet formation.

It is well known that the presence of the spew fillet is beneficial to the corner (Tsai & Morton, 1995; Bogdanovich & Kizhakkethara, 1999), so from this experience it is recommended that the adhesive is cut a few millimetres more in order to guarantee the fillet formation.

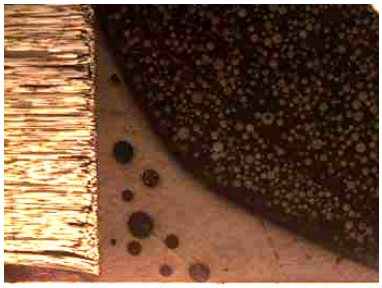

a) Left corner, face 1

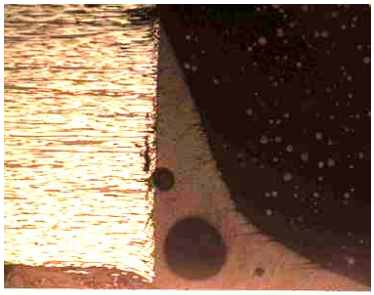

b) Right corner, face 1

c) Left corner, face 2

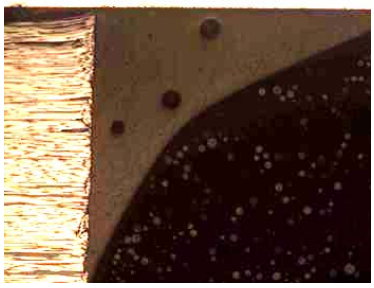

d) Right corner, face 2

Fig. 5.4 – Corners of HPP 1 specimen at 50×.

Also, for all cases where the rupture occurred and for the overlap region, the failure was predominantly cohesive, for both AC as well as HPP specimens.

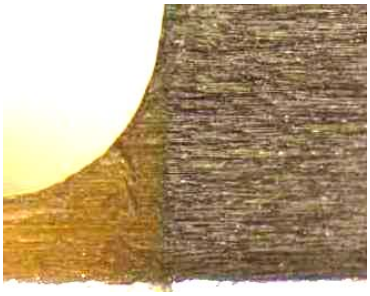

a) Left corner, face 1

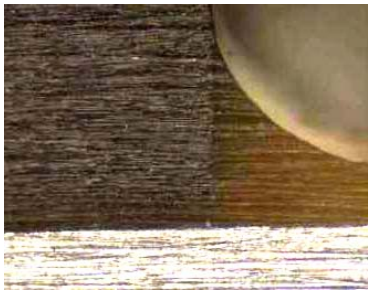

b) Right corner, face 1

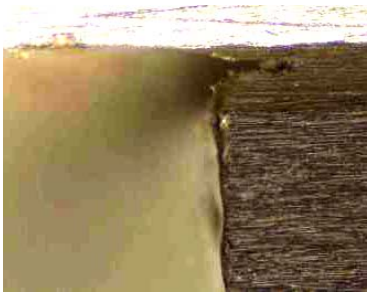

c) Left corner, face 2

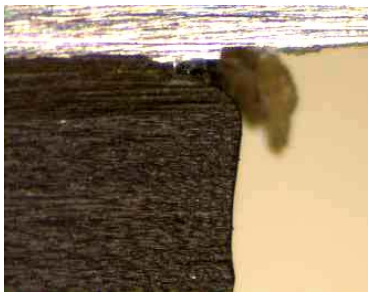

d) Right corner, face 2

Fig. 5.5 – Corners of AC 11 at 35×.

In addition, the aspect of the failure in the corners was checked in the failed specimens. It was verified that the crack path was not affected by the presence of the bubbles in HPP specimens. Figure 5.6 presents the microscope photograph of HPP 4 and AC 8 specimens, after 84752 and 1243767 cycles respectively, when the specimens failed (both corresponding to be loaded approximately $P_{\max} = 60\%\ P_u$).

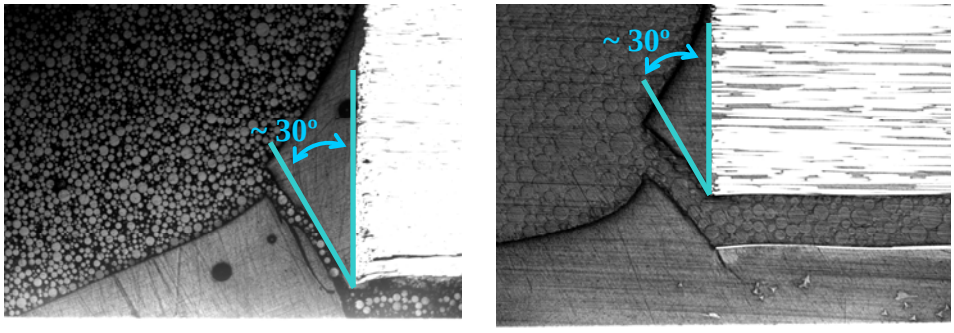

a) HPP 4 (50x) *b) AC 8 (100x)*

Fig. 5.6 – Crack path for both types of manufacturing.

For both specimens the failure presented similar patterns, considering the side in which the spew fillet was present, being situated about 30º from a vertical line as indicated in Fig. 5.6. This is in agreement with previous work (Barroso, 2007), in which the same angle was observed in experiments under static load.

5.4 Discussion

In this chapter, a particular adhesive DLJ was studied under static and fatigue load, in order to make a quantitative and comparative study of two manufacturing processes: AC and HPP. The experiments have revealed the presence of pores in the closed corner when manufactured by HPP, which can compromise the stress state of the joint and thus any prediction

of failure. The use of controlled vacuum and pressure in AC prevent void or pore formation, which can probably be associated with the highest quality of manufacturing. In the literature there is insufficient quantitative information with respect to how much the use of one of these techniques could reduce/improve the strength of a DLJ. In addition, the standards used in this work do not mention anything about the manufacturing process. The ASTM D3166 suggests that the final report should give information regarding the cure conditions such as pressure, time and temperature. ASTM D3528 and UNE-EN ISO 9664 suggest checking the manufacturer's recommendation, which describes the cure conditions without mention of which technique is more appropriate.

The specifications ASTM D3166 and UNE-EN ISO 9664 recommend considering a minimum of 25 and 12 specimens respectively for fatigue threshold determination. In static, according to ASTM D3528, a total of 5 specimens should be tested for a correct average value. Although the author is aware of this, there was insufficient material to allow comparison of both procedures, i.e. AC against HPP, available for preparation of further samples, and the tested specimens presented small scatter.

The specimens were tested under static and fatigue load, in both cases as double lap shear test by tensile loading. The static

test revealed that the AC tested specimens were approximately 25% stronger than the HPP tested specimens. For fatigue life, the AC threshold limit was 40% (4kN) superior to the HPP limit, when both processes were compared.

The experiments showed predominant cohesive debonding in every failed joint tested and through the microscopy it was verified that, for one face of the AC joints, an entering gap took place during the manufacturing process. However, this did not imply any significant reduction of the strength of this AC joint, as the strength and fatigue life were superior to the HPP joints. It is well known that the presence of the spew fillet is beneficial to the corner (Bogdanovich & Kizhakkethara, 1999 and Tsai & Morton, 1995), so from this experience the author recommends cutting the adhesive few millimetres more in excess to guarantee the fillet formation.

Despite some difficulties in carrying out this study, which compared specimens manufactured before 2007 and manufactured in 2010, with and without the spew fillet, bubbles or gap presence in some samples, few specimens and other issues, the final results presented small scatter, were consistent and can be considered satisfactory.

The P-N curves, together with observation by optical microscope, indicated the brittle nature of the adhesive, as some specimens were observed in a stage very close to the point in

which the failure was expected to initiate. However, no indication of failure was detected. This is in agreement with the experiments in Barroso's work (Barroso, 2007) in which the HPP specimens were tested under partial static load, suggesting that brittle failure occurs, and thus reinforces this position. Furthermore, the failure observed by microscopy presented similar paths for both processes of manufacturing and when tested under static and fatigue load. This indicated that the presence of bubbles does not seem to significantly affect the mode of failure of the joint under study.

Chapter

6 Failure under static loading

Chapters 1 and 2 presented some proposals to determine stress state in adhesive joints, in order to make an assessment regarding the prediction of failure in the joint. Barroso's experiments (2007) found that failure occurred in the critical corner of the adhesive joint, at the ends of the overlap shown in Fig. 1.1. This chapter studies this in detail, determining the GSIF associated with the corner. The aim of the study is to propose a failure criterion based on generalized fracture toughness related to the local singular stresses in the bimaterial corner. In order to allow a pure stress state in different directions, a variety of geometries were tested (analogous to the role that K_{IC} and K_{IIC} play in LEFM). The geometry which was finally adopted was inspired by the Brazilian Test (BT) specimen (Carneiro, 1953), which was used as if it was an amplification of the local corner of the adhesive joint. This geometry was chosen because it covers the entire range of mode mixities. Extensive experiments were carried out in order to gain the isolation and mixities of the modes of failure.

6.1 The stress state in a closed multimaterial corner

From the previous evidence, the failure of the joints is prone to start in the bimaterial corner enclosed by the adhesive and the CFRP adherend due to the high stresses/strains concentration at the end of the overlap (Tsai & Morton, 1995), so this is considered a critical point of the joint. In addition, several examples of experimental evidence, in particular geometrical and material combinations, show that failure can be controlled by the parameters which define the singularity stress state at these corners (Gradin, 1982; Groth, 1988; Barroso, 2007). Particularly for the configuration studied in this work (Fig. 1.1), Barroso's experiments suggested that the pattern of the failure followed a direction approximately 30º from the vertical CFRP-Adhesive interface (Fig. 1.1).

From a local point of view and assuming plane strain (or also generalized plane strain), the components of stress and displacement of a multimaterial corner are given by a sum of n serial terms as (Wieghardt, 1907; Williams, 1952; Dempsey and Sinclair, 1979, 1981; Vasilopoulos; 1988; Mantič et al., 1997):

$$\sigma_{ij}\left(r,\theta\right)=\sum_{k=1}^{n}\frac{K_k}{r^{1-\lambda_k}}f_{ij}^{k}\left(\theta\right) \tag{6.1}$$

$$u_i(r,\theta)=\sum_{k=1}^{n} K_k r^{\lambda_k} g_i^k(\theta) \tag{6.2}$$

which are equations 1.1 and 1.2, repeated here for convenience. r and θ are the polar coordinates, centred at the vertex of the corner, Fig. 6.1 a.

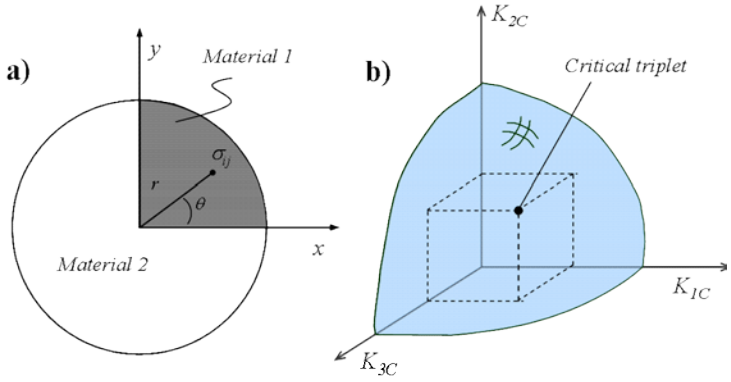

Fig. 6.1 – a) Coordinate system in generic bimaterial closed corner. b) Sketch of a failure surface for critical values of GSIF, considering three terms.

f_{ij}^k, g_i^k are the angular shape functions for stresses (f_{rr}^k, $f_{r\theta}^k$, $f_{\theta\theta}^k$) and displacements (g_r^k, g_θ^k) respectively. λ_k are the characteristic exponents, K_k are the GSIF in the expression (6.1) and (6.2). When r trends to zero, and when the power $(1-\lambda_k)$ is between 0 and 1, the stresses are unbounded, thus it is called order of stress singularity. The variables i, j $(i,j=r,\theta)$ and k $(k=1,...,n)$ are index. The angular shape functions and characteristic

exponents depend on the local geometry, material properties and local boundary conditions of the corner, while the GSIF additionally depend on the far field loading and global geometry. Actually, the GSIF K_k increases or decreases proportionally and according to the external applied load. In Eq. (6.1) and (6.2) the rigid body motions are included when $\lambda = 0$ and $\lambda = 1$, under appropriate assumptions of g_i and f_{ij} (see Barroso, 2007 for more details).

In configurations where the representation given by Eq. (6.1) applies, stress singularities appear when $r \to 0$ and thus the GSIF control the local stress field. If the extension of yielding at the corner tip is small compared to the zone dominated by K_k, the onset of failure can be assumed to be controlled by critical values of GSIF (K_{kC}, by analogy from LEFM). Nevertheless, the lack of symmetry in the stress field of anisotropic multimaterial corners makes it difficult to develop a general testing procedure for determination of K_{kC}.

The asymptotic expression presented in Eq. (6.1) can also be seen as the superposition of every mode acting on the corner, so it can be written in function of only one of these terms separated. If a pure mode is isolated when the corner is subjected to a maximum level of stresses or ultimate load, it is possible to correlate K_{kC} with that load and activate a pure mode for failure,

from which the failure would start. Then, if the critical value for each mode is achieved with other possible combinations, there is an envelope or surface which would enclose the safety region (Fig. 6.1 b), inside which the corner would not yet reach critical values for failure initiation.

Thus, the main challenge is to find a method of testing by which these terms are dominant and even includes possible combinations of them, in which the ultimate static load could be related to the GSIF, giving the critical value for each mode.

6.2 Numerical and analytical analyses

In this work, the GSIF K_k were determined numerically using the least squares technique (see Barroso et al., 2011 for more details), while the angular shape functions and characteristic exponents were determined analytically by means of the algorithm developed by Barroso in 2007 for generalized plane strain states, and numerically.

The dimensions of K_k were standardized following Pageau et al. (1996) and depend on the value of the associated characteristic exponent, being $MPa\ mm^{(1-\lambda_k)}$ the units for GSIF.

The values of K_k have been normalized taking $f_{\theta\theta}^{k}(r,0^{\circ})=(2\pi)^{\lambda_k-1}$ in order to have $\sigma_{\theta\theta}(r,0^{\circ})=\sum_{k=1}^{3}\frac{K_k}{(2\pi r)^{1-\lambda_k}}$.

The following geometry was proposed as an amplification of the corner, inspired by the Brazilian Test specimen (Carneiro & Barcelos, 1953).

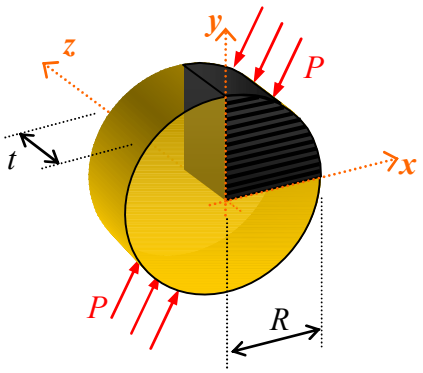

Fig. 6.2 – Geometry of the amplified corner.

In this figure a disk whose radius is represented by R is diametrically loaded along its thickness t, where P is the applied load (N/mm). Local axes are indicated in Fig. 6.2, were x is the direction aligned with the fibres.

With the purpose of looking for a stress state similar to the one developed in the DLJ under study (Fig. 1.1) and assuming that the failure starts in the critical corner, a numerical simulation with FEM was made, enclosing only the local

bimaterial corner (Fig. 6.2). The model has a regular mesh with nodes on radial lines at every 5º and 200 nodes along the radio. A progressive refinement was done towards to the corner tip, where the final element size is $7.4\times10^{-5}R$, where R is the radius of the specimen, so the mesh has 14400 finite elements and 14401 nodes in total. PLANE42 finite element (with 4 nodes and 2 DOF, displacement in x and y axis) was used in a simple linear elastic analysis with plain strain option (as in the 3D study it was seen that the stresses at the free edges are less severe, check Chapter 3 for more details). Restrictions in displacements were imposed to avoid the free body motion. The unidirectional laminate of CFRP [0º] was modelled as an equivalent linear elastic orthotropic material and the adhesive as a linear elastic isotropic material, whose properties are introduced in Tables 2.3 and 2.1 respectively. Fig. 6.3 shows the regular mesh used in the analyses.

In this model a diametric tensile load ($P=100N$) was used according to the Fig. 6.3, applying for different angles α.

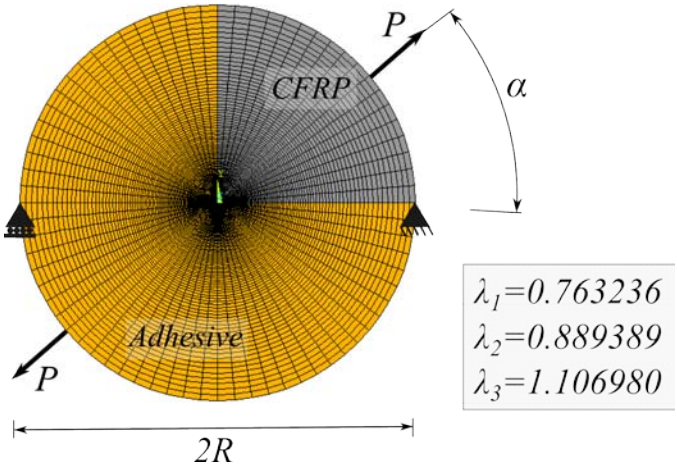

Fig. 6.3 – Mesh used for the amplified bimaterial critical corner and order of stress singularities for this corner.

Neglecting the terms of superior order and taking into account only the first three terms of the series expansion given by Eq. (6.1), in Fig. 6.3 the orders of stress singularities are shown (considering $Re\ \lambda_k > 0$) for this corner that were previously calculated (Barroso, 2007). Then the Eq. (6.1) and (6.2) can be written as:

$$\sigma_{ij}(r,\theta) \cong \frac{K_1}{r^{0.236764}} f_{ij}^1(\theta) + \frac{K_2}{r^{0.110611}} f_{ij}^2(\theta) + K_3 r^{0.10698} f_{ij}^3(\theta) \qquad (6.3)$$

$$u_i(r,\theta) = K_1 r^{0.763236} g_i^1(\theta) + K_2 r^{0.889389} g_i^2(\theta) + K_3 r^{1.10698} g_i^3(\theta) \qquad (6.4)$$

Next, the shape functions (being f_{ij} dimensionless and g_i with dimensions of MPa^{-1} for consistence) for this corner were

numerically computed at every degree from 0º to 360º, using the algorithm developed by Barroso. The angular shape functions $f_{ij}(\theta)$ and $g_{ij}(\theta)$ are shown in Fig. 6.4 to 6.6 for each of the three terms in the series expansion.

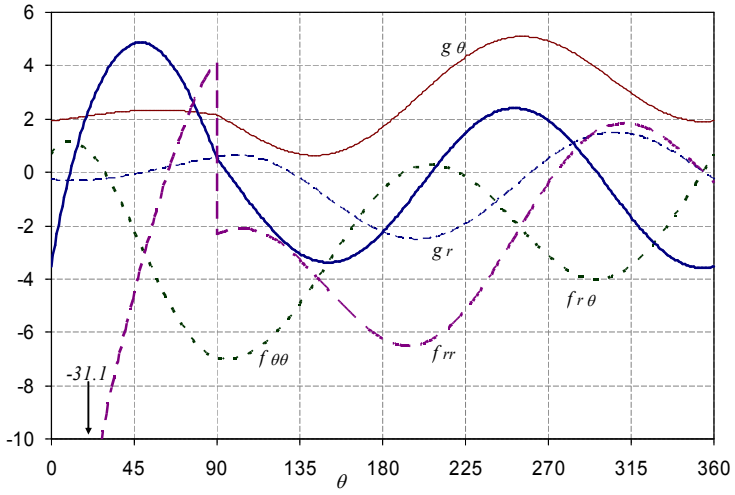

Fig. 6.4 – Angular shape functions $f_{\theta\theta}^{1}$, $f_{r\theta}^{1}$, f_{rr}^{1} (dimensionless) and g_{θ}^{1}, g_{r}^{1} (MPa^{-1}) associated with λ_1.

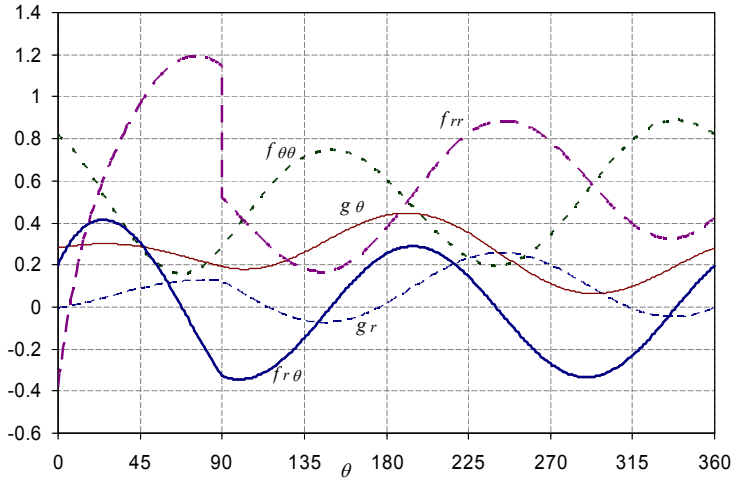

Fig. 6.5 – Angular shape functions $f_{\theta\theta}^2$, $f_{r\theta}^2$, f_{rr}^2 (dimensionless) and g_θ^2, g_r^2 (MPa^{-1}) associated with λ_2.

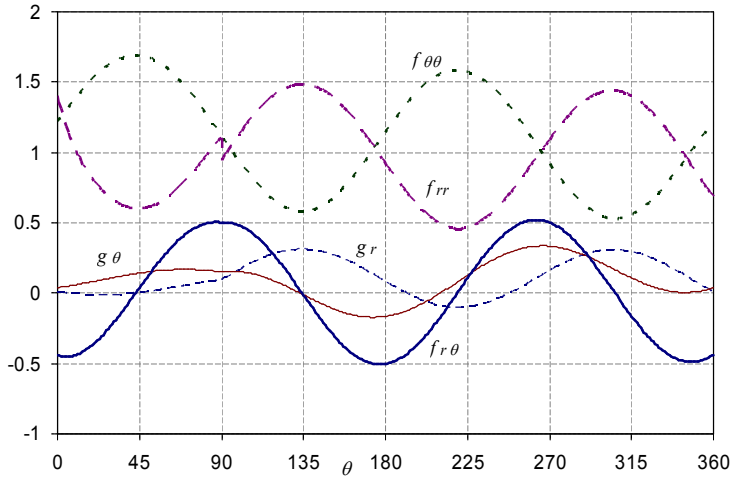

Fig. 6.6 – Angular shape functions $f_{\theta\theta}^3$, $f_{r\theta}^3$, f_{rr}^3 (dimensionless) and g_θ^3, g_r^3 (MPa^{-1}) associated with λ_3.

Table 6.1 shows the data (at every 15°) used for plotting of Fig. 6.4 to 6.6:

θ	g_r^1	g_θ^1	$f_{\theta\theta}^1$	$f_{r\theta}^1$	f_{rr}^1	g_r^2	g_θ^2	$f_{\theta\theta}^2$	$f_{r\theta}^2$	f_{rr}^2	g_r^3	g_θ^3	$f_{\theta\theta}^3$	$f_{r\theta}^3$	f_{rr}^3
0	-0.2891	1.9311	0.6472	-3.5404	-31.1077	-0.0056	0.2805	0.8160	0.1977	-0.3811	0.0058	0.0394	1.2173	-0.4368	1.4042
15	-0.3299	2.0661	1.0618	1.2386	-15.7554	0.0191	0.2972	0.6631	0.3854	0.3512	-0.0118	0.0721	1.4598	-0.4072	0.8879
30	-0.2586	2.2091	-0.1618	3.7880	-9.0372	0.0528	0.3002	0.4418	0.4060	0.7115	-0.0138	0.1100	1.6380	-0.2203	0.8655
45	-0.0880	2.3092	-2.2054	4.8281	-4.5288	0.0887	0.2873	0.2814	0.3054	0.9857	0.0015	0.1438	1.6885	0.0398	0.6002
60	0.1286	2.3353	-4.4043	4.4767	-0.7570	0.1123	0.2608	0.1742	0.1169	1.1319	0.0300	0.1646	1.5988	0.2899	0.6774
75	0.3510	2.2790	-6.1512	2.9151	2.2486	0.1238	0.2266	0.1727	-0.1130	1.1934	0.0631	0.1674	1.3847	0.4606	0.8885
90	0.5378	2.1512	-6.9653	0.5120	4.1729	0.1197	0.1924	0.2839	-0.3289	1.1449	0.0909	0.1523	1.1126	0.5923	1.1078
105	0.5540	2.1125	-6.9796	0.4213	-2.3127	0.1149	0.1904	0.2948	-0.3328	0.5081	0.0985	0.1537	1.0941	0.5932	0.9621
120	0.3262	1.0078	-6.1720	-2.1517	-2.4722	0.0448	0.1805	0.4523	-0.3381	0.3788	0.2011	0.1439	0.8446	0.4442	1.2158
135	-0.2448	0.6813	-4.8536	-3.0461	-3.3061	-0.0229	0.2057	0.6061	-0.2723	0.2566	0.2821	0.0815	0.6472	0.2531	1.4163
150	-0.9739	0.6748	-3.4464	-3.3816	-4.3970	-0.0667	0.2601	0.7120	-0.1492	0.1805	0.3101	-0.0116	0.5794	-0.0136	1.4856
165	-1.6979	1.0256	-1.9282	-3.0838	-5.4688	-0.0753	0.3289	0.7479	0.0048	0.1738	0.2767	-0.1032	0.6615	-0.2765	1.4033
180	-2.2540	1.6839	-0.6765	-2.2489	-6.2457	-0.0460	0.3935	0.7085	0.1500	0.2415	0.1918	-0.1614	0.8692	-0.4571	1.1938
195	-2.5137	2.5716	0.0899	-1.0290	-6.5107	0.0146	0.4364	0.6065	0.2529	0.3711	0.0806	-0.1641	1.1405	-0.5014	0.9191
210	-2.4099	3.5047	0.7558	0.3054	-6.1506	0.0928	0.4452	0.4694	0.2890	0.5349	-0.0240	-0.1059	1.3945	-0.3957	0.6801
225	-1.9511	4.3251	-0.1658	1.4703	-5.1803	0.1703	0.4156	0.3331	0.2498	0.6971	-0.0910	0.0006	1.5550	-0.1711	0.4830
240	-1.2183	4.8860	-1.0389	2.2177	-3.7399	0.2291	0.3526	0.2332	0.1449	0.8221	-0.1006	0.1285	1.5734	0.1065	0.4664
255	-0.3534	5.0825	-2.1237	2.3873	-2.0655	0.2556	0.2690	0.1965	-0.0003	0.8830	-0.0502	0.2446	1.4429	0.3550	0.5870
270	0.4804	4.9213	-3.1454	1.9402	-0.4402	0.2440	0.1824	0.2344	-0.1509	0.9882	0.0452	0.3190	1.2008	0.5012	0.8177
285	1.1227	4.4254	-3.8334	0.8671	0.8653	0.1976	0.1113	0.3406	-0.2705	0.7844	0.1571	0.3343	0.9170	0.5922	1.0885
300	1.4547	3.7232	-3.9879	-0.3308	1.8486	0.1280	0.0702	0.4821	-0.3302	0.6543	0.2522	0.2905	0.6737	0.3581	1.3172
315	1.4230	2.9735	-3.5194	-1.6839	1.8180	0.0523	0.0666	0.6549	-0.3156	0.5118	0.3019	0.2052	0.5409	0.1122	1.4339
330	1.0503	2.3421	-2.4684	-2.8103	1.4114	-0.0108	0.0868	0.7925	-0.2398	0.3937	0.2814	0.1062	0.5553	-0.1623	1.4018
345	0.4309	1.9674	-0.9964	-3.4754	0.5878	-0.0460	0.1565	0.8738	-0.0933	0.3308	0.2234	0.0328	0.7100	-0.3834	1.2278
360	-0.2891	1.9311	0.6472	-3.5404	-0.4058	-0.0442	0.2233	0.8817	0.0515	0.3404	0.1179	0.0057	0.9561	-0.4851	0.9610
	-0.2891	1.9311	0.6472	-3.5404	-0.4058	-0.0056	0.2805	0.8161	0.1977	0.4224	0.0058	0.0394	1.2173	-0.4368	0.6776

Table 6.1 – Shape functions for the first three terms of Eq. (6.1).

With the shape functions, order of singularities and the stresses from the far field loading previously calculated, the GSIF are the only unknowns of the series expansion. The GSIF are then normalized according to the procedure presented in Pageau et al. (1996) and evaluated by using the least square method (Barroso, 2007 and 2012). In Fig. 6.7 the variation of K_k with the angle α varying from 0º up to 180º (being $r = 0.0010583\ mm$ and $P = 100N$ the applied diametral tensile load) is shown.

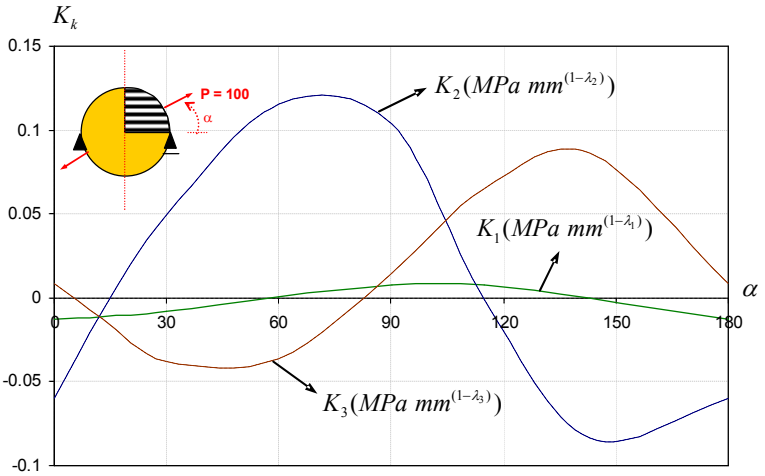

Normalized GSIF for tensile loading

α	K_1	K_2	K_3
0	-0.0126	-0.0601	0.0085
13	-0.0113	-0.0073	-0.0127
30	-0.0077	0.0490	-0.0376
60	0.0004	0.1158	-0.0367
90	0.0074	0.1037	0.0145
115	0.0074	-0.0011	0.0653
143	0.0001	-0.0832	0.0864
180	-0.0126	-0.0601	0.0085

Fig. 6.7 – Normalized GSIF evolution (for tensile loading) with the angle α (in degrees).

It is important to notice that the curves have different units, each of which is indicated in Fig. 6.7, and the absolute values are not comparable. Additionally, for very small distances (i.e. when $r \to 0$), the weight of each term is drastically affected by the singularity according to the Eq. (6.3). Thus for distances very close to the corner, the third term on the expression (6.3) tends to zero and only the first two terms play a much more important role in the Eq. (6.3). Thus the third term can be neglected close to the corner tip (in which $r \to 0$). The Eq. (6.3) and (6.4) can finally be rewritten as:

$$\sigma_{ij}(r,\theta) \cong \frac{K_1}{r^{0.236764}} f_{ij}^1(\theta) + \frac{K_2}{r^{0.110611}} f_{ij}^2(\theta) \tag{6.5}$$

$$u_i(r,\theta) = K_1 r^{0.763236} g_i^1(\theta) + K_2 r^{0.889389} g_i^2(\theta) \tag{6.6}$$

for $r \to 0^+$ and $Re\ \lambda_k > 0$.

Now, according to Fig. 6.7, the isolation of the terms seems to be feasible. Ignoring the third term and observing that $K_2 \cong 0$ when $\alpha = 13^o$ and $\alpha = 115^o$, given a pure mode in K_1. Analogue observation when $K_1 \cong 0$ (for $\alpha = 60^o$ and $\alpha = 143^o$), allowing pure mode in K_2. Once a representation similar to that shown in Fig. 6.7 is obtained, if the curves representing the dependencies of K_1 and K_2 (for the external load P) on the angle α, cut the x-axis

at angles $\alpha = 60º$ and $\alpha = 143º$ for K_1; $\alpha = 13º$ and $\alpha = 115º$ for K_2 respectively, four test configurations exist in which the singular terms can be isolated. Thus, in these configurations the local stress fields are controlled by only one singular term (one GSIF value).

It is necessary to try to find the geometry and testing procedure able to reproduce the stress state indicated in Fig. 6.3 and Fig. 6.7. This could be produced by a specimen such as that represented in Fig. 6.8, which however was not a good choice, as this type of test did not allow consider the stresses for all types of mode mixities. Section 6.3 will show the difficulties of testing a sample like this, together with other examples of geometries tested.

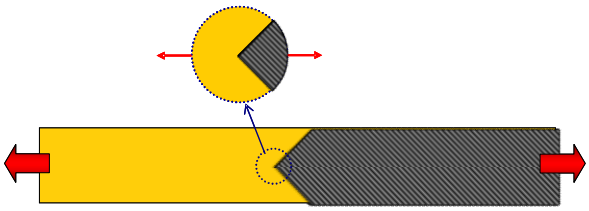

Fig. 6.8 – Another testing procedure achieving a local stress state allowing critical GSIF values.

The best option finally arises from the observation that by inverting the sign of the load (applying compression instead of tensile), this falls in the BT. This geometry is chosen because it allows the entire range of mode mixities to be covered. No

additional simulations are needed, because when linear elastic analysis is considered in numerical analyses, under compression the GSIF only changes the sign. Fig. 6.9 shows the GSIF evolution with the angle, for compression loading ($P=-100N$) and neglecting the term K_3.

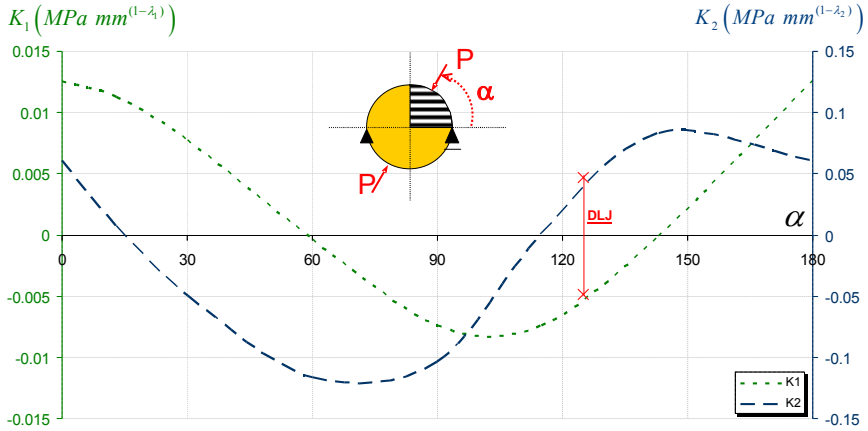

	Normalized GSIF (compressive loading)	
α	K_1	K_2
0	0.0126	0.0601
13	0.0113	0.0073
30	0.0077	-0.0490
60	-0.0004	-0.1158
90	-0.0074	-0.1037
115	-0.0074	0.0011
143	-0.0001	0.0832
180	0.0126	0.0601

	Normalized GSIF of the DLJ	
	K_1	K_2
DLJ	-0.0032	0.0312

Fig. 6.9 – Normalized GSIF evolution (for compressive loading) with the angle α (in degrees).

In this graph, K_1 is represented on the left vertical axis and K_2 is represented according to the scale on the right vertical axis. The angles α are indicated on the abscissas axis.

Again, it can be deduced that the isolation of the mode related to K_1 is achieved for $\alpha \approx 13º$ or $\alpha \approx 115º$ (when K_2 vanishes), and the mode related to K_2 for $\alpha \approx 60º$ or $\alpha \approx 143º$ (when K_1 vanishes).

The graph also shows the GSIF normalised according to Pageau et al. (1996), calculated on average for the joint represented in Fig. 1.1, together with other configurations of DLJ that include the same bimaterial corner (Barroso, 2007, page 159) shown for comparison. The presented averaged value for GSIF was multiplied by a scale factor of 1.5 in the graph in Fig. 6.9 (in the table the GSIF are presented in true value). When this type of joint is under tensile loading (for σ as represented in Fig. 1.1) the stress state induces GSIF similar to that in which the amplified corner is under $P = -100N$ and $\alpha \approx 125º$.

6.2.1 Additional analyses

It must be emphasized that due to the fact that the values of GSIF are normalized, their relative influence on the stress distribution depends not only on their absolute values, shown in

Figure 6.9, but also on the values of angular shape functions and the specific distance from the corner tip. This fact can be further clarified by representing stresses and displacements particularizing some cases of the amplified corner, for example the case in which $\alpha = 13º$, where $K_1 = 0.01125$, $K_2 = 0.007319$ and $K_3 = 0.01266$. In this particular case the normalized value of K_1 is only ≈ 1.5 times greater than the absolute value of K_2, and K_3 (which is not associated with a singular term) is higher than K_1.

Introducing these values into Eq. (6.3) and (6.4) the displacements and stresses are shown, for $r = 0.0010583\ mm$ (i. e. $r \cong 0.1\%\ R$), in Fig. 6.10 (u_r, u_θ, σ_θ, $\sigma_{r\theta}$, σ_r) together with the FEM results obtained for $P = -100N$. In Fig. 6.10 a) up to e), not only the total (i.e., the sum of each individual term) displacement and stress components are shown but also the individual contribution of each of the terms of the series expansion (6.3) and (6.4). Despite the values of the normalized GSIF obtained for $\alpha = 13º$ ($K_1 = 0.01125$, $K_2 = 0.007319$ and $K_3 = 0.01266$), it can be clearly observed in Fig. 6.10 that the displacement and stress fields are almost exclusively determined by the first term of the series expansion (6.3) and (6.4), the second and third term contributions being almost negligible.

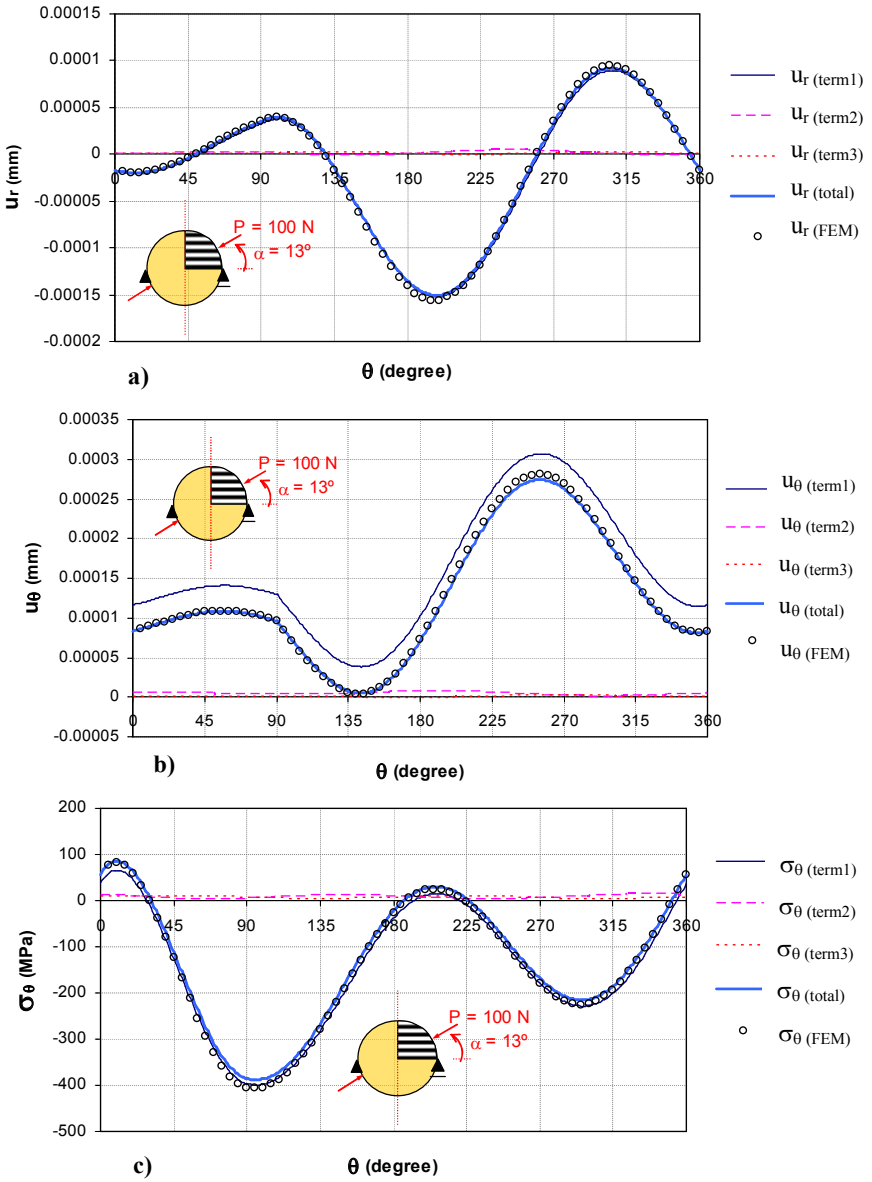
0.00015
0.0001
0.00005
0
-0.00005
-0.0001
-0.00015
-0.0002
ur (mm)
0 45 90 135 180 225 270 315 360
θ (degree)
P = 100 N
α = 13°
a)
ur (term1)
ur (term2)
ur (term3)
ur (total)
ur (FEM)
0.00035
0.0003
0.00025
0.0002
0.00015
0.0001
0.00005
0
-0.00005
uθ (mm)
0 45 90 135 180 225 270 315 360
θ (degree)
P = 100 N
α = 13°
b)
uθ (term1)
uθ (term2)
uθ (term3)
uθ (total)
uθ (FEM)
200
100
0
-100
-200
-300
-400
-500
σθ (MPa)
0 45 90 135 180 225 270 315 360
θ (degree)
P = 100 N
α = 13°
c)
σθ (term1)
σθ (term2)
σθ (term3)
σθ (total)
σθ (FEM)

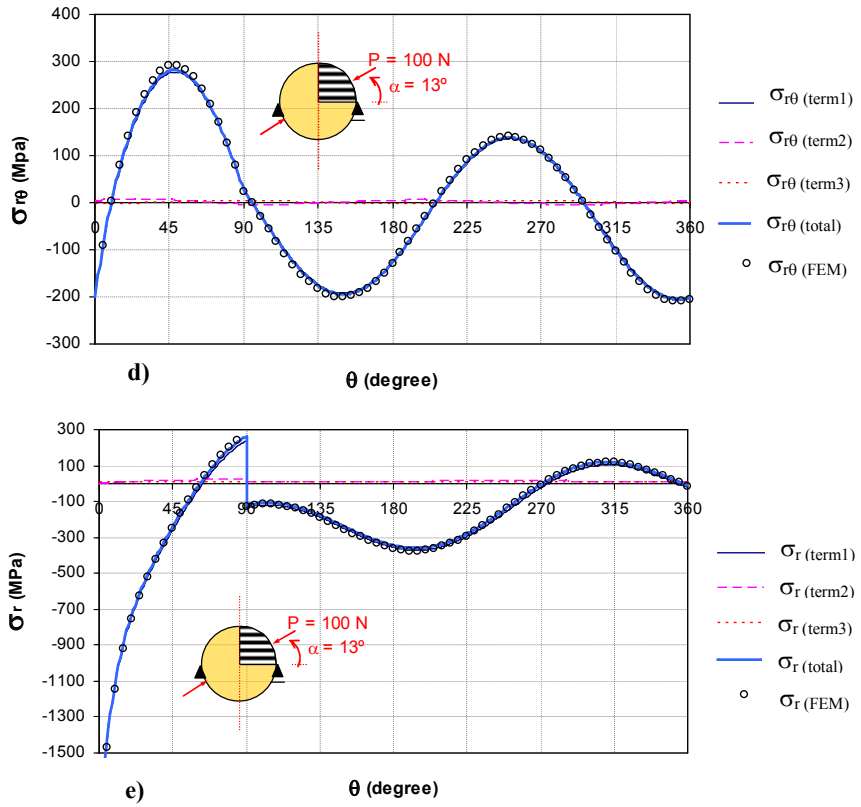

Fig. 6.10 – FEM and series expansion results for $\alpha = 13^{o}$. a), b) displacement and c), d), e) stress components for $\alpha = 13^{o}$ at $r \cong 0.1\%\ R$.

The difference in the displacement component u_θ observed in Fig. 6.10 b) is associated with a rigid body rotation, which has been taken into account in Eq. (6.3) and (6.4) as an independent linear term ($K_* r$, being associated with $\lambda = 1$), the difference

thus being constant all along the circumferential coordinate θ ($u_r = 0$ and $u_\theta = K_* r$, see Barroso 2007 for more details).

Although only displacements have been used in the post processing procedure for extraction of the values of K_k from FEM results, the fitting between the numerical (FEM) and the series expansion results in stresses (Fig. 6.10) is also excellent.

In the test configuration at which $K_1 = 0$ ($\alpha = 60^o$), Fig. 6.11 shows the displacements and stresses in a similar way to Fig. 6.10 (for the case $K_2 = 0$).

Both singular terms in the present configuration have weak singularities ($0.5 < \lambda_k < 1$), with the second (considered now $K_1 = 0$) being particularly weak $\lambda_2 = 0.889389$. Thus, although still having the unique singular term (the second) as the most important contribution to the total displacement and stress fields at the chosen distance $r \cong 0.1\% R$, the first regular term with $\lambda_3 = 1.10698$ sometimes shows a relatively significant contribution, as will be observed later on.

With reference to the displacement components u_r, u_θ and also to the shear stress $\sigma_{r\theta}$, Fig. 6.11 a, b and d respectively, the situation is similar to that observed in the previous case, ($K_2 \cong 0$,

$\alpha = 13^{o}$), with the non-vanishing singular term (K_2 in this case, K_1 in the previous one) having almost all the weight of the corresponding displacements and stress components.

The difference in the u_θ component is, as in the previous case, Fig. 6.10 b, associated with the rigid body rotation which has been taken into account in Eq. (6.3) and (6.4) as $K \cdot r$. In the case of σ_θ and σ_r (Fig. 6.11 c and e) the contribution of the regular term to the maximum total stress value is lower than 10%.

Thus, in this case, the critical value of K_2 at failure should be considered only as a good estimation of the real K_{2C}.

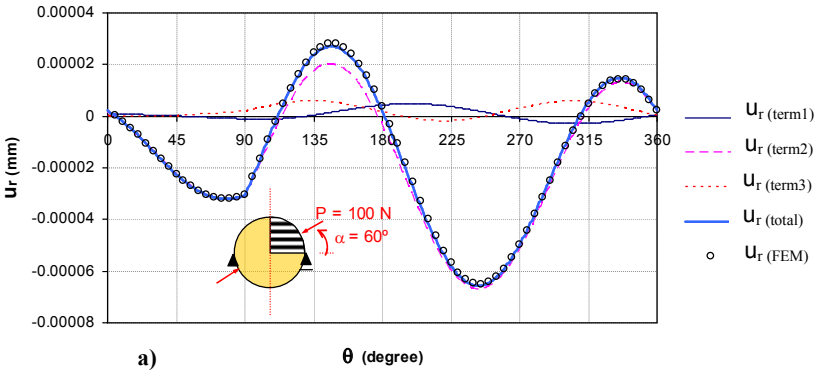

a)

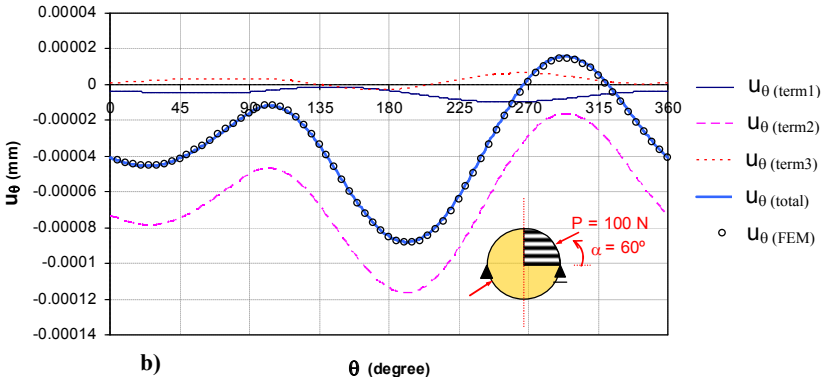
0.00004
0.00002
0
-0.00002
-0.00004
-0.00006
-0.00008
-0.0001
-0.00012
-0.00014
0
45
90
135
180
225
270
315
360
uθ (mm)
θ (degree)
P = 100 N
α = 60°
uθ (term1)
uθ (term2)
uθ (term3)
uθ (total)
uθ (FEM)

b)

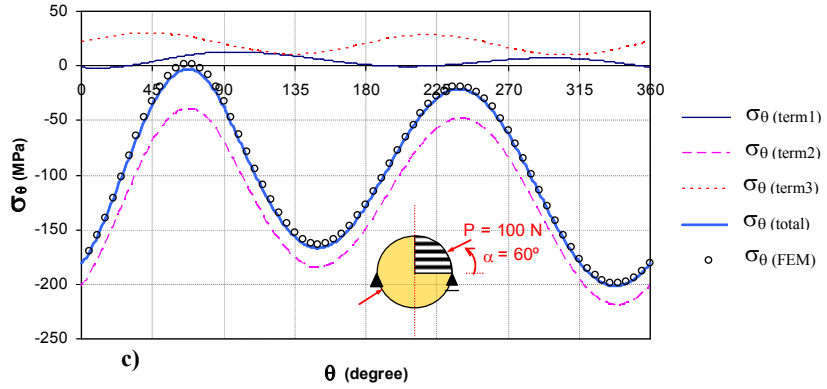
50
0
-50
-100
-150
-200
-250
0
45
90
135
180
225
270
315
360
σθ (MPa)
θ (degree)
P = 100 N
α = 60°
σθ (term1)
σθ (term2)
σθ (term3)
σθ (total)
σθ (FEM)

c)

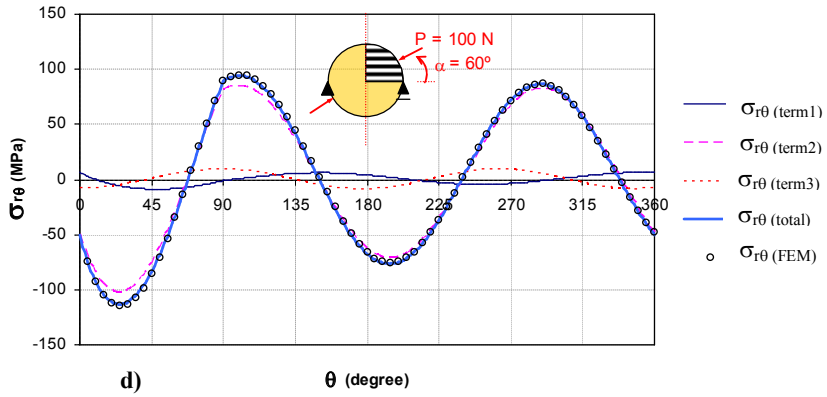
150
100
50
0
-50
-100
-150
0
45
90
135
180
225
270
315
360
σrθ (MPa)
θ (degree)
P = 100 N
α = 60°
σrθ (term1)
σrθ (term2)
σrθ (term3)
σrθ (total)
σrθ (FEM)

d)

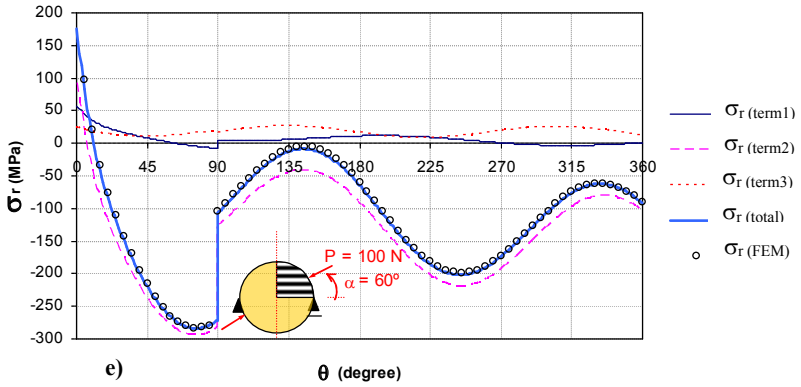

Fig. 6.11 - FEM and series expansion results for $\alpha = 60^{\circ}$. a), b) displacement and c), d), e) stress components for $\alpha = 60^{\circ}$ at $r \cong 0.1\%\ R$.

In Appendix B additional graphs covering other cases of α at $r \cong 0.1\%\ R$ are given as supplementary information.

The numerical elastic analysis was carried out in order to check the stress state of the bimaterial closed corner when loaded in a diametral compression according to different angles α. Fig. 6.12 and 6.13 show the principal stress σ_I for $\alpha = 13^{\circ}$ and $\alpha = 60^{\circ}$ respectively. In the pictures, a sketch of the principal stresses $\sigma_I > \sigma_{II} > \sigma_{III}$ is indicated for an arbitrary point A. The position of this point is chosen where σ_I is maximum (by the side of the adhesive), for reference. It is important to stress that the scale effect needs to be studied further because it is more

pronounced in stresses than GSIF (Barroso et al., 2012[B] and Vicentini et al., 2012[A]).

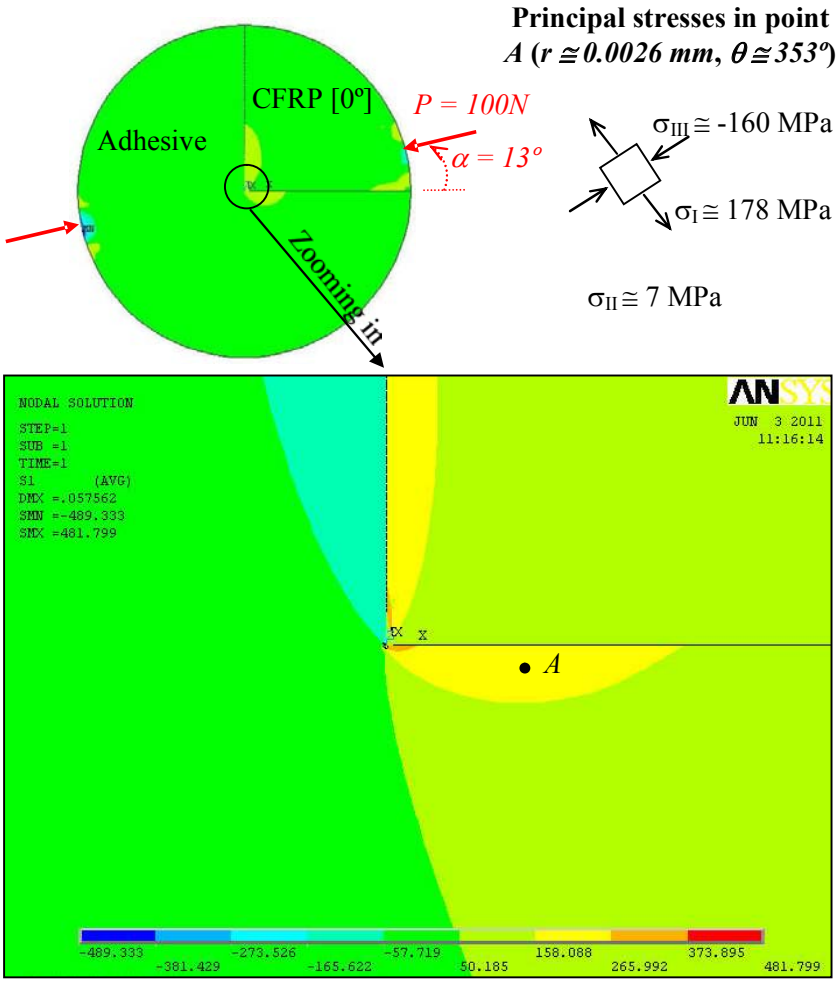

Fig. 6.12 – Picture of principal stress σ_I in the BT specimen when it is diametrically loaded in $\alpha = 13^{\circ}$.

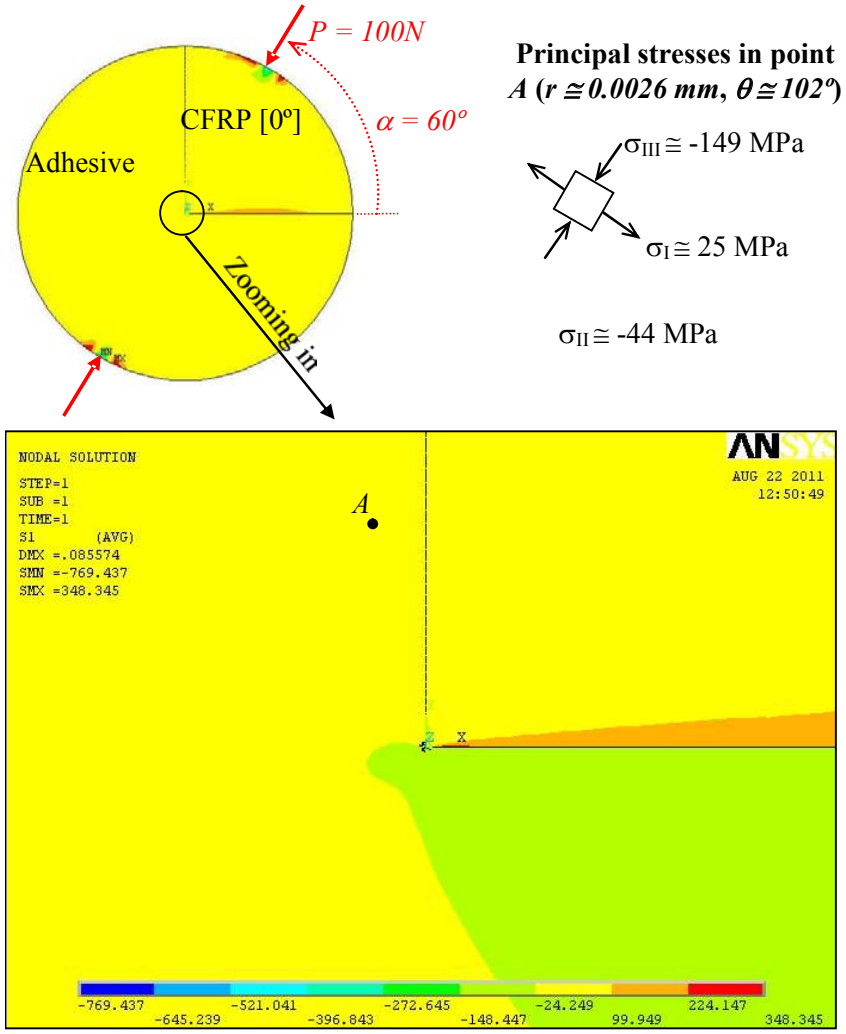

Fig. 6.13 – Picture of principal stress σ_I in the BT specimen when it is diametrically loaded in $\alpha = 60^{\circ}$.

Fig. 6.12 shows the maximum σ_I at the horizontal edge, looking at the CFRP-Adhesive interface from the adhesive side. It may be seen that that the stress state at point A, chosen very close to what seems to be the critical edge, is dominated by tensile in σ_I, followed by σ_{II}. In addition, it was observed that $|\sigma_{r\theta}| > \sigma_\theta > \sigma_r$ along the horizontal CFRP-Adhesive edge and this is verified up to $r \cong 0.55\ mm$ (practically a half of the radius $R = 1\ mm$ of the numerical model), being σ_θ positive up to $r \cong 0.44\ mm$. This suggests that the failure for this case (in which $\alpha = 13^o$, K_1 is dominant and $K_2 \approx 0$) could be mainly due to shear stress, followed by circumferential stress in relevance.

The same analysis can be made for Fig. 6.13, in which $\alpha = 60^o$. Looking at the CFRP-Adhesive interface from the adhesive side, Fig. 6.13 shows the maximum σ_I in the vertical edge. Here it may be seen that the stress state at point A, chosen very close to what seems to be the critical edge, is dominated by compression and slightly less tensile in the perpendicular direction. In addition, it was verified that $|\sigma_{r\theta}| > \sigma_\theta > \sigma_r$ along the vertical CFRP-Adhesive edge, and this is verified up to $r \cong 0.58\ mm$, which is practically a half of the radius $R = 1\ mm$ of the numerical model, as the sign of shear stress is not

comparable to the positive sense for σ_θ or σ_r, which are both in compression ($\sigma_\theta > \sigma_r$ up to $r \cong 0.58\ mm$). Thus the failure for this case (in which $\alpha = 60º$, K_2 is dominant and $K_1 \approx 0$) is probably related to shear stress.

More plots covering other loading cases (varying the load angle α) are presented in Appendix C.

In order to check the range of validity of the analyses, in Fig. 6.14 the GSIF are plotted against three different radii r (0.0010583, 0.0099279 and $0.08\ mm$, representing approximately 0.1, 1 and 8% of R respectively) for $\alpha = 13º$, $60º$ and $90º$. The GSIF (normalized according to Pageau et al., 1996), were obtained by means of the *V10_2008.MA* program, using the stresses and displacements. These were numerically obtained by the regular mesh presented in Fig. 6.3. Then 22 nodes were progressively spaced, in which the central node was taken for r, according to an internal parameter in the program, along the radius in every interface CFRP-adhesive, by the least square adjustment (Barroso, 2007 and Barroso et al., 2012[A]).

If K_3 is neglected, the graphs present small variations. In Fig 6.14 a), K_2 is halved for $8\%\ R$, being practically constant in most cases. Also it can be appreciated, for the considered range of study, that K_1 is not significantly affected, being almost

constant for all tested percentages of the radius. Particularly in this work the radius $r = 0.1\%\ R$ (i.e. $0.0010583\ mm$) was finally adopted.

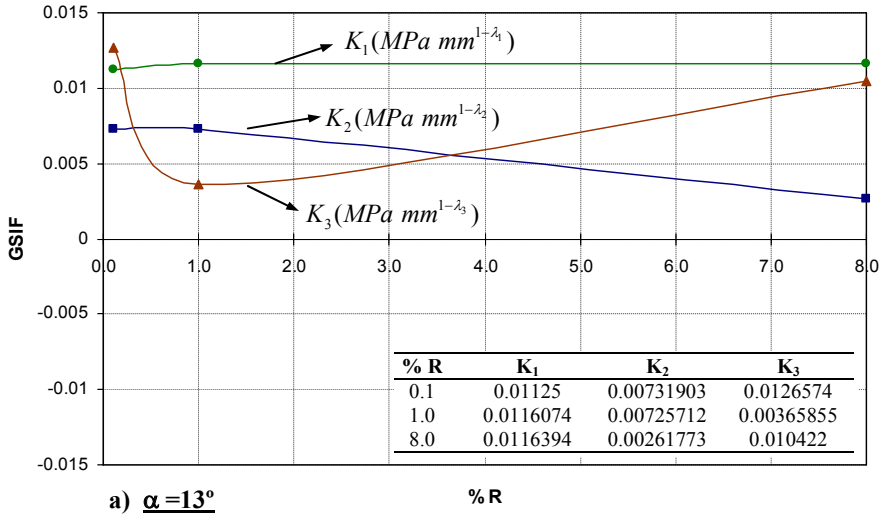

% R	K_1	K_2	K_3
0.1	0.01125	0.00731903	0.0126574
1.0	0.0116074	0.00725712	0.00365855
8.0	0.0116394	0.00261773	0.010422

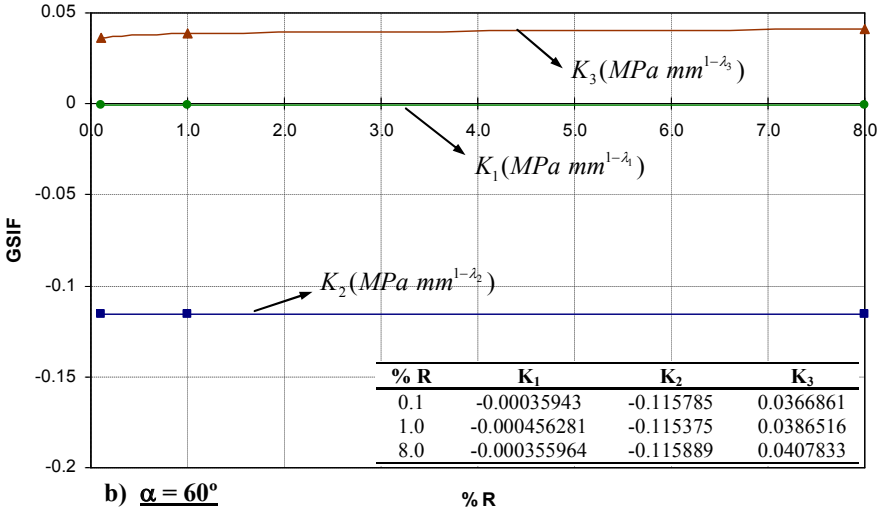

% R	K_1	K_2	K_3
0.1	-0.00035943	-0.115785	0.0366861
1.0	-0.000456281	-0.115375	0.0386516
8.0	-0.000355964	-0.115889	0.0407833

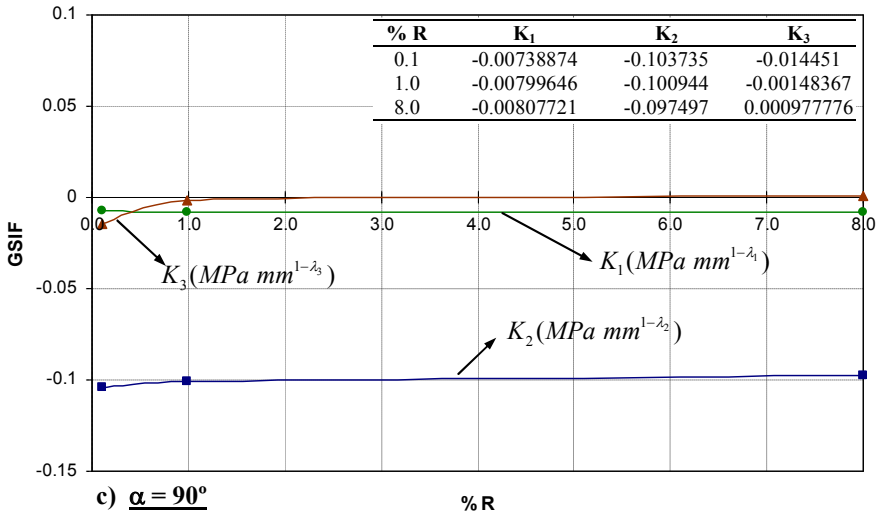

Fig. 6.14 – GSIF for different radii. a) $\alpha = 13^{\circ}$, b) $\alpha = 60^{\circ}$ and c) $\alpha = 90^{\circ}$.

Fig. 6.15 shows the relative weight of each term in Eq. (6.3). In the ordinates axis, the $1/r^{*}$ term is represented against the radius r (in logarithmic scale) in the abscissas axis, considering the asterisk as the power $1-\lambda_k$ (being λ_k given in Fig. 6.3) for the terms of the series in Eq. (6.3), or equal to $\lambda_k = 0.5$ for a generic crack problem as shown in Fig. 1.2, considering only one isolated term, for example, for comparison. The radius r varies from $(0,\infty)$ and the units are those for consistence (mm and $mm^{(1-\lambda_k)}$ for example).

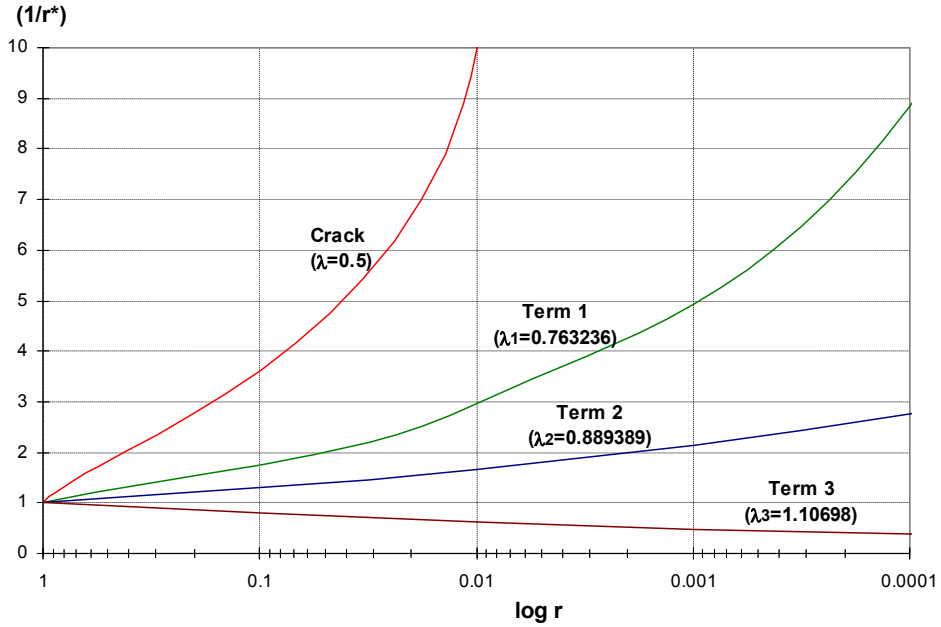

Fig. 6.15 – Checking the weight of each term of the sum.

Firstly, it is observable that the problem with a crack has a stronger singularity than every term of the bimaterial corner under study. From this graph the role of the first and second term in Eq. (6.3) is dominant over the third. The first and second terms tend to infinity when $r \to 0$ (the first term faster than the second one) while the third term tends to zero in the same situation. So for these analyses it is valid to assume that the third term may be neglected.

6.3 Configuration and manufacturing of the specimens

This section shows several configurations for experiments that were considered for testing. Some of these were unsuccessful, but they are presented here in order to show the evolution of knowledge, experience and reasoning, which led to the identification of the optimal geometry, inspired by BT specimens.

In the Laboratory of Elasticity and Strength of Materials (LERM, in Spanish) a rectangular bulk or plate previously manufactured with 150 plies laminated of 0º CFRP was available for use; which properties are the same as those given in Table 2.3. Rectangular bars of approximately $20\times20\times200\ mm$ were therefore cut from this bulk and used for each trial. One of these rectangular prisms is shown in Fig 6.16 a).

Initially the idea was try to test the specimens under pure tensile stress as possible. Thus, at the beginning the prismatic bulk (Fig. 6.16 a) surrounded by adhesive, was cut into small slices or rectangular pieces. These slices (or "cookies" as they were familiarly called later) would be tested under tensile load, rotating only the angle of the load in order to get convenient α angles (Fig. 6.7) and allowing pure modes; in fact, initially only the angles of $13º$, $60º$, $90º$ and $0º$ were tested. For all trials, the

adhesive was supplied as a tacky film which needed to be left out of the freezer some hours before bonding; it was then cut and layered with intermediate vacuum compaction between every five laminas of adhesive during a period of 10-15 min. The procedure was carried out inside a clean room. Later, the bulk was cured inside the autoclave (Fig. 6.16 b), being the cure cycle detailed in Chapter 2.

a)

b)

c)

Fig. 6.16 – a) A piece of unidirectional CFRP rectangular bar used in all manufactures, b) The autoclave and c) The rectangular aluminium mould used for the first preliminary trial.

For the first trials, a rectangular aluminium mould was available in the lab, so the rectangular CFRP bar was introduced inside it, followed by adhesive plies, being subjected to compaction as described previously. The mould used for the first preliminary configuration is presented in Fig. 6.16 c). Fig. 6.17 a) shows the mould with the CFRP bar and adhesive put inside.

This sample produced very rough specimens (Fig. 6.17 b), with a large number of defects and pores, as can be seen in Fig. 6.17 b (the prismatic bulk) and Fig. 6.17 c (a slice of the first trial bulk being tested under tensile). Thus these specimens were not considered for analysis. The pores arise because the rectangular aluminium closed mould does not allow the correct entrance of pressure induced by the autoclave.

a)

b)

c)

Fig. 6.17 – a) Mould with CFRP bar and adhesive inside, b) Final trial with a rough and porous surface, c) A slice of the bulk with lots of pores being tested.

Next, a second metallic (steel) mould was again considered, but on this occasion with a "U" shape profile (Fig. 6.18 a). In this case, approximately 400 plies of adhesive were layered more easily (representing an effort of two weeks of intensive work), allowing a better compaction (Fig. 6.18 b), and the fulfilment of a more important requirement: the correct application of the pressure during the cure inside the autoclave. Cork was used at the extremities of the bulk to prevent the spilling of the adhesive. This second trial bulk is shown in Fig. 6.18 c).

The quality of the "cookies" from this batch now was superior in comparison with the previous ones, having practically no pores (Fig. 6.18 c). The directions for tensile testing according to the angle α were then marked on some preliminary slices of this bulk. However, during the test difficulty was observed in gripping the slices and preventing them from sliding. In addition, the area by which the CFRP could be gripped was very small, which caused the specimen to slide easily (Fig. 6.19 a). Later, sandpaper was used around the extremities of the specimens (Fig. 6.19 b) in an attempt to avoid the sliding during the test. This did not solve the problem however, and the test had to be interrupted several times in order to obtain a stronger grip of the specimen. It was also observed that for some specimens the failure appeared where the grips were subjecting the specimen (Fig. 6.19 c). If it were possible to overcome these difficulties, it may be concluded that due to the geometry and boundary

conditions, this type of specimen does not lead to a pure stress state, as is achievable in the usual tensile test.

a)

b)

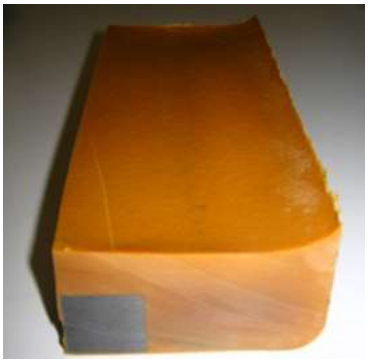

c)

Fig. 6.18 – a) The "U" shape profile, b) This mould allows a good compaction, c) Second trial bulk.

a) b) c)

Fig. 6.19 – a) A slice of the bulk being tested in tensile according to the angle α, b) Sandpaper being used in order to avoid the sliding of the specimen, c) Improper failure of the extremity of the specimen.

The experiment showed that it was impractical to carry out a tensile test. It was then proposed to use the remainder of the bulk to test slices under compression instead of tensile (Fig. 6.18 c), inspired by the BT configuration. 13 slices of this bulk were cut and polished into a rounded form, with the extremities where the load would be applied being parallel to the load direction, as shown in Fig. 6.20 a) and 6.20 b).

This configuration seems to be more suitable for testing, so it was kept until the end of this work.

The parallelism of the faces is made in order to produce better fixity of the specimen between the plates during the compression loading, but the literature for traditional BT (ASTM D3967) also allows the use of a rounded device for concentrating the load. A

rounded device for multimaterial corners is not recommended as it is extremely important to ensure control of the orientation of the specimens. According to the Saint-Venant principle and some preliminary numerical studies, the choice of parallel flat surfaces or rounded device (more similar to the model with a concentrated load) for load application does not significantly affect the stress state close to the centre of the specimen, as can be verified in Fahad (1996) for example, among other studies. The isolation of modes seems to be feasible with the proposed configuration (inspired by the BT specimens), only varying the angles α of the symmetrical applied load along the diameter of the specimen.

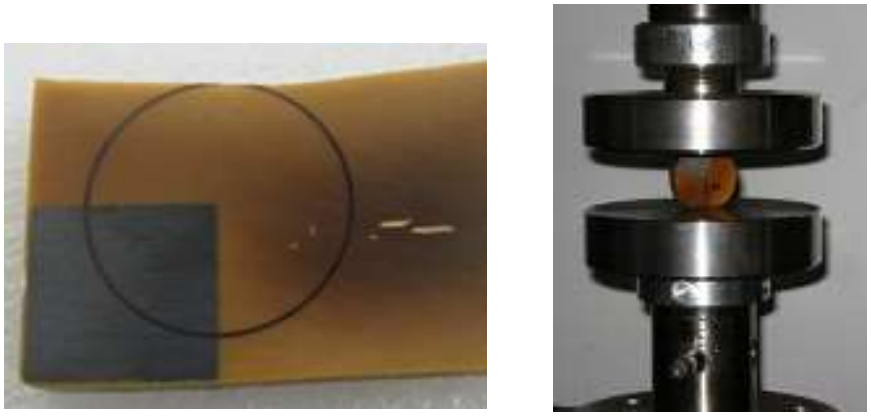

a) b)

Fig. 6.20 – a) A slice of the bulk with a circle marked, b) Test under compression of the first batch, the specimen with flat surfaces for load application.

Returning to the subject of the specimens presented on Fig. 6.20 b), in principle, if linear elastic behaviour is considered, the assumptions of equivalence when the specimen is loaded under compression is valid. It will be shown later that when the rounded specimen is loaded under compression, it fails by the indirect tensile induced, prone to be in perpendicular direction to the load. Proof of this can be observed from Fig. 6.9, in which the curves are inverted from $\alpha \cong 90^{o}$, and the GSIF cut the abscissa axis at every 90^{o} approximately.

Still observing Fig. 6.20 a), some pores were observed in the inner part of the bulk, being not considered for testing. Unfortunately only the most external parts of the entire bulk could be used for testing, giving rise to 13 specimens. In order to cover more test angles and repetition of some already tested, a second batch from the "U" profile was made (Fig. 6.21 a). The new bulk, however, presented significant spilling during manufacturing, and a considerable amount of pores in the inner part of the bulk, as in the first. From this new batch, only 4 specimens (in form of slices) could be considered valid for testing (Fig. 6.21 b).

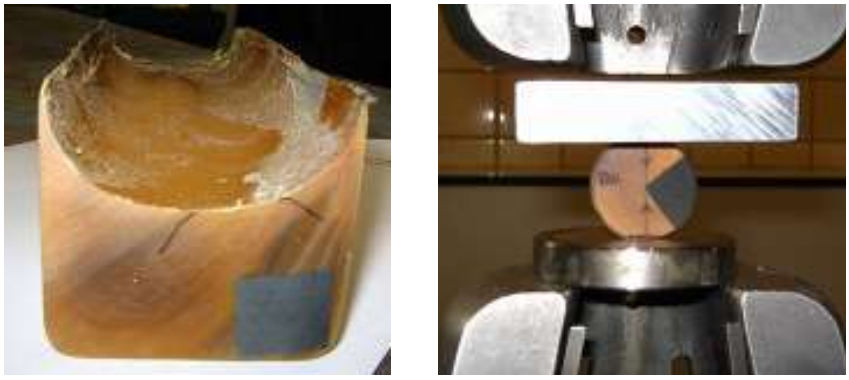

a) b)

Fig. 6.21 – a) New bulk from the "U" profile, b) One specimen being tested (second batch).

From these experiences, the appearance of pores is due to the release of gases which are present in the adhesive by its own chemical reaction, and thus the autoclave is not able to drive away completely the evaporation of the gases derived when the adhesive is in its fluid stage, during the manufacture (see Bascom & Cottington, 1972, for more details about the pores formation during the adhesive manufacturing). This effect is increased when a large number of plies (as in this work, the unusual ≈ 400 adhesive plies configuration) is being used.

Finally, the last proposal was to manufacture each specimen one by one directly (i. e. no further bulks being cut after the process). In this case, the CFRP bar was firstly cut and taking advantage of the isotropic property of the adhesive, it was plied surrounding the CFRP, being plied in the 3rd direction, i. e. along

the thickness. Fig. 6.22 a) shows the preparation of 9 new specimens, Fig. 6.22 b) the "cookie" manufactured and c) the final specimen being tested. From this batch, three specimens were used for additional test of $\alpha = 120^{o}$ (2 specimens) and $\alpha = 150^{o}$ (1 specimen). The rest of them were used for angles already tested in order to check the scatter and compare the validity of the actual specimens with the previous ones.

This last configuration had more effectiveness in the quality of the specimens, due to no pores were detected in the samples.

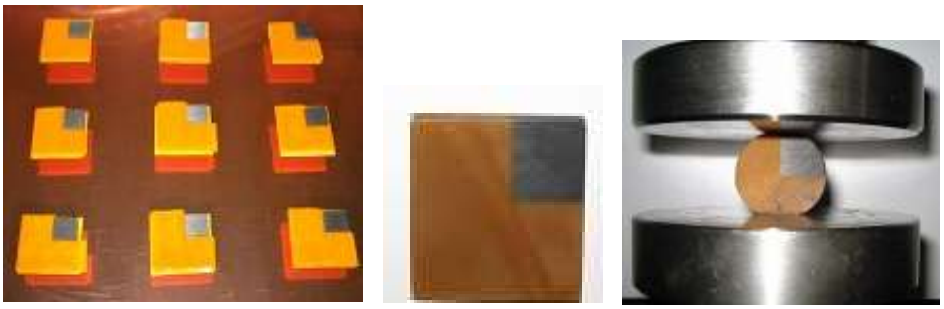

a) b) c)

Fig. 6.22 – a) Plies of adhesive prepared, b) The "cookie" after curing and c) One specimen being tested (third batch).

6.4 The Brazilian test

The so-called BT is used to obtain the tensile strength of brittle materials. The test is also known as the diametral

compression test, indirect tensile or sometimes the splitting tensile test. It was published firstly by Carneiro in 1943 as a procedure to evaluate the strength of concrete cylinders that could be used as an alternative to move the ancient São Pedro Church in Rio de Janeiro. Incidentally the church was eventually destroyed and replaced by what is now known as Presidente Vargas Avenue. This test was independently proposed by Akazawa due to their countries had cut relationship during the Second War (Fairbiairn & Ulm, 2002), generating some controversies about the authorship of the method. The references of both works are sometimes subject of confusion, because there is evidence that Carneiro as well as Akazawa published the method in 1943 (Akazawa only two months later). However, the papers are not correctly dated, and the only "official" available citation is in 1953, in their later articles (Carneiro & Barcellos, 1953 and Akazawa, 1953). This test is known by its versatility, usage and for presenting little dispersion (less then 10%) between the results against other methods (Tesoriere & Marino, 1990). Although it was initially designed to be used for concrete, it has increasingly been used in intact rocks (isotropic and anisotropic, see ASTM D3967; Newman & Bennett, 1990 and Jaeger & Hoskins, 1966), plaster of Paris (Fahad, 1996), pavement (Villar, 2006), ceramics (Spriggs et al., 1964; Marion & Johnstone, 1977 and Ovri & Davies, 1987), coal (Berenbaum & Brodie, 1959), polymers (Price & Murray, 1973; Lerch et al., 2007; Barroso et

al., 2012[B] and Vicentini et al., 2012[A]) and composites (Huang et al., 1996 and Liu et al., 1997). Other studies correlated the BT to the fracture mechanics (Awaji & Sato, 1978; Shetty et al., 1987; Huang et al., 1996; Liu et al., 1997; Liu et al., 1998 and Lerch et al., 2007) and others even considering an interfacial pre-crack in bimaterial systems, as in Wang & Suo (1990) and Banks-Sills & Ashkenazi (2000). Nevertheless, according to the author's knowledge, this is the first time in which the BT has been used for closed corners, without pre-crack.

The test consists of the diametrical loading (P) of a cylindrical specimen (with radius R and thickness t) under compression. In this situation, the strength of the specimen (in terms of tensile stress) is:

$$\sigma_{\perp} = \frac{P_u}{\pi R t} \tag{6.7}$$

where $\sigma_{\perp}$ is the tensile strength in the perpendicular direction of the applied load and P_u is the ultimate load (in compression).

It is important to note that the GSIFs depend on the specimen geometry, material properties and boundary conditions. From the observation that the GSIFs are proportional to the load and inversely proportional to the specimen radius and thickness, the critical GSIF value K_{kC}^{spec} (the value of GSIF at failure) can be

correlated to the numerical GSIF value K_{kC}^{num} by means of the following expression:

$$K_k^{spec} = \frac{P^{spec} R^{num} t^{num}}{P^{num} R^{spec} t^{spec}} K_k^{num} \left(\frac{R^{spec}}{R^{num}} \right)^{(1-\lambda_k)} \tag{6.8}$$

where K_k^{spec}, P^{spec}, R^{spec}, t^{spec} are the parameters from the tested specimens: GSIF (critical, calculated from Eq. (6.8)), ultimate (compressive) load (given by the test, thus $P^{spec} = P_u$), radius and thickness of the specimen (both measured before testing). K_k^{num}, P^{num}, R^{num}, t^{num} are the analogue parameters from the numerical analysis, the values used in this work being $R^{num} = t^{num} = 1\ mm$ and $P^{num} = 100N$ (P^{num} and P^{spec} have the same sign). The $(R^{spec}/R^{num})^{(1-\lambda_k)}$ term in Eq. (6.8) appears as the size-scale factor for the specimen/numerical adjustment.

At this point, it may be guessed by the reader that the amplified bimaterial corner in Fig. 6.2 and 6.3 is the same as that used in the numerical analyses, by analogy to the BT specimen.

6.5 Experimental test

The tests were carried out under displacement control ($1\ mm/min$), at room temperature. The tests were carried out in the LERM and all specimens followed the thickness-to-diameter ratio recommended by ASTM D3967, in the absence of another specific standard.

During the compression test, no strain gauges or extensometers were used for measuring the behaviour close to the corner tip (directly on the specimen), so only the cross-head information of the machine was used. Instron 4482 and 4483 machines were used for the tests.

For the different testing angles, the specimens generally failed between 7 and 13 KN compressive load. Fig. 6.23 shows the behaviour of three specimens for different batch tested. In principle, for this novel process, the failure was considered as the maximum load supported by the specimen or the load in which a visible crack was appreciated. Thus the ultimate load was taken according to indications in Fig. 6.23.

However, other procedures could be used as reference to the choice of the ultimate load instead, for example, the ASTM E399 and ASTM D5045, standards for fracture toughness in metals or

plastics respectively (with the method of the secant at 5% of the linear range).

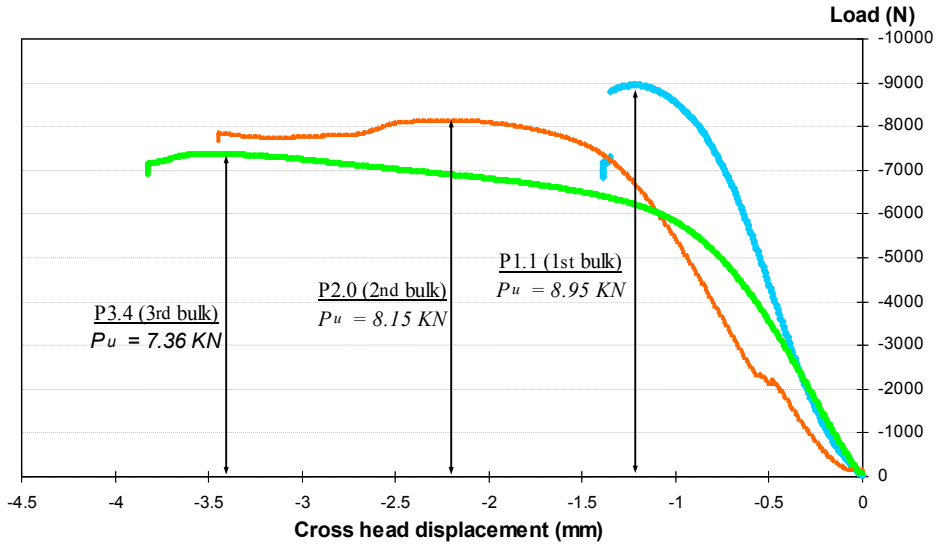

Fig. 6.23 – Behaviour of the BT tested specimens.

The apparently ductile behaviour observed in some specimens might in principle be related either to a local yielding effect in the neighbourhood of the corner or to a global yielding associated to the application of the load on the flat surfaces. Now then, on the one hand the effect of plasticity has been shown to be very tiny (Chapter 3). On the other hand, the different location in the specimen of the composite sector and its orientation with respect to the loading line, allows permanent plastic contraction in the direction of the load to be generated. To check this, the cases $\alpha = 143^{\circ}$ (with large observable permanent deformation, as will be

shown later in Fig. 6.24) and $\alpha = 13º$ (with almost no permanent deformation), can be compared. Consequently the apparent plastic behaviour observed in some cases (Fig. 6.23) has no connection with plasticity in the neighbourhood of the corner, but with the yielding of the adhesive when the location of the composite sector allows it (in Chapter 7 this will be studied in more detail). Based on this and in absence of an alternative criterion, the ultimate load has been taken as the maximum load existing in the diagram, as represented in Fig. 6.23.

6.6 Results

The numerical analysis performed in the Section 6.2 defined the angles α (Fig. 6.9) at which the compression of the samples would produce a pure singular term at the corner tip neighbourhood. There are two load orientations for which K_1 and K_2 vanish respectively ($\alpha = 60^o$ and $\alpha = 143^o$ for K_1 and $\alpha = 13^o$ and $\alpha = 115^o$ for K_2). These four cases should be analyzed, as well as additional cases in which none of the GSIF vanishes, in order to determine a large number of points in the failure envelope. Obviously, the choice of $\alpha = 60^o$ or $\alpha = 143^o$ will lead to different values of K_{1C}, which is conceptually acceptable, as both values are obtained using different stress states. These testing

orientations will enable the generalized fracture toughness K_{1C} and K_{2C} to be evaluated. The test of other angles will allow the evaluation of a failure envelope based on GSIF values (through the combinations of critical GSIF, generically named K_{kC}) at the corner tip. Table 6.2 shows, for each specimen, the thickness, radius and failure load. The numbers were intentionally coloured for better correlation with the corresponding samples in the envelope later.

Fig. 6.24 shows a schematic representation of the crack path after failure for some of the chosen load orientations $0º < \alpha < 180º$, including those where K_1 and K_2 vanish. In particular, Fig. 6.24 shows the cases of $\alpha = 0º$, $\alpha = 13º$, $\alpha = 30º$, $\alpha = 60º$, $\alpha = 90º$, $\alpha = 115º$, $\alpha = 120º$, $\alpha = 143º$ and $\alpha = 150º$, respectively.

Load angle (α)	Sample (internal code)	R^{spec} (mm)	t^{spec} (mm)	$P^{spec} = P_u$ (N)
$0° = 180°$	P1.10	16.94	7.5	10212
	P1.11	15.06	7.36	7675
	P2.2	15.67	6.2	7272
	P3.5	17.74	6.66	8275
$13° (K_2 \cong 0)$	P1.1	15.67	7.22	8952
	P1.6	15.8	8.2	12449
	P1.8	17.21	7.64	10565
$30°$	P1.3	15	7.5	8625
	P1.7	18.12	7.58	9859
	P1.9	17.94	7.64	9607
$60° (K_1 \cong 0)$	P1.2	15.2	7.34	8667
	P1.4	17.95	7.65	11998
	P1.5	18.03	7.7	12782
$90°$	P1.12	15.85	7.24	7624
	P1.13	16.68	7.69	9188
	P2.5	15.8	6.74	8295
	P3.6	17.47	6.4	7627
$115° (K_2 \cong 0)$	P2.1	15.93	7.36	9346
	P3.1	17.5	6.6	9898
	P3.2	18.5	5.8	9033
$120°$	P3.7	17.25	6.68	10879
	P3.8	18.19	6.23	10104
$143° (K_1 \cong 0)$	P2.0	15.78	7.45	8153
	P3.3	18.18	6.75	11252
	P3.4	16.81	6.65	7360
$150°$	P3.9	18.22	6.12	7209
Average values:		16.87	7.07	9343

Table 6.2 – Results of experimental tests.

$\alpha = 0^{\circ}$

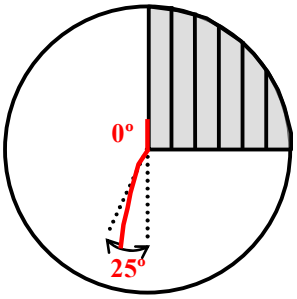

$\alpha = 13^{\circ}$

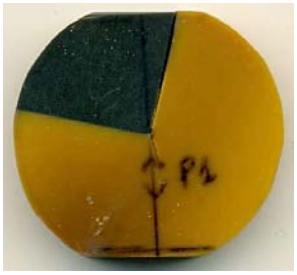

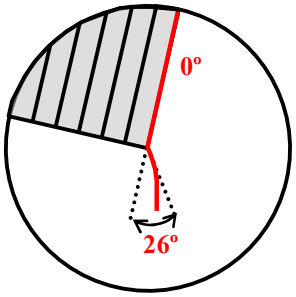

$\alpha = 30^{\circ}$

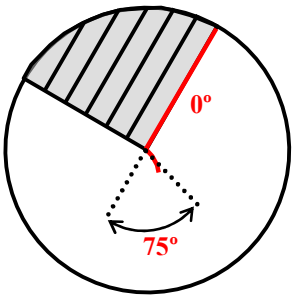

$\alpha = 60^{\circ}$

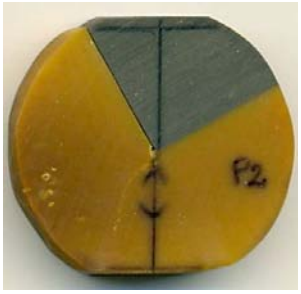

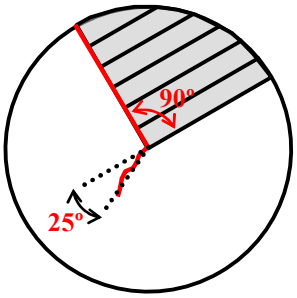

$\alpha = 90^{\circ}$

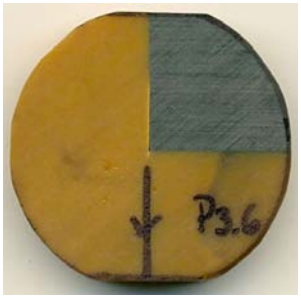

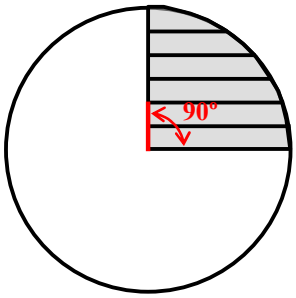

$\alpha = 115^{\circ}$

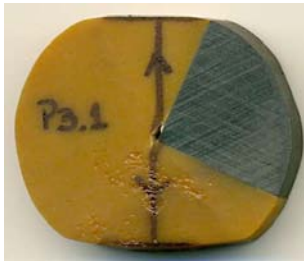

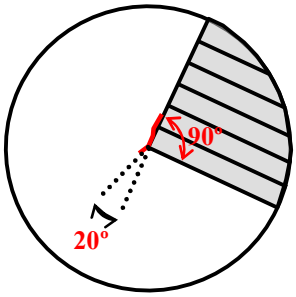

$\alpha = 120^{\circ}$

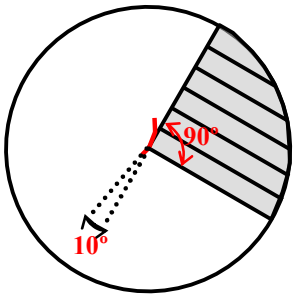

$\alpha = 143^{\circ}$

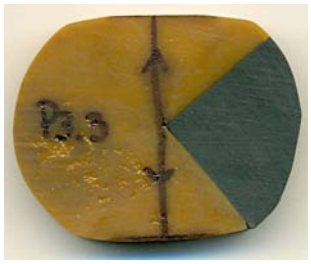

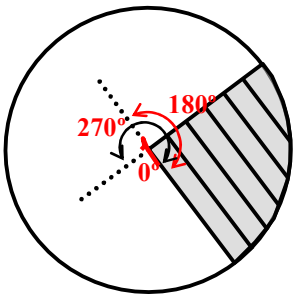

$\alpha = 150º$

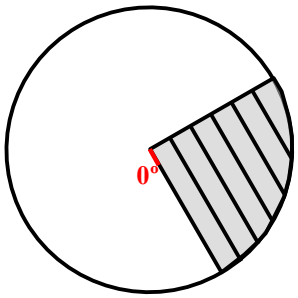

Fig. 6.24 – Tested samples and scheme of the failure path observed (static loading).

In Fig. 6.24 the failure path observed in each type of specimen is indicated. In some cases it was observed between the CFRP-adhesive interfaces together or not with the failure along the adhesive. Further studies about the location for failure initiation are presented in Chapter 7.

Due to the fact that K_1 and K_2 have different units ($MPa\ mm^{0.2367}$ and $MPa\ mm^{0.1106}$ respectively, because of the different values of the orders of stress singularities associated with each of the terms), it is advisable to divide the critical values of GSIF for other load orientations by the mean value of K_{kC} in order to eliminate these units. This will enable a simple graphical representation of all these critical values for all load orientations tested to be obtained. Fig. 6.25 thus shows the dimensionless values of critical values obtained by dividing K_1 and K_2 of every specimen for the average value of K_{1C} and K_{2C} of the cases in

which $\alpha = 13^{\circ}$ and $\alpha = 60^{\circ}$ respectively. The envelope cuts the abscissas and ordinates axes approximately at points $(1,0)$ and $(0,1)$ for the first quadrant. This representation allows a failure envelope based on generalized fracture toughness values of the corner to be proposed.

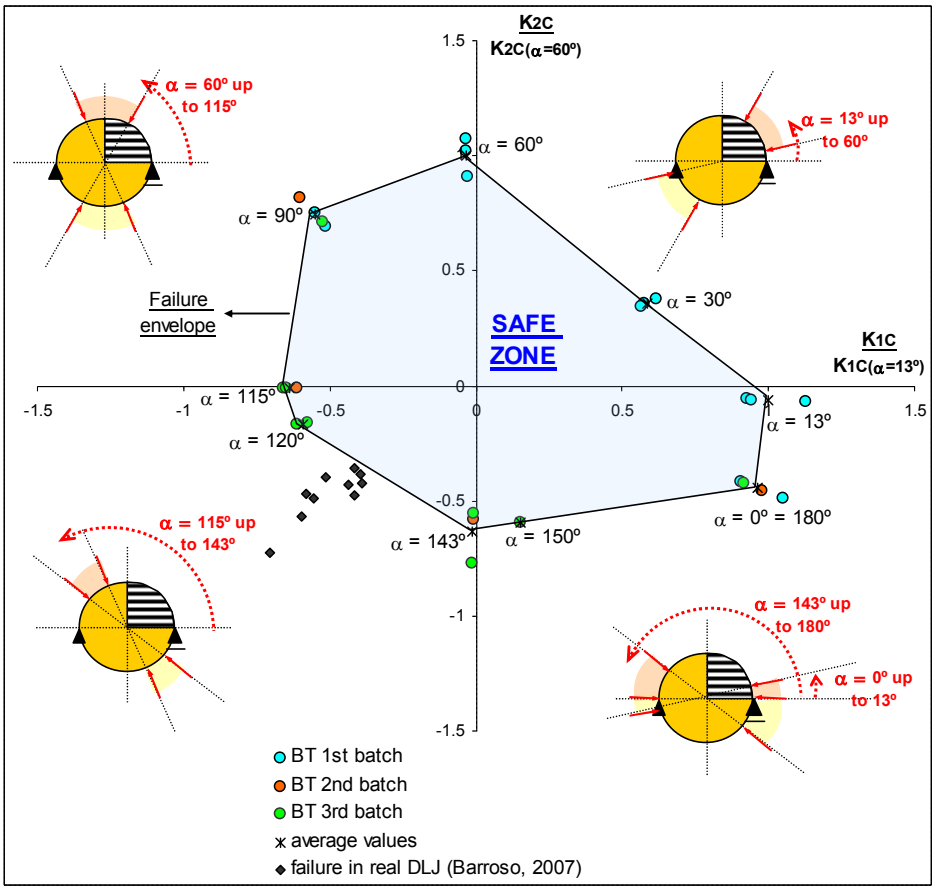

Fig. 6.25 – Failure envelope based on critical GSIF.

Auxiliary schemes of the corner being loaded for the corresponding angle α are indicated in every quadrant. It may be seen that the abscissa and ordinate axes in the graph do not correspond to the $\alpha = 0º$ and $\alpha = 90º$ respectively (as if it was a polar coordinate system). Furthermore, the BT specimens are indicated in Fig. 6.25 with the colours of the correspondent bulk tested (see Table 6.2 for a better correlation), presenting little dispersion between them (when tested at the same angle), where the first, second and third batches (blue-cyan, orange and green colour representation) were those shown in figures 6.18, 6.21 and 6.22, respectively.

Other authors attempted to obtain a failure envelope: Raghava et al. (1973) in an ellipse shape for several isotropic polymers separately in terms of principal stresses instead of GSIF and Hafiz et al. (2010) proposed a type of test (based on Fernlund & Spelt, 1991) for obtainment of an envelope based on energy release rate for other joint configurations.

Each set of experimental results associated with the same load orientation angle α falls along the same radial line in Fig. 6.25, due to the fact that the ratio between ($K_{1C}/K_{1C(\alpha=13º)}$) and ($K_{2C}/K_{2C(\alpha=60º)}$) is constant for a given value of α, the only difference being the value of the failure load (proportional to the distance to the origin in Fig. 6.25). The failure envelope was been

defined using the average values of critical GSIF for every loading angle tested, and linear interpolation between loading angles.

Fig. 6.25 includes Barroso's (2007:159) previous experimental results. These tested adhesively bonded double lap joints had the same local geometry at the end of the overlap zone, in the joint of the unidirectional laminate corner with the adhesive spew fillet. The radius $r = 0.025\ mm$ was considered in his analyses. Although the results fall outside the failure envelope obtained in the present work, they are very close to it. This result is highly significant because the samples tested in Barroso (2007) have the same local corner configuration although they were completely different in size, geometry and manufacturing process. While the BT specimens were manufactured in autoclave and have a characteristic distance from the corner of $14\ mm$ (the diameter), the DLJ have been manufactured in a hot plate press and have a characteristic distance of $0.1\ mm$ (the adhesive thickness). It is also important to remark that while the present failure envelope is obtained for failure initiation, results by Barroso (2007) correspond to complete failure of the DLJ specimens. This is probably the reason why these results fall outside the envelope (failure initiation). Table 6.3 presents the values used for plotting the graph in Fig. 6.25.

Load angle (α)	*Sample (internal code)*	$K_{1C}/K_{1C(\alpha=13°)}$	$K_{2C}/K_{2C(\alpha=60°)}$
$0° = 180°$	P1.10	1.05	-0.49
	P1.11	0.91	-0.42
	P2.2	0.98	-0.45
	P3.5	0.92	-0.42
$13° (K_2 \cong 0)$	P1.1	0.93	-0.06
	P1.6	1.13	-0.07
	P1.8	0.94	-0.06
$30°$	P1.3	0.62	0.38
	P1.7	0.58	0.35
	P1.9	0.56	0.35
$60° (K_1 \cong 0)$	P1.2	-0.03	0.91
	P1.4	-0.03	1.02
	P1.5	-0.03	1.07
$90°$	P1.12	-0.51	0.69
	P1.13	-0.55	0.75
	P2.5	-0.60	0.81
	P3.6	-0.53	0.71
$115° (K_2 \cong 0)$	P2.1	-0.61	-0.01
	P3.1	-0.66	-0.01
	P3.2	-0.65	-0.01
$120°$	P3.7	-0.61	-0.17
	P3.8	-0.58	-0.16
$143° (K_1 \cong 0)$	P2.0	-0.01	-0.58
	P3.3	-0.01	-0.77
	P3.4	-0.01	-0.55
$150°$	P3.9	0.15	-0.59

Table 6.3 – Results of $K_{1C}/K_{1C(\alpha=13°)}$ and $K_{2C}/K_{2C(\alpha=60°)}$.

As an additional task, photographs were taken from the specimens in an optical microscope after testing. In Fig. 6.26 a sequential composition along the failure of the photographs from

the specimen P2.2 ($\alpha = 0^o$) is shown. Indication of cohesive failure was detected, with some ligaments of the adhesive totally broken or stretched. In front of the crack tip (Fig. 6.26 b), indications of whitening (a clearer colour for the adhesive) or damage was observed. The CFRP does not appear in the photograph, but it is parallel to the failure (being localized at the lower surface), with the fibres parallel to the fracture.

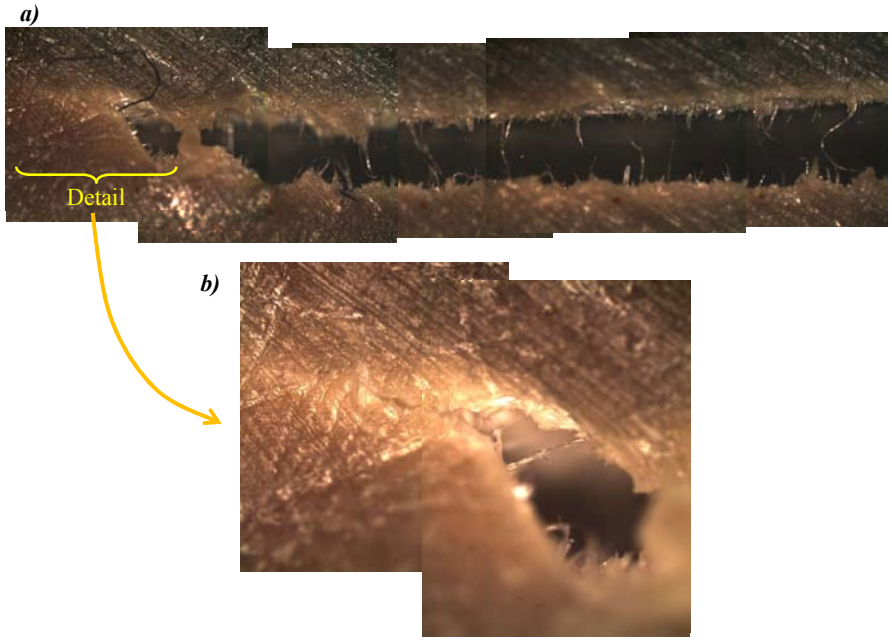

Fig. 6.26 – Composition of the photographs of the failure from specimen P2.2 ($\alpha = 0^o$): a) 50 and b) 100 times amplification.

6.7 Summary of the procedure

The proposal presented in this chapter seems to be a novel and suitable procedure that could further be used for generalized fracture toughness determinations in multimaterial corners under certain conditions. Nevertheless the scope for the presented procedure is limited to the following:

- It is valid for closed corners with all material wedges perfectly bonded;
- the expression for the stress field, Eq. (6.1), that represents the problem under study must allow the isolation of two singular terms as maximum;
- it is limited to materials in which linear-elastic and configurations in which plane-strain conditions can be assumed, also brittle behaviour and negligible plastic-zone in the closed corner zone (i.e. local plastic zone is small compared to the K-dominated zone);
- curing stresses are not considered.

As a guide, the procedure for failure prediction in real joints can be summed up as:

a) Numerical analysis of the joint under study and, together with experiments, detection of the critical corner of the problem;

b) Knowledge of the characteristic exponents (λ) and the angular shape functions (f_{ij} and g_i) which control the problem. Evaluation of the most significant terms in Eq. (6.1) – the development in series – to consider;

c) Accomplishment of a simpler numerical model of the BT only for the critical closed corner under different angles (α) to obtain the evolution of stresses (see Fig. 6.9 as example) and estimate if the isolation and combinations of the GSIF are possible.

d) Selection of some angles of interest to carry out the experimental test (for the complete envelope at least two sets of points for each quadrant; or for only one quadrant, more specimens can be manufactured in order to get a more precise envelope in the region of interest).

d) Particularization of the stress state for points very closed to the corner tip for the selected angles of study (in this work $r = 0.1\%\ R$ was considered).

e) Accomplishment of an adjustment (in this work the Least Square Method was used) of σ_{ij} and u_i functions to obtain the GSIF (K_k).

f) Experiments on BT specimens for the amplified critical corner in selected angles in order to obtain the K_k^{spec} given by Eq. (6.8), for pure and mixed modes (failure envelope).

g) Plot the envelope of the curve in the entire or only in the region of interest.

Once the envelope is built, the result can be used for failure prediction in real adhesive bonded joints. In this work, the procedure adopted was the following: the critical GSIF, calculated from the admissible load (admissible GSIF) during the tensile test for adhesive joints (ASTM D3528) is evaluated. After this, the normalization of all data is needed, in order to allow the comparison between the responses and obtain dimensionless values. In this work the values of K_1 and K_2 of the real joint were normalized with $K_{1C(\alpha=13^o)}$ and $K_{2C(\alpha=60^o)}$ of the BT, with the same corner configuration (see Fig. 6.9).

Finally, the averaged critical values from the experimental data (Fig. 6.25) were taken in order to find an approximate analytical function of the failure envelope. Fig. 6.27 shows an example of three different possibilities of approximation, considering the functions as indicated. This considered a polar coordinate system which coincided with the centre of the envelope in Fig. 6.25 and trigonometric functional series.

Least squares method was used to obtain the best fitting function, based on the minimization of the error between the experimental point (which modulus is M and the angle of measurement is represented by ω) and the tested approximation.

The function f_3, which is a relatively simple expression, seems to be a good first estimation for the failure envelope. A, B, C, D and F are constants which are obtained by the least squares method.

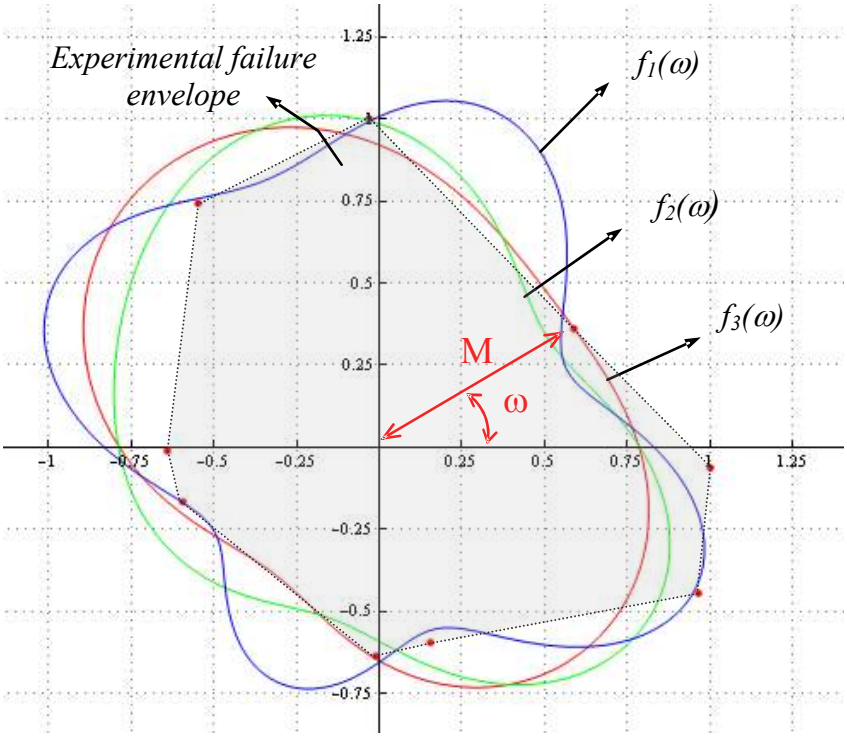

$$f_1(\omega) = A + B + \sin(\omega) + C\sin(2\omega) + D\sin(3\omega) + F\sin(4\omega)$$

$$f_2(\omega) = A + B + \sin(\omega) + C\sin(2\omega) + D\sin(3\omega)$$

$$f_3(\omega) = A + B + \sin(\omega) + C\sin(2\omega)$$

Fig. 6.27 – Some possible approximations of the envelope.

6.8 Discussion

A numerical and experimental test procedure has been developed for generalized fracture toughness determination in multimaterial closed corners having two terms with stress singularities. The procedure is inspired on the well-known BT, by applying it to the geometry of the critical corner under study, for which reason the method is – in principle – valid for closed corners, which can be loaded in compression at any position along the whole external perimeter. Indeed, the procedure is especially suitable for unsymmetrical multimaterial corners involving materials whose nature is essentially isotropic and anisotropic, having two stress singularities. The method is able to isolate any of the singular modes, which is not possible with standard test procedures defined for homogeneous isotropic materials, due to the lack of symmetries of the stress states at these corners.

The method has been applied to a particular bimaterial corner, typically appearing in adhesive joints involving composites, and the test configurations seem to be suitable for the experimental evaluation of the generalized fracture toughness values K_{1C} and K_{2C}.

The experimental procedure has shown to be feasible, relatively simple to carry out and the results presented little

dispersion among them (see Fig. 6.24). It may be concluded that this method can further be extended to other types of multimaterial corners.

Once the tests have been carried out and the generalized fracture toughness values calculated, a failure envelope can be obtained by testing the samples at different angles, which originate mixed mode stress states. Thus the presented procedure can be used as a failure criterion in joints of this type. The proposed failure envelope have proved to be in a good agreement with previous experimental results already published (Barroso, 2007), involving the same local corner configuration but completely different global geometry.

In conclusion, this chapter has suggested new possibilities for in-depth studies and increased understanding of some aspects of this subject. Consequently, the following chapter presents a complementary study in order to corroborate and clarify some aspects of the proposed criterion and testing procedure.

Chapter

7 Failure under fatigue loading

The static tests presented in the previous chapter enabled the evaluation of the generalized fracture toughness by means of the proposal of a configuration based on the Brazilian disk specimen. The present chapter focuses on the fatigue failure initiation and propagation in BT specimens, which represent the amplification of the bimaterial corner (analyzed in Chapter 6) that is present in real adhesive joints, under appropriate conditions. These specimens were tested under static compressive loads in the previous chapter, in which local yielding effects might affect the asymptotic two-dimensional linear elastic stress representation under consideration. Fatigue loading minimizes this effect due to the lower load levels used. In this chapter, the fatigue tests are carried out with the aim of the crack initiation and failure characterization of such specimens, for further application in adhesive joints.

The work described in this chapter was carried out by means of a collaboration between the GERM/LERM and the Research Group led by the Professor Andrew Crocombe, in the Mechanical Medical and Aerospace Engineering of the University of Surrey, Guildford (UK). The BT specimens were manufactured in the

LERM facilities and the tests were carried out at the University of Surrey.

The tests were performed using load control, video microscopy and still cameras were used for monitoring initiation and crack growth. The fatigue tests were halted periodically and photographs of the corner were taken, allowing monitoring of the crack formation and growth along the corner, for different testing angles α along the diameter of the BT specimens.

However, it is known that the influence of the thermal stresses are more severe in the DLJ than the BT specimen, and according previous studies (see Chapter 4), the thermal stresses were not considered in this and the previous chapter.

7.1 Numerical analysis, configuration and manufacturing of the specimens

The problem under study is the same as that in the previous chapter and the numerical analyses carried out are valid for this chapter. Fig. 6.2 presents a scheme of the BT specimen, which can be seen as an amplification of the critical corner of the DLJ under study (Fig. 1.1). The properties of the materials are given in Tables 2.1, 2.2 and 2.3. For these analyses and according to previous experience, 24 new specimens were manufactured

according to the procedure described in Section 6.3, in which the adhesive was cured in autoclave (the details about the curing cycle were described in Chapter 2) in order to minimize the number of defects inside the samples. Fig. 7.1 shows photographs taken during the manufacturing process.

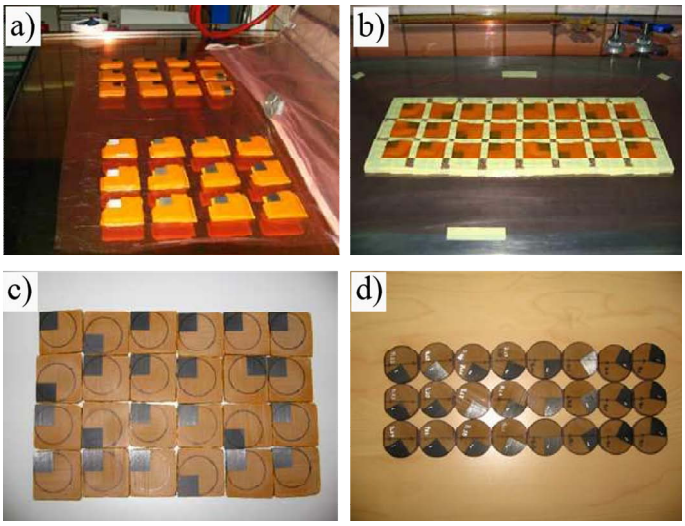

Fig. 7.1 – Manufacture of specimens. a) Adhesive film being layered; b) Cork covered with high temperature tape delimitating the region; c) After curing, specimens are like "cookies" and d) Final geometry of samples.

The Fig. 7.1 a) shows the adhesive film surrounding the slice of CFRP bar. The adhesive was cut and layered with intermediate vacuum compactions between every five laminas (for 10-15 min). The procedure was carried out inside a clean room. The entire set was placed on an aluminium plate covered with Teflon®. After

this, cork was used to separate and contain all specimens, accommodating and fixing them to the plate. Next, the cork was covered with a high temperature tape to avoid spilling of the adhesive during the curing process (Fig. 7.1 b). The entire set was covered with Teflon®, followed by an Airweave® breather fabric. Then a vacuum bag was prepared, and the specimens were cured inside the autoclave (the curing cycle was detailed in Chapter 2). After the curing process, every specimen was a square plate (see Fig. 7.1 c).

Once the curing cycle was finished, every sample was carefully cut, using a water-cooled diamond for cutting the circular disk, around the marked circumference of the final geometry (Fig. 7.1 c). Then the specimens were abraded in order to smooth the cut surfaces, leaving them as round as possible. Finally, the angle of the load application was marked and both "flats" on which the load was applied (Fig. 7.1 d) were cut. This allowed a uniform application of the compressive load during the test (by Saint-Venant principle the stress state at the corner tip is not affected by the local detail of the load application, as can be verified in Fahad, 1996; for example, among other studies).

Figure 7.2 shows a schematic figure of the whole manufacturing process.

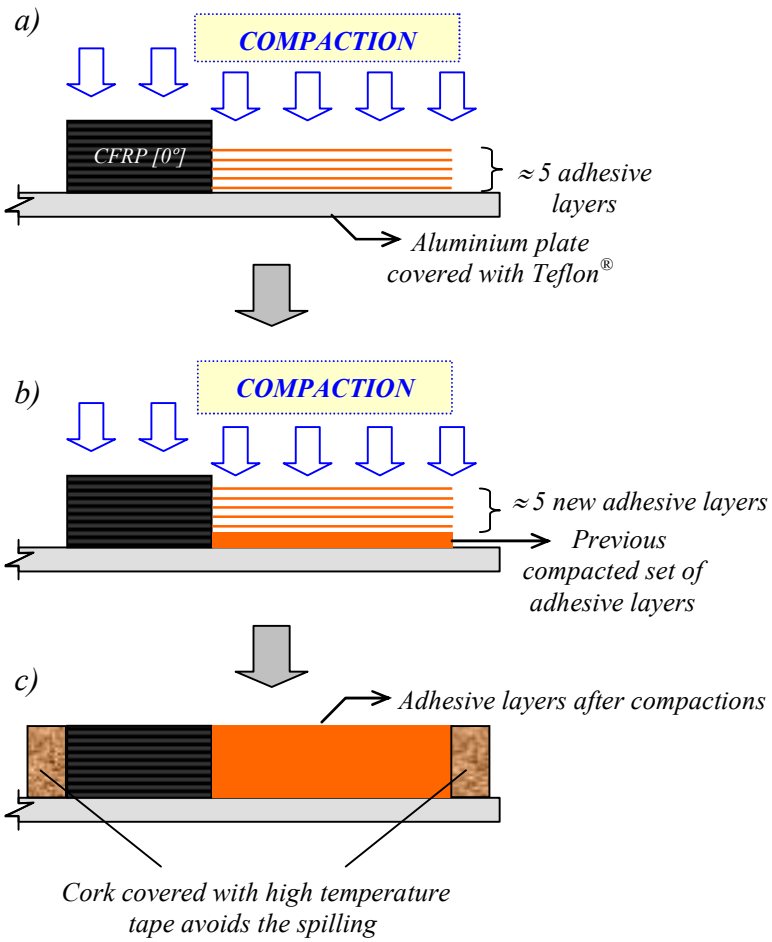

Fig. 7.2 – Scheme of the sample fabrication: a) adhesive layers on the aluminium plate, b) new adhesive layers being prepared for compaction and c) adhesive layers after compactions with the cork with high temperature tape avoiding the spilling for the curing process.

Once the 24 specimens were manufactured, they were divided into 8 groups, being 3 specimens known as “PC” followed by the number of the specimen, for internal control, for each angle of testing. This choice covers all quadrants in a graphical representation the same as in Fig. 6.25. Table 7.1 presents the final dimensions (in terms of R and t) of the specimens and angles of testing.

Specimen	*a (º)*	*R (mm)*	*t (mm)*	P_u *(N)*	K_1^*	K_2^*	N_0	N_{1mm}	N_{3mm}
PC1		20,24	8,24	14207			1141	1141	1141
PC2	13	20,4	8,28	14389	1	-0,063	1600	1600	1600
PC3		20,38	8,16	14167			1521	1521	1521
PC4		20,23	8,3	12232			7500	12500	27500
PC5	30	20,12	8,14	11931	0,585	0,360	2500	2500	-
PC6		20,12	8,23	12063			2500	7500	82500
PC7		20,16	8,19	14151			-	-	-
PC8	60	20,5	8,21	14425	-0,032	1	-	-	-
PC9		20,6	8,27	14602			-	-	-
PC10		20,67	8,26	12130			2500	2500	7500
PC11	90	20,18	8,32	11928	-0,548	0,743	2500	2500	4250
PC12		20,28	8,08	11642			2500	2500	5000
PC13		20,36	8,28	14026			2500	2500	7500
PC14	115	20,6	7,97	13660	-0,639	-0,009	2500	2500	22500
PC15		20,55	8,22	14054			2500	7500	32500
PC16		20,5	8,17	15373			2500	27500	37500
PC17	120	20,63	8,3	15716	-0,592	-0,165	2500	22500	67500
PC18		20,65	8,34	15807			2500	17500	52500
PC19		20,87	8,24	13006			72500	87787	87787
PC20	143	20,44	8,46	13078	-0,011	-0,634	92500	-	-
PC21		20,84	8,25	13003			27500	47500	82500
PC22		20,72	8,1	10851			7500	22500	57500
PC23	150	20,64	8,26	11022	0,154	-0,595	2500	17500	27500
PC24		20,72	8,04	10770			2500	32500	67500

Where: α is the tested angle; R is the specimen radius (or R^{spec}); t is the specimen thickness (or t^{spec});
P_u is the ultimate static load (estimated from static results in [18]);
K_1^*, K_2^* (or K_{1C}^{spec}, K_{2C}^{spec} normalized in order to obtain dimensionless values) are K_1 and K_2 at the instant of failure divided by the critical GSIF (estimated from static results in [18]);
N_0 is the corresponding number of cycles at which the first change was observed in the corner; and
N_{1mm}, N_{3mm} are the corresponding numbers of cycles necessary for the observed damage to reach at least 1 mm and 3 mm in length, respectively.

Table 7.1 – Summary list of data from numerical and experimental analyses. K_1^* and K_2^* were obtained from the estimation of P_u (results), being presented as averaged and normalized values.

7.2 Experimental test

In the previous chapter, BT disk specimens were tested under static load in a displacement controlled machine for different angles α, in order to achieve the failure envelope according to the theory presented in Chapter 6. A failure envelope based on the critical combinations of a pair of GSIF at the corner tip was presented and proposed as a criterion for joints having the corner shown in Fig. 6.2. The results were compared with real adhesively DLJ loaded in tension, as previously tested in Barroso (2007), presenting good agreement. In those analyses however, devices such as cameras and strain gauges for monitoring and checking the initiation and progression of the cracks were not used. In addition, if plasticity occurred it could affect the stress state of the corner. In this sense, fatigue tests could be useful to avoid possible yielding effects. The tests described in the present chapter were carried out in the present chapter in order to further characterize the crack initiation and damage progression. Failure initiation was defined in the current chapter as the first of the following phenomena: initial observation of whitening or a crack.

The fatigue tests were halted every 5000 cycles to check the integrity of the specimen on both planar surfaces. The test was considered to be finished either when the failure length was

approximately equal to, or greater than $3\ mm$, or when the specimen reached a total of 10^5 cycles (equivalent to a couple of days of cycling). This failure length was chosen in order to optimize the visualization of one or more cracks, the time needed for testing and the safety of the machine.

7.2.1 Mechanical testing and parameters

The tests were carried out in a servo-hydraulic Instron 8511 machine, in sinusoidal load control at a frequency of $5\ Hz$. The room temperature was 25±3ºC during the testing. Additionally, the machine was provided with automatic amplitude control for better stability of the tests. No static test was undertaken for this series of specimens, so the ultimate compressive load (P_u) was estimated from the data presented in the previous chapter. P_u was estimated to be $13260\ N$ on average (a small variation was observed between specimens due to small changes in geometry). Thus, a compressive load $P_{\max} = 6540\ N$ was used (corresponding to nearly 50%, of the estimated P_u, in most cases) in the first tests. However, this load did not allow the initiation of failure in the majority of the initial batch of test specimens. Thus $P_{\max}$ was changed to $8409\ N$ (corresponding to around 60% of the

estimated P_u). The minimum load was chosen as 10% of $P_{\max}$, giving a fully compressive load cycle and a load ratio ($P_{\min}/P_{\max}$) of 0.1. Also, a fan was used to help maintain the specimens at room temperature and compensate for the slight heat generation caused by the lights required for the cameras. Two flat plates were used as platens to apply compression on the "flats" machined in the specimen. Initially for a better monitoring of temperature, a thermocouple was used with the first few samples. However, as it was later verified that the temperature was quite constant, it was no longer necessary to check temperature during the tests. Fig. 7.3 shows two views with the cameras while the tests were been carried out.

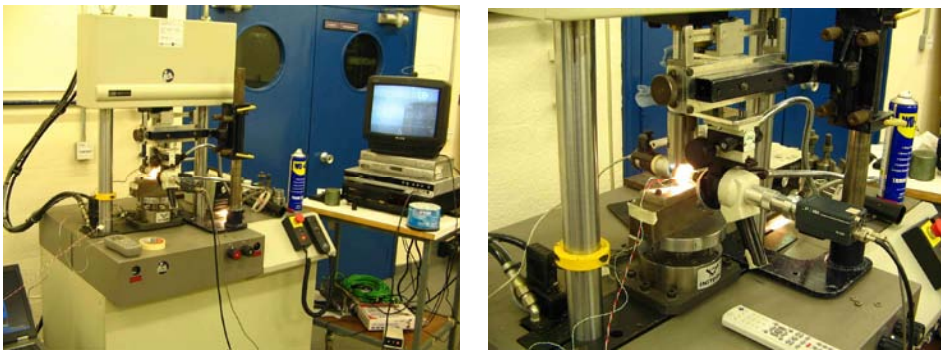

Fig. 7.3 – Photographs during the tests showing the cameras.

7.2.2 Strain gauges measurement

Inspired by the back strain technique (Shenoy et al., 2009), Strain Gauges (SG) were used in order to measure any sudden variations in the strain measurements during the tests. One SG (TML Strain Gauge type FLA-1-23) was positioned on every specimen, only at one surface for monitoring the strain close to the corner tip (as will be showed later in figures 7.5 and 7.6). The unidirectional SG used, with a gauge length of $1\ mm$, had a $2.18 \pm 1\%$ gauge factor, 120 ± 0.3 ohms of resistance and $23 \times 10^{-6}\ ℃^{-1}$ as the coefficient of thermal expansion.

During the tests, it was observed for all specimens that the measurement of the SG "jumped" in some occasions. Fig. 7.4 shows the maximum and minimum SG measurement for specimen PC14, as an example of this behaviour. Indeed the first tests were interrupted at this moment due to the suspicion that this jump could be associated with the failure detection, measuring extremely high values that however did not correspond with the visual observation. For prevention, in the following specimens, some changes were proposed in order to avoid the observed phenomenon: changing the SG location on the surface, touching or not touching both materials, positioning them close (approximately 1 mm of distance) or relatively far from the corner tip (approximately 4 mm of distance), see schemes

indicated as a), b), c) in Fig. 7.4. In these schemes the direction of measurement is indicated as an arrow inside of the SG representation.

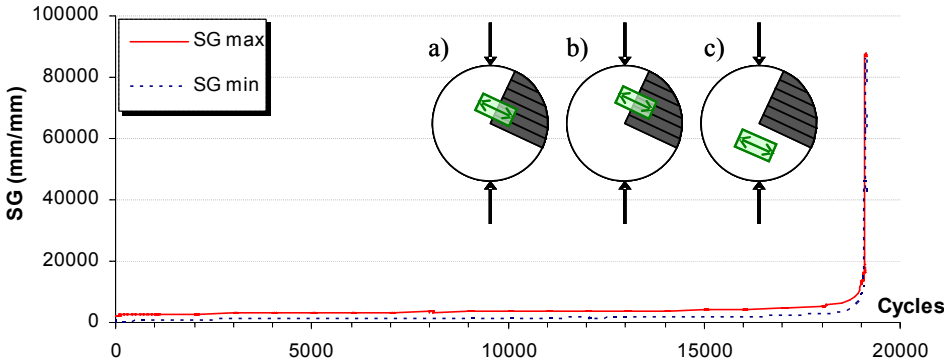

Fig. 7.4 – Graph showing the SG jump and schemes of different locations tested (PC14, $\alpha = 115^{o}$).

In two tests, in which the position of the camera was allowed to monitor the region, the breaking of the SG terminals was observed, as illustrated in Fig. 7.5 b), but it could not be generalized as no detailed and careful inspection was carried out for all SG on the specimens. Consequently, the data from SG were not considered as a valid indication for failure initiation in this work.

7.2.3 Damage monitoring

Photographs from three different cameras were taken to capture the initiation and eventually the progression of failure.

The cameras were set to different magnifications and qualities of images and videos, and were positioned close to the corner tip, where the failure was expected to initiate. At every programmed interruption of the machine test (every 5000 cycles), one or two photographs (or a video) were taken of one (or both, when possible) surfaces of the specimen (see Fig. 7.3). The photographs were viewed successively at the end of the test, providing visualisation of the initiation and progression of the failure. Figures 7.5 and 7.6 show examples of sequential photographs for two specimens.

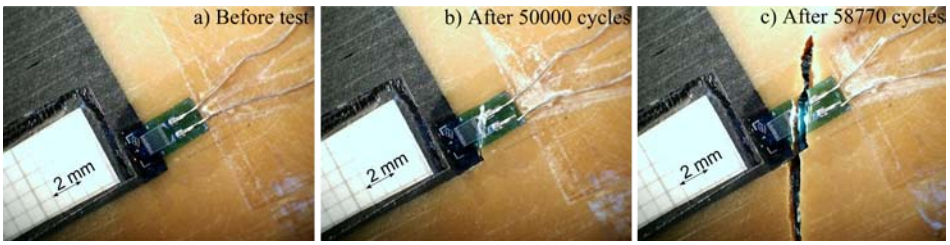

Fig. 7.5 – Examples of sequential frames of photographs of PC16, case $\alpha = 120^{\circ}$. The strain gauge is seen in these photographs.

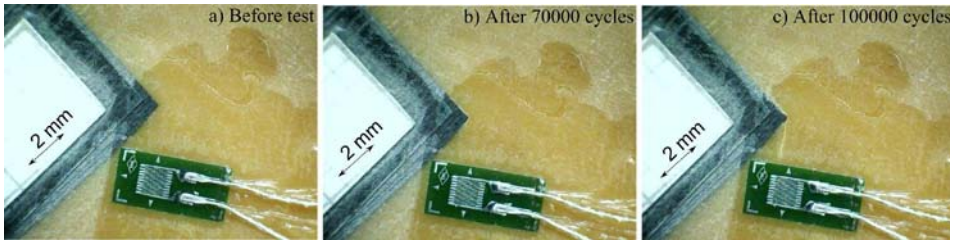

Fig. 7.6 – Examples of sequential frames of photographs of PC21, case $\alpha = 143^{\circ}$. The strain gauge is seen in these photographs.

Figures 7.5 a) and 7.6 a) show the specimens before testing, without any cracks. Figures 7.5 b) and 7.6 b) show the photographs taken after 50000 and 70000 cycles, respectively. In Fig. 7.6 b), a crack/whitening can be seen at the CFRP-adhesive interfaces around both sides of the corner, while in Fig. 7.5 b) a visible crack is appreciated. Figures 7.5 c) and 7.6 c) were taken at the end of test, in which the crack grew from one CFRP-adhesive interface through the adhesive.

A small piece of graph paper (with a grid of $1\ mm \times 1\ mm$) was attached to the CFRP for scale measurement in each specimen, (Fig. 7.5 and 7.6). The resolution of the camera was $50\ pixels/mm$ (1270 dpi); the accuracy of the crack length measurement being 0.02 mm per pixel, which was sufficiently precise for the prescribed 1 mm and 3 mm measurements. Extracting the information from the images, N_0 was defined as the number of cycles at which the first change was observed in the corner, N_{1mm} as the number of cycles necessary for the observed damage to reach at least 1 mm in length, and N_{3mm} as the number of cycles necessary for the observed damage to reach at least 3 mm in length.

The analysis of photographs was based only on visual measurement of the scaled images, i.e., no image analysis software was used. For irregular damage/whitening/cracks the

approach outlined in Fig. 7.7 was taken as a guide, and when the failure was slightly different on both sides, the most extreme situation was considered for the analyses.

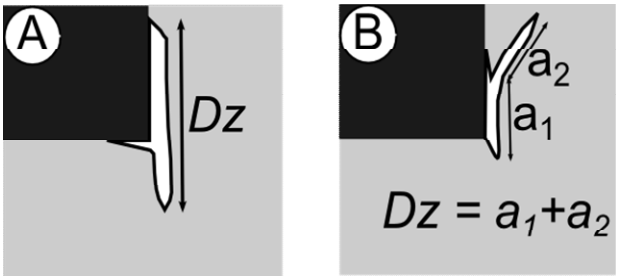

Fig. 7.7 – Measurements of the size for irregular failure paths a) type I and b) type II, where Dz is the damage zone (or crack) length.

7.3 Results and discussions

The fatigue tests were interrupted every 5000 cycles, except when an instantaneous and/or sufficiently large crack occurred, in which case the test was ended. At every interruption of the test, the number of cycles was recorded. For regular tests at every 5000 cycles, it was assumed that any damage event occurred mid-way through the prior band, i.e., in the intermediate number of cycles corresponding to the centre of the actual range of cycles.

7.3.1 Failure evolution

Figure 7.8 shows the failure evolution for every group of specimens which for internal control, is here referred to as "PC", followed by the number of the specimen. The angles considered for every set of specimen are shown in Table 7.1. In Fig. 7.8, the load level applied is indicated in each graph. The group of specimens with $\alpha = 60^{\circ}$ (PC7 to PC9) did not present any visible failure, so this configuration was not represented in Fig. 7.8.

In the cases where the failure started quickly, some specimens were tested under two load levels (PC7, PC8, PC10, PC11, PC13, PC14 and PC22), as mentioned previously. In this case, the Miners' law (Miner, 1945; Ashcroft et al., 2010) was used in order to homogenize the number of cycles under different load levels. However, it was seen that the effect of the number of cycles corresponding to the lowest load level was negligible. Thus, although plotted in Fig. 7.8, these data were not considered in the analysis.

Due to the fact that the crack length could be observed from both sides of the specimen, some discontinuities can appear, as in Fig. 7.8 c for PC10, when reproducing the data obtained from the two sides for different load levels. For example, PC10 under 8409 N does not start with a crack length corresponding to that obtained at 6540 N load level.

Generally speaking, the progression of the crack for every group of specimens presented only small scatter, although some exceptions appeared. For instance, the photographs of PC23 were taken on different days, which can justify the high value of *Dz* (up to 60000 cycles) that can be observed in Fig. 7.8 g.

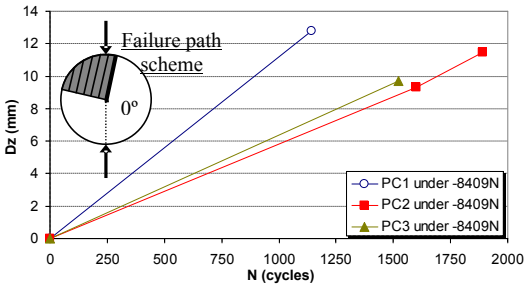

a) α=13º

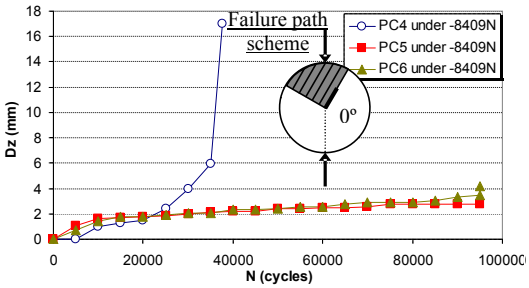

b) α=30º

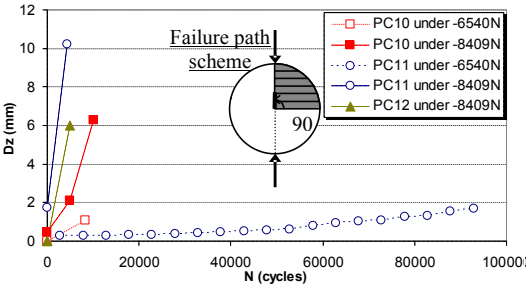

c) α=90º

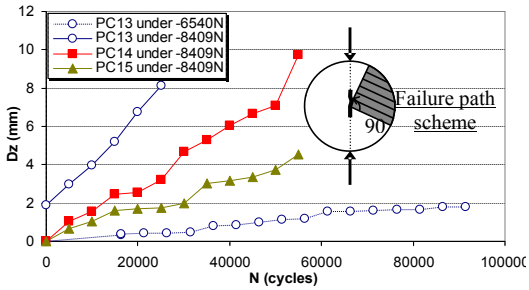

d) α=115º

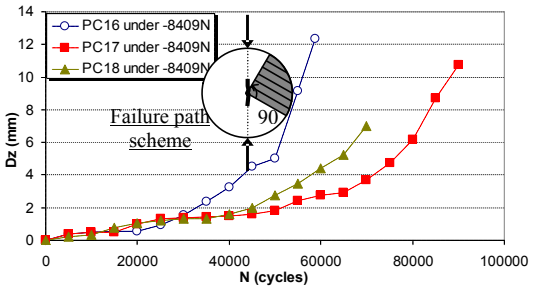

e) α=120º

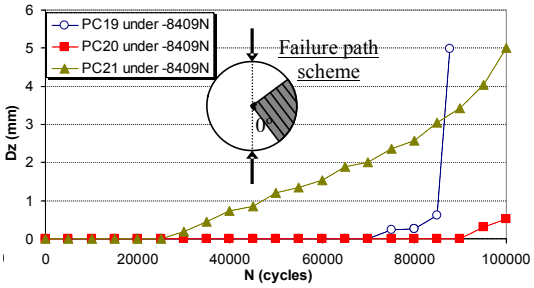

f) α=143º

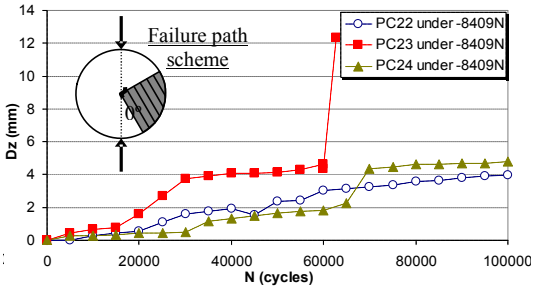

g) α=150º

Fig. 7.8 – Damaged zone (Dz) vs. number of cycles (N) for every tested angle (α). A scheme of the failure path observed during the test is also indicated in each case.

The angle of failure initiation is indicated in the schematic of the corner for each case in Fig. 7.8, showing the direction of

propagation at the initiation stage and the applied load. Thus, when the first failure was observed at 0º it meant that the failure started at the corner tip and propagated through the CFRP-adhesive interface, along the x-axis or parallel to the fibres, according to the coordinate system of Fig. 6.2. By analogy, the angle of 90º for initiation meant that the failure went along the CFRP-adhesive interface, after starting at the corner tip. But in this case the failure propagated through the y-axis i.e., perpendicular to the fibres. Although the crack generally started at angles of 0º or 90º, when it propagated through the adhesive, the rupture tended to adopt a straight vertical line, i.e. the same direction as the applied load and perpendicular to the indirect tensile stress that is typically developed in the original BT (Carneiro & Barcellos, 1953). However, when the CFRP was involved in the failure mechanism, as for example the cases in which $\alpha = 13^o$ or 30^o in which the load line passed through the CFRP, the interface failure prevailed followed by the failure in the adhesive. In all specimens with $\alpha = 13^o$, 30^o, 143^o and 150^o, the failure started at 0º interface, with the exception for PC20 ($\alpha = 143^o$) where is not fully clear that the failure started at 0º (parallel to the fibres, taking the coordinate system of Fig. 6.2 as reference). For $\alpha = 90º$, $115º$, $120º$ the failure started at the 90º interface (perpendicular to the fibres).

It is clear that the direction of the applied load governs the behaviour, the closest interface to the line in which the load was applied being the one failing first. A proof of this can be obtained by comparing the failure paths for $\alpha = 120º$ and $\alpha = 150º$ configurations. In both cases, the closest interfaces are 30º from the line of load application, but closest to the fibres in 0º for $\alpha = 120º$ (Fig. 7.8 e) and to the fibres in 90º for $\alpha = 150º$ (Fig. 7.8 g). The observed initial failure path direction suggests that the initiation of the damage or visible crack started independently of the fibre orientation, due to the lack of symmetry and to the different stiffness and strength properties of the CFRP and the interface. This is clear for $\alpha = 120^o$, in which the specimens reached $Dz \geq 10\ mm$ faster than for $\alpha = 150^o$.

The following classification was used for failure detection, according to the speed of the "final" event (when the crack reaches at least 3 mm length): Fast, which is associated with a more brittle fracture of the joint and when the final failure was observed during the firsts cycles; moderate when the final failure was observed around 20000 cycles and slow when the final failure was observed beyond 50000 cycles. Fig. 7.9 shows a summary of these results.

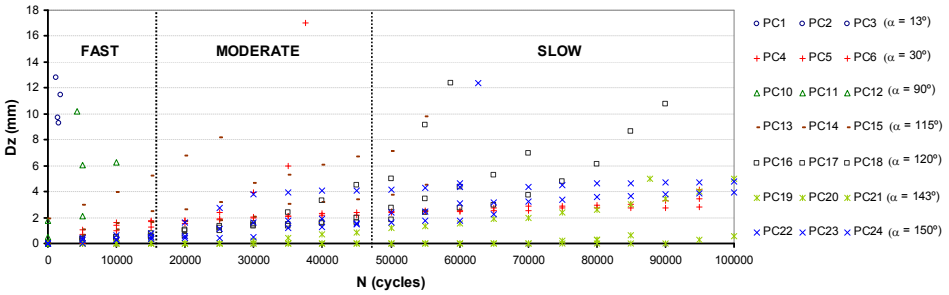

Fig. 7.9 – Global data and speed of failure progression (damaged zone vs. number of cycles, specimens subjected to 8409N).

For simplicity, in Fig. 7.9 the initial load level of cycling (6540N) was not taken into consideration. The configurations $\alpha = 13º$ and $\alpha = 90º$ showed faster failure, i.e. brittle fracture. The $\alpha = 115º$ configuration was between moderate to slow and the rest of specimens slow or extremely slow ($\alpha = 143º$). The brittle or quasi instantaneous failure of the joint was probably associated with the alignment of the interfaces between CFRP-Adhesive with the vertical direction of the load application. The slow failure suggests that a different type of mechanism may be involved.

Fig. 7.10 shows the averaged number of cycles N_0, N_{1mm} and N_{3mm}, over the three specimens in each configuration. This is represented on the left side of the axis for each angle tested (α). P_{max} (applied in all specimens) was normalized with P_u and extrapolated from the static tests in the previous chapter to the dimensions of the actual specimens. This is represented as $\%P_u$

on the right side axis of the graph. For the configuration $\alpha = 60^{\circ}$, where failure did not occur, the infinite life was indicated with an arrow.

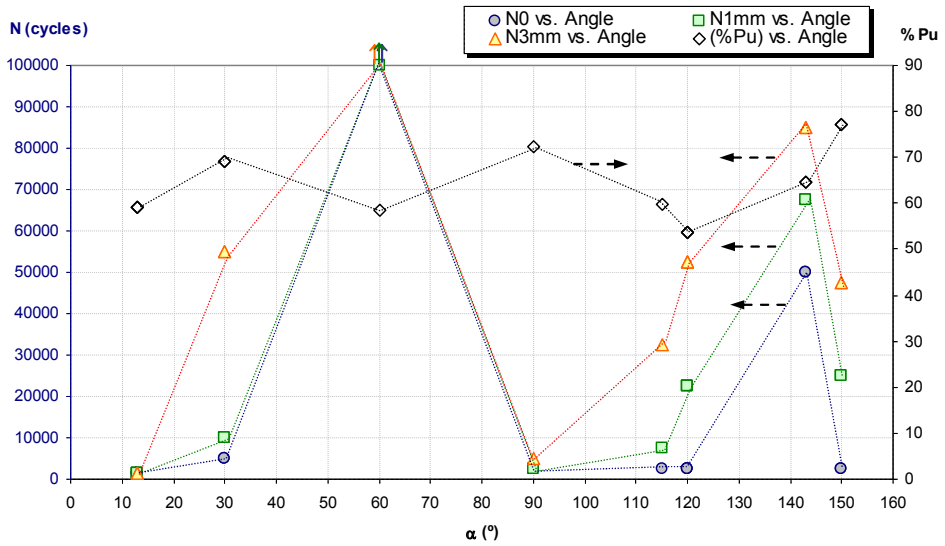

Fig. 7.10. Averaged number of cycles (N_0, N_{1mm} and N_{3mm}, left axis) and % of ultimate load (right axis) versus load orientation (α).

It can be appreciated from Fig. 7.10 a similar trend of fatigue damage with loading angle, particularly for the range between $\alpha = 120^{o}$ and $\alpha = 150^{o}$. In this graph, the initiation is represented by the N_0 curve while the 1 mm damage by N_{1mm} curve and analogue, the 3 mm by N_{3mm} curve. With $\alpha = 90^{\circ}$ and $\alpha = 13^{\circ}$ the failure began immediately, reaching a length of 3 mm. This is the fast mode, according to previous definition. An important

observation from Fig. 7.10 is the evidence that the brittle fracture was not due to the value of the extreme $P_{\max}$ load during the tests. For example when $\alpha = 60^{\circ}$ the $P_{\max}$ applied during the test corresponded to approximately 58% of P_u and no fatigue damage was noted. However, the percentage was slightly lower for $\alpha = 120^{\circ}$ (54% of P_u) and for this configuration the failure started earlier, i.e. $N_0 = 2500$ *cycles* approximately, see Table 7.1. However, it grew slower i.e., the number of cycles needed to reach 1 mm is relatively high, namely $N_{1mm} = 22500$ *cycles* on average. It is further observable from Fig. 7.10, that when K_1 tends to zero (see also Fig. 6.9), fatigue life increases significantly. This might imply that fatigue is driven by K_1. Conversely, no significant influence on fatigue failure is observed when K_2 tends to zero, implying that K_2 may not play as important role in fatigue as K_1.

For the sake of clarity, Fig. 7.11 depicts the normalized values of K_1^* and K_2^*, which shows N_0/N_{1mm} and N_0/N_{3mm} ratios versus the angle (α). This normalization was made in order to obtain $K_1 = 1$ on x-axis and $K_2 = 1$ on y-axis in the dimensionless failure envelope as in the previous chapter.

The GSIF (indicated in parentheses) are related to the results from fatigue tests, giving the limits for initiation (ratio N_0/N_{1mm})

and final failure (ratio N_0/N_{3mm}). The case of $\alpha = 60^o$ is not included in Fig. 7.11. The physical meaning for the behaviour shown in this plot can be found when the ratio N_0/N_{1mm} was close to 1, meaning that the crack quickly reached the length of 1 mm. It was also observed that the ratios followed a similar trend to the angle. The progression of the observable damage was then represented in the plots as the area included between these ratios, i.e. the area represents the region in which the whitening/visible crack is developing. Comparing Fig. 7.11 with Fig. 6.9, it is observed that the fatigue damage increases when K_1^* increases. Nevertheless, it is important to notice that the GSIF were not updated with the progression of damage, only values corresponding to intact Brazilian disk specimens having been used.

All the data acquired during the tests and numerically obtained are summarized in Table 7.1.

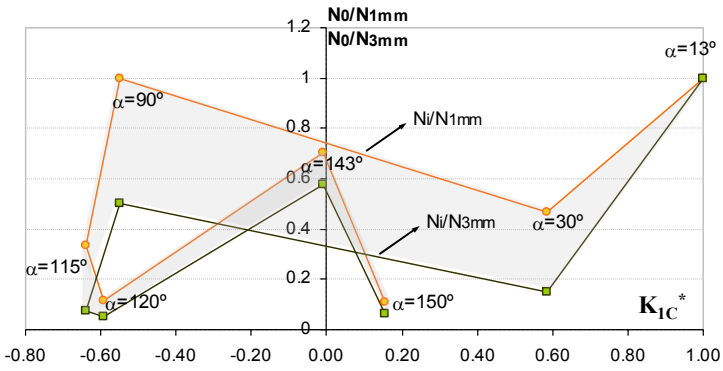

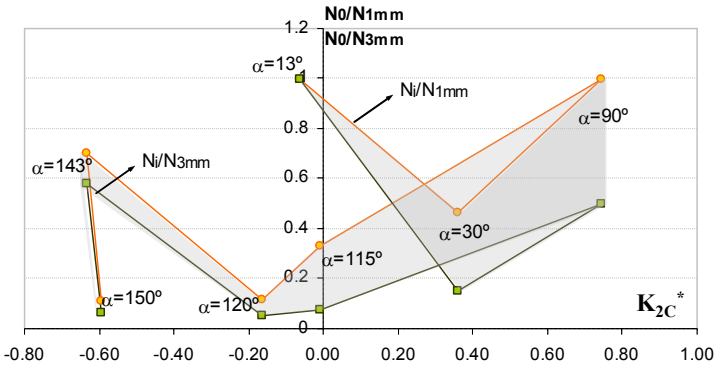

Fig. 7.11 – Normalized K_{1C} and K_{2C} against the N_0/N_{1mm} and N_0/N_{3mm} ratios.

The ratio between the number of cycles for the failure to start (N_0) and the number of cycles necessary for the failure to reach 1 and 3 mm long respectively (N_{1mm} and N_{3mm}) is shown in Fig. 7.12, versus the angle (α).

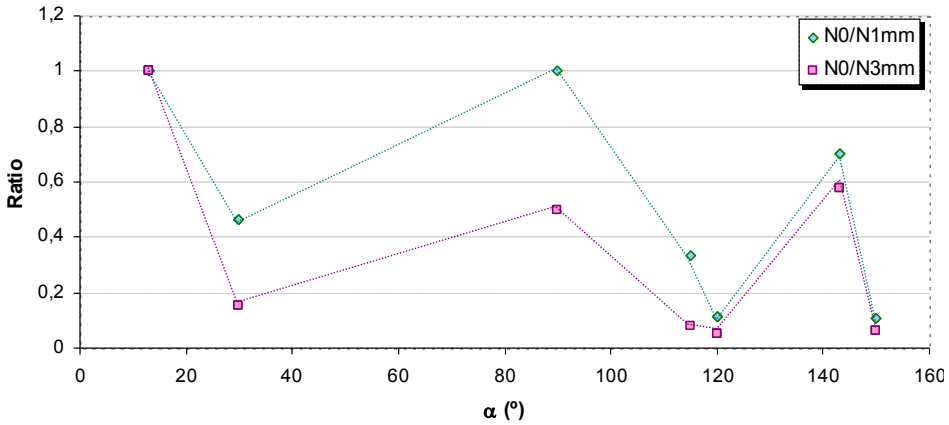

Fig. 7.12 – N_0/N_{1mm} and N_0/N_{3mm} ratios against the angle α.

According to this figure, ratios (N_0/N_{3mm}) close to 0 seems to be associated with the slow failure growth. This is in agreement with the results from Fig. 7.9 in which the cases $\alpha = 13º$ and $\alpha = 90º$ are classified as fast growing, and $\alpha = 115º$, $\alpha = 120º$, $\alpha = 150º$ as the slowest ones.

7.3.2 Crosshead data

The information on the crosshead displacement of the machine (specimen compliance) during the test was analyzed in order to check if the compliance change could be correlated with the crack onset, thus providing a way of anticipating fatigue damage. Figure 7.13 shows the maximum and minimum displacement (i.e. *Max* and *min* as red and blue curves), and the difference between them (i.e., $Max - min$ as green curve). The displacement range is shown on the left vertical axis during the test for specimen PC16 ($\alpha = 120^o$) and the *Max* and *min* values were represented in Fig. 7.13, by subtracting them from the mean value, i.e. $(Max + min)/2$ of the first cycle.

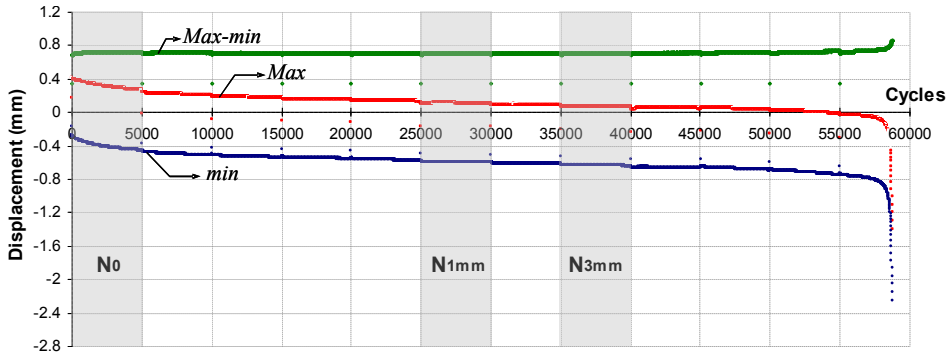

Fig. 7.12 – Cross head position during the test for PC16 ($\alpha = 120^{o}$).

The visual data in Fig. 7.8 shows that the crack exceeded 3 mm by 37500 cycles for specimen PC16 (Fig. 7.12), so this would imply that compliance change is not a very satisfactory way to detect local fatigue damage up to 3 mm. Consequently, the crosshead data can be considered as a poor indicator for failure initiation and progression.

7.4 Additional analyses

Once the failure path was identified, it was possible to compare the numerical analyses of the stress state presented in Chapter 6 (Fig. 6.12, Fig. 6.13 and Appendix C) with the failure pattern observed in Fig. 7.8.

Knowing the principal stress σ_1 for the case in which $\alpha = 13^{o}$ (Fig. 6.12) and that the failure (Fig. 7.7 a) occurred very close to

the horizontal CFRP-Adhesive edge, and by comparing the results in Fig. 6.12 with the ones shown in Fig. 6.10 c, it may be seen that the maximum circumferential stress ($\sigma_\theta \cong 57\ MPa$) and the maximum shear stress ($|\sigma_{r\theta}| \cong 209\ MPa$) also occur close to this edge, when observing only results by the side of the adhesive ($90^o \le \alpha \le 360^o$ range) for $r = 0.0010583\ mm$. This suggests that σ_θ and $\sigma_{r\theta}$ could be related to the failure mechanism for this specimen. Note that for $\alpha = 13^o$, K_1 is dominant and $K_2 \approx 0$.

Following this reasoning, σ_1 for the case in which $\alpha = 60^o$, in Fig. 6.13 shows that the failure is prone to occur very close to the vertical CFRP-Adhesive edge. By comparing the results in Fig. 6.13 with the ones shown in Fig. 6.11 c, d and e, the shear stress seems most likely to be the responsible for the failure, once the radial and circumferential stresses are in compression along the adhesive sector ($90^o \le \alpha \le 360^o$). The maximum shear stress occurs close to the vertical CFRP-Adhesive interface, in which the value is $|\sigma_{r\theta}| \cong 95\ MPa$. This suggests that $\sigma_{r\theta}$ could be related to the failure mechanism for this specimen ($\alpha = 60^o$, K_2 is dominant and $K_1 \approx 0$), despite the fact that in the experiments the fatigue under the level of loading was not able to initiate the failure of the specimens PC7, PC8 and PC9.

By comparing Fig. B.1 up to Fig. B.7 (Appendix B) and C.1 up to C.7 (Appendix C), it may also be seen that the observed failure in experiments (Fig. 7.8) corroborates the stress state for each case of α. This information can be used for future works as monitoring the crack initiation and progression under static load as well for the correct positioning the SG in the specimens.

Based on the aspect of the failure presented in Fig. 7.5 for the case of $\alpha = 120^{o}$ and keeping in mind that according to Fig. 6.9 the GSIF of the DLJ under study is situated reasonably close to the GSIF of the BT configuration when $\alpha = 125^{o}$, the following qualitative development can be taken.

Fig. 7.13 shows that the photographs of the PC16, PC17 and PC18 (loaded under $\alpha = 120^{o}$) have very similar pattern of failure to that presented by Barroso (2007) for the same DLJ under study. The 30º angle from the CFRP-Adhesive is indicated in each specimen for reference. Failure presents a trend; following approximately the imaginary line rotated 30º from the CFRP-Adhesive interface, i. e., the direction of the spew fillet of the adhesive according to an angle of approximately 30º. As can be seen, the BT specimens in Fig. 7.13 present a similar pattern, indicating that the analogy with the BT specimens can be taken for comprehension of the failure path of the real DLJ.

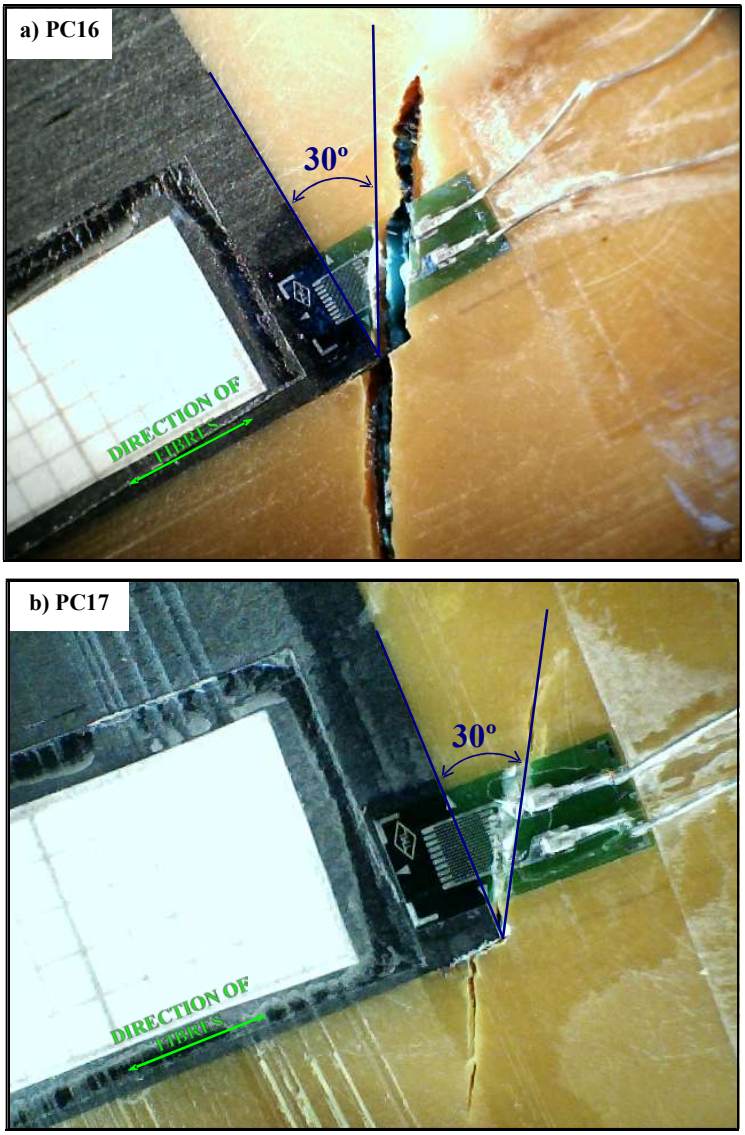
a) PC16
30º
DIRECTION OF FIBRES
b) PC17
30º
DIRECTION OF FIBRES

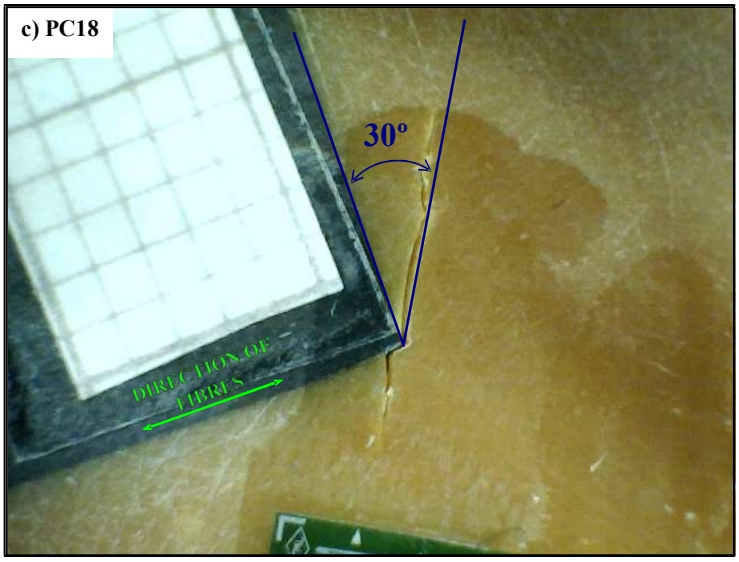

Fig. 7.13 – Failure path presented in the BT specimens ($\alpha = 120º$).

To reinforce this analogy, the triaxial stress state (see Fig. 3.15 and Fig. C.5 in Appendix C) for both types of specimen is present at the vertical CFRP-Adhesive surface, the position in which the failure is prone to start (by just verifying that σ_1 is maximum at this interface).

Fig. 7.14 presents a scheme of the evolution of failure in the DLJ, based on the analogy of the BT specimens loaded diametrically in $\alpha = 120º$. In the first stage (Fig. 7.14 a), a very small crack arises in the vertical CFRP-Adhesive interface. Next, the small crack opens in an angle of approximately 30º from the vertical CFRP-Adhesive interface and, almost simultaneously, another small crack in the horizontal CFRP-Adhesive interface

arises (Fig. 7.14 b). The 30º angled crack grows increasingly following approximately the same direction, while the horizontal small crack starts to develop along the aligned direction to the other 30º angled crack, as indicated in Fig. 7.14 c. From this point it is supposed that both cracks grow approximately together until the first touches and emerges from the adhesive spew fillet, while the other needs to run along the entire overlap until it meets another crack, which is not indicated in the schemes of Fig. 7.14. This seems to be feasible and in agreement with the studies of Shenoy et al. (2009), who present experimental evidence of the progression of failure in the joint. Still it is important to bear in mind that these schemes are not to scale, because the relationship between the both problems is not the subject of the current study. The scale effect is an important aspect to consider and in the last chapter of this work it is suggested as future development. A brief discussion is presented in Barroso et al. (2012[B]) and Vicentini et al. (2012[A]).

Fig. 7.15 shows a schematic representation of the crack/damage path after failure for some specimens tested under fatigue loading. For clarification, the direction of the first failure is indicated in a bigger scheme than that in Fig. 7.8. In particular, Fig. 7.15 shows the cases of $\alpha = 13º$, $\alpha = 30º$, $\alpha = 90º$, $\alpha = 115º$ $\alpha = 120º$, $\alpha = 143º$ and $\alpha = 150º$, respectively. The group

of specimens with $\alpha = 60^{o}$ is not presented in Fig. 7.15 because these specimens did not present any visible failure.

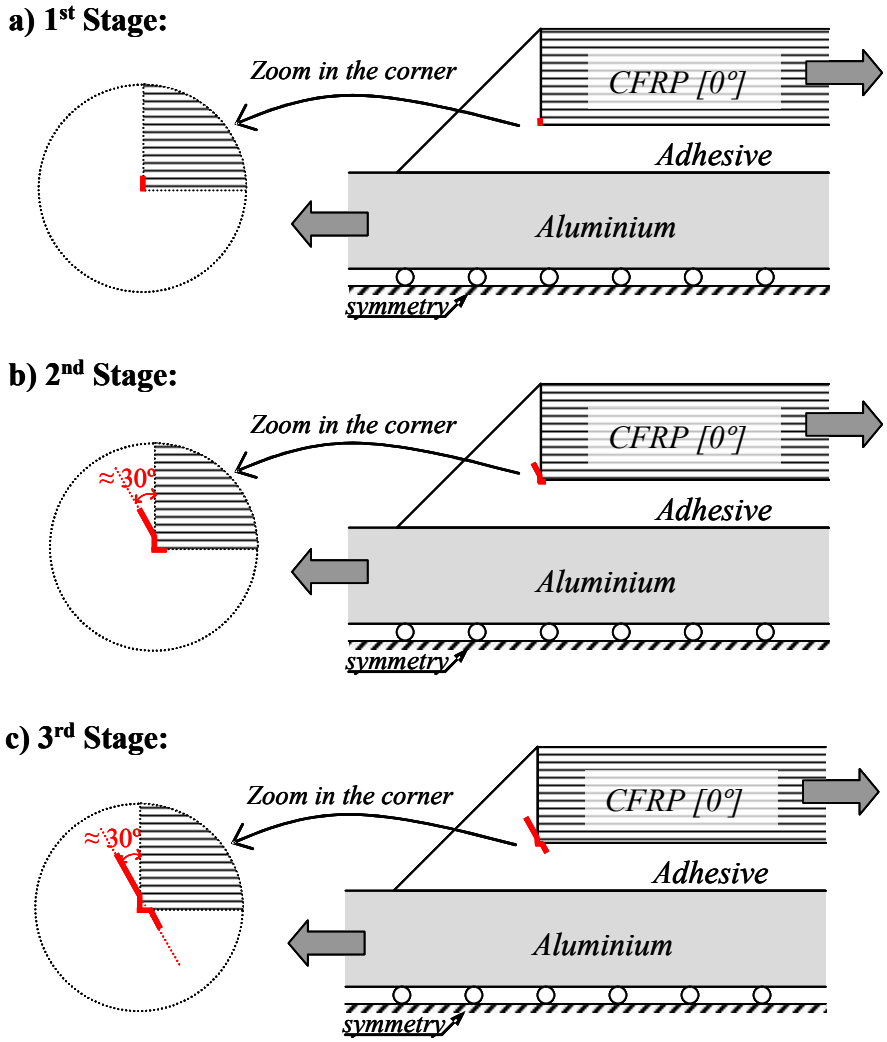

Fig. 7.14 – Qualitative evolution of the failure in the DLJ.

$\alpha = 13^{o}$

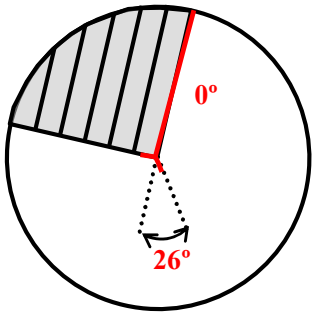

$\alpha = 30^{o}$

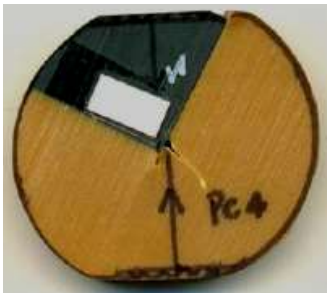

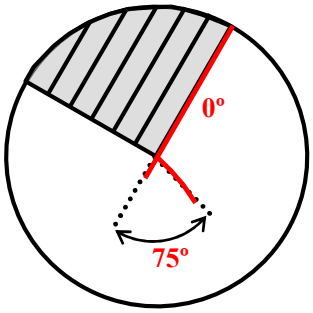

$\alpha = 90^{o}$

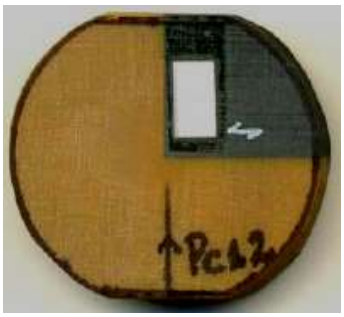

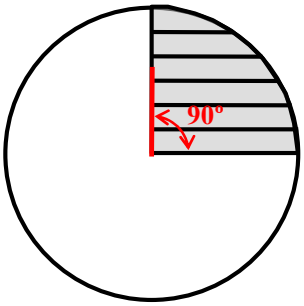

$\alpha = 115^{\circ}$

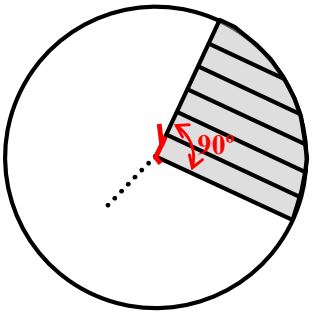

$\alpha = 120^{\circ}$

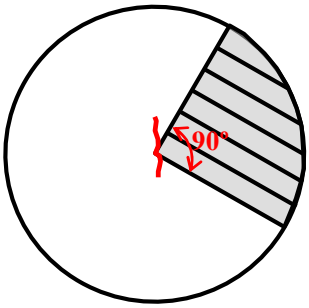

$\alpha = 143^{\circ}$

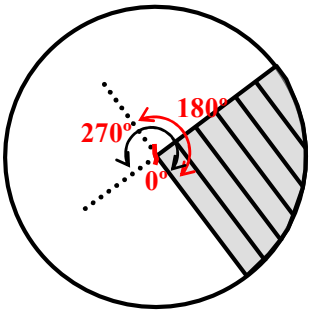

$\alpha = 150^{\circ}$

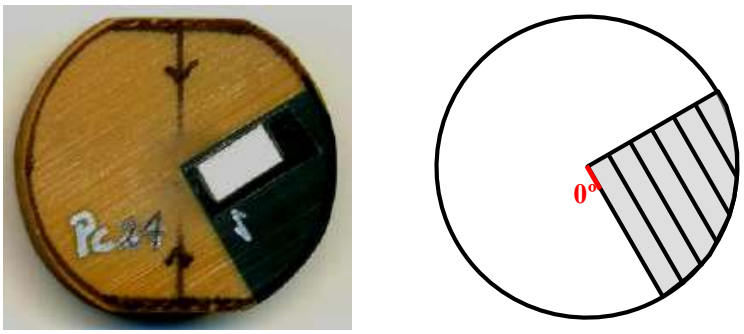

Fig. 7.15 – Tested samples and scheme of the failure path observed (fatigue loading).

The failure started at the corner tip for all specimens. When the first photograph was taken, i.e. after 5000 cycles or less, in the cases in which the fast failure occurred as defined previously, there was a crack along the CFRP-adhesive interface (in 0º or 90º according to the schemes). Similarities between Fig. 7.15 (BT under fatigue loading) and Fig. 6.24 (BT under static loading) are evident, being an indication that probably plasticity is not significantly affecting the local stress state of the corner and the failure mechanism.

7.5 Discussion

In this chapter, Brazilian disk specimens having a bimaterial closed corner at the centre of the disk were tested under fatigue load at different diametral compression angles. Video cameras,

SG and photographs were used for monitoring the crack initiation and progression in the closed corner for the specimens.

Under static load condition these specimens were successfully used for failure prediction in adhesive DLJ (Chapter 6). The tests in the present chapter allowed the complete mapping of the initiation and progression of the damage or crack in such bimaterial corner configuration.

In previous analyses (Chapter 6) under static load the failure observed was sometimes very sudden, with a brittle behaviour; it was not possible to verify experimentally that the failure really started at the corner tip. Thus, one of the main conclusions/contributions of this work is that it has been verified experimentally that the failure started at the corner tip, for all specimens where failure was observed, corroborating and validating previous analyses and other theoretical studies.

All specimens tested with the same angle presented similar failure mechanisms, although different angles gave rise to distinct failure mechanisms. The data from the fatigue testing were classified according to the number of cycles to reach the final failure (associated with a 3 mm crack length). It was observed that for all cases the failure initiation occurred along one of the CFRP-adhesive interfaces, an indication that the interface most aligned to the load is prone to initiate the failure. The failure path direction was not influenced by the lack of

symmetry, since it was observed that the failure always started at one of the CFRP-adhesive interfaces.

The development of the failure observed in the experiments can be summarized in three main stages: 1) Initiation at the corner tip, where whitening, damage or a visual crack arose; 2) Propagation, along the interface that could go simultaneously or independently through the adhesive, depending on the load angle; 3) Final failure of the component (3 mm crack length).

The group of specimens with $\alpha = 60^o$ did not show any visible failure. This fact, together with the retarded failure observed in the specimen with $\alpha = 143^o$ (angles 60º and 143º, where $K_1 \cong 0$), suggests that K_1 drives the fatigue failure. Thus, fatigue life diminishes drastically when approaching angles with significant K_1 values associated, Figs. 6.9 and 7.10.

Additionally, the failure path observed from static (Fig. 6.24) and fatigue tests (Fig. 7.15) is practically the same, indicating that if there is plasticity involved, it probably does not significantly affect the local stress state.

The study carried out corresponds to a critical point for the prediction of failure in the most commonly found bimaterial corner in structural adhesive joints. This study can be easily extended to other corner configurations also present in adhesive joints.

Chapter

8 Conclusions and future developments

In this chapter, the main conclusions of the Thesis will be summarized. A chronological sequence has been followed to present the most important achievements. Also some ongoing work and future developments will be outlined.

8.1 Conclusions

The present work has presented different aspects of the stress and failure analysis of an adhesive joint between CFRP and aluminium as adherends.

The complexity of the stress state that appears in the corners of adhesive joints is mainly due to the presence of stress singularities. This work has enabled increased understanding of mechanisms related to the failure of multimaterial corners that can be found in typical adhesive joints in industry.

As mentioned previously, the main conclusions obtained in the work will be presented chronologically. The starting point of the present Thesis was the need to close a certain number of open questions from previous works.

In this sense, the first task carried out was to validate the 2D results. The 3D edge effects were never taken into account in previous works of the research group (GERM) and a 3D model was built accordingly.

1. The comparison of the results of the 3D and 2D models showed that the 3D edge effects were located at a very short distance of the free lateral edge and the stress state at this free edge was, for the particular configuration under analysis, less severe than that obtained with the 2D models.

A second open question was the validity of the linear elastic behaviour at the neighbourhood of the corner tip. Thus, different yielding models were analyzed to see the influence of the local plasticity effects.

2. The results of the different models incorporating plasticity effects showed that although plasticity takes place at a neighbourhood of the corner tip, its extension is restricted to a very close area of the corner tip.

A final open point was the influence of neglecting the stresses appearing during the curing process. The origin of curing stresses involves different complex process. Only the thermal effects due to the cooling step, from the curing temperature to room temperature, were analyzed in this Thesis.

3. The main conclusion regarding this point is that, although thermal effects have a very strong influence on the nominal stress state, no experimental evidence of influence of curing stresses was found when including temperature. The failure path was unaltered when testing at different temperatures and at different times from the end of manufacturing. This leads to assume a relaxation effect in the nominal singular curing stress state, a question already mentioned by other authors.

After validating these open points, some aspects regarding the manufacturing process were studied. In previous studies of the group, only the HPP was available to cure the specimens. Afterwards, an AC was also available as a curing procedure. Due to the differences between both methods, a study was carried out to see the influence of these two curing procedures on the mechanical response and failure of the adhesive joints.

4. Joints manufactured by AC had mechanical properties better than those manufactured by HPP, with an increase of 25% and 40% in the strength and fatigue life of the tested specimens, respectively. Neither the usual standards nor the adhesive manufacturer's data sheet specify which technique is more appropriate. Furthermore, the failure path was not significantly affected by the manufacturing procedures.

Once all open points were clarified and the influence of different curing procedures was checked, a new procedure for the evaluation of the generalized fracture toughness in closed multimaterial corners was attempted. A numerical study and an experimental program were carried out giving rise to the definition of a new failure proposal based on critical values of the generalized stress intensity factors at the corner tip.

5. A new test definition was proposed based on the configuration of the Brazilian disk specimen and a failure envelope was obtained. This allows the failure envelop of closed corners in terms of GSIF to be defined. The failure envelope generated has been proved to agree very well with previous published results of CFRP-Al DLJ.

The possibility of performing the same test using fatigue loading instead of static loading, made possible to reduce any uncertainty about the local yielding effects and the failure sequence. As the main conclusions of these new experiments:

6. Failure was checked to start always at the corner tip (in some static tests where failure was brittle, this was not possible to check) and K_1 term was dominant in fatigue failure.
7. The failure path in the fatigue test had almost the same orientation than those obtained in the static tests. This

fact supports that the local singular stress state controls failure in both situations and yielding effect are not influencing failure onset.

If only one had to be chosen, the main contribution of this Thesis has been the proposal of a failure criterion, together with a new testing procedure to obtain the generalized fracture toughness for multimaterial corners. Additionally, this work has contributed to the study of other important aspects for improving the knowledge of performance of adhesive joints.

In all chapters where experiments were carried out, the results were consistent and presented small scatter.

From a more generic point of view of multimaterial corners, the subjects studied in this work may also be extended to improve the understanding of stress states in closed corners in general.

8.2 Future developments

The work carried out and presented in this Thesis is not by any means complete. On the contrary, the subjects developed here require further exploration; some aspects in particular deserve more attention. For example, adhesive characterization would need detailed study, in order to verify its properties under

temperature and fatigue experimentally. This would enable knowledge of more exact parameters for calibration of the models used here.

From experimental observations of the failure in the adhesive, as shown for example, in Fig. 6.24, a cohesive model could be very suitable and reliable for simulation of this material, so the inclusion of this type of behaviour is suggested for future work.

Also the failure onset at the singular point should be explored by means of the approach of Finite Fracture Mechanics, which has given reliable results in similar problems where a finite damage has to appear from a singularity point.

The author is aware of the importance of the size effect. Citing Bažant (2001): *"Scaling is the most fundamental characteristic of any physical theory"*. Consequently, a further study is desirable of the scale effect between the DLJ and different dimensions of the BT specimen in order to quantify how this may affect the experimental results.

The adopted linear elastic model for temperature might be insufficient to represent and identify the complex behaviour of the adhesive during the cure cycling. It is suggested to explore the use of a viscoelastic model for the simulation of the curing effect, as well as to explore other complex phenomena giving rise to curing stresses (chemical shrinkage for example).

It is suggested that the proposed criterion and testing procedure in Chapter 6 could be applied to other configurations in which the failure is expected, applying the criterion for real structures. In addition, the comparison between the BT and another method of testing would be very interesting for acquisition of critical GSIF. A factor for correction may be necessary, as for the original Brazilian Test.

A further interesting line of research may be the search for other geometries, load and boundary conditions in real specimens, whose GSIF could fall in the other quadrants of the failure envelope.

Programming an automatic and user friendly interface for distribution and computing of the GSIF and shape functions for all types of multimaterial corners would be very useful and encourage widespread use of the procedure.

By analogy, the proposed methodology for testing and acquisition of the GSIF could be possibly extended to opened corners, under certain requirements. Thus, the proposals of modifications are also suggested.

Once the fatigue behaviour of the BT specimens is known, the tests carried out in Chapter 7 could be repeated, but optimizing the number of photographs taken with the shortest cycling period, for example at every 500 or 1000 cycles, in order to catch more precise data for specimens which exhibited brittle failure.

Another interesting analysis would be to build an equivalent Paris' law for fatigue in BT specimens, i.e., the crack growth curve for the bimaterial corner under study. The experimental data for crack initiation and progression are already given in Chapter 7, and further work would involve the updating of the GSIF for every stage of the crack growth.

Appendix

A Analytical expressions in adhesive bonded joints

In this appendix, some expressions of main analytical models of adhesively bonded joints are presented. These expressions where referred in Chapter 2. The symbols presented here are not specified in the List of symbols and abbreviations, since they are only showed as additional information.

A.1 Volkersen model

For an origin coordinate system located in the middle of the overlap, being the x axis along the overlap, the adhesive shear stress distribution according to this model is given by:

$$\sigma_{x'y'} = \frac{P}{A_{lap}} f_V^1 + f_V^2 \tag{A.1}$$

where P is the applied load and $A_{lap} = w\, L_0$ is the overlap area (L_0 being the overlap length and w the joint width). The functions of Volkersen model are given by:

$$f_V^1 = \frac{c}{2}\frac{\cosh(cX)}{\sinh(c/2)} \text{ and } f_V^2 = \left(\frac{t_t - t_b}{t_t + t_b}\right)\frac{c}{2}\frac{\sinh(cX)}{\cosh(c/2)} \tag{A.2}$$

where $c=\sqrt{\left(1+\frac{t_t}{t_b}\right)\frac{G_a L_0^2}{E t_t t_a}}$ and $X=\frac{x}{L_0}$, for $-\frac{1}{2}\le X\le\frac{1}{2}$. t_t is the top adherend thickness, t_b is the bottom adherend thickness, E the adherend modulus (similar adherends must be used according to this model), G_a the adhesive shear modulus and t_a the adhesive thickness.

For more details regarding this model, see Volkersen (1938) and da Silva (2009[A,B]).

A.2 Goland and Reissner model

For an origin coordinate system located in the middle of the overlap, being the x axis along the overlap, the adhesive shear stress is given by:

$$\sigma_{x'y'}=\frac{P}{4L_0}f_{GR}^1 \tag{A.3}$$

where P is the applied tensile load per unit width and L_0 is the overlap length. The function f_{GR}^1 is given by:

$$f_{GR}^{1} = -\frac{\beta L_0 (1+3k)}{2t} \frac{\cosh\left[\left(\frac{\beta L_0}{2t}\right)\left(\frac{2x}{L_0}\right)\right]}{\sinh\left(\frac{\beta L_0}{2t}\right)} - 3 + k \qquad \text{(A.4)}$$

where t is the adherend thickness (must be equal), $\beta = \sqrt[2]{\frac{8G_a t}{Et_a}}$,

$k = \frac{\cosh\left(u_2 \frac{L_0}{2}\right)}{\cosh\left(u_2 \frac{L_0}{2}\right) + 2\sqrt{2}\sinh\left(u_2 \frac{L_0}{2}\right)}$ and $u_2 = \frac{1}{t}\sqrt{\frac{3(1-\nu^2)P}{2tE}}$.

The expression for the adhesive peel stress, according to their model, is given by:

$$\sigma_{y'} = \frac{4Pt}{L_0^2} f_{GR}^{2} \qquad \text{(A.5)}$$

The function f_{GR}^{2} is given by:

$$f_{GR}^{2} = \frac{1}{\Delta}\left\{\left[R_2\lambda^2\frac{k}{2} + \lambda k' \cosh(\lambda)\cos(\lambda)\right]\cosh\left(\frac{2\lambda x}{L_0}\right)\cos\left(\frac{2\lambda x}{L_0}\right) + \left[R_1\lambda^2\frac{k}{2} + \lambda k' \sinh(\lambda)\sin(\lambda)\right]\sinh\left(\frac{2\lambda x}{L_0}\right)\sin\left(\frac{2\lambda x}{L_0}\right)\right\} \qquad \text{(A.6)}$$

where $\lambda = \gamma \frac{L_0}{2t}$, $\gamma = \sqrt[4]{6\frac{E_a t}{E t_a}}$ and E_a is the adhesive Young's modulus. The other parameters are: $k' = \frac{kL_0}{2t}\sqrt{3\left(1-\nu^2\right)\frac{P}{tE}}$, $R_1 = cosh(\lambda)sin(\lambda) + sinh(\lambda)cos(\lambda)$, $R_2 = sinh(\lambda)cos(\lambda) - cosh(\lambda)sin(\lambda)$ and $\Delta = \frac{1}{2}(sinh 2\lambda + sin 2\lambda)$.

For more details regarding this model, see Goland & Reissner (1944) and da Silva (2009[A,B]).

A.3 Hart-Smith model

For an origin coordinate system located in the middle of the joint, being the x axis along the overlap, the adhesive shear stress for DLJ with dissimilar adherends is given by:

$$\sigma_{x'y'} = f_{HS}^1 + f_{HS}^2 \tag{A.7}$$

where the functions of this model are given by:

$$f_{HS}^1 = A\,sinh(\lambda x) \text{ and } f_{HS}^2 = B\,cosh(\lambda x) \tag{A.8}$$

The coefficients of these functions are:

$$A=\frac{\frac{P}{2L_0}\left(\frac{\lambda L_0}{2}\right)\left(1-\frac{E_i t_i}{2E_0 t_0}\right)}{cosh\left(\frac{\lambda L_0}{2}\right)\left(1+\frac{E_i t_i}{2E_0 t_0}\right)},\ B=\frac{\frac{P}{2L_0}\left(\frac{\lambda L_0}{2}\right)}{sinh\left(\frac{\lambda L_0}{2}\right)}. \tag{A.9}$$

where $\lambda=\sqrt{\frac{G_a}{t_a}\left(\frac{1}{E_0 t_0}+\frac{2}{E_i t_i}\right)}$. The adhesive shear modulus and thickness are represented by G_a and t_a, respectively. $E_0 t_0$ and $E_i t_i$ are the outer and inner adherend stiffness, respectively.

For more details regarding this model, see Hart-Smith (1973[A,B,C], 1974) and da Silva (2009[A,B]).

A.4 Bigwood and Crocombe model

For an origin coordinate system located in the left end of the overlap, the adhesive shear stress (by the simplified analysis) according to this model, for dissimilar adherends is given by:

$$\sigma_{x'y'} = f_{BC}^1 + f_{BC}^2 + f_{BC}^3 \tag{A.10}$$

where the functions of this model are given by:

$$f_{BC}^1 = B_1\, cosh\left(K_6 x\right),\ f_{BC}^2 = B_2\, sinh\left(K_6 x\right),\ f_{BC}^3 = \frac{b_3}{L_0}-\frac{\left(b_2-b_1\right)}{K_6^2 L_0} \tag{A.11}$$

and $K_6 = \sqrt{\frac{4G_a}{t_a}\left[\frac{\left(1-\nu_1^2\right)}{E_1 t_1}+\frac{\left(1-\nu_2^2\right)}{E_2 t_2}\right]}$, with constants G_a, t_a being the shear modulus and thickness of the adhesive, respectively; E_1, ν_1 and t_1 are the Young modulus, Poisson ratio and thickness of the adherend 1, while E_2, ν_2 and t_2 are the analogous parameters for adherend 2.

The constants B_{1-2} and b_{1-3} which appear in functions (A.11) can be found in Bigwood & Crocombe (1989). Further expressions for peel stress, for full analysis and nonlinear model can also be found in Bidwood & Crocombe (1989, 1990).

Appendix

B FEM and series expansion results

The evolution of displacements and stresses (measured at the radius $r \cong 0.1\%\ R = 0.0010583\ mm$) for BT specimens loaded in different angles is presented below. In Fig. 6.9 and 6.10 in Chapter 6, the cases for $\alpha = 13^{o}$ and $\alpha = 60^{o}$ were already presented.

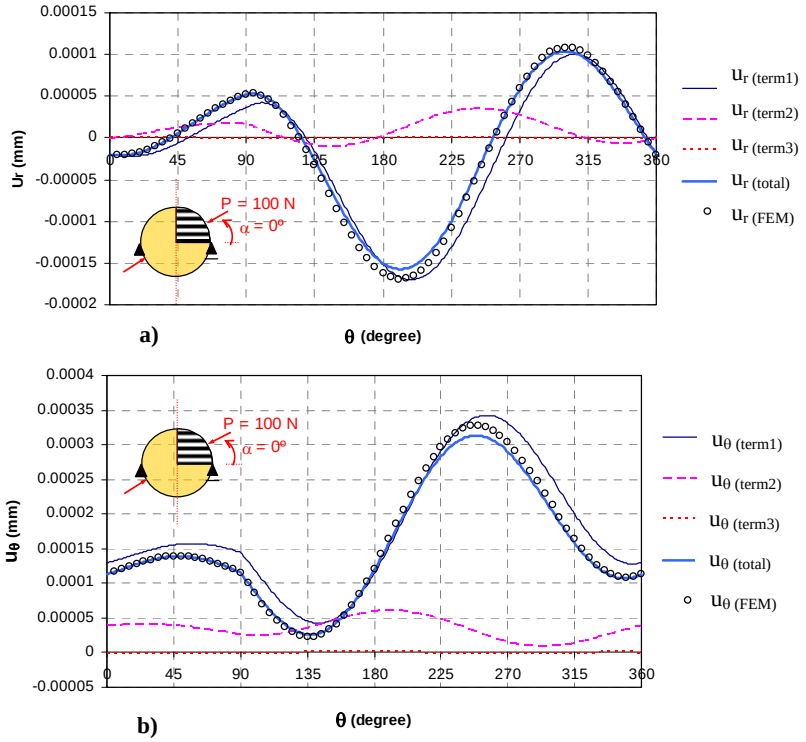

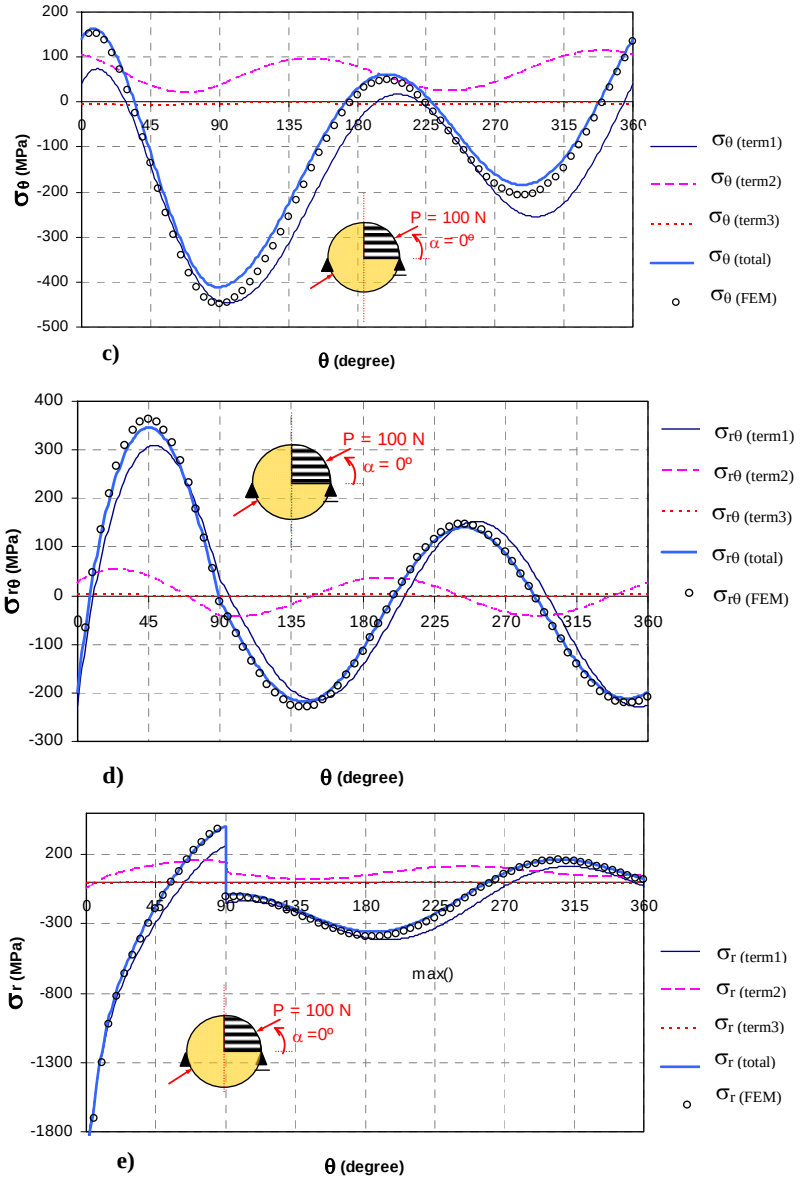

Fig. B.1 – a), b) displacements and c), d), e) stress components, for the case in which $\alpha = 0^{o}$.

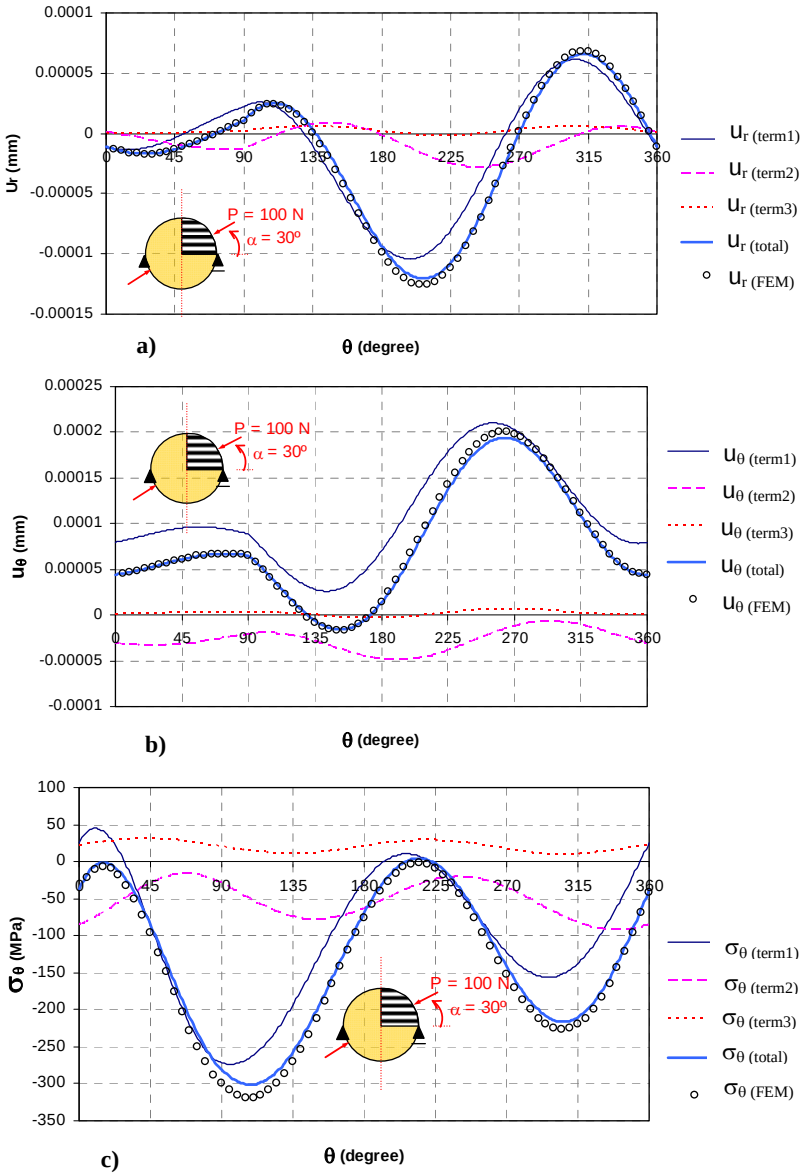
0.0001
0.00005
0
-0.00005
-0.0001
-0.00015
Ur (mm)
0
45
90
135
180
225
270
315
360
P = 100 N
α = 30º
ur (term1)
ur (term2)
ur (term3)
ur (total)
ur (FEM)
a)
θ (degree)
0.00025
0.0002
0.00015
0.0001
0.00005
0
-0.00005
-0.0001
uθ (mm)
P = 100 N
α = 30º
uθ (term1)
uθ (term2)
uθ (term3)
uθ (total)
uθ (FEM)
b)
θ (degree)
100
50
0
-50
-100
-150
-200
-250
-300
-350
σθ (MPa)
P = 100 N
α = 30º
σθ (term1)
σθ (term2)
σθ (term3)
σθ (total)
σθ (FEM)
c)
θ (degree)

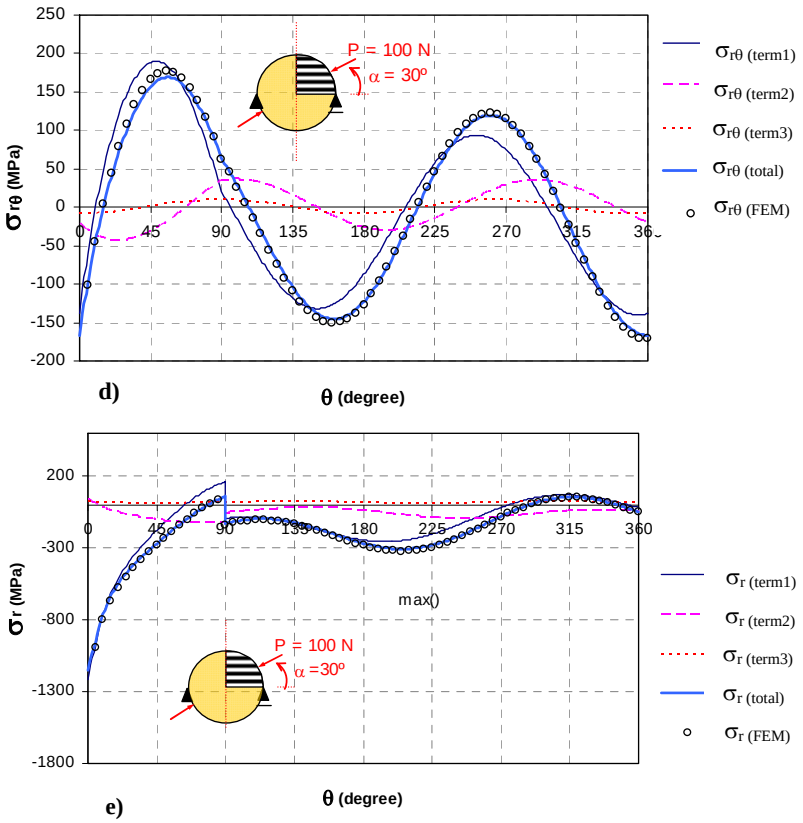

Fig. B.2 – a), b) displacements and c), d), e) stress components, for the case in which $\alpha = 30^{o}$.

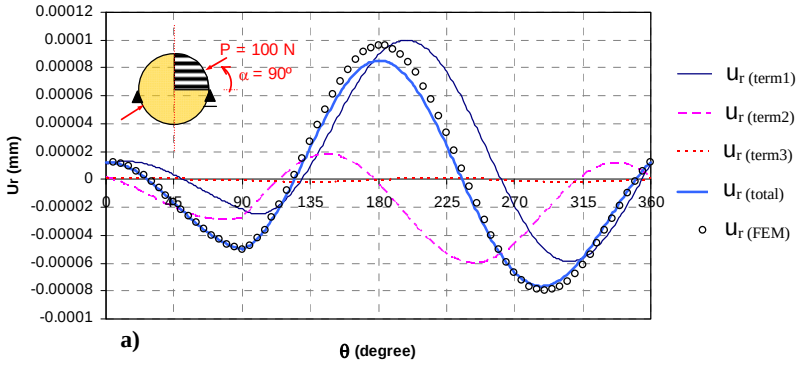
0.00012
0.0001
0.00008
0.00006
0.00004
0.00002
0
-0.00002
-0.00004
-0.00006
-0.00008
-0.0001
Ur (mm)
P = 100 N
α = 90º
0
45
90
135
180
225
270
315
360
θ (degree)
ur (term1)
ur (term2)
ur (term3)
ur (total)
ur (FEM)

a)

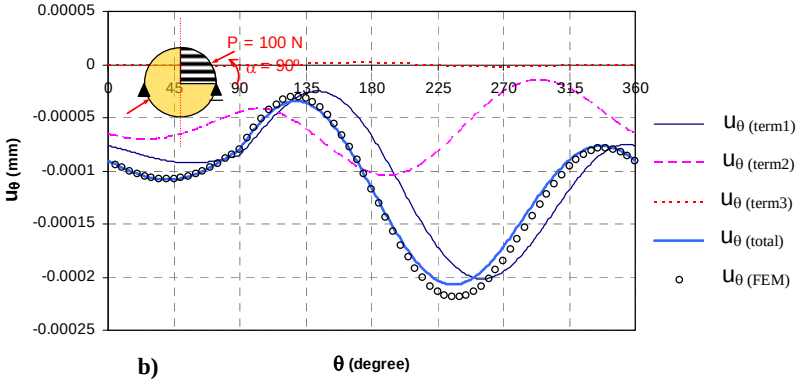
0.00005
0
-0.00005
-0.0001
-0.00015
-0.0002
-0.00025
Uθ (mm)
P = 100 N
α = 90º
0
45
90
135
180
225
270
315
360
θ (degree)
uθ (term1)
uθ (term2)
uθ (term3)
uθ (total)
uθ (FEM)

b)

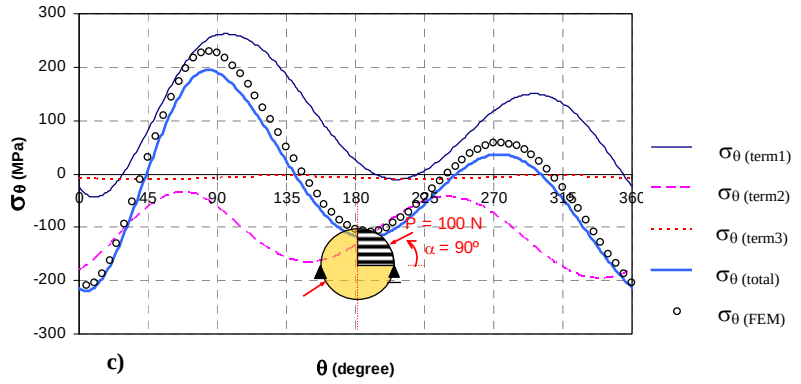
300
200
100
0
-100
-200
-300
σθ (MPa)
0
45
90
135
180
225
270
315
360
P = 100 N
α = 90º
θ (degree)
σθ (term1)
σθ (term2)
σθ (term3)
σθ (total)
σθ (FEM)

c)

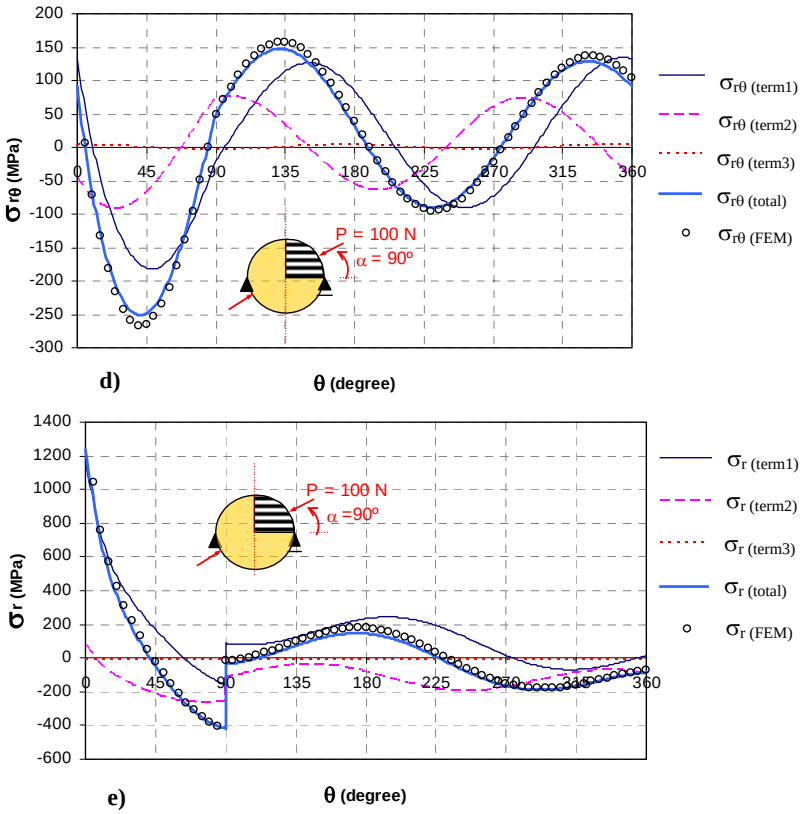

Fig. B.3 – a), b) displacements and c), d), e) stress components, for the case in which $\alpha = 90^{o}$.

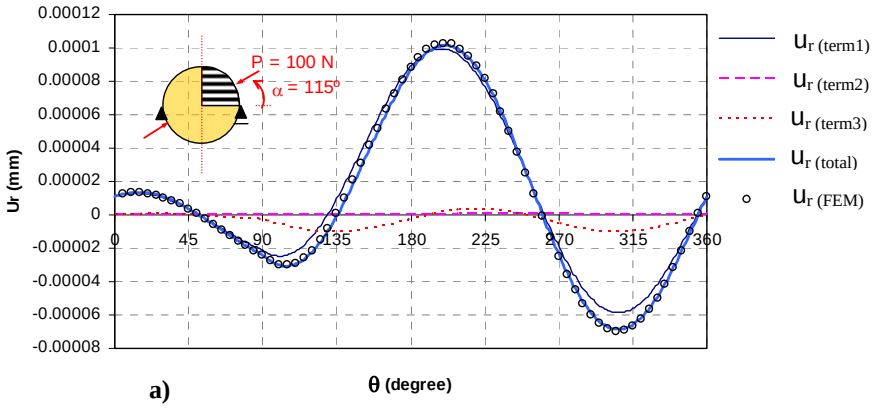
0.00012
0.0001
0.00008
0.00006
0.00004
0.00002
0
-0.00002
-0.00004
-0.00006
-0.00008
Ur (mm)
0
45
90
135
180
225
270
315
360
θ (degree)
P = 100 N
α = 115º
ur (term1)
ur (term2)
ur (term3)
ur (total)
ur (FEM)
a)

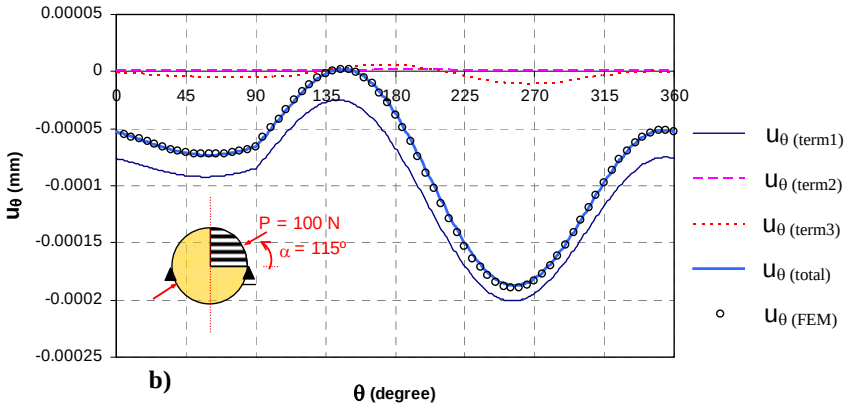
0.00005
0
-0.00005
-0.0001
-0.00015
-0.0002
-0.00025
uθ (mm)
0
45
90
135
180
225
270
315
360
θ (degree)
P = 100 N
α = 115º
uθ (term1)
uθ (term2)
uθ (term3)
uθ (total)
uθ (FEM)
b)

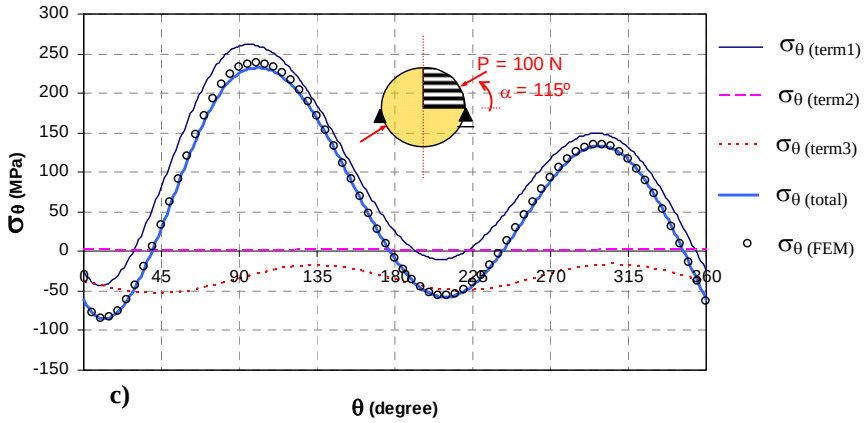
300
250
200
150
100
50
0
-50
-100
-150
σθ (MPa)
0
45
90
135
180
225
270
315
360
θ (degree)
P = 100 N
α = 115º
σθ (term1)
σθ (term2)
σθ (term3)
σθ (total)
σθ (FEM)
c)

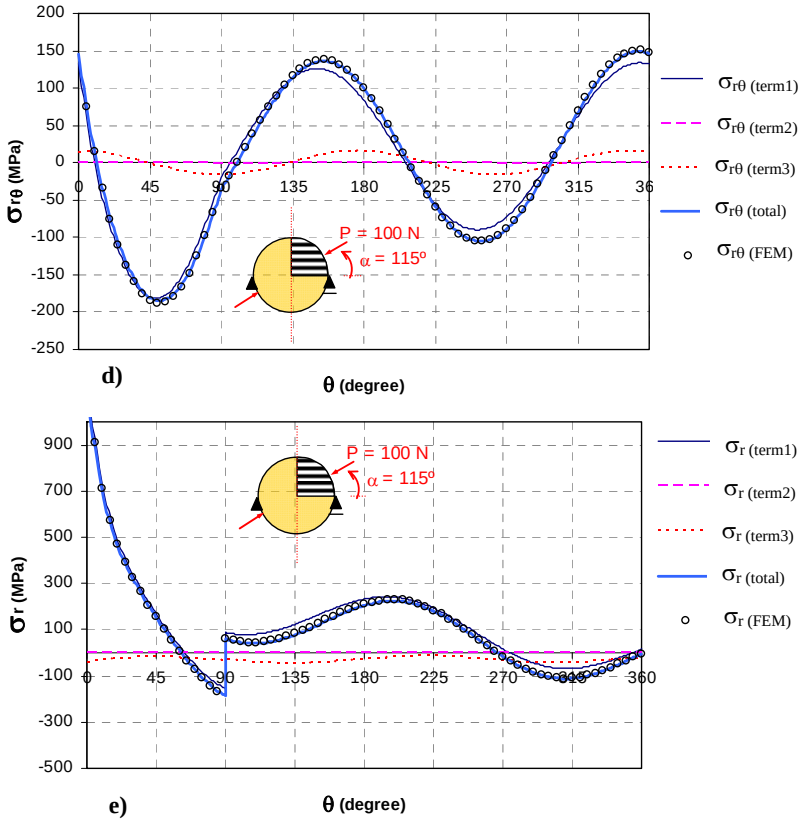

Fig. B.4 – a), b) displacements and c), d), e) stress components, for the case in which $\alpha = 115^{o}$.

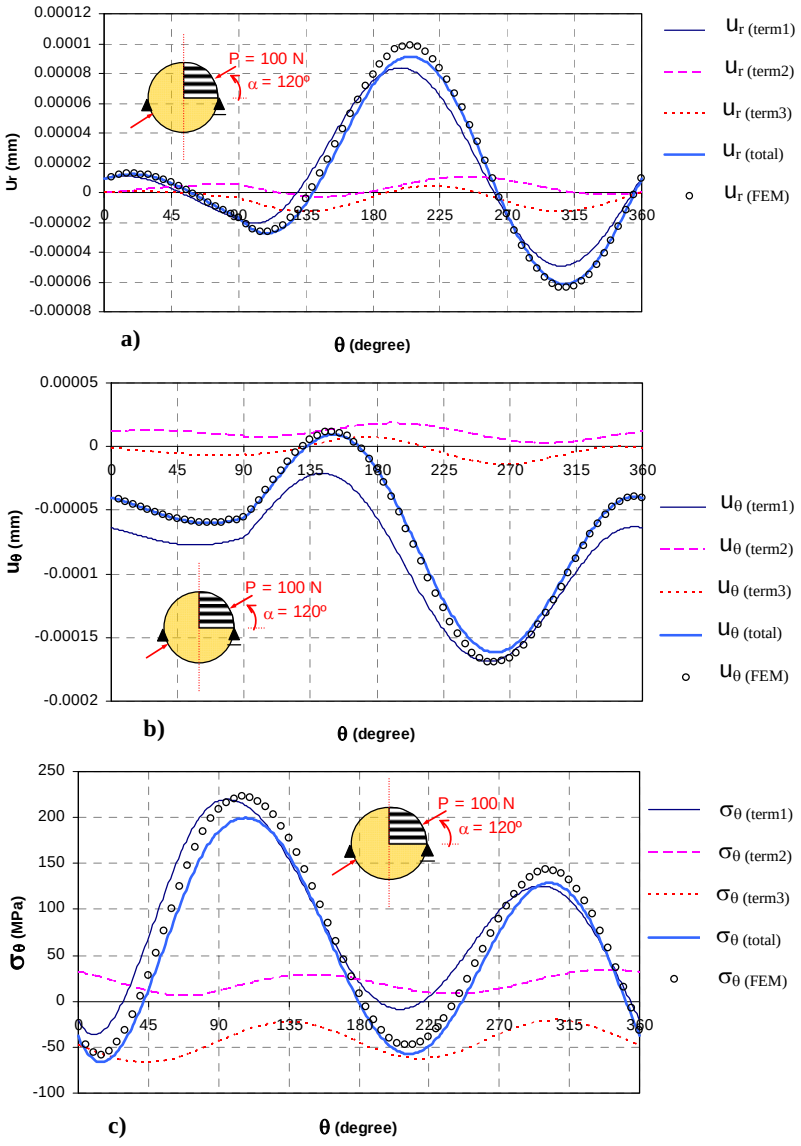
0.00012
0.0001
0.00008
0.00006
0.00004
0.00002
0
-0.00002
-0.00004
-0.00006
-0.00008
Ur (mm)
P = 100 N
α = 120º
0
45
90
135
180
225
270
315
360
θ (degree)
a)
ur (term1)
ur (term2)
ur (term3)
ur (total)
ur (FEM)
0.00005
0
-0.00005
-0.0001
-0.00015
-0.0002
uθ (mm)
P = 100 N
α = 120º
θ (degree)
b)
uθ (term1)
uθ (term2)
uθ (term3)
uθ (total)
uθ (FEM)
250
200
150
100
50
0
-50
-100
σθ (MPa)
P = 100 N
α = 120º
θ (degree)
c)
σθ (term1)
σθ (term2)
σθ (term3)
σθ (total)
σθ (FEM)

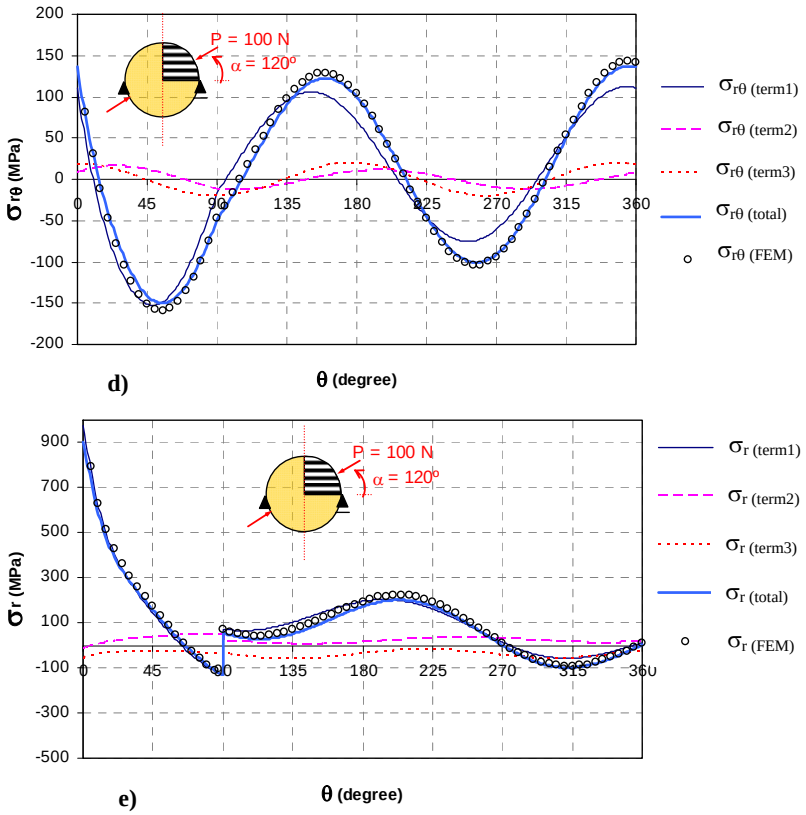

Fig. B.5 – a), b) displacements and c), d), e) stress components, for the case in which $\alpha = 120^{o}$.

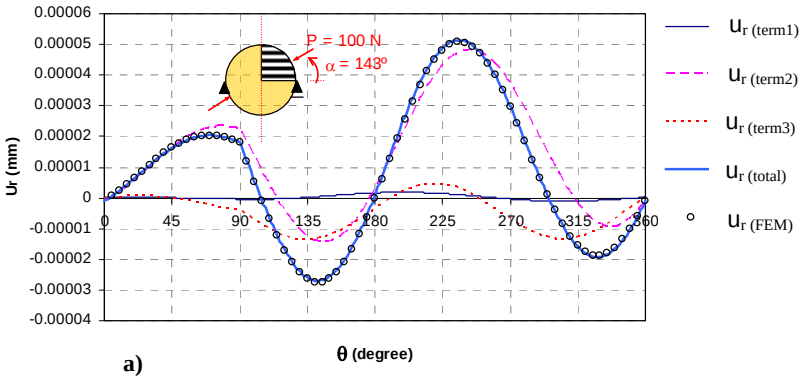
P = 100 N
α = 143º
Ur (mm)
θ (degree)
ur (term1)
ur (term2)
ur (term3)
ur (total)
ur (FEM)

a)

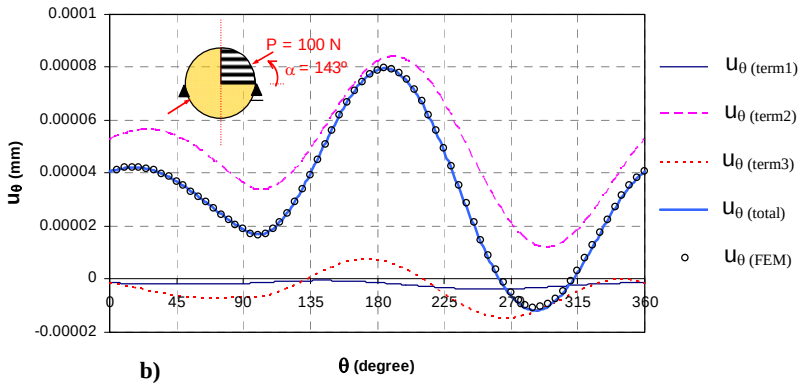
P = 100 N
α = 143º
Uθ (mm)
θ (degree)
uθ (term1)
uθ (term2)
uθ (term3)
uθ (total)
uθ (FEM)

b)

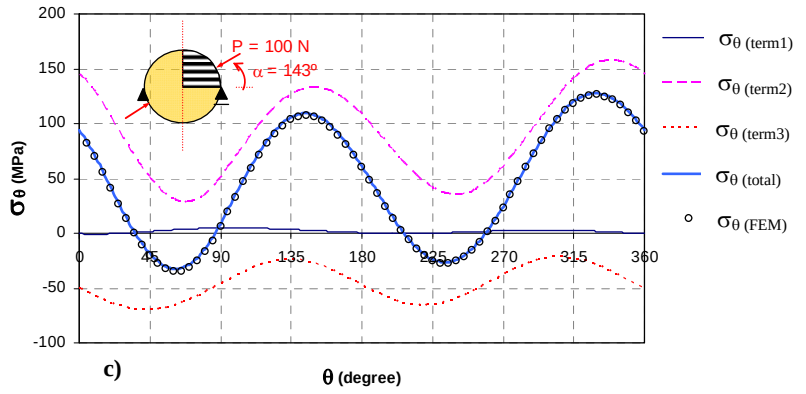
P = 100 N
α = 143º
σθ (MPa)
θ (degree)
σθ (term1)
σθ (term2)
σθ (term3)
σθ (total)
σθ (FEM)

c)

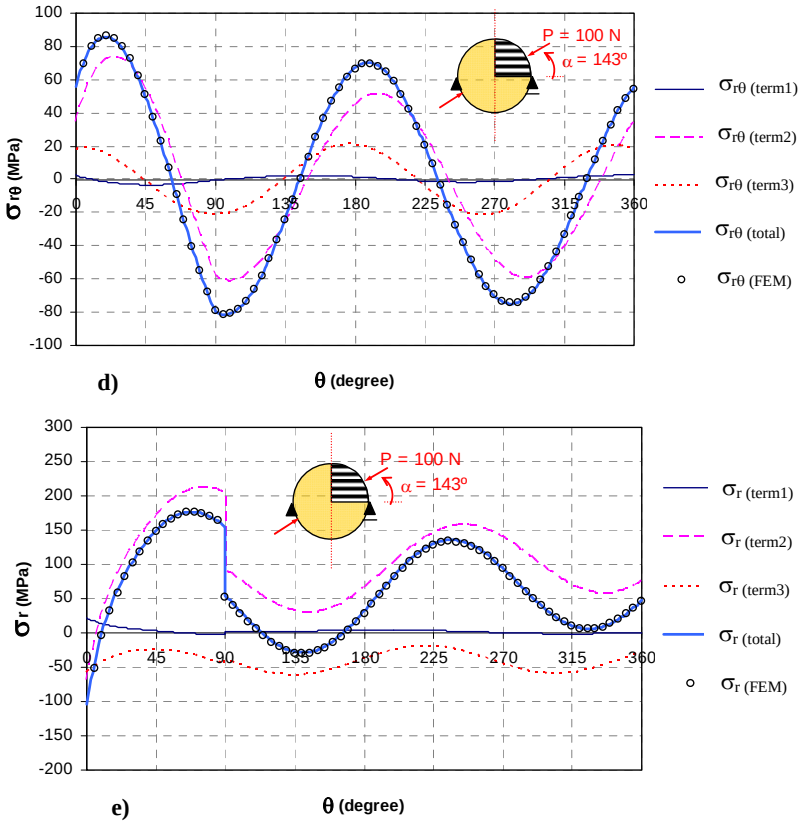

Fig. B.6 – a), b) displacements and c), d), e) stress components, for the case in which $\alpha = 143^{o}$.

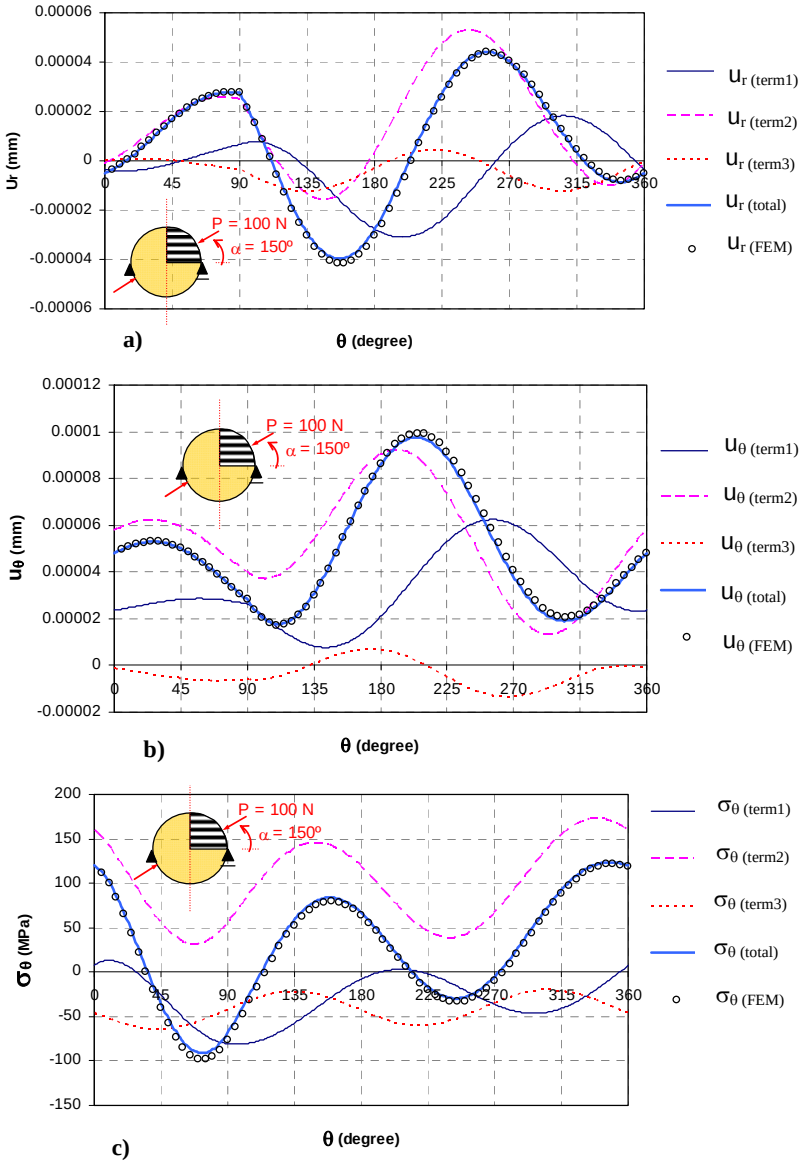
0.00006
0.00004
0.00002
0
-0.00002
-0.00004
-0.00006
Ur (mm)
0
45
90
135
180
225
270
315
360
P = 100 N
α = 150º
θ (degree)
ur (term1)
ur (term2)
ur (term3)
ur (total)
ur (FEM)
a)
0.00012
0.0001
0.00008
0.00006
0.00004
0.00002
0
-0.00002
uθ (mm)
P = 100 N
α = 150º
θ (degree)
uθ (term1)
uθ (term2)
uθ (term3)
uθ (total)
uθ (FEM)
b)
200
150
100
50
0
-50
-100
-150
σθ (MPa)
P = 100 N
α = 150º
θ (degree)
σθ (term1)
σθ (term2)
σθ (term3)
σθ (total)
σθ (FEM)
c)

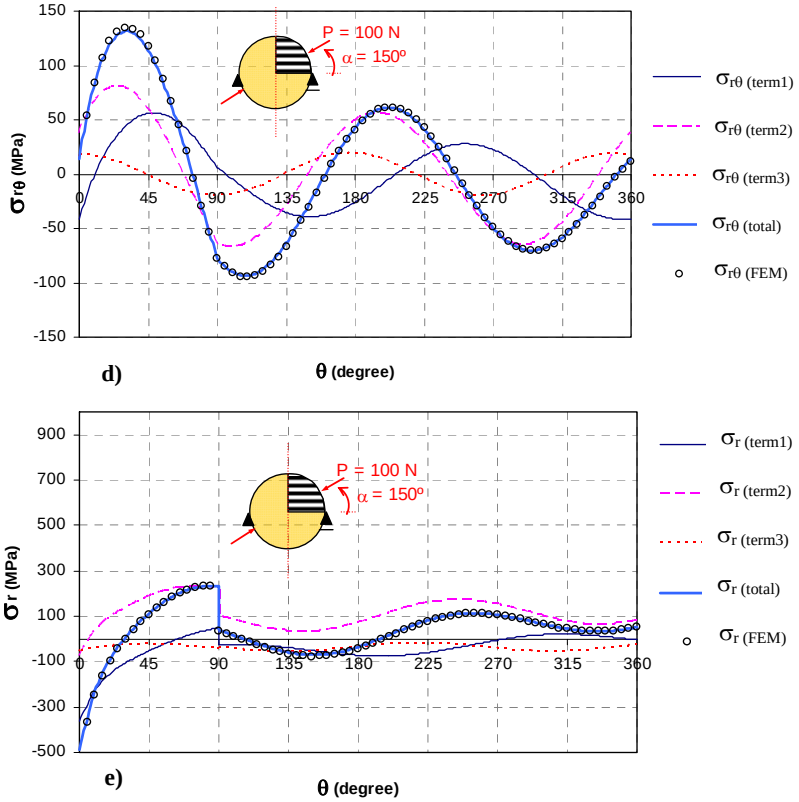

Fig. B.7 – a), b) displacements and c), d), e) stress components, for the case in which $\alpha = 150^{o}$.

Appendix

C Stress state in BT specimens

Figures from numerical study of the stress state are presented following, in order to complete the documentation. The cases in which $\alpha = 13^{o}$ and $\alpha = 60^{o}$ were already presented in Chapter 6 (Fig. 6.11 and 6.12 respectively).

Some observations and comments are presented at the end of this appendix. Point A is an arbitrary point localized closed to the critical surface (based on experimental evidences presented in Chapter 7, more specifically the Fig. 7.8), which r was approximately in the same order of the studied radius for the critical GSIF.

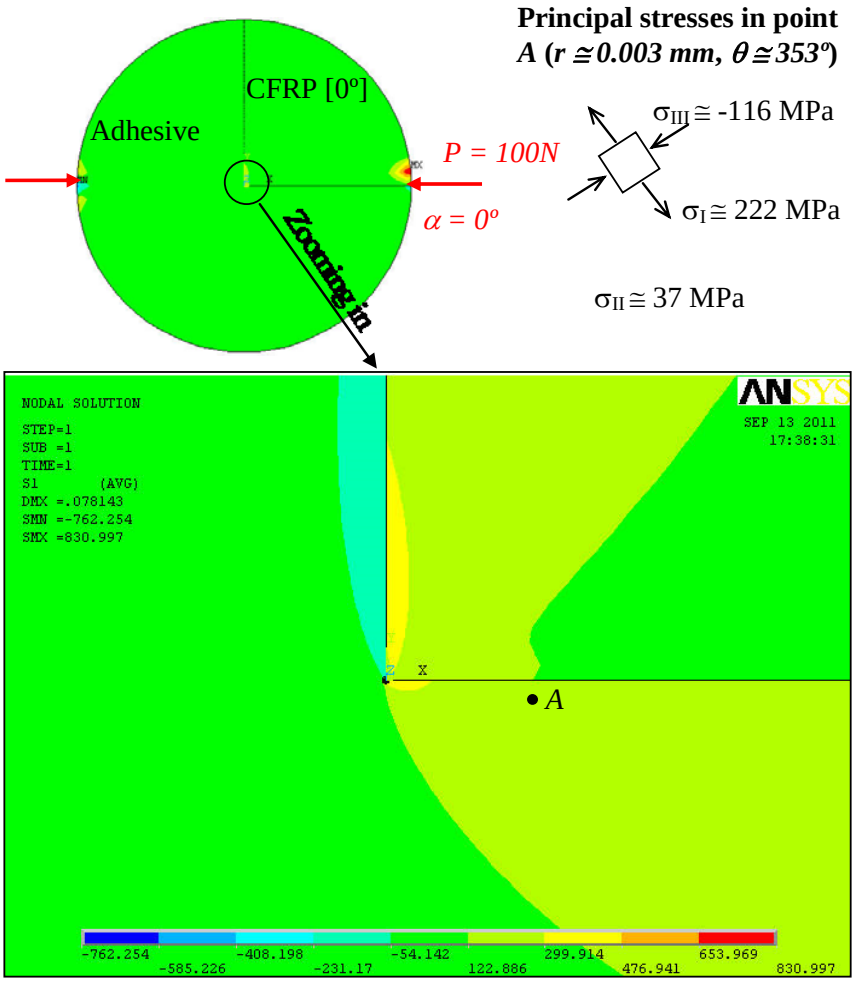

Fig. C.1 – Principal stresses at point A for $\alpha = 0^{o}$ and detail of σ_I.

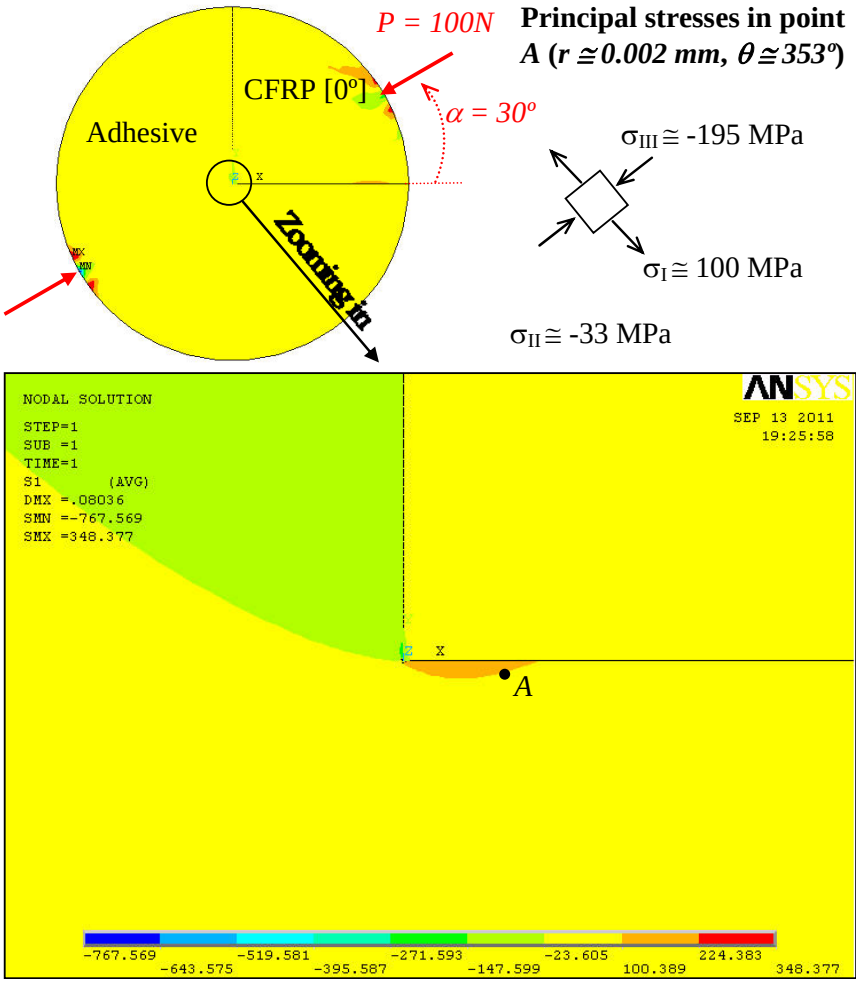

Fig. C.2 – Principal stresses at point A for $\alpha = 30^{o}$ and detail of σ_I.

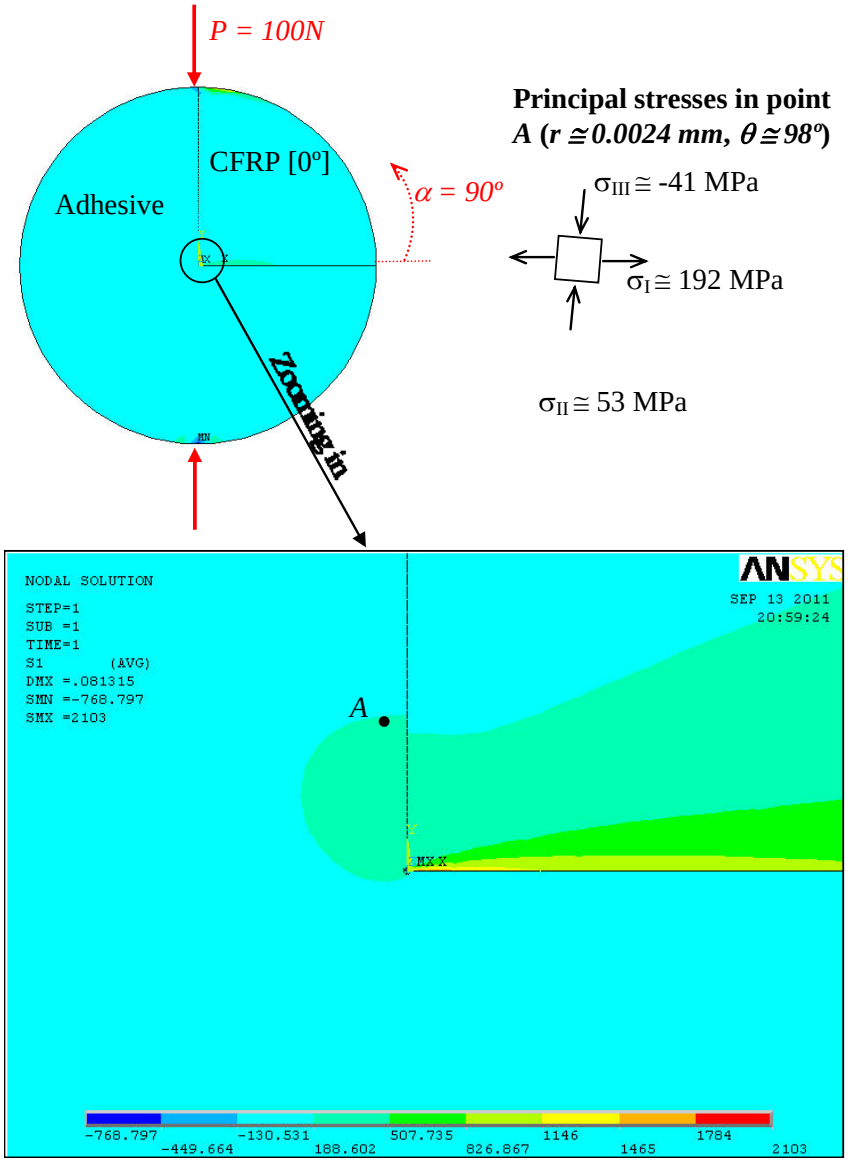

Fig. C.3 – Principal stresses at point A for $\alpha = 90^{o}$ and detail of σ_I.

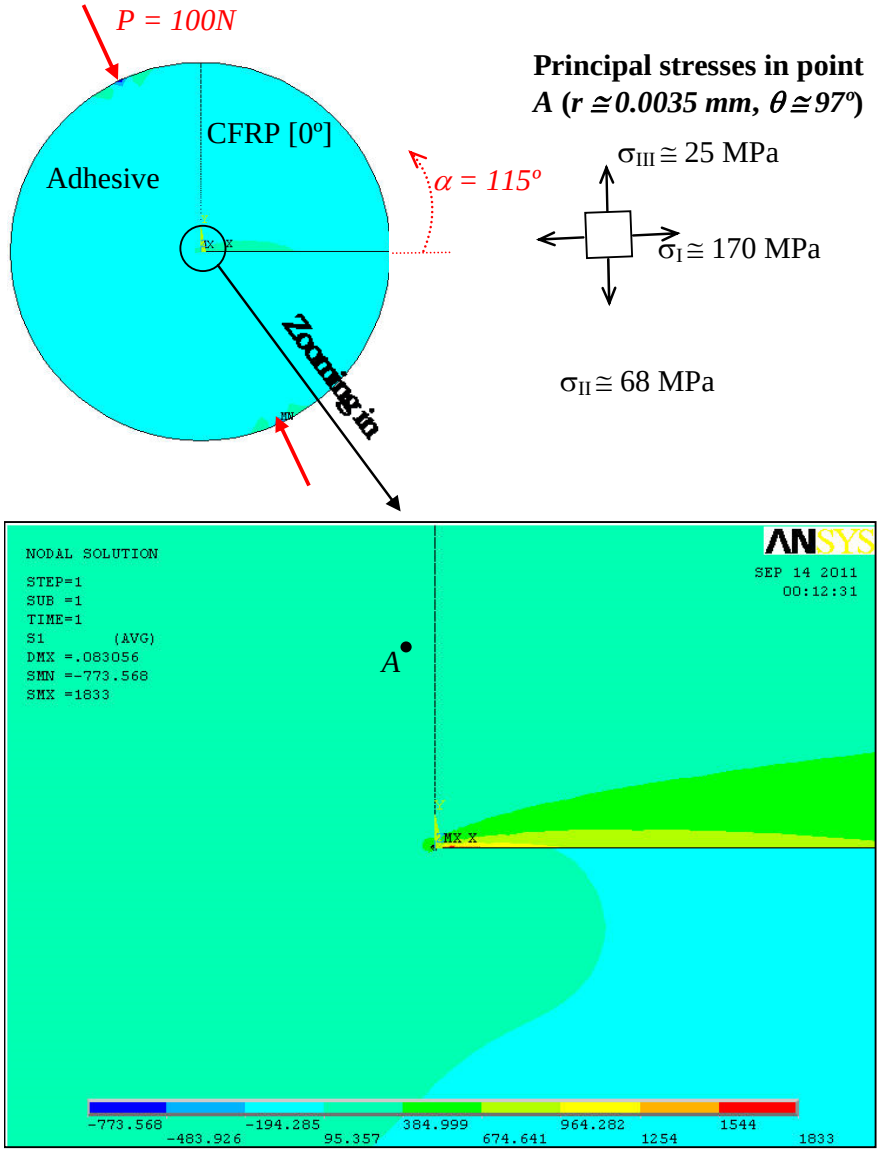

Fig. C.4 – Principal stresses at point A for $\alpha = 115^{o}$ and detail of σ_I.

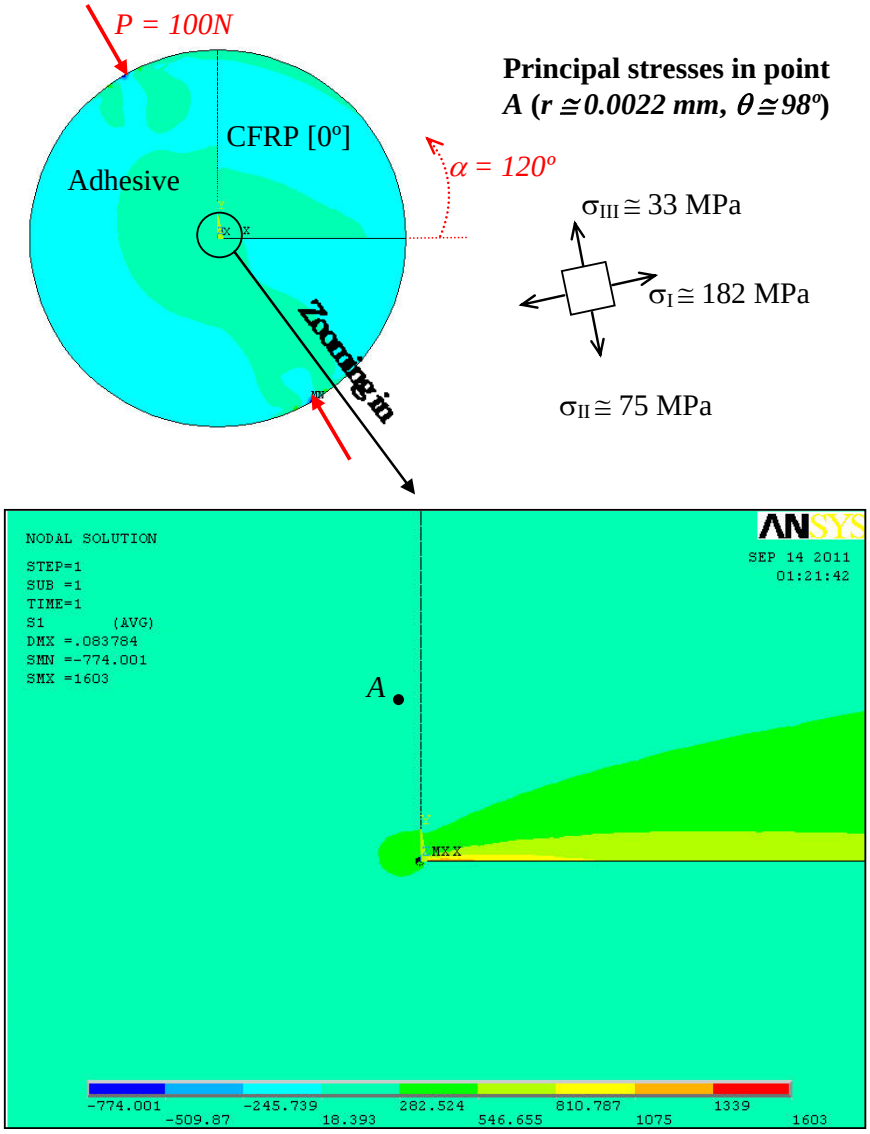

Fig. C.5 – Principal stresses at point A for $\alpha = 120^{o}$ and detail of σ_I.

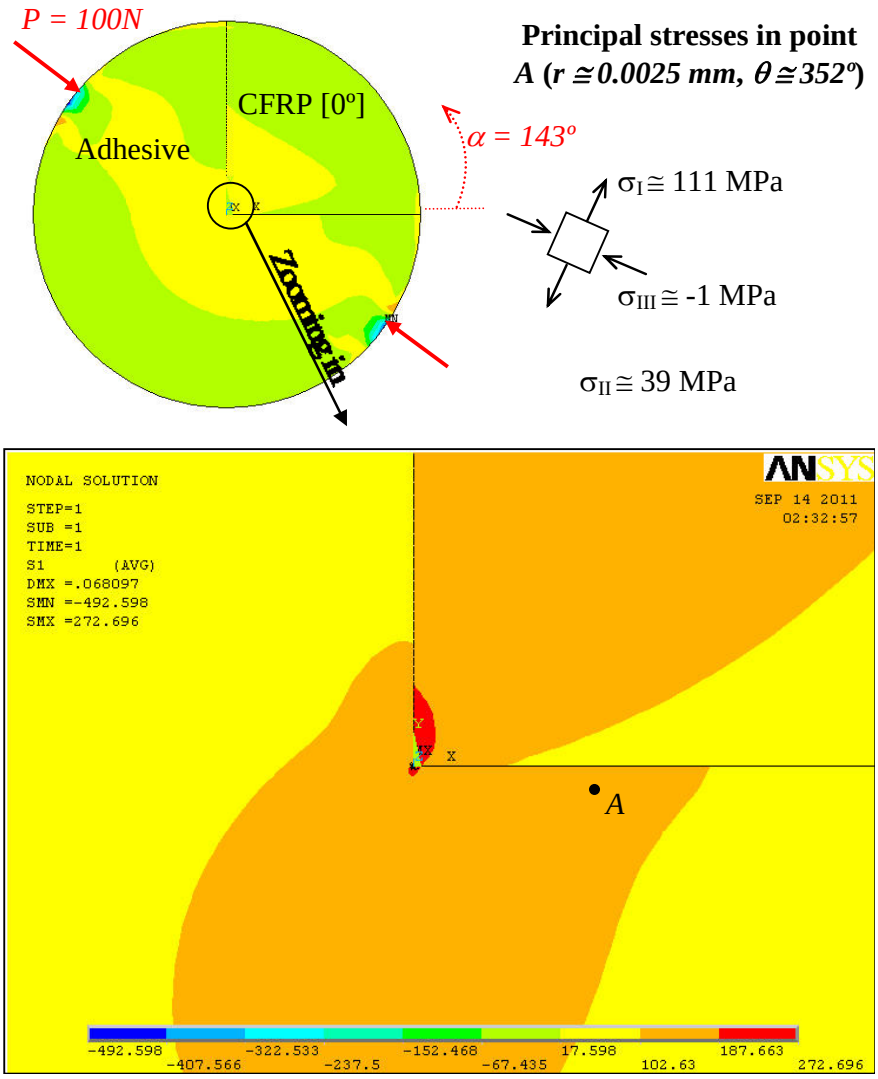

Fig. C.6 – Principal stresses at point A for $\alpha = 143^{o}$ and detail of σ_I .

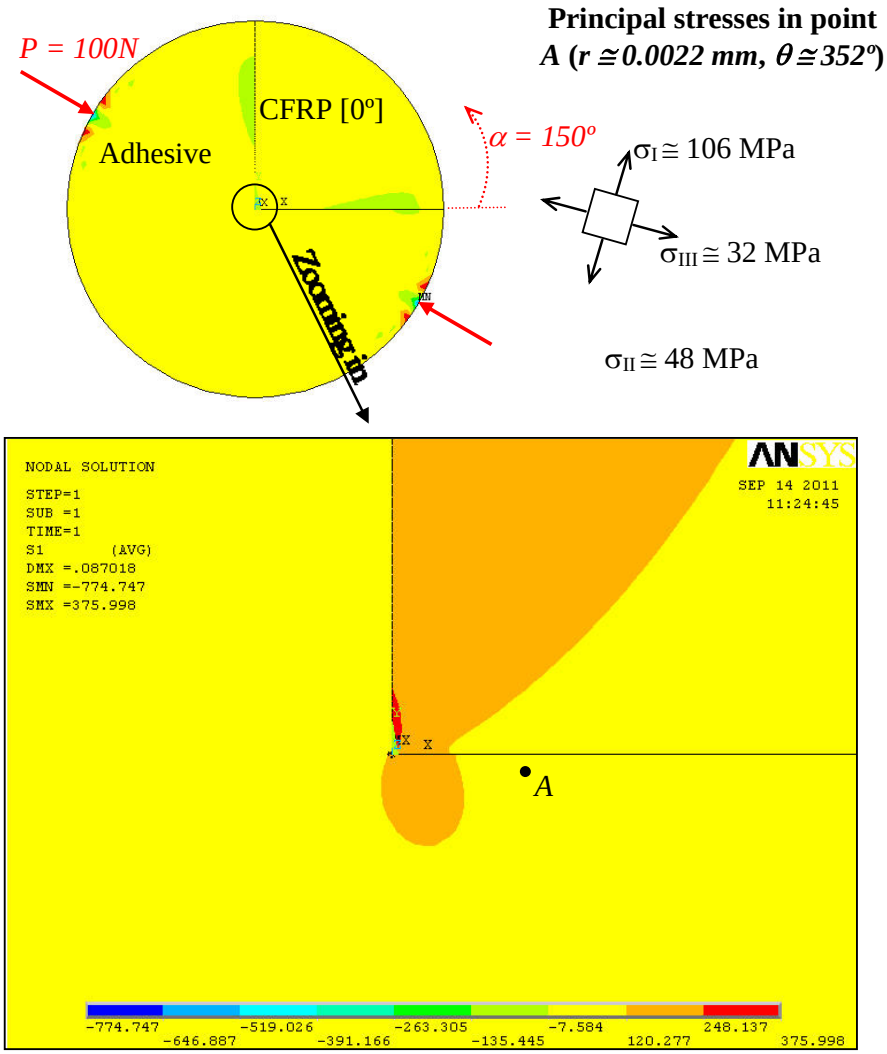

Fig. C.7 – Principal stresses at point A for $\alpha = 150^{o}$ and detail of σ_I.

Following, some comments and some observed aspects for each figure are presented.

In Fig. C.1: $|\sigma_{r\theta}| > \sigma_\theta > \sigma_r$ at the horizontal CFRP-Adhesive edge (this is valid up to $r \cong 1\ mm$). σ_r and σ_θ are both in tensile ($\sigma_\theta > \sigma_r$ up to $r \cong 0.18\ mm$). By the side of the adhesive (see Fig. B.1 c, in Appendix B) and for $r \cong 0.0010583\ mm$, σ_θ and $\sigma_{r\theta}$ are maximum at the horizontal CFRP-Adhesive interface.

In Fig. C.2: $|\sigma_{r\theta}| > \sigma_\theta > \sigma_r$ at the horizontal CFRP-Adhesive edge (this is valid up to $r \cong 0.3266\ mm$). σ_r and σ_θ are both in compression ($\sigma_\theta > \sigma_r$ up to $r \cong 0.3266\ mm$). By the side of the adhesive (see Fig. B.2 c and d, in Appendix B) and for $r \cong 0.0010583\ mm$, σ_θ is practically null for all range and $\sigma_{r\theta}$ is maximum at the horizontal CFRP-Adhesive interface.

In Fig. C.3: $\sigma_\theta > |\sigma_{r\theta}| > \sigma_r$ at the vertical CFRP-Adhesive edge (this is valid up to $r \cong 0.655\ mm$). σ_r is in compression and σ_θ in tensile almost the entire range ($\sigma_\theta > \sigma_r$ up to $r \cong 1\ mm$). By the side of the adhesive (see Fig. B.3 c and d in Appendix B) and for $r \cong 0.0010583\ mm$, σ_θ is maximum at the vertical CFRP-Adhesive interface.

In Fig. C.4: $\sigma_\theta > \sigma_r > |\sigma_{r\theta}|$ at the vertical CFRP-Adhesive edge (this is valid up to $r \cong 0.0045\ mm$). σ_r and σ_θ are in tensile (σ_r up to $r \cong 0.034\ mm$). By the side of the adhesive (see Fig. B.4 c and d in Appendix B) and for $r \cong 0.0010583\ mm$, σ_θ is maximum at the vertical CFRP-Adhesive interface.

In Fig. C.5: $\sigma_\theta > \sigma_r > |\sigma_{r\theta}|$ at the vertical CFRP-Adhesive edge (this is valid up to $r \cong 0.003\ mm$). σ_r and σ_θ are in tensile (σ_r up to $r \cong 0.044\ mm$). By the side of the adhesive (see Fig. B.5 c and d in Appendix B) and for $r \cong 0.0010583\ mm$, σ_θ is maximum close to the vertical CFRP-Adhesive interface (at $\alpha \cong 105^o$).

In Fig. C.6: $\sigma_\theta > \sigma_r > |\sigma_{r\theta}|$ at the horizontal CFRP-Adhesive edge (this is valid up to $r \cong 0.0004\ mm$). $\sigma_\theta > |\sigma_{r\theta}| > \sigma_r$ at the horizontal CFRP-Adhesive edge (this is valid from $0.0004 < r < 0.0079\ mm$). σ_θ and σ_r are in tensile (up to $r \cong 0.1123\ mm$ and $r \cong 0.085\ mm$ respectively). By the side of the adhesive (see Fig. B.6 c and d in Appendix B) and for $r \cong 0.0010583$, σ_θ maximum is close to the horizontal CFRP-Adhesive interface (at $\alpha \cong 330^o$).

In Fig. C.7: $\sigma_\theta > \sigma_r > |\sigma_{r\theta}|$ at the horizontal CFRP-Adhesive edge (this is valid up to $r \cong 0.0099\ mm$). $\sigma_\theta > |\sigma_{r\theta}| > \sigma_r$ at the horizontal

CFRP-Adhesive edge (this is valid from $0.0099 < r < 0.041\ mm$). σ_θ and σ_r are in tensile (up to $r \cong 0.207\ mm$ and $r \cong 0.131\ mm$ respectively). By the side of the adhesive (see Fig. B.7 c and d in Appendix B) and for $r \cong 0.0010583$, σ_θ maximum at the horizontal CFRP-Adhesive interface.

References

ADAMS, R. D.; COPPENDALE, J.; PEPPIATT, N. A. (1978) "Adhesion 2", Allen, K. W. ed., Applied Science Publishers, London, 105-120.

AKAZAWA, M. T. (1943). "Méthode pour l'essai de traction de bétons". Journal of the Japanese Civil Engineering Institute (November).

AKAZAWA, M. T. (1953). "Methode pour l'essai de traction des betons". RILEM Bulletin, 16, 12-23.

ANDERSON, T. L. (1995). "Fracture mechanics Fundamentals and applications". 2nd ed., CRC Press,

ANDRUET, R. H.; DILLARD, D. A.; HOLZER, S. M. (2001). "Two and three-dimensional geometrical nonlinear finite elements for analysis of adhesive joints". Int. J. Adh. & Adhesives, 21, 17-34.

ANSARIFAR, M. A.; ZHANG, J., BAKER, J.; BELL, A.; ELLIS, R. J. (2001). "Bonding properties of rubber to steel, aluminium and nylon 6,6". Int. J. Adhesion Adhesives 21, 369.

ARGESO, H.; ERASLAN, A. N. (2008). "On the use of temperature-dependent physical properties in thermomechanical calculations for solid and hollow cylinders." Int. J. Therm. Sci., 47, 136-146.

ASHCROFT, I. A.; CROCOMBE, A. D. (2008) "Modelling Fatigue in Adhesively Bonded Joints". Modeling of Adhesively Bonded Joints, ed. L. M. Silva and A. Öchsner, Springer.

ASHCROFT, I. A.; HUGHES, D. J.; SHAW, S. J.; WAHAB, M. A.; CROCOMBE, A. (2001). "Effect of temperature on the quasi-static strength and fatigue resistance of bonded composite double lap joints", J. Adhesion, Vol. 74, 61 – 88.

ASHCROFT, I. A.; SHAW, S. J. (2002). "Mode I fracture of epoxy bonded composite joints 2. Fatigue loading". Int. J. Adhesion & Adhesives, 22, 151 – 167.

ASHCROFT, I. A.; SHENOY, G. W.; CRITCHLOW, G. W.; CROCOMBE, A. D. (2010). "A comparison of the prediction of fatigue damage and crack growth in adhesively bonded joints using fracture mechanics and damage mechanics progressive damage methods". J. Adhesion 86, 1203.

ASTM D3166 (1979). "Standard Test Method for Fatigue Properties of Adhesives in Shear by Tension Loading (Metal/Metal)".

ASTM D3528-96 (2002). "Standard test method for strength properties of double lap shear adhesive joints by tension loading".

ASTM D3967 (2005). "Standard test method for splitting tensile strength of intact rock core specimens."

ASTM D5045-99 (2007). "Standard test methods for plane-strain fracture toughness and strain energy release rate of plastic materials".

ASTM E399-05. "Standard test method for linear-elastic plane-strain fracture toughness K_{IC} of metallic materials".

ATKINSON, C.; BOURNE, J. P. (1990). "Stress singularities in angular sectors of viscoelastic media." Int. J. Eng. Sci., 28, 615-630.

AWAJI, H.; SATO, S. (1978). "Combined mode fracture toughness measurement by the disk test". Trans. ASME, J. Eng. Mater. Technology, 100, 175-182.

AYDN, M. D. (2008). "3D Nonlinear stress analysis on adhesively bonded single lap composite joints with different ply stacking sequences". The Journal of Adhesion, 84, 15 - 36.

BALDAN, A. (2004). "Review adhesively-bonded joints in metallic alloys, polymers and composite materials: mechanical and

environmental durability performance". J. Mat. Science, 39, 4729-4797.

BALKOVA, R.; HOLONEROVA, S.; CECH, V. (2002). Ibid. 22, 291, Locitite Corporation. In: Locitite Worlwide Design Handbook, Edition 1996/1997.

BANKS-SILLS, L.; ASHKENAZI, D. (2000). "A note on fracture criteria for interface fracture". Int. J. Fracture, 103, 177-188.

BARENBLATT, G. I. (1962). "The mathematical theory of equilibrium cracks in brittle fracture". In: Advances in Applied Mechanics. 7, 55-129.

BARROSO, A. (2007). "Singular stress state characterization in multimaterial corners. Application to adhesive joints with composite materials." PhD Thesis (in Spanish), University of Seville.

BARROSO, A.; GRACIANI, E.; MANTIČ, V.; PARÍS, F. (2012). "A least squares procedure for the evaluation of multiple generalized stress intensity factors at 2D multimaterial corners by BEM". Eng. Analysis with Boundary Elements, 36, 458-470.

BARROSO, A.; MANTIČ, V.; PARÍS, F. (2003). "Singularity analysis of anisotropic multimaterial corners". Int. J. Fracture, 119, 1-23.

BARROSO, A.; MANTIČ, V.; PARÍS, F. (2009). "Computing stress singularities in transversely isotropic multimaterial corners by means of explicit expressions of the orthonormalized Stroh-eigenvectors". Eng. Fract. Mech., 76, 250-268.

BARROSO, A.; PARÍS, F.; MANTIČ, V. (2009). "Representativity of the singular stress state in the failure of adhesively bonded joints between metals and composites". Composites Science and Technology, 69, 1746-1755.

BARROSO, A.; VICENTINI, D.; MANTIČ, V.; PARÍS, F. (2012). "Determination of Generalized Fracture Toughness in composite multimaterial closed corners with two singular terms – Part I: Test proposal and numerical analysis" Eng. Fracture Mech. (accepted).

BARROSO, A.; VICENTINI, D.; PARÍS, F.; MANTIČ, V. (2011). "Representativity of thermal stresses in designing composite joints based on singular stress states at multimaterial corners." Composites: Part A, 42, 1084-1092.

BASCOM, W. D.; COTTINGTON, R. L. (1972). "Air entrapment in the use of structural adhesive films". J. Adhesion, 4, 193-209.

BAŽANT, Z. P. (2001). "Size effect on structural strength". Handbook of Materials Behaviour Models, sec. 1.3, Academic Press.

BELINGARDI, G.; GOGLIO, L.; TARDITI, A. (2002). "Investigating the effect of spew and chamfer size on the stresses in metal/plastics adhesive joints". Int. J. Adh. & Adhesives, 22, 273-282.

BERENBAUM, R.; BRODIE, I. (1959). "Measurement of the tensile strength of brittle materials". Br. d. Appl. Phys., 10, 281-287.

BIGWOOD, D. A.; CROCOMBE, A. D. (1989). "Elastic analysis and engineering design formulae for bonded joints". Int. J. Adhesion and Adhesives, 9, 229-242.

BIGWOOD, D. A.; CROCOMBE, A. D. (1990). "Non-linear adhesive bonded joint design analyses". Int. J. Adhesion and Adhesives, 10, 31-41.

BOGDANOVICH, A. E.; KIZHAKKETHARA, I. (1999). "Three-dimensional finite element analysis of double-lap composite adhesive bonded joint using submodeling approach". Composites: Part B 30, 537-551.

BOWDEN, P. B.; JUKES, J. A. (1972). "The plastic flow of isotropic polymers". J. Mat. Science, 7, 52-63.

BREBBIA, C. A.; DOMINGUEZ, J. (1992). "Boundary elements: an introductory course", 2nd edition, Computacional Mechanics Publications, Southampton, Mcgraw-Hill Book Company.

BROEK, D. (1984). "Elementary engineering fracture mechanics", 3rd edition, Martinus Nijhoff Publishers, Netherlands, page 88.

BROUGHTON, W. R.; CROCKER, L. E.; URQUHART, J. M. (2001). "Strength of adhesive joints: a parametric study". NPL Report MATC(A)27.

CADDELL, R. M.; RAGHAVA, R. S.; ATKINS, A. G. (1973). "A yield criterion for anisotropic and pressure dependent solids such as oriented polymers". J. of Materials Science, 8, 1641-1646.

CAMPBELL, C. F. (2006). "Manufacturing Technology for Aerospace Structural Materials". 1st edition, Elsevier, Great Britain.

CARNEIRO, F. L. L. B. (1943). "A new method to determine the tensile strength of concrete". Proceedings of the 5th meeting of the ABNT, 3rd section (September), 126-129 (in Portuguese).

CARNEIRO, F. L. L.; BARCELLOS, A. (1953). "Resistance a la traction des betons". International Association of Testing and Research Laboratories for Materials and Structures, RILEM Bulletin num. 13, 103-108.

CHEN, W. F.; HAN, D. J. (1988). "Plasticity for structural Engineers". Springer-Verlag Ed.

CHIANG, M. Y. M.; CHAI, H. (1994). "Plastic deformation analysis of cracked adhesive bonds loaded in shear". Int. J. Solids Struct., 31, 2477-2490.

CHOWDHURY, S. R.; NARASIMHAN, R. (2000). "A finite element analysis of quasistatic crack growth in a pressure sensitive constrained ductile layer". Eng. Fract. Mech., 66, 551-571.

COGNARD, P. (2006). "Adhesives and sealants General knowledge, application techniques, new curing techniques Handbook of adhesives and sealants", Vol. 2, Ed. Elsevier.

CRISFIELD, M. A. (1997). "Non-linear finite element analysis of solids and structures", Vol. I, Vol. II (Advanced Topics).

CROCOMBE, A. D.; ADAMS, R. D. (1981). "Influence of the spew fillet and other parameters on the stress distribution in the single lap joint." J. Adhesion, 13, 141-155.

CROCOMBE, A. D.; RICHARDSON, G.; SMITH, P. A. (1995). "A unified approach for predicting the strength of cracked and non-cracked adhesive joints". J. Adhesion, 49, 211-244.

DA SILVA, L. F. M.; ADAMS, R. D.; GIBBS, M. (2004). "Manufacture of adhesive joints and bulk specimens with high-temperature adhesives". Int. J. Adhesion & Adhesives, 24, 69-83.

DA SILVA, L. F. M.; NEVES, P. J. C.; ADAMS, R. D.; SPELT, J. K. (2009). "Analytical models of adhesively bonded joints – Part I: Literature survey". Int. J. Adhes. & Adhesives, 29, 319–330.

DA SILVA, L. F. M.; NEVES, P. J. C.; ADAMS, R. D.; WANG, A.; SPELT, J. K. (2009). "Analytical models of adhesively bonded joints – Part II: Comparative study". Int. J. Adh. & Adhesives, 29, 331–341.

DAVIS, M.; BOND, D. (1999). "Principles and practices of adhesive bonded structural joints and repairs". Int. J. Adhesion Adhesives 19, 91.

DE BRUYNE, N. A. (1944). "The strength of glued joints". Aircraft Eng. and Aerospace Technology, 16, 115-118.

DEAN, G.; CROCKER, L. (2000). "Comparison of the measured and predicted deformation of an adhesively bonded lap-joint specimen". Project PAJex1, Report nº2, NPL Report CMMT(A)293.

DEAN, G.; CROCKER, L. (2001). "The use of finite element methods for design with adhesives". Measurement Good Practice Guide, 48.

DEMPSEY, J. P.; SINCLAIR, G. B. (1979). "On the stress singularities in the plane elasticity of the composite wedge". J. Elasticity, 9, nº 4.

DEMPSEY, J. P.; SINCLAIR, G. B. (1981). "On the singular behaviour at the vertex of a bi-material wedge". J. Elasticity, 11, nº 3.

DENG, J.; LEE, M. M. K. (2007). "Fatigue performance of metallic beam strengthened with a bonded CFRP plate". Composite Structures, 78, 222 – 231.

DRUCKER, D. C.; PRAGER, W. (1952). "Soil mechanics and plastic analysis or limit design", Q. Appl. Math., 10, 157-165.

DUNDURS, J. (1969). "Edge-bonded dissimilar orthogonal elastic wedges under normal and shear loading". J. Applied Mech., 650-652.

DUNN, M. L.; HUI, C. Y.; LABOSSIERE; P. E. W.; LIN, Y. Y. (2001). "Small scale geometric and material features at geometric discontinuities and their role in fracture analysis". Int. J. Fract., 110, 101-121.

ERPOLAT, S.; ASHCROFT, I. A.; CROCOMBE, A. D.; ABDEL-WAHAB, M. M. (2004). "A study of adhesively bonded joints

subjected to constant and variable amplitude fatigue", Int. J. Fatigue, 26, pp. 1189 – 1196.

FAHAD, M. K. (1996). "Stresses and failure in the diametral compression test". J. of Mater. Sci., 31, 3723-3729.

FAIRBIAIRN, E. M. R.; ULM, F. -J. (2002). "A tribute to Fernando L. L. B. Carneiro (1913-2001) Engineer and scientist who invented the Brazilian Test". Materials and Structures, Vol. 35, 195-196.

FELDSTEIN, M. M. (2009). "Contribution of relaxation processes to adhesive-joint strength of viscoelastic polymers." Polym. Sci., 51, 1341-1354.

FERNLUND, G.; SPELT, J. K. (1991). "Failure load prediction of structural adhesive joints: part 2 experimental study". Int. J. Adhes. & Adhesives, 11, 221-227.

FISH, J.; BELYTSCHKO, T. (2007). "A first course in Finite Elements", John Wiley & Sons, Ltd.

GDOUTOS, E. E. (2005). "Fracture mechanics an introduction. Solid mechanics and its applications". Kluwer Academic Publishers, Springer.

GOLAND, M.; REISSNER, E. (1944). "The stresses in cemented joints", J. Appl. Mech., 11, A17-A27.

GONÇALVES, J. P. M.; MOURA, M. F. S. F.; CASTRO, P. M. S. T. (2002). "A three-dimensional finite element model for stress analysis of adhesive joints". Int. J. Adh. & Adhesives, 22, 357-365.

GOPAL, A. K.; ADALI, S.; VERIJENKO, V. E. (2000). "Optimal temperature profiles for minimum residual stress in the cure process of polymer composites." Compos. Struct., 48, 99-106.

GRACIANI, E. (2006). "Boundary element method formulation and implementation for axisymetric problems with contact. Application to the characterization of the fibre-matrix interface in composite materials". PhD Thesis (in Spanish), University of Seville.

GRADIN, P. (1982) "A fracture criterion for edge bonded bimaterial bodies". J. of Composite Materials 16, 448-456.

GROTH, H. L. (1985). "A method to predict fracture in an adhesive bonded joint", International Journal of Adhesion and Adhesives 5, No. 1, 19-22.

GROTH, H. L. (1988). "Stress singularities and fracture at interface corners in bonded joints". Int. J. of Adhesion and Adhesives 8, No. 2, 107-113.

HADAVINIA, H.; KINLOCH, A. J.; LITTLE, M. S. G.; TAYLOR, A. C. (2003). "The prediction of crack growth in bonded joints under cyclic-fatigue loading, I. Experimental studies". Int. J. Adhesion & Adhesives, 23, 449 – 461.

HAFIZ, T. A.; ABDEL WAHAB, M. M.; CROCOMBE, A. D.; SMITH, P. A. (2010). "Mixed-mode fracture of adhesively bonded metallic joints under quasi-static loading". Eng. Fract. Mech., 77, 3434-3445.

HART-SMITH, L. J. (1973). "Adhesive bonded double lap joints". NASA CR-112235.

HART-SMITH, L. J. (1973). "Adhesive bonded single lap joints". NASA CR-112236.

HART-SMITH, L. J. (1973). "Adhesive-bonded scarf and stepped-lap joints". NASA CR-112237.

HART-SMITH, L. J. (1974). "Analysis and design of advanced composite bounded joints". NASA CR-2218.

HATTORI, T. (1991). "A stress-singularity-parameter approach for evaluating the adhesive strength of single-lap joints". Jpn. Soc. Mech. Eng., 34, 3, 326-331.

HIGGINS, A. (2000). "Adhesive bonding of aircraft structures". Int. J. Adh. & Adhesives, 20, 367-376.

HILLERBORG, A., MODEER, M.; PETERSSON, P.E. (1976). "Analysis of crack formation and crack growth in concrete by means of fracture mechanics and finite elements". Cem. Concr. Res., 6, 773-782.

HOJJATI, M.; JOHNSTON, A.; HOA, S. V.; DENAULT, J. (2004). "Viscoelastic Behaviour of Cytec FM73 adhesive during cure." J. Appl. Polym. Sci., 91, 2548-2557.

HUANG,Y.; LIU, C.; STOUT, M. G. (1996). "A Brazilian disk for measuring fracture toughness of orthotropic materials." Acta mater., 44, 1223-1232.

ICHIKAWA, K.; SHIN, Y.; SAWA, T. (2008). "A three-dimensional finite element stress analysis and strength evaluation of stepped-lap adhesive joints subjected to static tensile loadings". Int. J. Adh. & Adhesives, 28, 464-470.

IRWIN, G. R. (1957). "Analysis of stresses and strains near the end of a crack traversing a plate." Trans. ASME J. Appl. Mech., Vol. 24, 361-364.

JAEGER, J.C.; HOSKINS, E. R. (1966). "Rock failure under confined Brazilian Test". J. Geophy. Res., 71, 2651-2659.

JONES, R. M. (1999). "Mechanics of composite materials". Taylor & Francis Ed., USA.

JUMBO, F.; RUIZ, P. D.; YU, Y.; SWALLOWE, G. M.; ASHCROFT, I.; HUNTLEY, J. M. (2007). "Experimental and numerical investigations of mechanical and thermal residual strains in adhesively bonded joints". Strain, 43, 319-331.

KAY, N.; BARUT, A.; MADENCI, E. (2002). "Singular stresses in a finite region of two dissimilar viscoelastic materials with traction-free edges." Comput. Methods Appl. Mech. Eng., 191, 1221-1244.

KINLOCH, A. J.; OSIYEMI, S. O. (1993). "Predicting the fatigue life of adhesively-bonded joints". J. Adhesion, 43, 79 – 90.

LANDROCK, A. H. (1985). "Adhesive Technology Handbook" (Noyes Publication, Park Ridge, NJ.

LEE, S.S. (1998). "Boundary element análisis of the stress singularity at the interface corner of viscoelastic adhesive layers". Int. J. Solids Struct., 35, 1385-1394.

LEGUILLON, D. (2001). "A criterion for crack nucleation at a notch in homogeneous materials." CR Acad. Sci. , Paris, 329 (II B), 97-102.

LEGUILLON, D. (2002). "Strength or toughness? A criterion for crack onset at a notch." Eur. J. Mech. A./Solids, 21, 61-72.

LEGUILLON, D.; SANCHEZ-PALENCIA, E. (1987). “Computation of singular solutions in elliptic problems and elasticity”. Masson Ed., Paris, France.

LEKHNITSKII, S. G. (1981). “Theory of elasticity of an anisotropic body”. Mir Publishers, Moscow.

LERCH, B. A.; THESKEN, J. C.; BUNNELL, C. T. (2007). “Polymethylmethacrylate (PMMA) material test results for the capillary flow experiments (CFE)”, NASA/TM, 214835.

LILJEDAHL, C. D. M.; CROCOMBE, A. D.; WAHAB, M. A.; ASHCROFT, I. A. (2006). “Modelling the Environmental degradation of the interface in adhesively bonded joints using a cohesive zone approach”. The Journal of Adhesion, 82, 1061-1089.

LIU, C; HUANG, Y.; LOVATO, M. L.; STOUT, M. G. (1997). “Measurement of the fracture toughness of a fiber-reinforced composite using the Brazilian disk geometry”. Int. J. Fract., 87, 241–263.

LIU, C; HUANG, Y.; STOUT, M. G. (1998). “Enhanced mode-II fracture toughness of an epoxy resin due to shear banding”. Acta Mater., 46, 5647-5661.

LIU, S. C. (1999). "Residual stress characterization for laminated composites." PhD Thesis, University of Florida.

LOPES, M. C.; VENTURINI, W. S. (1997). "Cohesive crack analysis by the boundary element method". In: Complas V, eds. Oñate, E. & Owen, D.R.J., Pineridge Press.

MANTIČ, V.; PARÍS, F.; CAÑAS, J. (1997). "Stress singularities in 2D orthotropic corners". Int. J. Fract., 83, 67-90.

MARION, R. H.; JOHNSTONE, J. K. (1977). "A parametric study of the diametral compression test for ceramics". Am. Ceram. Soc. Bull.56, 998-1002.

MARKOLEFAS, S. I.; PAPATHANASSIOU, TH. K. (2009). "Stress redistributions in adhesively bonded double-lap joints, with elastic-perfectly plastic adhesive behaviour, subjected to axial lap-shear cyclic loading". Int. J. Adhesion & Adhesives, 29, 737 – 744.

MATSUMOTO, T.; GUZIK, A.; TANAKA, M. (2005). "A boundary element method for análisis of thermoelastic deformations in materials with temperatura dependent properties." Int. J. Numer. Meth. Eng., 64, 1432-1458.

MATTHEWS, F. L. (1994). “Handbook of polymer composites for engineers”, Chapter 8, Edited by Leonard Hollaway, Woodhead Publising Ltd., Cambridge, England.

MAYS, G. C.; HUTCHINSON, A. R. (1992). Adhesives in civil engineering. Cambridge University Press, UK.

MIL-HDBK-17. “Composite materials handbook. Materials usage, design, and analysis,” Vol. 3, Lancaster, PA, USA: Published jointly by Technomic Publishing Co. Inc. and Materials Sciences Corporation in Cooperation with ASTM. p. 4–60.

MINER, M. A. (1945). “Cumulative damage in fatigue” ASME Trans., J. Appl. Mech. 67, A159- A164.

NEWMAN, D. A.; BENNETT, D. G. (1990). “The effect of specimen size and stress rate for the Brazilian Test – a statistical analysis”. Rock Mechanics and Rock Engineering, 23, 123-134.

NODA, N. (1986). “Stresses in materials with temperatura dependent properties.” In: Hetnarsky RB, ed. Thermal stresses I, North-Holland, Amsterdam. Elsevier Science, chapter 6, 391-483.

OÑATE, E. (1992). “Cálculo de estructuras por el método de elementos finitos: análisis elástico-lineal”, CIMNI, Barcelona.

ORTIZ, J.; BARROSO, A., MANTIČ, V.; PARÍS, F. (2005). "Numerical characterization of 3-D multimaterial corners", Proc. MATCOMP'05, Valencia, Spain (in Spanish).

OVRI J.E.O.; DAVIES, T. J. (1987). "Diametral compression of silicon nitride". Mater. Sci. Eng. 96, 109-116.

PAGEAU, S. S.; GADI, K. S.; BIGGERS, S. B.; JOSEPH, P. F. (1996). Standardized complex and logarithmic eigensolutions for n-material wedges and junctions. Int. J. Fract., 77, 51-76.

PARÍS, F.; CAÑAS, J. (1997). "Boundary element method fundamentals and applications" Oxford, Oxford University Press.

PARÍS, F.; CAÑAS, J.; MARÍN, J. (2006). "Introducción al análisis y diseño con materiales compuestos" Sección de publicaciones, Escuela Técnica Superior de Ingenieros, Universidad de Sevilla, Seville (in Spanish).

PARLEVLIET, P. P.; BERSEE, H.; BEUKERS, A. (2006). "Residual stresses in thermoplastic composites – a study of the literature – Part I: Formation of residual stresses". Composites: Part A, 37, 1847-1857.

PATE, K. D. (2002). "Applications of adhesives in aerospace", Adhesion science and engineering 2: Surfaces, Chemistry and Applications, Chap. 25, 1129-1192.

PIRONDI, A.; MORONI, F. (2009). "An investigation of fatigue failure prediction of adhesively bonded metal/metal joints". Int. J. Adhesion & Adhesives, 29, 796 – 805.

POTTER, K. D.; GUILD, H. J.; HARVEY, M. R.; WISNOM, R. D.; ADAMS, R. D. (2001). "Understanding and control of adhesive crack propagation in bonded joints between carbon fibre composite adherends I. Experimental". Int. J. Adhesion & Adhesives, 21, 435 – 443.

PRICE, H.L.; MURRAY, K. H. (1973). "Finite element analysis of the diametral test of polymer moldings". J. Eng. Mater. Tech. July, 186-191.

QIAN, Z. Q.; AKISANYA, A. R.; IMBABI, M. S. (2000). "Edge effects in the failure of elastic/viscoelastic joints subjected to surface tractions". Int. J. Solids Struct., 37, 5973-5994.

QUARESIMIN, M.; RICOTTA, M. (2006). "Life prediction of bonded joints in composite materials". Int. J. Fatigue, 28, 1166 – 1176.

QUARESIMIN, M.; RICOTTA, M. (2006). "Stress intensity factors and strain energy release rates in single lap bonded joints in composite materials." Compos. Sci. Technol., 66, 647-656.

RAGHAVA, R.; CADDELL, R. M.; YEH, G. S. Y. (1973). "The macroscopic yield behaviour of polymers". J. Mat. Science, 8, 225-232.

REEDY, JR. E. D. (2000). "Connection between interface corner and interfacial fracture analyses of an adhesively bonded butt joint." Int. J. Solids Struct., 37, 2443-2471.

RICHARDSON, G., CROCOMBE, A. D. Y SMITH, P. A. (1993). "A comparison of two and three-dimensional finite element analyses of adhesive joints". Int. J. Adh. & Adhesives, 13, 3, 193-200.

SAUER, J. A.; RICHARDSON, G. C. (1980). "Fatigue of polymers", Int. J. of Fracture, vol. 16, 6, 499 – 532.

SCHÖN, J.; STARIKOV, R. (2003) "Fatigue of joints in composite structures" – from book "Fatigue in composites", ed. Bryan Harris, CRC Press.

SHENOY, V.; ASHCROFT, I.A.; CRITCHLOW, G.W.; CROCOMBE, A.D.; ABDEL WAHAB, M.M. (2009). "An investigation into the crackinitiation and propagation behaviour of bonded single-lap joints using backface strain." Int. J. Adhes. & Adhesives, 29, 361-371.

SHETTY, D. K.; ROSENFIELD, A. R.; DUCKWORTH, W. H. (1987). "Mixed-mode fracture in biaxial stress state: application

of the diametral-compression (Brazilian disk) test". Eng. Fract. Mech., 26, 825-840.

SPRIGGS, R.M.; BRISSETTE, L. A.; VASILOS T. (1964). "Tensile strengths of dense polycrystalline ceramics by the diametral-compression test". Mater. Res. Stand., May 4, 218-220.

STROH, A.N. (1962). "Steady state problems in anisotropic elasticity". J. Math. Physics, 41, 77-103.

TESORIERE, G.; MARINO, S. (1990). "Thermic Effects for Rupture Tests at Indirect Tensile Test on Asphalt Concrete". Proceedings of the Fourth International Symposium Held by RILEM, Budapest, 320-328.

TING, T. C. T. (1996). "Anisotropic elasticity: Theory and applications". Oxford University Press, United States.

TING, T. C. T. (1997). "Stress singularities at the tip of interfaces in polycrystals". Damage and Failure of Interfaces, Rossmanith (ed.), Balkema, Rotterdam, 75-82.

TSAI, M. Y.; MORTON, J. (1994). "Three-dimensional deformations in a single-lap joint". J. Strain An. 29, 1, 137 – 145.

TSAI, M. Y.; MORTON, J. (1995). "The effect of a spew fillet on adhesive stress distributions in laminated composite single-lap joints". Composite Structures, 32, 123-131.

TSAI, M.Y.; MORTON, J.; OPLINGER, D. W. (1996). "In Situ Determination of Adhesive Shear Moduli Using Strain Gages". Experimental Mechanics, 36, 297-304.

TSAI, M.Y.; OPLINGER, D. W.; MORTON, J. (1998). "Improved theoretical solutions for adhesive lap joints". lnt. J. Solids Structures, 35, 1163-1185.

UNE-EN ISO 9664 (1996) – "Adhesivos, Métodos de ensayo para la resistencia a la fatiga por esfuerzo de cizalla de adhesivos estructurales".

VASILOPOULOS, D. (1988). "On the determination of higher order terms of singular elastic stress fields near corners". Numer. Math., 53, 51-95.

VICENTINI, D. F. (2006). "Boundary element formulations applied to fracture mechanics". M.Sc. Dissertation (in Portuguese), São Carlos School of Engineering. University of São Paulo.

VICENTINI, D.; BARROSO, A.; JUSTO, J.; MANTIČ, V.; PARÍS, F. (2012). "Determination of Generalized Fracture Toughness in composite multimaterial closed corners with two singular terms – Part II: Experimental results". Eng. Fracture Mech. (under review).

VILLAR, E. G. (2006). "Efecto de la temperatura en la tenacidad de diferentes mezclas bituminosas". MSc. Dissertation (in Spanish), Polytechnic University of Catalonia. Available (24 of May, 2011) in: http://hdl.handle.net/2099.1/3324

VOLKERSEN, O. (1938). "Die Nietkraftverteilung in zugbeanspruchten Nietverbindungen mit konstanten Laschenquerschnitten". Luftfahrtforschung; 15, 41-47.

WAH T. (1973). "Stress distribution in a bonded anisotropic lap joint". J. Eng. Materials and Technology, ASME, 95, 174-181.

WANG, C. H.; CHALKLEY, P. (2000). "Plastic yielding of a film adhesive under multiaxial stresses". Int. J. Adh. & Adhesives, 20, 155-164.

WANG, J. S.; SUO, Z. (1990). "Experimental determination of interfacial toughness curves using brazil-nut-sandwiches." Acta Metall. Mater., 38, 1279-1290.

WEITSMAN, Y. (1980). "Residual thermal stresses in a symmetric double lap joint." J. Them. Stresses, 13, 521-535.

WIEGHARDT K. (1907). "Über das spalten und zerreissen elastischer körper". Z. Math. Phys. 55, 60–103.

WILLIAMS, M. L. (1952). “Stress singularities resulting from various boundary conditions in angular corners of plates in extension”. J. Appl. Mech., 19, 526 – 528.

WILLIAMS, M. L. (1957). “On the stress distribution at the base of a stationary crack”. J. Appl. Mech., 24, 109-114.

WILSON, C. D. (2002). “A Critical re-examination of classical metal plasticity”. J. App. Mech., 69, 63-68.

YADAGIRI, S.; REDDY, C. P.; REDDY, T. S. (1987). “Viscoelastic analysis of adhesively bonded joints.” Comput. Struct., 27, 445-454.

ZHANG, Y.; VASSILOPOULOS, A. P.; KELLER, T. (2008). “Stiffness degradation and fatigue life prediction of adhesively-bonded joints for fiber-reinforced polymer composites”. Int. J. Fatigue, 30, 1813 – 1820.

ZHANG, Y.; XIA, Z.; ELLYN, F. (2004). “Evolution and influence of residual stresses/strains of fibre reinforced laminates.” Compos. Sci. Technol., 64, 1613-1621.

ZHAO, L. G.; WARRIOR, N. A.; LONG, A. C. (2006). “A micromechanical study of residual stress and its effect on transverse failure in polymer-matrix composites.” Int. J. Solids Struct., 43, 5449-5467.

Internet references

Cytec.com	http://www.cytec.com/engineered-materials/products/FM73.htm
Broncesval.com	http://www.broncesval.com/catalogo/index.asp?categoria=1&producto=4
ALU-Stock.com	http://www.alu-stock.es/catalogo/cap.11_Aleaciones.pdf
Alcoa.com	http://www.alcoa.com/aerospace/en/products/product.asp?market_cat_id=347&prod_id=595
MakeItFrom.com	http://www.makeitfrom.com/data/?material=2024_Alum
Hexcel.com	http://www.hexcel.com/
	http://www.hexcel.com/Markets/Space%20and%20Defense

Publications

The following international and national publications have been originated during the work in the present Thesis.

a) International Journal Papers

1. BARROSO, A.; VICENTINI, D.; PARÍS, F.; MANTIČ, V. (2011). "Representativity of thermal stresses in designing composite joints based on singular stress states at multimaterial corners." Composites: Part A, 42, 1084-1092.

2. BARROSO, A.; VICENTINI, D.; MANTIČ, V.; PARÍS, F. (2012). "Determination of Generalized Fracture Toughness in composite multimaterial closed corners with two singular terms – Part I: Test proposal and numerical analysis" Eng. Fracture Mech., 89, 1-14.

3. VICENTINI, D.; BARROSO, A.; JUSTO, J.; MANTIČ, V.; PARÍS, F. (2012). "Determination of Generalized Fracture Toughness in composite multimaterial closed corners with two singular terms – Part II: Experimental results". Eng. Fracture Mech., 89,15-23.

4. VICENTINI, D.; CROCOMBE, A.; BARROSO, A.; PARÍS, F.; MANTIČ, V. (2012). "Fatigue crack initiation and damage characterization in Brazilian Test specimens for adhesive joints". J. Adhes. Sci. Technol., iFirst Article, 1-14 (DOI: http://dx.doi.org/10.1080/01694243.2012.698099).

5. BARROSO, A.; VICENTINI, D.; MANTIČ, V.; PARÍS, F. "Numerical models for design with adhesive joints" (in preparation).

6. VICENTINI, D.; BARROSO, A.; MANTIČ, V.; PARÍS, F.; CANALES, D. "Mechanical performance of adhesive joints manufactured with autoclave and hot plate press techniques" (in preparation).

b) Monograph

1. VICENTINI, D. (2011). "Failure characterization of aeronautical adhesive joints under fatigue loading". Monograph ECSES2012-1, EADS Chair of Aeronautical Studies, SAND, Seville.

c) Chapter of encyclopedia

1. BARROSO, A.; VICENTINI, D.; PARÍS, F.; MANTIČ, V. (2014). "Thermal stresses in composite joints". Encyclopedia of Thermal Stresses, Springer, Section T, 5333-5344 (DOI: 10.1007/978-94-007-2739-7_419).

d) Conference papers

International

1. BARROSO, A.; VICENTINI, D.; MANTIČ, V.; PARÍS, F.; GRACIANI, E. (2009). "Effect of curing stresses at corners in adhesive joints with composite materials". ETDCM9 – 9th Seminar on Experimental Techniques and Design in Composite Materials, 30th September, Padova Vicenza, Italy.

2. BARROSO, A.; VICENTINI, D.; MANTIČ, V.; PARÍS, F. (2009). "Plasticity in bimaterial joints". Proceedings of V International Conference on Science and Technology of Composite Materials, 7th October, Donostia San Sebastian, Spain. ISBN 978-84-692-5483-7.

3. BARROSO, A.; VICENTINI, D.; MANTIČ, V.; PARÍS, F. (2009). "3D edge effects in adhesive CFRP-Al double-lap joints". Proceedings of V International Conference on Science and Technology of Composite Materials, 7th October, Donostia San Sebastian, Spain. ISBN 978-84-692-5483-7.

4. BARROSO, A.; VICENTINI, D.; MANTIČ, V.; PARÍS, F. (2010). "Plasticity effects in CFRP-Al adhesive joints". Proceedings of 11th Pan-American Congress of Applied Mechanics PACAM XI, 4th January, Foz do Iguaçu, Brazil. ISBN 978-85-85205-97-3 (available in: http://www.set.eesc.usp.br/pacam2010/)

5. BARROSO, A.; VICENTINI, D.; MANTIČ, V.; PARÍS, F. (2010). "Representativity of 2D numerical models near bimaterial corners in adhesive CFRP-Al lap joint". Proceedings of 11th Pan-American Congress of Applied Mechanics PACAM XI, 4th January, Foz do Iguaçu, Brazil. ISBN 978-85-85205-97-3 (available in: http://www.set.eesc.usp.br/pacam2010/)

6. VICENTINI, D.; BARROSO, A.; CROCOMBE, A.; PARÍS, F.; MANTIČ, V. (2011). "Fatigue crack initiation and damage characterization in Brazilian test specimens for adhesive joints". Proceedings of 1st edition of the International Conference on Structural Adhesive Bonding AB2011, 7th Jully, Porto, Portugal. ISBN 978-972-752-135-7.

7. VICENTINI, D.; BARROSO, A.; JUSTO, J.; MANTIČ, V.; PARÍS, F. (2011). "Toughness determination in composite multimaterial closed corners". Proceedings of The 18th International Conference on Composite Materials ICCM18, 21st August, Jeju, Korea.

National

1. VICENTINI, D.; BARROSO, A.; MANTIČ, V.; PARÍS, F.; CANALES, D. (2011). "Influence of the curing method on the failure of composite adhesive joints". IX Congreso Nacional de Materiales Compuestos, 5th July, Girona, Spain.

2. VICENTINI, D.; BARROSO, A.; JUSTO, J.; MANTIČ, V.; PARÍS, F. (2011). "A modified Brazilian test for the generalized-fracture-toughness determination in multimaterial corners. Numerical and experimental results". IX Congreso Nacional de Materiales Compuestos, 5th July, Girona, Spain.